CARRIER ESCAPE FROM SEMICONDUCTOR QUANTUM WELLS

By

BRUCE WARREN TAKASAKI, M.Sc., B.Sc

A Thesis
Submitted to the School of Graduate Studies
In Partial Fulfillment of the Requirements
for the Degree
Doctor of Philosophy

McMaster University

© copyright by Bruce Warren Takasaki, January 1996

DOCTOR OF PHILOSOPHY (1996) McMASTER UNIVERSITY
(physics) Hamilton, Ontario

TITLE: Carrier Escape from Semiconductor Quantum Wells.

AUTHOR: Bruce Warren Takasaki, M.Sc. (McMaster University)
B.Sc. (University of Waterloo)

SUPERVISOR: Dr. John S. Preston

NUMBER OF PAGES: xix, 190

CARRIER ESCAPE FROM SEMICONDUCTOR QUANTUM WELLS

Abstract.

The escape of photogenerated carriers from semiconductor quantum wells is investigated theoretically and experimentally. Calculations of the tunnelling, thermionic emission, and thermally-assisted tunnelling escape times are given, where the thermionic emission process is split into low and high field regimes. At low fields, the escape rate is limited by the diffusion of the continuum carriers away from the well, while at high fields, the scattering rate from the confined to continuum states is the limiting process.

Barrier lowering effects are reviewed. The image force barrier lowering in a quantum well is calculated in the classical quasi-static approximation where the diffusion current is included for the first time. Both bipolar and unipolar wells are considered. In each case, the diffusion current inhibits the image charge formation, resulting in significant reductions in the barrier lowering; this is quantified by the concept of the *effective image charge*. At high carrier densities in the well ($\geq 10^{12}$ cm^{-2}), it has a value approaching the electronic charge, while at low densities ($\leq 10^{10}$ cm^{-2}), it tends to zero. The only exception is in the case of majority carrier escape from a unipolar well, where at sufficiently high fields the barrier lowering is *independent of the electric field.*

Calculations of the 2D-to-3D scattering rate required for the high field description of thermionic emission are presented where the effects of a transverse electric field are explicitly included. Deformation potential and piezoelectric scattering by acoustic phonons are considered for the first time, as well as polar scattering by longitudinal optical (LO) phonons. It is found that polar LO phonon absorption dominates the thermionic emission rate at all temperatures despite its infinitesimal occupation factor at low temperatures. This is attributed to lowering of the effective barrier by an amount equal to the phonon energy. As the electric field is increased, the scattering function is smeared such that the rate is

reduced just above the barrier, while a low energy tail extends to energies below the barrier. The scattering function does *not* shift with the potential barrier as expected, nor does the scattering rate rise abruptly at the barrier energy. As a result, it is expected that image charge lowering of the barrier will have only a minor effect on thermionic emission rates, particularly at higher temperatures. Calculations are presented for a range of well widths and depths. It is found that the emission rate oscillates as a function of the well width, with the jumps in emission rate corresponding to the confinement of a new upper subband.

Fits to the calculated scattering functions are presented as the basis for a simplified thermionic emission calculation. The step function approximation gives a simple analytic formula but performs well only in limited cases. A more complex approach, where the scattering function is approximated as a Fermi-Dirac function, reproduces the results of the full calculation to within 10% in most situations.

Calculated electron escape times are compared with reported experimental values from an asymmetric GaAs/AlGaAs quantum well (Cavaillès, 1992) with qualitative success. While the bias dependence was well reproduced, the calculated thermionic emission times were slow by factors of ~3-5. The principal causes of this discrepancy are believed to be band non-parabolicities and inaccuracies in the 3D density of states.

Measurements of hole escape times in an InGaAsP/InP multiple quantum well laser structure using time-resolved photoconductivity (PC) are presented as a function of temperature and bias. These are compared with calculated values which reproduce the qualitative behaviour but underestimate the thermionic emission time by one to two orders of magnitude. This is attributed primarily to the complexity of the valence band structure, further illustrating its impact on thermionic emission calculations.

Acknowledgements.

I would like to thank my supervisor, Dr. John Preston, for his guidance and assistance throughout the course of my graduate career. Even when you didn't quite know what I was talking about, you managed to solve my toughest problems. You *are* the quick-answer-man. Thanks also to the members of my supervisory committee, Dr. David Venus and Dr. John Simmons, for their input and advice. The third chapter on image charge lowering is the result of your questions.

A very special thanks to my parents for supporting me throughout my academic career. This thesis would not have been possible without you. Yes, your children are finally finished school. And better yet: I have a job.

Thanks to Frank Hegmann for machining, buying, assembling, and buying so many things in the lab that I needed to use. Also for giving me so many great stories. Don't worry Frank, we're laughing *with* you... Thanks to Gary Dyck, for putting together our new cryostat and PL system and generally helping me out with experiments and keeping the lab running. Sorry I'm leaving you to defend the lab against those superconductivity guys all by your lonesome, but the battle was lost long ago anyways.

Thanks to Dr. Jack Evans and Dr. Norbert Peutz for the only samples I studied that actually worked, and all the stuff that went along with them. Thanks also to Kent Nickerson (wherever you are) for help with the gain-switched diode laser, and many other questions on high-speed measurements.

To Dr.'s Sylvain Charbonneau, Philip Poole, Ken McGreer, Dave Moss and all the other people I worked with at M23A (NRC): thanks for getting me started in carrier escape studies and being such prodigious writers. Maybe one day we'll actually finished what we started. A special thanks to Sylvain for being like a second supervisor and answering so

many questions. A very, very special 'thank you' goes to Dr. Michael Davies for all the effort he put into processing things for me when he really had no reason too. I only wish we could have made one work.

I would like to thank Eugene Tan for processing samples for me and for helping me in my one foray into the clean room, despite its unpleasant memory. A general thanks to all the guys in the Engineering Physics department for all their help, discussions, games of cards at lunch, and the occasional Friday afternoon beer.

A great big thanks to the Physics secretaries, Wendy, Rose, and Marg, the IMR secretaries, Marg and Laurie, the CEMD secretaries, Fran and Debbie, and the Eng. Phys. secretaries Bobby and Elaine, for all their help over the many, many years I have been here.

To all my friends on the softball, touch football, basketball and hockey teams: you no longer have any excuses. Thanks for all the fun, especially in softball. I'm just sorry I'm going to miss the steaks (pay up, Weasal!). A special thanks to all of the friends I've made here in Hamilton over the years. Thanks also to all the people who kept me from studying, especially the boys from Kingsmount and Paisley: Billy (B-Minor), Donny (Corncob), Duncan (Dirty Ducats), Eddy (L.L.), Mikey (Flair). I'm finally getting out of here. Hang in there, Billy.

Thanks to my roommate Pete, for being my roommate.

Thanks to Sidney, for being my deaf, dumb, and blind-in-one-eye pet rabbit. Not to mention all those little 'gifts' you've given me.

Finally, a special thanks to a dear friend who was there for me for so much of it.

This thesis and all of the calculations contained within were written, compiled, run (mostly), and printed on Apple Macintosh computers. The code for the numerical calculations was written in Metrowerks CodeWarrior C for the PowerMac. I shudder to think what life would have been like without these invaluable tools. Now if only I could stop playing Risk!...

Financial support was provided by the Natural Sciences and Engineering Research Council, the Ontario Centre for Materials Research, and McMaster University.

Table of Contents.

Table of Contents. vii
List of Figures. xi
List of Tables. xix

Chapter 1: Introduction. 1

Chapter 2: Escape from Semiconductor Quantum Wells. 9
2.1. The Quantum Well with No Electric Field: The Square Well Potential. 9
2.2. Quantum Well in an Electric Field. 11
2.3. Tunnelling from a Quantum Well in an Electric Field. 16
2.4. Thermionic Emission. 17
2.4.1. Thermionic emission at bulk-barrier junctions. 17
2.4.2. Thermionic emission from a quantum well under small electric fields. . 19
2.4.3. Thermionic emission from a quantum well under large electric fields. . . 22
2.5. Barrier Lowering Effects in Thermionic Emission. 24
2.5.1. Change in energy solution in triangular well. 25
2.5.2. The inclination of the potential well in an electric field. 26
2.5.3. Image charge lowering. 26
2.6. Thermally-Assisted Tunnelling. 31
2.7. Summary. 31

Chapter 3: Image Charge Lowering in Semiconductor Quantum Wells. 33
3.1. Introduction. 34
3.2. Calculating the Image Charge Effect in a Quantum Well. 35
3.2.1. The drift-diffusion equations. 35
3.2.2. Details of the calculation. 37
3.3 Results. 41
3.3.1. The oppositely charged unipolar well (minority unipolar). 41
3.3.2. The similarly charged unipolar well (majority unipolar). 47
3.3.3. The bipolar quantum well. 56
3.4. Summary of Drift-Diffusion Simulation Results. 64

Chapter 4: Electron-Phonon Scattering From 2D To 3D States. 65
4.1. Basic Properties of Phonons in Semiconductors. 66
4.2. Electron-phonon Scattering in Semiconductors. 69
4.2.1. The wavefunctions. 69
4.2.2. The summation over final states. 73
4.2.3. The general electron-phonon scattering rate. 76
4.3. Polar Optical Phonon Scattering. 77
4.4. Deformation Potential Scattering by Acoustic Phonons. 79
4.5. Piezoelectric Scattering by Acoustic Phonons. 80
4.6. Evaluation of the 2D-to-3D Scattering Rates. 84
4.7. Results. 88
4.7.1. The 60Å symmetric GaAs/$Al_{0.20}Ga_{0.80}As$ well. 89
4.7.2. The overlap function, $G_{n,n}(q_z)$. 91
4.7.3. 2D-to-3D scattering rates: polar optical phonons. 93
4.7.4. 2D-to-3D scattering rates: longitudinal acoustic phonons via the deformation potential. 95
4.7.5. 2D-to-3D scattering rates: longitudinal and transverse acoustic phonons via piezoelectric coupling. 98
4.7.6. 2D-to-3D scattering rates: summary. 99
4.7.7. Electron thermionic emission rates. 101

4.7.8. The effect of a transverse electric field. 104
4.7.9. Simplified calculations of the electron thermionic emission rate. 106
4.7.10. Well width dependence. 114
4.7.11. Barrier height dependence. 121
4.7.12. Multiple subbands. 128
4.7.13. Summary of dependence on well configuration. 132
4.7.14. Case Study: 95 Å $Al_{0.2}Ga_{0.8}As/GaAs/Al_{0.4}Ga_{0.6}As$ asymmetric well. 133
4.8. Summary. 143

Chapter 5: Experimental Determination of Quantum Well Carrier Escape Rates. 145
5.1. Time-Resolved Photoconductivity (PC): Introduction. 145
5.2. Measurement Apparatus. 146
5.2.1. Pulsed light source: gain switched diode laser. 147
5.2.2. High speed current measurements. 147
5.2.3. Microwave transmission lines. 148
5.3. Sample/Mount Requirements. 150
5.3.1. Device parasitics. 150
5.3.2. Sample mounts. 150
5.4. The Time-Resolved Photoconductivity Setup. 151
5.5. Test structures: Strained InGaAsP/InP Multiple Quantum Well Laser Structure. 155
5.5.1. Material characteristics. 156
5.6. Experimental Results. 158
5.6.1. Current-voltage characteristics. 158
5.6.2. Time-resolved photoconductivity. 158
5.7. Summary. 170

Chapter 6: Conclusions. 171

Appendix A: Reduced Notation for the Strain and Piezoelectric Tensors. 175
Appendix B: Angular Dependence of Transverse Mode Piezoelectric Scattering. . . . 177

Appendix C: Symbol Definitions. 181
Appendix D: Physical Constants 185

References. 187

List of Figures.

Fig. 1.1: Energy band diagrams of (a) a semiconductor heterojunction and (b) a semiconductor quantum well showing the discontinuity of the band edge energies at the heterojunction(s). 2

Fig. 1.2: Quantized energy states and wavefunctions for a 1D quantum well. 2

Fig. 1.3: a) Two-dimensional subbands. b) 2D density of states. 3

Fig. 1.4: Schematic absorption spectrum of a quantum well showing the exciton peaks and steps corresponding to the various electron and hole subbands. . . . 4

Fig. 1.5: Schematic illustration of the quantum confined Stark effect (QCSE). 5

Fig. 1.6: Relaxation processes in a quantum well in an electric field. 5

Fig. 1.7: Tunneling from a quantum well in an electric field. 6

Fig. 2.1: Energy band diagram for a single quantum well. 11

Fig. 2.2: Calculated energies and wavefunctions for a 70 Å $GaAs/Al_{0.7}Ga_{0.3}As$ quantum well. 12

Fig. 2.3: Potential profile and continuum wavefunctions (solid curves) for a quantum well system in an electric field. 12

Fig. 2.4: The Airy and Bairy functions. 14

Fig. 2.5: Calculated energies and wavefunctions for a 70Å $GaAs/Al_{0.7}Ga_{0.3}As$ quantum well. 15

Fig. 2.6: Calculated tunnelling times for the electron ground state of a $GaAs/Al_{0.2}Ga_{0.8}As$ quantum well as a function of the electric field across the well. 17

Fig. 2.7: Thermionic emission over a bulk-barrier junction. 18

Fig. 2.8: Energy of the first confined state as a function of electric field for a 50 Å $GaAs/Al_{0.2}Ga_{0.8}As$ quantum well. 25

Fig. 2.9: Barrier lowering due to the inclination of the well potential in an electric field. 26

Fig. 2.10: Image charge formation in a perfect conductor. 27

Fig. 2.11: Potential energy profile for a metal-semiconductor barrier including the image charge (a) without an applied field (b) with an applied field. 28

Fig. 2.12: Calculated image charge lowering of the barrier at a metal-GaAs interface. 29

Fig. 3.1: Coordinate scheme used in the image charge simulations. 36

Fig. 3.2: Concentric rings/bins used in image charge simulations. 38

Fig. 3.3: Calculated sheet charge distributions for an escaping minority carrier at distances of (a) 0.1 nm, (b) 10 nm, and (c) 30 nm from a unipolar quantum well. 42

Fig. 3.4: Image charge potentials calculated by the minority unipolar simulation. 43

Fig. 3.5: Image charge barrier lowering as a function of the total electric field for minority unipolar case. 44

Fig. 3.6: Image charge lowering as a function of the total electric field for the minority unipolar case. 45

Fig. 3.7: Effective charges as a function of the sheet carrier density as obtained from fits to the minority unipolar barrier lowering curves. 46

Fig. 3.8: Sheet charge distributions calculated with (solid) and without (dotted) the diffusion current for an escaping majority carrier at a) 0.1 nm, b) 10 nm , and c) 30 nm from the surface of a unipolar quantum well. 47

Fig. 3.9: Comparison of the image charge carrier distributions obtained from the perfect conductor (dotted), minority unipolar (dash-dotted), and majority unipolar (solid) calculations. 48

Fig. 3.10: Calculated image potentials for carrier densities of 10^{10}, 10^{11}, and 10^{12} cm^{-2} for a majority carrier escaping from a unipolar quantum well. 49

Fig. 3.11: Calculated majority unipolar image charge barrier lowering as a function of the total electric field. 50

Fig. 3.12: The minimum field due to the net charge density in the well. 51

Fig. 3.13: Total potential energy profile for an external charge in the field of its image in a 50 kV/cm electric field for the majority unipolar drift-diffusion (solid) and perfect conductor (dashed) solutions. 52

Fig. 3.14: Sheet field cutoff (open) and sheet field (filled) as a function of the sheet carrier density. 52

Fig. 3.15: Majority unipolar barrier lowering as a function of the sheet carrier density. 53

Fig. 3.16: Image charge barrier lowering calculated for the majority unipolar case (dash-dotted) compared with the result obtained from the minority unipolar simulation (dotted) for carrier densities of (a) 10^{10} cm^{-2}, (b) 10^{11} cm^{-2}, (c) 10^{12} cm^{-2}, and (d) 10^{13} cm^{-2}. 54

Fig. 3.17: Square root fits (solid lines) to the barrier lowering in the field independent regime for the majority unipolar case for carrier densities of (a) 10^{12} cm^{-2} and (b) 10^{13} cm^{-2}. 55

Fig. 3.18: Effective image charge for the majority unipolar case as a function of carrier density. 56

Fig. 3.19: Image charge distributions in a bipolar quantum well for equal electron and hole carrier densities of 10^{11} cm^{-2}. 57

Fig. 3.20: Calculated total image carrier densities for a bipolar quantum well with equal electron and hole densities of 10^{11} cm^{-2}. 58

Fig. 3.21: Calculated image charge potentials for equal electron and hole carrier densities of 10^{10}, 10^{11}, 10^{12}, and 10^{13} cm^{-2}. 59

Fig. 3.22: Calculated barrier lowering for an electron escaping from a bipolar quantum well with electron densities of (a) 10^{10}, (b) 10^{11}, (c) 10^{12}, and (d) 10^{13} cm^{-2} and hole densities of (e) 10^{10}, (f) 10^{11}, (g) 10^{12}, and (h) 10^{13} cm^{-2}. 60

Fig. 3.23: Square root fits (solid line) to the calculated bipolar barrier lowering for equal electron and hole densities of (a) 10^{10}, (b) 10^{11}, (c) 10^{12}, and (d) 10^{13} cm^{-2}. 62

Fig. 3.24: Effective charge plot as a function of the hole population for an electron escaping from a bipolar quantum well. 63

Fig. 4.1: Schematic illustration of typical phonon dispersion curves in a zinc blende or diamond structure semiconductor. 68

Fig. 4.2: Comparison of exact normalization constant from numerical integration with the asymptotic approximation as a function of the normalization length. . . 72

Fig. 4.3: Schematic illustration of the quantum well in the infinite triangular well approximation. 74

Fig. 4.4: Illustration of the potential profile for the 60 Å $GaAs/Al_{0.20}Ga_{0.80}As$ quantum well in a 10 kV/cm electric field. 89

Fig. 4.5: Contour plots of the overlap function $G_{n,n'}(q_z)$ for a 60 Å $GaAs/Al_{0.20}Ga_{0.80}As$ quantum well in (a) 5 kV/cm and (b) 50 kV/cm electric fields as a function of q_z and E_z'. 91

Fig. 4.6: The overlap function, $G_{n,n'}(q_z)$, vs. E_z' integrated over q_z for electric fields of (a) 5 kV/cm and (b) 50 kV/cm. 92

Fig. 4.7: The 2D-to-3D electron scattering rate via polar optical phonon scattering for the 60 Å GaAs/AlGaAs testbed well at 300 K. 93

Fig. 4.8: The 2D-to-3D electron scattering rate via polar optical phonon scattering for the 60 Å GaAs/AlGaAs testbed well, where the phonon occupation factors have been set to unity for both emission and absorption. 94

Fig. 4.9: The 2D-to-3D electron scattering rate via longitudinal acoustic phonon deformation potential scattering for the 60 Å GaAs/AlGaAs testbed well. 96

Fig. 4.10: Contour plot of the deformation potential scattering rate versus the phonon wavevector perpendicular (q_z) and in-plane ($q_{||}$) components for (a) absorption and (b) emission. 97

Fig. 4.11: The 2D-to-3D electron scattering rate via longitudinal acoustic phonon piezoelectric scattering for the 60 Å GaAs/AlGaAs testbed well. 98

Fig. 4.12: The 2D-to-3D electron scattering rate via transverse acoustic phonon piezoelectric scattering for the 60 Å GaAs/AlGaAs testbed well. 99

Fig. 4.13: The 2D-to-3D electron scattering rates given by each of the different phonon scattering mechanisms for the 60 Å GaAs/AlGaAs testbed well in a 5 kV/cm electric field. 100

Fig. 4.14: The 2D-to-3D electron scattering rates given by each of the different phonon scattering mechanisms for the 60 Å GaAs/AlGaAs testbed well. . . . 100

Fig. 4.15: Calculated thermionic emission times for the 60 Å GaAs/AlGaAs testbed well as a function of temperature and for several electric fields. 101

Fig. 4.16: Schematic illustration of the effect of smearing in the scattering function at (a) high temperature and (b) low temperature. 102

Fig. 4.17: Comparison of the emission times for the different scattering processes as a function of temperature. 103

Fig. 4.18: Final state wavefunctions near the top of the barrier for the 60 Å GaAs/AlGaAs testbed well in a 50 kV/cm electric field. 105

Fig. 4.19: Illustration of the calculated average scattering times for cutoffs of 1% (light) and 25% (heavy) for electric fields of (a) 5 kV/cm and (b) 50 kV/cm. . 107

Fig. 4.20: (a) Cutoff (dash-dotted) and midpoint (dotted) energies for 1% and 25% criteria and effective barrier heights obtained from Arrhenius plots (solid) of the calculated thermionic emission rates as a function of the electric field. . . . 108

Fig. 4.21: Arrhenius plots of the calculated thermionic emission times from the 60 Å GaAs/AlGaAs testbed well for electric fields of (a) 5 kV/cm and (b) 50 kV/cm. 109

Fig. 4.22: Fermi-Dirac fit to the LO phonon absorption scattering function for the 60 Å GaAs/AlGaAs testbed well in a (a) 5 kV/cm and (b) 50 kV/cm electric field. 110

Fig. 4.23: The fitting parameters for the scattering function: (a) W_o, (b) E_b, and (c) δE versus the electric field, where the filled circles represent emission and the open circles absorption. 111

Fig. 4.24: Comparison of the electronic thermionic emission times calculated using the full scattering treatment (solid), the Fermi-Dirac fit (dotted), and the step-function approximation (dashed and dash-dotted) at (a) 5 kV/cm and (b) 50 kV/cm. 112

Fig. 4.25: Comparison of the electronic thermionic emission times calculated using the full scattering treatment (solid), the Fermi-Dirac fit (dotted), and the step-function approximation (dashed) at (a) 100 K and (b) 300 K. 113

Fig. 4.26: LO phonon absorption rates for GaAs/$Al_{0.20}Ga_{0.80}As$ wells with widths of 50 Å, 55 Å, 60 Å, and 65 Å in electric fields of (a) 5 kV/cm and (b) 50 kV/cm. 115

Fig. 4.27: Confinement ratio near the barrier energy for the 50 Å (solid) and 65 Å (dotted) quantum wells. 116

Fig. 4.28: The (a) average scattering rate, W_0, (b) effective barrier height, E_b, and (c) field dependence parameters of the transition width, δE, obtained from Fermi-Dirac fits to the scattering function. 117

Fig. 4.29: Thermionic emission times calculated for GaAs/$Al_{0.20}Ga_{0.80}As$ wells with 50 Å, 55 Å, 60 Å, and 65 Å widths at a field strength of 5 kV/cm. 118

Fig. 4.30: Thermionic emission times calculated for GaAs/$Al_{0.20}Ga_{0.80}As$ wells with 50 Å, 55 Å, 60 Å, and 65 Å widths at a field strength of 50 kV/cm. 119

Fig. 4.31: Thermionic emission times for the 50 Å GaAs/$Al_{0.2}Ga_{0.8}As$ well calculated according to the step function (dashed) and Fermi-Dirac function (dotted) approximations compared with the full calculations (solid) for electric fields of (a) 5 kV/cm and (b) 50 kV/cm. 120

Fig. 4.32: Fermi-Dirac function fits to the LO-phonon scattering functions for the 50 Å GaAs/AlGaAs well for electric fields of (a) 5 kV/cm and (b) 50 kV/cm. 121

Fig. 4.33: LO phonon absorption rates for 60 Å GaAs/$A_xGa_{1-x}As$ wells where the Al content in the barriers ranges from 14% to 20%, in electric fields of (a) 5 kV/cm and (b) 50 kV/cm. 122

Fig. 4.34: The confinement ratio near the barrier energy for 60 Å GaAs/$Al_xGa_{1-x}As$ wells with 14% (dotted) and 20% (solid) Al content in the barriers. 123

Fig. 4.35: The (a) average scattering rate, W_0, (b) effective barrier height, E_b, and (c) field dependence parameters of the transition width, δE, obtained from Fermi-Dirac fits to the scattering function as a function of the well depth. . . . 124

Fig. 4.36: Fermi-Dirac function fits (solid curve) to the LO-phonon scattering function (dotted curve) for 60 Å GaAs/$Al_xGa_{1-x}As$ wells with barrier Al contents of (a) 14% and (b) 20%. 125

Fig. 4.37: Thermionic emission rates calculated for 60 Å GaAs/$Al_xGa_{1-x}As$ wells with barrier Al mole concentrations of 14% (dash-dotted), 16% (dashed), 18% (dotted), and 20% (solid) in electric fields of (a) 5 kV/cm and (b) 50 kV/cm. 126

Fig. 4.38: Comparison of thermionic emission times calculated according to the Fermi-Dirac function (dotted) and step-function approximations (dashed) for the LO-phonon scattering function for the 60 Å GaAs/$Al_{0.14}Ga_{0.86}As$ well in electric fields of (a) 5 kV/cm and (b) 50 kV/cm. 127

Fig. 4.39: Confinement ratio for a 100 Å GaAs/$Al_{0.2}Ga_{0.8}As$ well in an electric field of 5 kV/cm (solid) and 50 kV/cm (dotted). The dashed line indicates the barrier energy. 129

Fig. 4.40: The effective barrier heights (open) and potential barriers (filled) for GaAs/$Al_{0.20}Ga_{0.80}As$ wells as a function of the well width. 130

Fig. 4.41: The average scattering rate as a function of the well width for GaAs/$Al_{0.20}Ga_{0.80}As$ wells. 131

Fig. 4.42: Calculated thermionic emission times for GaAs/$Al_{0.20}Ga_{0.80}As$ wells as a function of well width, at temperatures of 100 K, 200 K, and 300 K, in a 5 kV/cm electric field. 132

Fig. 4.43: Calculated energies and envelope functions for confined states in a 95 Å asymmetric GaAs/$Al_xGa_{1-x}As$ well. 134

Fig. 4.44: Confinement ratio, $\xi(Ez)$, for the symmetric ($Al_{0.20}Ga_{0.80}As$ barriers - dotted) and asymmetric ($Al_{0.20}Ga_{0.80}As$/GaAs/$Al_{0.40}Ga_{0.60}As$ - solid) 95 Å well in a 5 kV/cm electric field. 134

Fig. 4.45: 2D-to-3D electron-LO phonon scattering rates from the ground subband of the symmetric (dotted) and asymmetric (solid) 95 Å GaAs/AlGaAs quantum wells. 135

Fig. 4.46: 2D-to-3D LO phonon scattering rates from the ground subband of the symmetric (dotted) and asymmetric (solid) 95 Å GaAs/AlGaAs quantum wells in a 50 kV/cm electric field. 136

Fig. 4.47: Calculated thermionic emission times for the symmetric (dotted) and asymmetric (solid) 95 Å GaAs/AlGaAs quantum wells for electric fields of 5 kV/cm and 50 kV/cm. 137

Fig. 4.48: Measured electron escape times (open circles) from a 95 Å $Al_{0.20}Ga_{0.80}As/GaAs/Al_{0.40}Ga_{0.60}As$ quantum well compared with calculated values. 138

Fig. 5.1: Bias-tee. 149

Fig. 5.2: DC coupled bias-tee configuration. 149

Fig. 5.3: InGaAsP/InP laser mount. 151

Fig. 5.4: InGaAsP laser sample holder. 152

Fig. 5.5: Time-resolved photoconductivity measurement system. 153

Fig. 5.6: Band structure of 1.2% tensile strained InGaAsP/InP multiple quantum well laser structure under 0 V external bias. 156

Fig. 5.7: Schematic illustration of the ridge-waveguide structure. 157

Fig. 5.8: Current-voltage characteristics of 1.2% tensile strained InGaAsP/InP MQW laser structure. 158

Fig. 5.9: Time-resolved photoconductivity trace showing two exponential decays. . . 159

Fig. 5.10: Measured hole escape times in a 1.2% tensile strained InGaAsP/InP MQW laser structure as a function of temperature, for applied biases of -0.5 V, 0.0 V and 0.5 V. 160

Fig. 5.11: Arrhenius plots of the hole escape time for the strained InGaAsP/InP MQW laser structure for biases of (a) 0.0 V, (b) 0.25 V, (c) 0.5 V, and (d) 0.75 V. 161

Fig. 5.12: Measured barrier heights obtained from Arrhenius plots. 162

Fig. 5.13: Calculated band structure for the tensile strained InGaAs quantum well. . . 164

Fig. 5.14: Schematic illustration of light and heavy hole subbands in (a) unstrained, (b) compressively strained, and (c) tensile strained wells. 166

Fig. 5.15: Comparison of measured and calculated holes escape times for a tensile strained InGaAsP/InP MQW laser structure under applied biases of -0.5 V, 0.0 V and 0.5 V. 166

Fig. 5.16: Calculated LO-phonon scattering curves for the strained InGaAsP/InP MQW laser structure under -0.5 V reverse bias. 167

Fig. 5.17: Comparison of the measured and calculated hole escape times for a strained InGaAsP/InP MQW laser structure where the valence band offset has been increased to 70%. 168

Fig. B.1: Coordinate axes defined by the wavevector and the two transverse polarization vectors in relation to the crystal axes, x, y, z. 179

List of Tables.

TABLE 4.1: Material parameters used in the GaAs/$Al_xGa_{1-x}As$ quantum well scattering calculations. 90

TABLE 5.1: Bulk material parameters for the strained InGaAsP/InP multiple quantum well laser. 163

TABLE 5.2: Calculated hole energies and effective masses at subband minima for the strained InGaAsP/InP multiple quantum well laser. 164

Chapter 1: Introduction.

The development of epitaxial growth techniques which provide compositional control on an atomic layer scale, such as molecular beam epitaxy (MBE) and metallorganic chemical vapour deposition (MOCVD), has led to a new generation of photonic and electronic devices (for a review of the field, see Weisbuch (1991)). In particular these devices make use of abrupt interfaces between two materials where the lattice structure is maintained across the junction. This is referred to as a *heterojunction*, and is illustrated in Fig. 1.1 (a). As the two materials that make up the junction will have different atomic compositions, the electronic properties will also change abruptly. In particular, the band gaps will differ so that a free electron at the conduction band edge will see a sudden change in potential energy as it traverses the interface. This discontinuity in conduction band energy is referred to as the *conduction band offset*, ΔE_c, while holes see the *valence band offset*, ΔE_v.

If a layer of narrow gap semiconductor is sandwiched between layers of wider gap material, a potential well is formed in the direction perpendicular[1] to the interface. If the central layer is sufficiently thin, the quantization of the electron (or hole) energy will become important. This structure is then referred to as a *quantum well*, and is illustrated in Fig. 1.1 (b).

Quantum wells have been both an important technological building block and a rich source of fundamental physics. For energies below the barrier, the electronic states are essentially those found in introductory quantum mechanics texts for the square well

[1]Throughout the remainder of the thesis, the direction perpendicular to the plane of the interface, i.e.: the growth direction, will be referred to as *perpendicular*, while directions in the plane of the interface will be termed *parallel*.

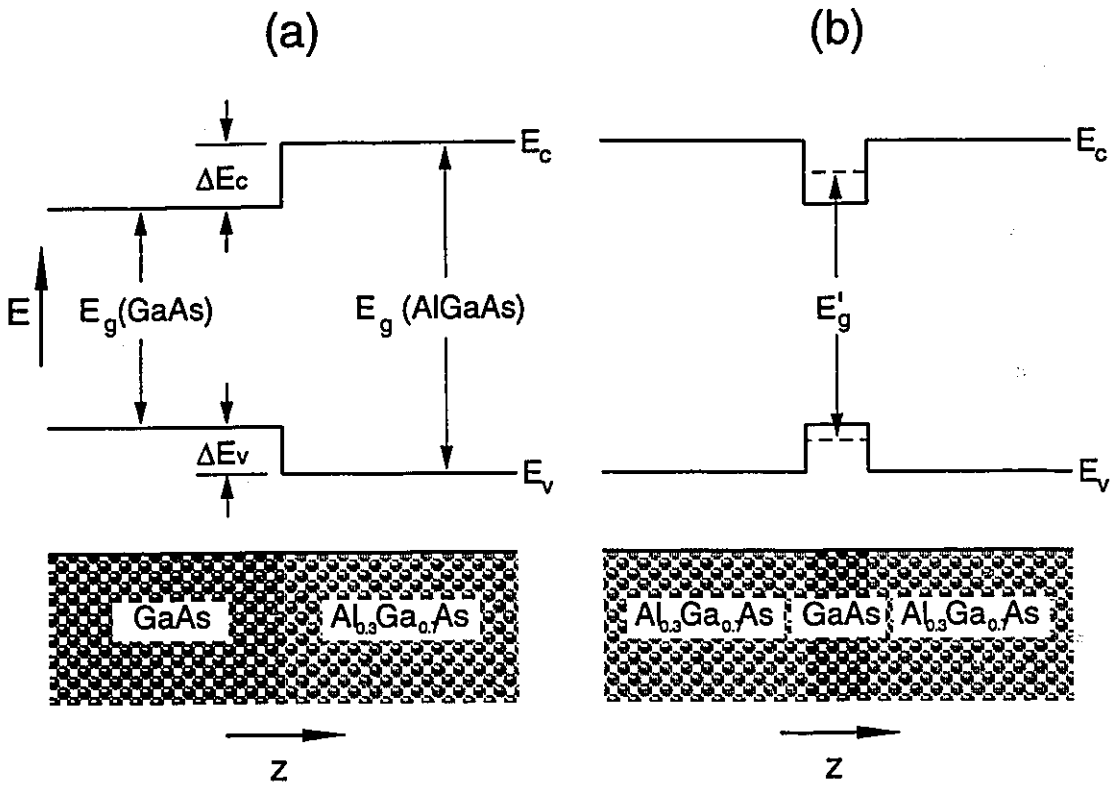

Fig. 1.1: Energy band diagrams of (a) a semiconductor heterojunction and (b) a semiconductor quantum well showing the discontinuity of the band edge energies at the heterojunction(s). The quantization of the electron and hole energies within the quantum well region result in an effective bandgap energy, E_g', which is greater than the bulk bandgap of the well material. Below are schematic illustrations of the material structure.

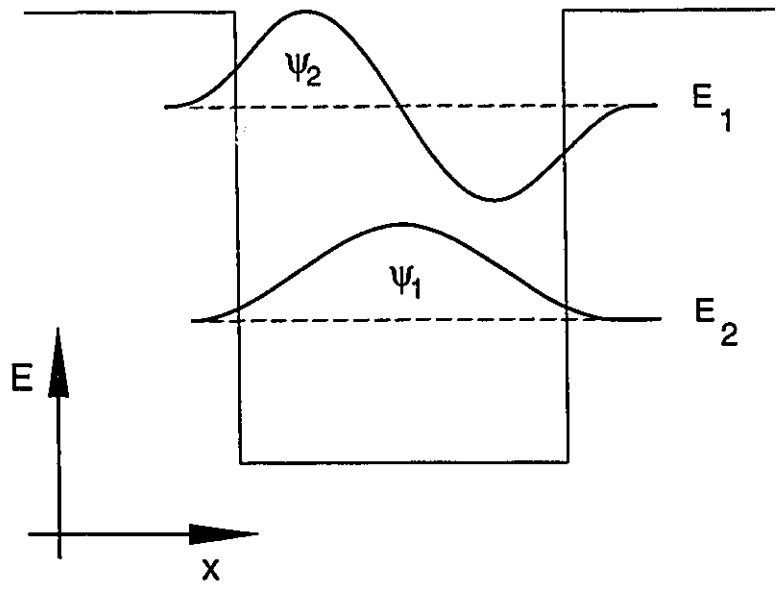

Fig. 1.2: Quantized energy states and wavefunctions for a 1D quantum well.

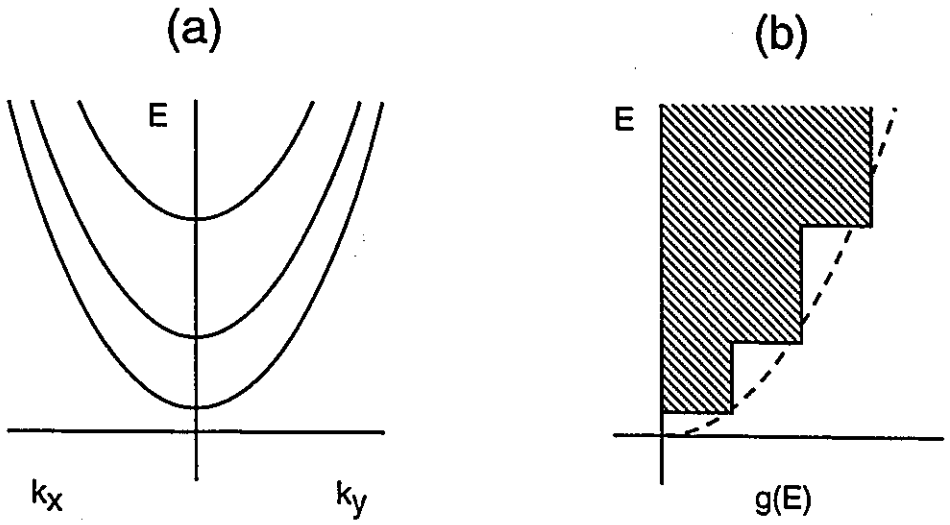

Fig. 1.3: a) Two-dimensional subbands. Each curve corresponds to a different quantized k_z value. b) 2D density of states. Each step arises from the contribution of a single subband. The dashed curve represents the 3D density of states.

potential, illustrated schematically in Fig. 1.2 (see, for example, Bransden and Joachain (1989)). As a result, the lowest energy state within the well is no longer at the band edge. The exact energy of the state is a function of the well depth and width and the effective masses in the well and barrier materials. Therefore, the effective energy gap can be selected by the appropriate choice of well parameters. This is often referred to as *band-gap engineering*, a capability that is extremely useful in photonic devices as it allows device engineers to choose the operating wavelengths of their optoelectronic systems.

The quantization of the electron (and hole) energy in the direction perpendicular to the heterointerfaces restricts the carrier motion so that there is freedom only in the two-dimensional (2D) plane of the well. As a result, the electron is said to reside in a *2D subband* and the density of states becomes that for a 2D free-electron gas. This is illustrated in Fig. 1.3, where each step in Fig. 1.3 (b) represents the contribution from a 2D subband in Fig. 1.3 (a). For comparison, the dashed curve in Fig. 1.3 (b) shows the corresponding 3D density of states which is parabolic in form. The relative increase in the band edge density of states between the three-dimensional (3D) and 2D cases has been exploited in the quantum well laser where it results in a reduced threshold current (see, for example, Weisbuch (1991)).

The confining potential of the well also acts to increase the binding energy of excitons. An exciton is an electron and a hole bound together by their mutual Coulomb attraction, much like a hydrogen atom (for a review of both bulk and 2D excitons, see

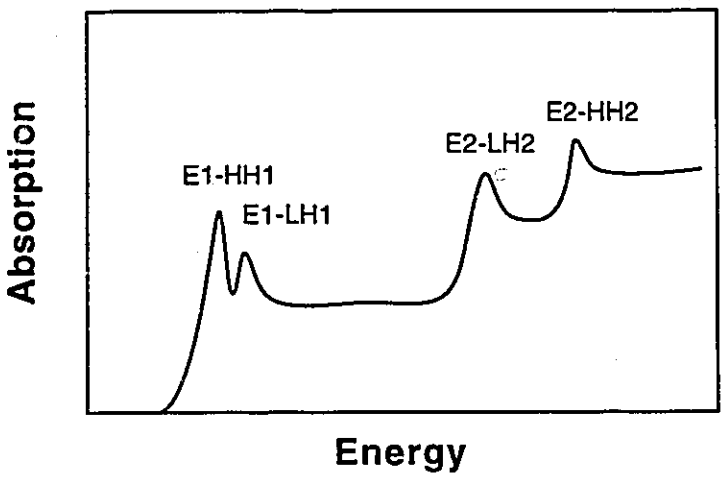

Fig. 1.4: Schematic absorption spectrum of a quantum well showing the exciton peaks and steps corresponding to the various electron and hole subbands.

Singh (1993)). While excitons do form in bulk semiconductors, their binding energies are generally so small that they are observed only at cryogenic temperatures. In a quantum well, however, the perpendicular localisation of the electron and hole wave functions increases the Coulomb energy and, as a result, raises the binding energy. The presence of the exciton shows up as a peak in the absorption spectrum at the edge of the subband absorption, shown schematically in Fig. 1.4. Note that each of the light and heavy hole subbands shows up as a step corresponding to their respective contributions to the density of states, and that an exciton peak appears at each step.

The increased binding energy of the exciton also gives rise to a technologically important phenomenon called the Quantum Confined Stark Effect (QCSE), (Miller, 1984a). In atomic physics, the Stark effect refers to the shifting of atomic energy levels under the application of an electric field (see, for example, Bransden and Joachain (1989)); the same effect takes place for an exciton in a quantum well. As an electric field is applied, the absorption edge shifts to longer wavelengths, as shown schematically in Fig. 1.5. Due to the sharpness of the exciton peak, large changes in the absorption can be achieved with one or two volt changes in the applied voltage. Furthermore, the confining potential allows much greater perpendicular electric fields to be applied before the exciton dissociates and the effect vanishes. The QCSE is exploited in devices such as optical modulators (Fox, 1991), (Susa, 1993), wavelength tunable detectors (Larsson, 1988), (Wood, 1990), and self electro-optic effectdevices (SEED's), (Miller, 1984b).

When a photon is absorbed in a quantum confined Stark effect modulator, it generates a free electron-hole pair. For the modulator to be effective, these carriers must

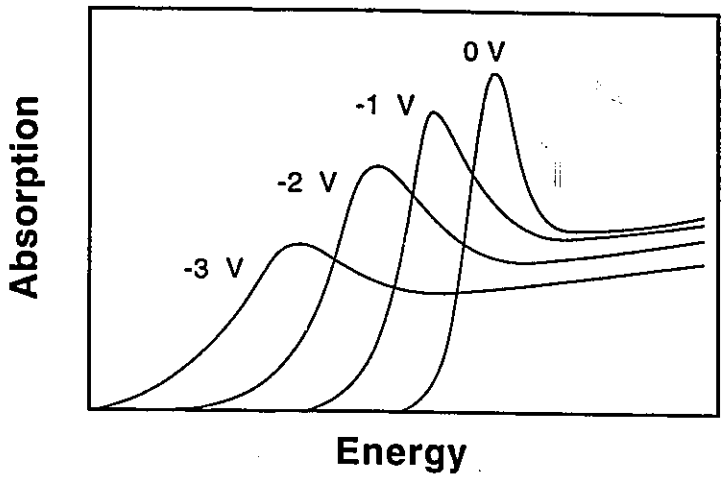

Fig. 1.5: Schematic illustration of the quantum confined Stark effect (QCSE). As the electric field is increased the exciton absorption peak shifts to lower energy. The peak also broadens as the exciton lifetime decreases due to tunnelling.

then relax quickly to prevent the conduction and valence band states from becoming filled and hence saturating the absorption (Fox, 1991). There are a number of mechanisms by which these free carriers can relax, as illustrated in Fig. 1.6. The first is the recombination of an electron and a hole. This can be accompanied by the generation of another photon or by the emission of phonons, usually with the assistance of a defect state. The former is

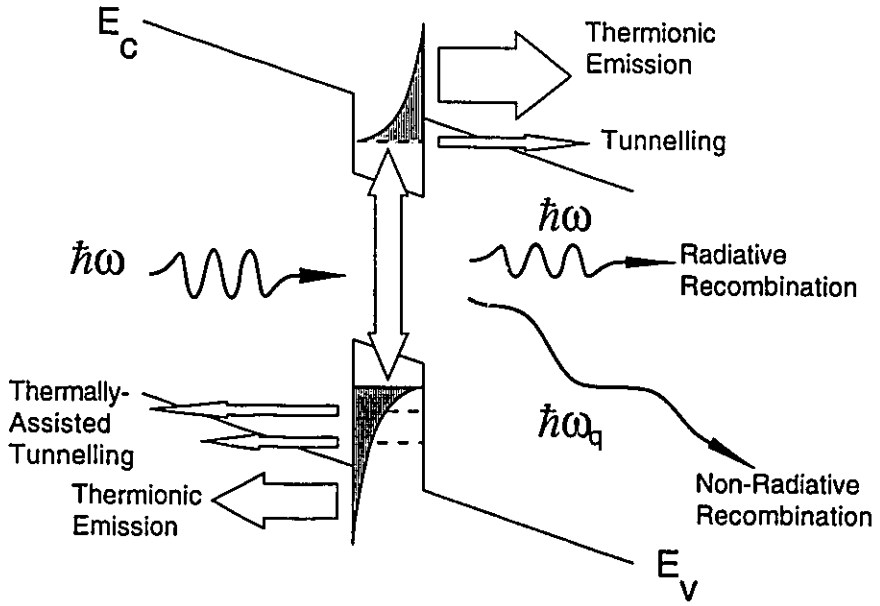

Fig. 1.6: Relaxation processes in a quantum well in an electric field. Carriers can recombine radiatively or non-radiatively, via the emission of phonons. Escape can occur via tunnelling, thermionic emission or thermally-assisted tunnelling.

referred to as radiative recombination, the latter as non-radiative recombination. Alternatively, the electron or hole can escape the confining potential of the well and recombine elsewhere. If the quantum well is situated within the depletion region of a *pn* or *p-i-n* junction then these escaping carriers will be swept to the contacts to form a photocurrent. By measuring this current, the device acts as a photodetector. Since the absorption edge can be shifted via the QCSE by applying an electric field, the detector is said to be wavelength-tunable.

There are basically two types of processes by which the carriers can escape from the well. Tunnelling processes are those where the carrier passes through the barrier by virtue of the quantum mechanical tunnelling effect. In a thermal process, the carrier is ejected over the barrier by the absorption of thermal energy from other particles in the system. Combining the two basic processes results in thermally-assisted tunnelling where the carrier is scattered into a higher energy confined subband where it subsequently tunnels out of the well (Halliday, 1992).

If the barriers are very thick, then the tunnelling processes are only possible when an electric field is applied to the well. In this case, the well is tilted and the barrier becomes triangular, as illustrated in Fig. 1.7. As the field increases, the height and thickness of the barrier are reduced so that the tunnelling rate increases with electric field (Larsson, 1988), (Fox, 1991).

The thermal processes do not require an electric field for escape to occur; however, the presence of an electric field will affect the emission rate. This results from two distinct

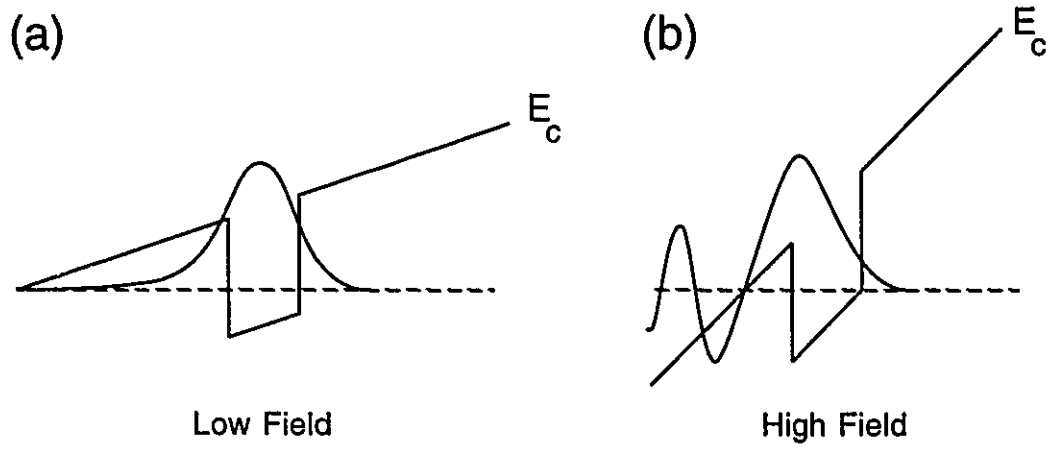

Fig. 1.7: Tunnelling from a quantum well in an electric field. In (a) the field is small and the wavefunction decays to near zero amplitude before it traverses the barrier. The wavefunction is well-confined and the tunnelling lifetime is long. At high fields (b) the amplitude outside the well is still large, which corresponds to a short tunnelling lifetime. Furthermore, the barrier height is lowered as the well is inclined in the electric field, resulting in faster thermal escape rates.

effects. First, the strength of the electric field will determine how quickly the escaping carriers leave the region of the well from which they escaped. If the field is weak, then the carriers will remain in the vicinity of the well long enough for thermal equilibrium between the confined and continuum states to be maintained (Schneider and Von Klitzing, 1988), (Moss, 1994). If the field is strong then the carriers are swept away before re-capture can occur. In this case, the limiting factor in the escape rate will be the scattering time from the 2D confined state into a 3D continuum state (Liu, 1993), (Gurioli, 1992). As a result, the electric field also enhances the thermal escape rate.

The second manner in which the electric field affects the thermionic emission rate is by altering the height of the potential barrier that must be surmounted (Schneider and Von Klitzing, 1988), (Moss, 1994). This occurs primarily because the well is tilted in the electric field so that the 'front' of the well is lowered, as seen in Fig. 1.7. The barrier will be further reduced by a phenomenon known as image charge lowering which has long been known to significantly increase the thermal emission rates in metal-vacuum and metal-semiconductor junctions (Sze, 1964), (Mead, 1966). However, unlike in the case of a metal, the relatively low carrier densities in a semiconductor quantum well require that the diffusion current be included in the calculations. As will be seen in Chapter 3, the diffusion contribution counteracts the build-up of the image charge distribution resulting in a reduced image charge effect. Nonetheless, both barrier lowering effects will act to increase the thermionic emission rate.

It is apparent that for high speed modulators or detectors it is necessary to have rapid relaxation times so that absorption saturation does not occur (Manning, 1989), (Fox, 1991), (Miller, 1992). In particular, it is important for detectors to have fast escape times to optimize both the quantum efficiency and high frequency response (Larsson, 1988). Carrier escape from quantum wells or similar 2D structures has importance in other devices as well. For example, the leakage currents in lasers (Tsai, 1994b) and high electron mobility transistors (HEMT's), (Ruden, 1988), (Fawaz, 1993), and the dark currents in quantum well infrared detectors (QWIP's), (Liu, 1993) are attributed to carrier escape from the 2D active regions. Therefore, device engineers require ways to calculate the escape times for a given structure as a function of the electric field. It is the goal of this research to make a significant contribution to the development of these calculation tools. While tunnelling calculations have been treated numerous times in the past (Larsson, 1988), (Ghatak, 1988, 1990), (Jonsson, 1990), the thermal escape processes have received less attention. Currently, the most commonly used expression for the thermionic emission time does not include any aspects of the two-dimensional nature of the initial state (Schneider

and Von Klitzing, 1988). As a result, the calculated times often underestimate the measured times by one or two orders of magnitude (Halliday, 1992), (Cavaillès, 1992), (Tsai, 1994a). In this thesis, thermionic emission will be examined in detail both theoretically and experimentally.

In the following chapter, the physics and equations necessary to calculate the tunnelling and thermionic emission rates from quantum wells will be given. The tunnelling lifetime is calculated from the width of the energy resonance obtained from full Airy function solutions to the Schrödinger equation. The thermionic emission treatment will be divided into two sections: low and high electric field, where at low fields the limiting process is the diffusion of the 3D carriers away from the well, while at high fields the scattering from confined to continuum states (2D-to-3D) determines the emission rate. Chapter 3 will contain a detailed treatment of image charge barrier lowering in the case of an occupied quantum well. The effects of diffusion on the image charge formation will be included for the first time and shown to significantly reduce the amount of barrier lowering at low carrier densities. The 2D-to-3D scattering rate required by the high field thermionic emission treatment will be calculated in chapter 4. Polar optical phonon as well as acoustic phonon scattering via deformation potential and piezoelectric coupling will be considered; polar optical phonon scattering will be shown to dominate at all temperatures. The effects of a perpendicular electric field, varying well width and barrier height, and well asymmetry on the scattering and thermionic emission rates will be examined. Measurements of carrier escape rates by time-resolved photoconductivity in strained InGaAsP/InP multiple quantum well laser structures will be presented in chapter 5. The hole escape times will be compared with the calculated values with limited success. Finally, the conclusions of this research will be presented in chapter 6.

Chapter 2: Escape from Semiconductor Quantum Wells.

In this chapter descriptions of the two basic escape processes, tunnelling and thermionic emission, will be presented. First, the wavefunctions for electronic states that are localised in the well will be examined. The methods for obtaining the wavefunctions for a square well potential will be described, with particular attention paid to the situation where there is an electric field applied across the well. In this case, the tunnelling lifetimes of the confined states can be determined from the finite energy widths of the resonances. Next, the thermal escape will be considered. Under small transverse electric fields, conventional approaches can be applied to determine the emission rate. However, in the presence of large electric fields, thermal equilibrium is partially destroyed and the scattering rate between the 2D and 3D states limits the escape rate. Both descriptions will be presented in detail, preceded by a brief review of the bulk-barrier problem. Barrier lowering effects will be described, including image charge lowering in the quasi-static perfect conductor approximation. Finally, a description of thermally-assisted tunnelling will be given.

2.1. The Quantum Well with No Electric Field: The Square Well Potential.

In a layered semiconductor heterostructure, the wavefunction of an electronic state is altered by the variations in the conduction band energy from one layer to the next. Provided the layer is not too thin, the usual Bloch wavefunction

$$\psi_{\mathbf{k}}(\mathbf{r}) = u_{\mathbf{k}}(\mathbf{r}) \frac{e^{i\mathbf{k}\cdot\mathbf{r}}}{\sqrt{V}} \tag{2.1}$$

can be modified in the perpendicular, or z, direction, by replacing the plane wave component by $\phi_n(z)$, the *envelope function*. This gives, to a good approximation, (Bastard, 1981, 1982)

$$\psi_{n,k}(r) = u_k(r)\phi_n(z) \frac{1}{\sqrt{L_x L_y}} e^{i(k_x x + k_y y)} \tag{2.2}$$

where L_x and L_y are the crystal dimensions in the x and y directions respectively and are included to normalize the plane wave components of the wavefunction. The envelope function is found by solving Schrödinger's equation for a free electron in the potential profile given by the conduction band minimum. This ignores the potential variations of the lattice on the atomic scale; these are taken care of by the Bloch functions, $u_{\mathbf{k}}(\mathbf{r})$. The reduction of the problem to that of a particle in a piecewise linear potential is called the *envelope function approximation* (Bastard, 1981, 1982).

To solve for the envelope function in such a potential, the usual boundary conditions must be satisfied, but with an important difference. Since the effective mass will generally differ from one region to the next, continuity of the envelope function derivative is insufficient for conservation of the probability flux. The proper boundary condition for the envelope function derivative is then (Bastard, 1981)

$$\frac{1}{m_I^*} \frac{\partial \phi_{n,I}(z)}{\partial z}\bigg|_{z=z_0} = \frac{1}{m_{II}^*} \frac{\partial \phi_{n,II}(z)}{\partial z}\bigg|_{z=z_0} \tag{2.3}$$

where the m_I^* and m_{II}^* are the effective masses[1] in regions I and II and the boundary between the two regions is situated at z_0. The other condition, continuity of the envelope function, remains as

$$\phi_{n,I}(z_0) = \phi_{n,II}(z_0). \tag{2.4}$$

For the simple square well potential with infinitely thick barriers shown in Fig. 2.1,

[1]Note that parabolic bands will be assumed throughout this thesis unless otherwise indicated. As a result, a single effective mass will describe each band.

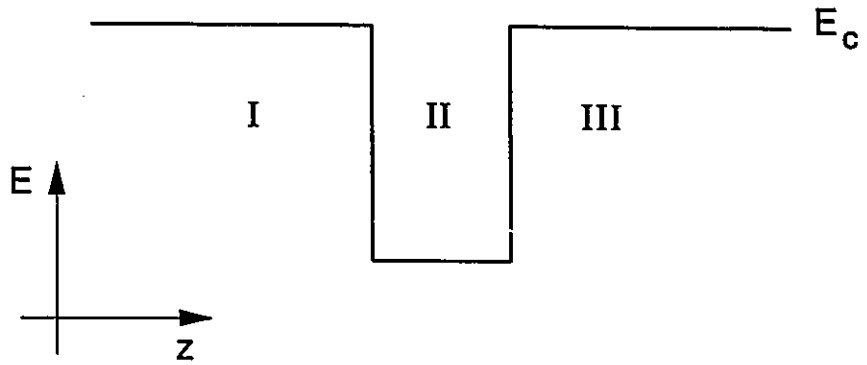

Fig. 2.1: Energy band diagram for a single quantum well. The middle layer has a smaller conduction band energy giving the square potential well.

this leads to equations very similar to those given in standard quantum mechanics texts. For confined solutions, i.e.: energies less than V_0, the envelope function is comprised of plane waves in the well layers and exponential decays in the barrier regions. Applying the boundary conditions (2.3) and (2.4) gives the pair of transcendental equations

$$\tan\left(\sqrt{\frac{m_w^* E_n w^2}{2\hbar^2}}\right)=\sqrt{\frac{m_b^*(V_b-E_n)}{m_w^* E_n}} \qquad (2.5)$$

$$\cot\left(\sqrt{\frac{m_w^* E_n w^2}{2\hbar^2}}\right)=-\sqrt{\frac{m_b^*(V_b-E_n)}{m_w^* E_n}}$$

for the energies of the confined states, E_n, where m_w^* and m_b^* are the effective masses in the well and barrier materials respectively, and V_b and w are the well depth and width.

Once the energy solutions have been found, the wavefunction coefficients can easily be determined from the boundary conditions. As an example, the calculated wavefunctions and energies for a 70 Å $GaAs/Al_{0.3}Ga_{0.7}As$ quantum well are shown in Fig. 2.2.

2.2. Quantum Well in an Electric Field.

When an electric field is applied in the perpendicular direction, the potential energy profile becomes inclined, where the slope is given by the electric field strength. This is illustrated in Fig. 2.3. The envelope function then becomes a linear combination of Airy and Bairy functions, replacing the plane waves and exponential decays of the zero-field case (see, for example, Ghatak *et al* (1990)).

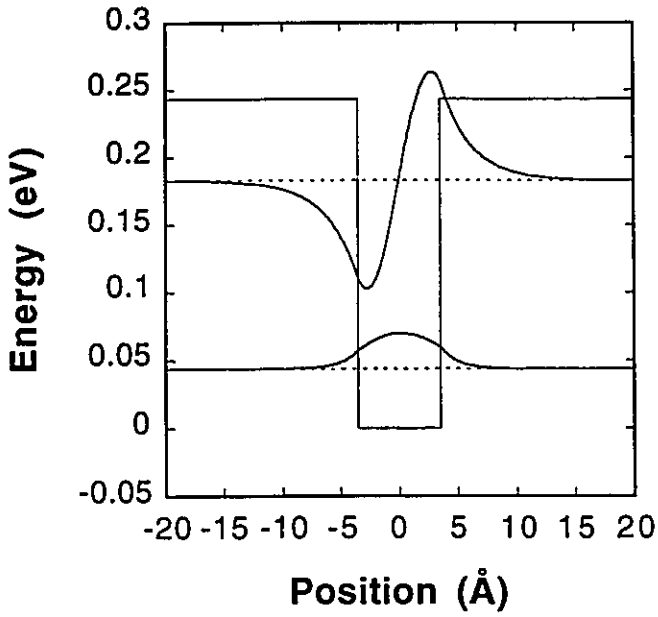

Fig. 2.2: Calculated energies and wavefunctions for a 70 Å GaAs/$Al_{0.7}Ga_{0.3}As$ quantum well. The dotted lines indicate the confined state energies while the solid curves give the wavefunction amplitude.

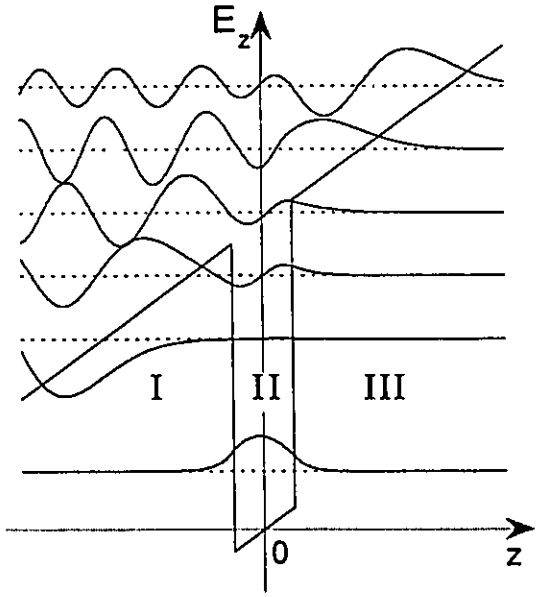

Fig. 2.3: Potential profile and continuum wavefunctions (solid curves) for a quantum well system in an electric field. The dotted lines indicate the wavefunction energies. Due to the inclination of the potential in the electric field, continuum states can be found at any energy, even below the top of the barrier.

The Schrödinger equation for an electron of effective mass m^* in a uniform electric field is

$$-\frac{\hbar^2}{2m_j^*}\frac{\partial^2\phi(z)}{\partial z}+[V_j-e\mathscr{E}z]\phi(z)=E\phi(z) \tag{2.6}$$

where V_j is the potential in the jth layer in the absence of an electric field, and $\mathscr{E}$ is the magnitude of the electric field in the z direction. Note that the natural choice for the origin of the energy-position axes is at the centre of the bottom of the well, as shown in Fig. 2.3. This eliminates any shifts in energy that do not reflect a change in the energy solution for the confined state, but are merely the result of the raising or lowering of the entire potential well in the electric field.

By making the substitution

$$z_j=\left(\frac{2m_j^* e\mathscr{E}}{\hbar^2}\right)\left[z+\frac{(V_j-E)}{e\mathscr{E}}\right] \tag{2.7}$$

this can be rearranged into the form

$$\frac{\partial^2\phi(z_j)}{\partial z_j^2}-z_j\phi(z_j)=0. \tag{2.8}$$

This equation has solutions which are linear combinations of Airy and Bairy functions, as given by

$$\phi_j(z_j)=C_jAi(z_j)+D_jBi(z_j)\,. \tag{2.9}$$

The Airy and Bairy functions are defined by

$$Ai(z)=\frac{1}{\pi}\sqrt{\frac{z}{3}}\,K_{1/3}(u) \tag{2.10}$$

and

$$Bi(z)=\sqrt{\frac{z}{3}}\,[I_{1/3}(u)+I_{-1/3}(u)] \tag{2.11}$$

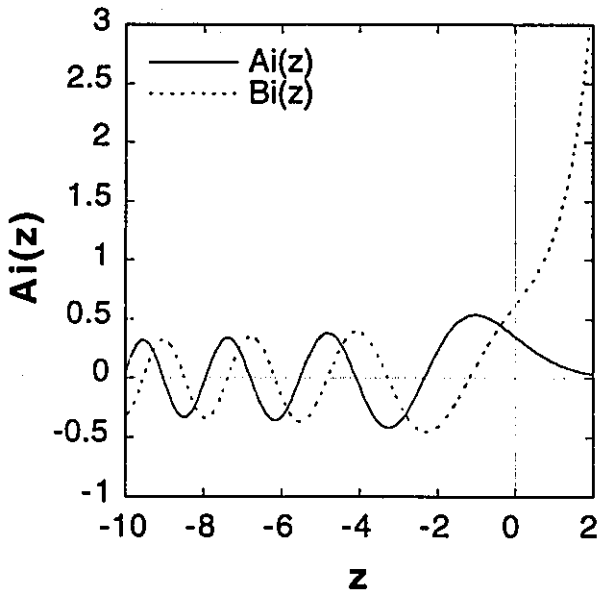

Fig. 2.4: The Airy and Bairy functions. Both functions are oscillatory for negative x. For positive x the Bairy function diverges while the Airy function decays.

where

$$u=\frac{2}{3}z^{\frac{3}{2}} \tag{2.12}$$

and the $K_{1/3}(u)$ and $I_{\pm 1/3}(u)$ are the modified Bessel functions of order $\pm 1/3$. Both $Ai(z)$ and $Bi(z)$ are oscillatory functions for negative z while for positive z, $Ai(z)$ decays rapidly and $Bi(z)$ diverges. These features are illustrated in Fig. 2.4.

To solve for the envelope functions we apply the boundary conditions given by Eqs. (2.3) and (2.4). However, the situation is now dramatically altered by the electric field. Whereas in the square well potential there were only a few well-defined allowed energies below the barrier, the sloping of the potential profile now implies that the barrier energy is position dependent. Therefore, any energy is above the barrier *in some region of space*. As a result, solutions can be found at *any* energy, where in most cases these are considered to be 3D continuum or above-barrier states. This was illustrated in Fig. 2.3. The desired bound state solutions are characterized by large amplitudes in the well region relative to the barrier regions of space. These are referred to as *resonances* or *quasi-bound states* since the amplitude outside of the well region, while not zero, is small relative to that inside the well.

Since the Bairy function diverges for positive z_j, C_{III} can be set equal to zero. The

boundary conditions (2.3) and (2.4) generate a set of four equations for the five remaining unknowns. The fifth equation that fully specifies the coefficients is the normalization condition.

Following the method of Ghatak *et al* (1988, 1990), the degree of localisation can be quantified by the ratio of the amplitude of the wavefunction inside the well over that outside the well, as given by

$$\xi(E)=\frac{C_{II}^2+D_{II}^2}{C_I^2+D_I^2}. \tag{2.13}$$

This function will be referred to as the *confinement ratio*. Since four of the coefficients can be expressed in terms of the fifth, which then cancels out in the ratio, the boundary conditions are sufficient to calculate $\xi(E)$. The resonance energy is then located by a maximum in $\xi(E)$, where the peaks are found by numerical techniques. This is illustrated by the dashed curve in Fig. 2.5, showing the confinement ratio superimposed on the well potential and wavefunctions for a GaAs/AlGaAs quantum well in an electric field.

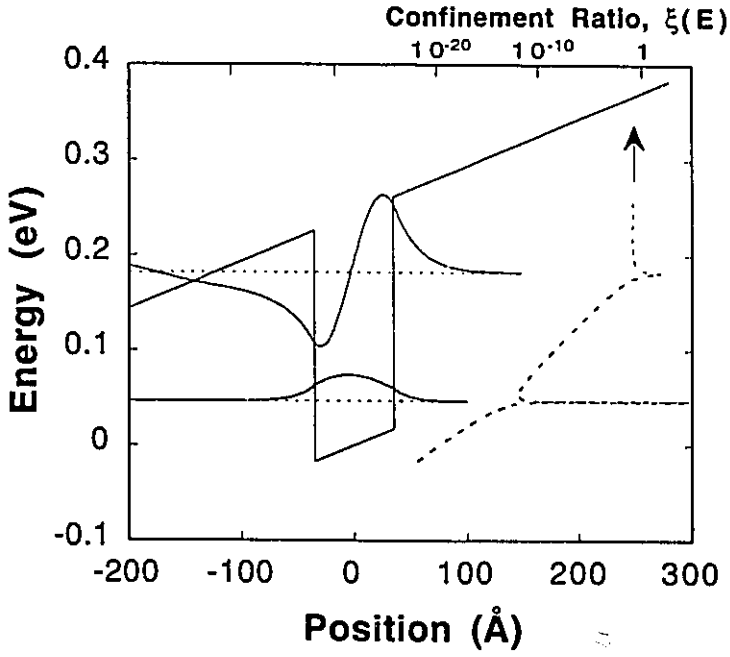

Fig. 2.5: Calculated energies and wavefunctions for a 70Å $GaAs/Al_{0.7}Ga_{0.3}As$ quantum well. The dotted lines indicate the confined state energies while the solid curves give the wavefunction amplitude. The dashed curve on the right is the confinement ratio, $\xi(E)$, as defined by Eq. 2.13. The peaks in ξ correspond to the quasi-confined states of the well.

2.3. Tunnelling from a Quantum Well in an Electric Field.

As alluded to in the previous section, under an electric field the bound states broaden into resonances with a finite width in energy. According to the Heisenberg relation,

$$\Gamma \cdot \tau \geq \frac{\hbar}{2}, \tag{2.14}$$

the spread in energy, Γ, translates into a finite lifetime, τ. Therefore, the lifetime of the resonance can be determined from its width in energy. Since the origin of the broadening is the penetration of the wavefunctions through the triangular barrier into the continuum, this lifetime corresponds to the tunnelling lifetime.

Ghatak *et al* (1988, 1990) have shown that in the vicinity of a resonance centred at E_n, $\xi(E)$ is Lorentzian in form:

$$\xi(E) \propto \frac{1}{(E-E_n)^2+\Gamma^2}, \tag{2.15}$$

where Γ is the width parameter for the peak. Eq. (2.14) can then be rearranged to give the tunnelling lifetime:

$$\tau_{tun} = \frac{\hbar}{2\Gamma}. \tag{2.16}$$

The procedure for calculating the resonance energy and lifetime is as follows. The wavefunction is assembled as in Eq. (2.9). The energy range from the bottom of the well to the top of the barrier is divided into intervals, and at each point the coefficients are determined and the ratio $\xi(E)$ is calculated. Peaks in $\xi(E)$ are then located with respect to the energy grid. When a peak is found, the search is refined to determine the position of the peak to within a specified accuracy. $\xi(E)$ is then fitted to a Lorentzian function to determine the width parameter, Γ, and hence the lifetime of the resonance using Eq. (2.15).

The calculated ground state tunnelling lifetime for the well in Fig. 2.5 is presented in Fig. 2.6 as a function of the electric field. As expected, the lifetime is strongly dependent on the electric field, decreasing for increasing field strength.

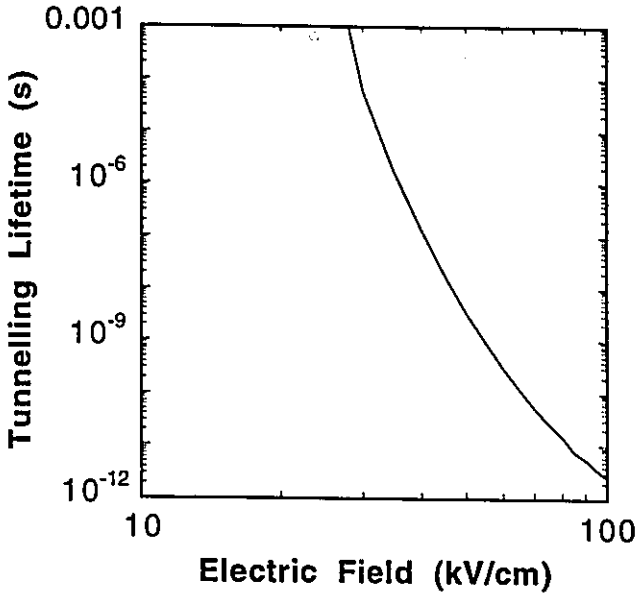

Fig. 2.6: Calculated tunnelling times for the electron ground state of a GaAs/$Al_{0.2}Ga_{0.8}As$ quantum well as a function of the electric field across the well.

2.4. Thermionic Emission.

Formulations of the thermionic emission current in bulk-barrier systems have been in wide use for many years (see, for example, Sze (1981)). However, this description cannot be directly applied in the case of a quantum well due to the quantization of the perpendicular momentum and the resultant differences in the density of states. Hence, a new treatment is required. In this section, I will begin by briefly reviewing the 3D bulk-barrier description. This will be followed by a description of the quantum well formulation derived by Moss *et al* (1994), which applies in the limit of small perpendicular electric fields. Finally, I will present the description for the situation where the field is strong and the emission time is governed by the 2D-to-3D scattering rate.

2.4.1. Thermionic emission at bulk-barrier junctions.

The bulk-barrier thermionic emission calculation is presented briefly to familiarize the reader with the classical description of the process (See Wu *et al* (1979) for a detailed discussion). The potential profile considered is shown in Fig. 2.7. It is assumed that the emission rate is slow enough that the carriers in the lower potential region are well

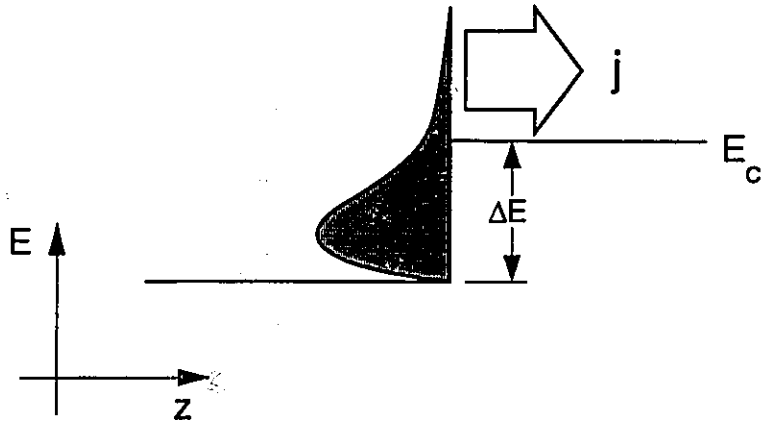

Fig. 2.7: Thermionic emission over a bulk-barrier junction. The shaded curve schematically shows the carrier distribution in the lower energy side of the junction. Only carriers with sufficient momentum in the z-direction will overcome the barrier.

described by a Fermi-Dirac distribution. For non-degenerate carrier densities, this can be approximated by a Boltzmann distribution

$$f(E)=e^{-(E-E_F)/k_BT} \tag{2.17}$$

where E_F is the Fermi energy. The current over the barrier per unit area is given by

$$\begin{aligned} j_z &= \bar{e}\int_{v_{z,min}}^{\infty} n(E)v_z Tr(E)dE \\ &= \bar{e}\int_{v_{z,min}}^{\infty} g(E)f(E)v_z Tr(E)dE \end{aligned} \tag{2.18}$$

where $\bar{e}$ is the charge on the carrier, including its sign, $Tr(E)$ is the quantum mechanical transmission function of the barrier, and $g(E)$ is the density of states, given in this case by the 3D form,

$$g_{3D}(E)=\frac{1}{2\pi^2}\left(\frac{2m^*}{\hbar^2}\right)^{\frac{3}{2}}E^{\frac{1}{2}}. \tag{2.19}$$

The lower limit $v_{z,min}$ in Eq. (2.18) indicates that only those carriers with sufficient momentum in the direction perpendicular to the barrier can actually escape and contribute.

To a first approximation, we can set $Tr(E)$ equal to unity for energies above the barrier and zero below. Then the integration is most easily performed in momentum space,

where the lower limit becomes

$$k_{z\min}=\sqrt{\frac{2m^*\Delta E}{\hbar^2}} \tag{2.20}$$

where ΔE is the barrier height as illustrated in Fig. 2.7. This gives for the thermionic emission current density

$$j_z=\bar{e}\frac{1}{4\pi^2}\frac{2m^*(k_BT)^2}{\hbar^3}\exp\left[\frac{-(\Delta E-E_F)}{k_BT}\right]. \tag{2.21}$$

The Fermi energy, E_F, is determined by the condition

$$n=\int_{E_{min}}^{\infty} f(E)g(E)dE \tag{2.22}$$

which leads to the result

$$j_z=\bar{e}n\left(\frac{k_BT}{2m^*\pi}\right)^{\frac{1}{2}}\exp\left(-\frac{\Delta E}{k_BT}\right) \tag{2.23}$$

for the thermionic emission current density over a bulk-barrier, as would be encountered at a semiconductor heterointerface. This differs from the well-known Richardson-Dushman equation, which is derived in the case of a metal-insulator or metal-semiconductor interface, due to the differences in the evaluation of the Fermi energy; however, the approach is the same in both cases.

2.4.2. Thermionic emission from a quantum well under small electric fields.

When the electric field across the well is small or zero, the problem of thermionic emission from a quantum well can be treated following the steps given in the preceding section for the bulk-barrier interface. The main difference is in the density of states used in the calculation of the Fermi energy.

In the bulk-barrier derivation, the basic assumption is that the escape rate is slower than the thermalization rate so that thermal equilibrium is maintained amongst all states on the lower energy side of the barrier. For a quantum well under low electric fields, the

situation is similar. Since the field across the well is small, the motion away from the well is dominated by diffusion and there is a significant probability of recapture by the well. If the diffusion is slow when compared to the scattering rate between the 2D confined states and the 3D continuum states, then the two 'subsystems' will be in thermal equilibrium. As a result they will be characterized by the same Fermi energy and hence the carrier distribution is obtained by applying a single occupation function to the total density of states.

We follow the derivation of Moss *et al* (1994). The thermionic emission current out of the well is calculated by applying Eq. (2.18) as before. In the quantum well system, the density of states in k-space for states above the barrier remains the same as in the bulk case. Therefore the integration is identical as for the bulk-barrier interface, giving Eq. (2.21) where the barrier height, ΔE, is replaced by the effective barrier height, ΔE_{eff}, as given approximately by

$$\Delta E_{eff} = \Delta E - \frac{e\mathscr{E}w}{2} \tag{2.24}$$

where w is the well width. The effective barrier height will be discussed in greater detail later in this chapter when barrier lowering effects are considered. To fully evaluate the thermionic emission current, the Fermi energy must be determined. This is again accomplished by integrating Eq. (2.22).

In a quantum well system, the total density of states is the sum of the 2D contribution from the quantum well subbands, as given by

$$g_{2D}(E) = \frac{m^*}{\pi\hbar^2 w}\sum_i H\left(E - E_i\right), \tag{2.25}$$

and the 3D contribution for states above the barrier. In Eq. (2.25), E_i is the energy of the i^{th} state, $H(E)$ is the Heaviside step function, and the summation is over all confined subbands. Note that the factor w, the well width, is introduced to make g_{2D} a density of states per unit volume. The above-barrier density of states is given by (Moss, 1994)

$$\begin{aligned} g_{3D}(E) &= \frac{m^*}{\pi^2\hbar^2}\left(\sqrt{\frac{2m^*E}{\hbar^2}} - k_{barr}\right)H\left(E - \Delta E_{eff}\right) \\ &= \frac{1}{2\pi^2}\left(\frac{2m^*}{\hbar^2}\right)^{\frac{3}{2}}\left(\sqrt{E} - \sqrt{\Delta E_{eff}}\right)H\left(E - \Delta E_{eff}\right) \end{aligned} \tag{2.26}$$

where k_{barr} is defined as

$$k_{barr}=\sqrt{\frac{2m^*\Delta E_{eff}}{\hbar^2}}. \tag{2.27}$$

Eq. (2.26) differs from the usual 3D result, Eq. (2.19), by the offset k_{barr}. The total density of states is then

$$g(E)=\frac{m^*}{\pi\hbar^2 w}\sum_i H\left(E-E_i\right)+\frac{1}{2\pi^2}\left(\frac{2m^*}{\hbar^2}\right)^{\frac{3}{2}}\left(\sqrt{E}-\sqrt{\Delta E_{eff}}\right)H\left(E-\Delta E_{eff}\right). \tag{2.28}$$

Substituting Eq. (2.28) for the density of states and Eq. (2.17) for the occupation factor in Eq. (2.22) gives (Moss, 1994)

$$n=2\bar{n}\left(\frac{m^*k_BT}{2\pi\hbar^2}\right)^{\frac{3}{2}}\exp\left(\frac{E_F}{k_BT}\right) \tag{2.29}$$

where

$$\bar{n}=\frac{2}{\sqrt{\pi}}\left[\frac{\pi}{w}\sqrt{\frac{\hbar^2}{2m^*k_BT}}\sum_i e^{-E_i/k_BT}+\int_{\Delta E_{eff}}^{\infty}\sqrt{x}\,e^{-x}dx-\sqrt{\overline{\Delta E_{eff}}}\,e^{-\overline{\Delta E_{eff}}}\right] \tag{2.30}$$

and

$$\overline{\Delta E_{eff}}\equiv\frac{\Delta E_{eff}}{k_BT}. \tag{2.31}$$

The emission current density out of the well is then (Moss, 1994)

$$j=\frac{n}{\bar{n}}\left(\frac{k_BT}{2\pi m^*}\right)^{\frac{1}{2}}e^{-\Delta E_{eff}/k_BT}. \tag{2.32}$$

In general, the quantity of interest is actually the thermionic emission time, τ_{TE}, as defined by

$$\frac{dn}{dt}=\frac{n}{\tau_{TE}}. \tag{2.33}$$

Since the emission current density gives the rate at which carriers escape the well *per unit area*, the rate of decay of the carrier density *per unit volume* is obtained by dividing by the well width, w. Hence the thermionic emission time, in the low field regime, is given by

$$\begin{aligned}\tau_{TE}&=\frac{w}{j}\\ &=wn^{-}\left(\frac{2\pi m^{*}}{k_{B}T}\right)^{\frac{1}{2}}e^{\Delta E_{qf}/k_{B}T}\end{aligned} \tag{2.34}$$

2.4.3. Thermionic emission from a quantum well under large electric fields.

If the electric field across the quantum well is large then the motion in the continuum states will be dominated by drift instead of diffusion and carriers in above-barrier states will be quickly swept away. In this case, the assumption of thermal equilibrium between the carriers in above-barrier and confined states breaks down and the thermionic emission time is determined by the scattering rate into the above-barrier states (Gurioli, 1992), (Liu, 1993).

The decay rate for the population of a particular state is given by Eq. (2.33) where τ_{TE} is replaced by $\tau_s(E)$, the scattering lifetime at energy E. To determine the overall decay rate for the confined states, we integrate Eq. (2.33) over all energies in the confined subbands:

$$\begin{aligned}\left(\frac{dn}{dt}\right)_{tot}&=\int_{E_0}^{\infty}\frac{n(E)}{\tau_s(E)}dE\\ &=\int_{E_0}^{\infty}\frac{f(E)g_{2D}(E)}{\tau_s(E)}dE\end{aligned} \tag{2.35}$$

where E_0 is the ground state energy. If the scattering rate out of the well, as given by $1/\tau_s(E)$, is slow relative to the scattering rate within the confined subbands, then thermal equilibrium within these states can be assumed and the carrier distribution will be given by Fermi-Dirac statistics. Approximating the Fermi-Dirac distribution by the Boltzmann function given by Eq. (2.17), and substituting Eq. (2.25) for the 2D confined density of

states gives

$$\frac{n}{\tau_{TE}}=\frac{1}{\pi\hbar^2 w}\sum_i m_i^* \int_{E_i}^{\infty}\frac{e^{-(E-E_F)/k_BT}}{\tau_s(E)}dE. \tag{2.36}$$

The Fermi energy can be determined by applying Eq. (2.22) which gives

$$n=\frac{1}{\pi\hbar^2 w}e^{E_F/k_BT}\sum_i m_i^* e^{-E_i/k_BT}. \tag{2.37}$$

When substituted in Eq. (2.36), we obtain

$$\frac{1}{\tau_{TE}}=\frac{\left(\sum_i m_i^* \int_{E_i}^{\infty}\frac{e^{-E/k_BT}}{\tau_s(E)}dE\right)}{\left(\sum_i m_i^* e^{-E_i/k_BT}\right)} \tag{2.38}$$

Evaluation of Eq. (2.38) requires the scattering function, $\tau_s(E)$. The scattering processes that will contribute include electron-phonon, carrier-carrier, alloy or interface roughness, and impurity or defect scattering. In high quality epitaxial semiconductor layers at low or moderate carrier densities, electron-phonon scattering is believed to dominate, except at low temperatures ($\leq$100 K) (Mendez, 1986) (Weisbuch, 1991). Detailed calculations of the electron-phonon, 2D-to-3D scattering rate will be presented in the following chapter.

If an effective barrier energy, $E_{b,eff}(E)$, can be defined, above which the scattering time is independent of energy and below which it is infinite, then Eq. (2.38) takes on the simpler form

$$\frac{1}{\tau_{TE}}=\frac{\sum_i \frac{m_i^*}{\tau_{s,i}}}{\left(\sum_i m_i^* e^{\Delta E_{eff,i}/k_BT}\right)} \tag{2.39}$$

where $\Delta E_{eff,i}$ is the effective barrier height for the i^{th} level as given by

$$\Delta E_{eff,i}=E_{b,eff}-E_i. \tag{2.40}$$

and $\tau_{s,i}$ is the average above-barrier scattering time for the i^{th} subband.

It is apparent from the preceding descriptions that there is a significant difference between the two descriptions of thermionic emission from a quantum well and so it is necessary to examine what is meant by 'large' or 'small' electric fields. We define the following rough criteria for use of the high field treatment. If the time required for the escaping carrier to be accelerated away from the well is shorter than the scattering time between the well and continuum states, i.e.: the recapture time, then thermal equilibrium cannot be established and the high field description will apply. We neglect the initial kinetic energy of the carrier and assume that it must travel the entire width of the well to escape. From simple kinematics, the sweepout time is then given by

$$\tau_{esc}=\sqrt{\frac{2m^{*}w}{e\mathscr{E}}} \tag{2.41}$$

which, for a well width of 100 Å, an effective mass of $0.067m_0$, and an electric field strength of 1 kV/cm, gives a time of 280 fs. As will be seen in Chapter 4, a typical scattering time is slightly less than a picosecond; assuming a value of ~0.5 ps, the sweepout time is still faster than the capture time. Considering that the *built-in* fields in *p-i-n* structures are generally an order of magnitude greater, and that this approach should, if anything, overestimate the sweepout time, in most cases of practical interest the high field description will apply.

2.5. Barrier Lowering Effects in Thermionic Emission.

As is evident from the preceding descriptions of the thermionic emission rates from quantum wells, the barrier height strongly influences the escape rate. There are three principal mechanisms by which an electric field alters the potential barrier. First is the reduction of the confined state energy in the triangular potential. This is a small effect and is generally neglected. Next we consider the inclination of the well potential which raises the barrier height on one side while lowering it on the other. Finally, there is image charge lowering due to the response of the free carriers remaining in the well as a single charge leaves. While the latter effect has been understood for many years in the case of a metal-insulator junction, the case of a semiconductor heterojunction has yet to be treated correctly. Detailed calculations of image charge formation in a semiconductor quantum

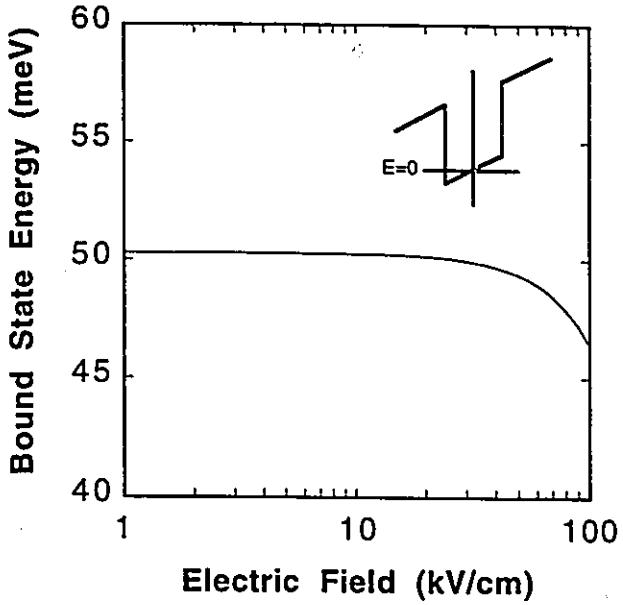

Fig. 2.8: Energy of the first confined state as a function of electric field for a 50Å $GaAs/Al_{0.2}Ga_{0.8}As$ quantum well. The energy is measured relative to the centre of the well as shown in the inset.

well will be presented in chapter 3, where the finite carrier density will be shown to dramatically reduce the effects of image charge lowering.

2.5.1. Change in energy solution in triangular well.

When an electric field is applied to a quantum well, the bottom of the well becomes triangular, as shown in the inset to Fig. 2.8. When measured relative to the potential at the centre of the well, we find that the energy levels shift slightly downwards. This results in an increase in the effective barrier height relative to the unshifted case.

There is no simple analytical formula to calculate the shift in energy with electric field. Instead, Fig. 2.8 shows the energy of the first confined state as a function of electric field for a 60 Å $GaAs/Al_{0.2}Ga_{0.8}As$ quantum well as calculated by the resonance method described previously. It reveals that the energy shifts are of the order of an meV and as a result are generally neglected in escape rate calculations.

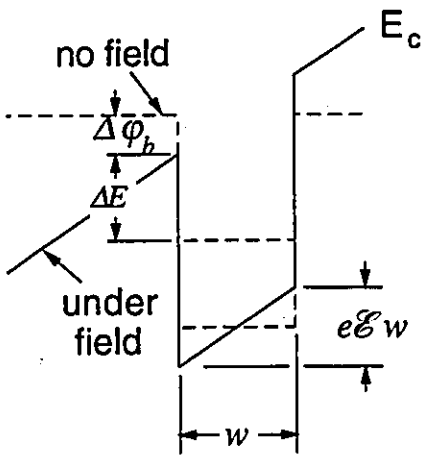

Fig. 2.9: Barrier lowering due to the inclination of the well potential in an electric field. The front of the well is lowered while the back of the well is raised. ΔE is the potential barrier height.

2.5.2. The inclination of the potential well in an electric field.

Since relative to the centre of the well, the energy of the confined state remains roughly unchanged as the potential is tilted under the electric field, the 'front' of the well will be lowered while the 'back' of the well is raised. As shown in Fig. 2.9, if the well has a width w then the barrier will be lowered by an amount

$$\Delta\varphi_b = \frac{e\mathscr{E}w}{2}. \tag{2.42}$$

For a 50 Å quantum well, this translates into a 2.5 meV drop for every 10kV/cm of electric field; a significant amount that increases with the well width.

2.5.3. Image charge lowering.

Image charge lowering effects have been observed at metal-vacuum and metal-semiconductor interfaces for many years (Crowell and Sze, 1966), (Lin and Eng, 1989). In these systems, it has been shown to be well described by the ideal conductor solution given in most electricity and magnetism textbooks (see, for example, Lorrain (1988)). To date this effect has generally been ignored in calculations of semiconductor quantum well escape times or, if included, the perfect conductor formulation has been applied. As will be shown in detail in Chapter 3, this result does not strictly apply due to the effects of the finite carrier density in the well. For now, however, the results of the perfect conductor

analysis will be reviewed.

In an ideal conductor, the carrier density is assumed to be infinite so that the conductivity is also infinite. As a result, when a free charge is placed in front of the conductor, the carriers in the conductor redistribute themselves to shield the electric field of the free charge from the interior of the conductor. This must occur since any non-zero fields would produce infinite currents. The steady state boundary conditions are then

$$\mathscr{E}_t = 0 \tag{2.43a}$$

$$\mathscr{E}_p = \frac{\sigma}{\varepsilon} \tag{2.43b}$$

where σ is the surface charge density, ε is the dielectric constant of the insulator, and $\mathscr{E}_t$ and $\mathscr{E}_p$ are the tangential and perpendicular components of the electric field, just outside the conductor. The latter condition can easily be derived from Gauss' Law. This results in the formation of a surface charge distribution which produces a field within the conductor that is exactly equal and opposite to the field of the free charge. At the surface itself, the total field is everywhere perpendicular to the interface.

In the simplest method of solution for the electric fields and the charge distribution at the surface of the conductor, a fictitious charge of opposite sign is placed at an equal distance on the other side of the interface. This charge is referred to as the *image charge* and is illustrated in Fig. 2.10. The total electric field is then given by the sum of the

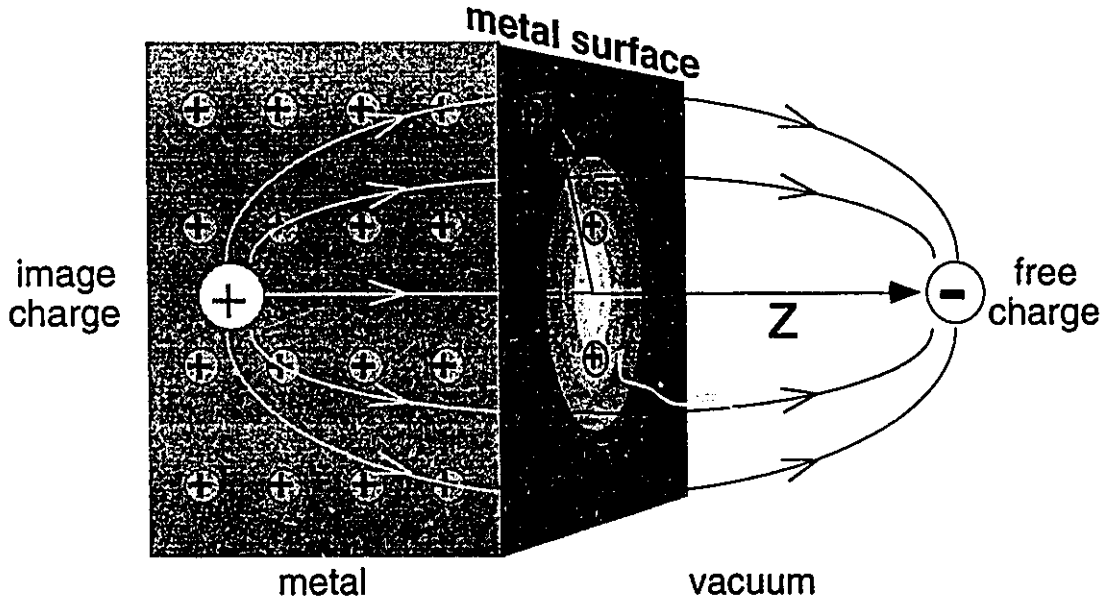

Fig. 2.10: Image charge formation in a perfect conductor. The fictitious image charge is placed at an equal distance on the opposite side of the interface.

contributions due to the image charge and the free charge. The surface charge distribution is obtained from the electric field at the surface and the boundary condition on the perpendicular component given in Eq. (2.43b). This gives

$$\sigma(\rho)=-\frac{\bar{e}}{2\pi}\frac{z}{\left(z^2+\rho^2\right)^{3/2}} \tag{2.44}$$

where ρ is the radial distance from the point directly opposite the external charge, and $\bar{e}$ is the charge on the external carrier, including its sign. The potential energy of the free charge is obtained by calculating the work done on the carrier in moving it from ∞ to z. This gives the result

$$V_{im}(z)=-\frac{e^2}{16\pi\varepsilon}\frac{1}{z}. \tag{2.45}$$

For an electron on the semiconductor side of a metal-semiconductor junction, the potential energy profile in the absence of an applied electric field is shown in Fig. 2.11 (a). When an electric field is applied, the image potential is added to the triangular barrier formed in the semiconductor as depicted in Fig. 2.11 (b). The total potential is then given by a peaked function where the potential at the peak is lower than the peak in the triangular barrier by an amount

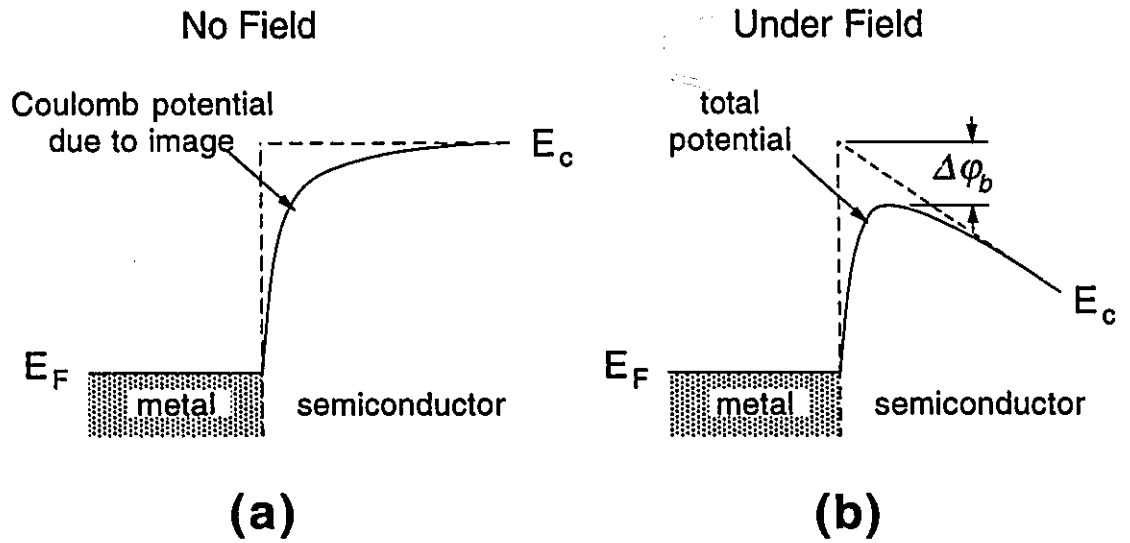

Fig. 2.11: Potential energy profile for a metal-semiconductor barrier including the image charge (a) without an applied field (b) with an applied field. The presence of the image charge potential results in the barrier being lowered by an amount $\Delta\phi_b$.

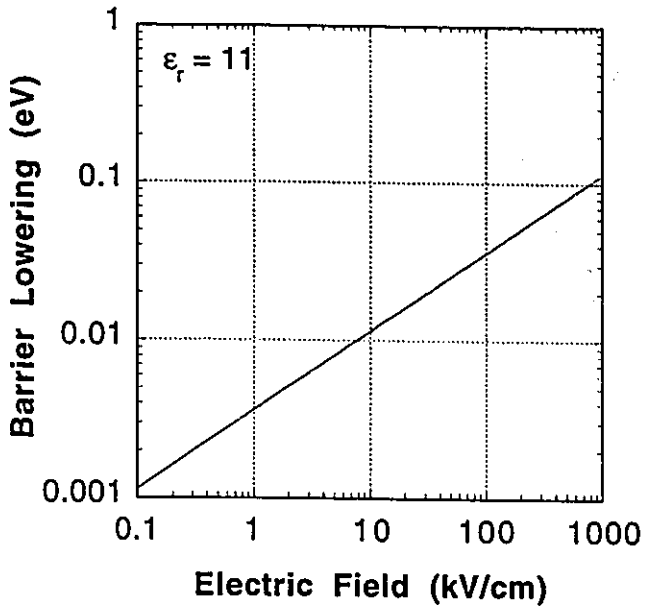

Fig. 2.12: Calculated image charge lowering of the barrier at a metal-GaAs interface. Even at moderate fields of a few kV/cm the barrier lowering is of the order of 10 meV.

$$\Delta\varphi_b = \left(\frac{e\mathscr{E}}{4\pi\varepsilon}\right)^{\frac{1}{2}}. \tag{2.46}$$

This is the so-called image charge lowering effect as it applies to metal-semiconductor or metal-vacuum interfaces. For a metal-GaAs interface, the amount of barrier lowering can be substantial, as shown in Fig. 2.12.

Since the motion of the external charge is neglected, the classical treatment described above is a quasi-static approximation. It is based on the assumption that the response of the conductor will be fast on the timescale of the escape of the free charge. This will be true if the escape time is much less than $1/\omega_p$, the plasma frequency of the conductor (Korotkov, 1994). A typical value for the plasma frequency in a metal is ~10^{16} Hz (Ashcroft and Mermin, 1976). Even if we assume the saturation velocity of ~10^7 cm/s and a distance of 10 Å to the peak of the potential, the escape time is 10^{-14} s, two orders of magnitude longer than the plasma response time. In fact, we should expect the escape velocity to be considerably less since the emission will be dominated by those carriers that have just enough energy to overcome the barrier. It is apparent then, that the approximation is valid in the case of metal-vacuum interfaces. In metal-semiconductor interfaces, the barrier lowering is also affected by the dielectric response. For the static dielectric constant to apply, the escape time must be less than the dielectric relaxation time. This condition has been verified experimentally for Au-Si barriers (Sze, 1964).

Since a semiconductor has a much lower conductivity than a metal, the overall situation can be quite different in the case of a semiconductor heterojunction. In this case the steady state boundary condition of Eq. (2.43) becomes

$$\mathbf{j} = \mathbf{j}_{drift} + \mathbf{j}_{diff} = 0 \tag{2.47}$$

where $\mathbf{j}_{drift}$ and $\mathbf{j}_{diff}$ are the drift and diffusion surface current densities, or, in the case of a quantum well, the 2D in-plane current densities. The addition of the diffusion current precludes the existence of an analytic solution and hence a numerical approach is required.

The effect of the diffusion current is very important. By acting against the local accumulation or depletion of carriers, it reduces the effective image charge and hence diminishes the amount of barrier lowering. The significance of this effect increases as the carrier density decreases, so that at very low densities, image charge lowering will become negligible at semiconductor heterojunctions. The effects of the diffusion current and the 2D nature of the charge carriers in a quantum well will be considered in detail in Chapter 3, where numerical simulations of image charge formation in a quantum well will be presented.

Since the reduced carrier density will also result in a lower plasma frequency, it is possible that the quasi-static approximation may no longer be valid. If we assume a carrier density of 10^{16} cm^{-3}, the GaAs electron effective mass of $0.067 m_0$, and a dielectric constant of 11, we obtain a $1/\omega_p$ time of 4×10^{-14} s. This is now on the same order of magnitude as the estimated escape time. However, as noted earlier, the vast majority of carriers contributing to the current will have much smaller velocities. Therefore, the quasi-static approximation should not result in any significant errors in the thermionic emission calculations.

As stated earlier, image charge lowering has been generally ignored in relation to thermal escape rates from semiconductor quantum wells. This may be due to the assumption that the heterojunction barrier occurs at the interface between two *dielectrics*. Since the dielectric constants will differ, the polarizations induced in the two materials will also differ and there will be a net polarization and hence a net electric field at the interface. The field and potential can again be deduced by the proper choice of an hypothetical image charge, and following a similar analysis the barrier lowering can be determined. Since the difference in dielectric constants between the two materials is generally quite small, this effect has been shown to be negligible for semiconductor heterojunctions (Gabovich and Rozenbaum, 1984) (Coon and Liu, 1987). However, as discussed above, since semiconductors may contain significant carrier densities, they must be treated not only as

dielectrics, but as conductors as well. As such, we must also consider the heterojunction as an interface between a conductor and a dielectric, and the corresponding image charge effects should be included.

2.6. Thermally-Assisted Tunnelling.

If more than one subband is confined in the quantum well system, there exists the possibility of a hybrid escape process called *thermally-assisted tunnelling*. In this case, a carrier is thermally excited into an upper subband from which it tunnels through the barrier into a continuum state. This can be considered as the 2D equivalent of Fowler-Nordheim tunnelling (see, for example, Bransden and Joachain, 1989).

The escape rate via the i^{th} subband (where $i > 1$) is given by the product of the subband occupation and its lifetime. This gives for the thermally-assisted tunnelling lifetime

$$\frac{1}{\tau_{TT,i}} = \frac{1}{\tau_i} \int_{E_i}^{\infty} f(E) g_{2D,i}(E) dE \tag{2.48}$$

where τ_i is the tunnelling lifetime of the i^{th} subband. Since the tunnelling lifetime is roughly independent of the in-plane energy (Meshov, 1986), it can be considered as a constant for that particular subband. Approximating $f(E)$ by a Boltzmann distribution and taking only the i^{th} subband's contribution to the 2D density of states of by Eq. (2.25) gives

$$\frac{1}{\tau_{TT,i}} = \frac{m_i^* e^{-E_i/k_B T}}{\tau_i \left(\sum_j m_j^* e^{-E_j/k_B T} \right)}. \tag{2.49}$$

where Eq. (2.37) has been used to eliminate the Fermi energy.

2.7. Summary.

In this chapter I have reviewed the calculations of the escape rates from quantum wells via tunnelling, thermionic emission and thermally assisted tunnelling. The tunnelling

calculation stems from the resonance method for a quantum well in an electric field. The lifetime is obtained from the width of the energy resonance by applying the Heisenberg uncertainty relation. The thermionic emission calculation was split into two regimes: high and low electric field. Under low field, the treatment is similar to the conventional bulk-barrier case where the 2D and 3D states are assumed to be in thermal equilibrium. The emission rate is then obtained by considering those carriers in 3D states whose momentum carries them away from the well. Under high fields, the equilibrium between the well and continuum states breaks down and the limiting process becomes the scattering rate out of the well. Calculations of this rate will be presented in Chapter 4. A brief review of barrier lowering effects is presented including the shift in the resonance energy, the inclination of the potential well, and image charge lowering. The latter will be considered in detail in the following chapter. Finally, the hybrid process of thermally-assisted tunnelling was described. This mechanism is only possible when there are multiple subbands confined to the well, where escape occurs when carriers tunnel out of a thermally occupied upper subband.

Chapter 3: Image Charge Lowering in Semiconductor Quantum Wells.

The quasi-static theory of image charge formation at the surface of an ideal perfect conductor was described in Chapter 2. However, this treatment assumed that the conductivity was infinite as a consequence of the infinite carrier density. This condition breaks down in the case of even a highly doped semiconductor where the carrier densities are still typically three orders of magnitude less than in a metal. As a result, the boundary condition requiring that the electric field vanish within the conductor is no longer accurate and we must return to the more fundamental requirement of zero current flow at steady state. The steady-state boundary condition is then given by Eq. (2.47), ie:

$$\mathbf{j}_{tot} = \mathbf{j}_{drift} + \mathbf{j}_{diff} = 0 \,. \tag{3.1}$$

where in a quantum well, the carriers are confined to a quasi-2D sheet so that the current densities are expressed per unit length instead of per unit area.

In this chapter, I will present a detailed examination of image charge lowering in a semiconductor quantum well in the quasi-static approximation, where the effects of the finite carrier density will be included. There are three possible scenarios to consider. The most general case is one in which both electrons and holes contribute to the conductivity of the well layer. This will be referred to as *bipolar* image charge formation. However, first we will consider the case in which one of the carrier species dominates the conductivity, i.e.: unipolar image charge formation. Here we must distinguish between two cases depending on the polarity of the escaping charge. If its polarity is opposite to that of the

species in the well, i.e.: a minority carrier, then the sheet charge will be accumulated near the escaping carrier. We will refer to this as *minority unipolar* image charge formation. If the escaping charge and the sheet charge are of the same sign, i.e.: a majority carrier, then the image charge will be formed by depleting the sheet charge. This will be referred to as *majority unipolar* image charge formation. A brief discussion of each of the three scenarios will be presented in the first section.

The equations required to solve for the steady-state carrier distribution(s) and potential energy of the external charge as a function of its position relative to the well layer are essentially the same in each case. These will be given in §3.2. Results of the numerical simulations will then be presented for each of the three cases in §3.3. The diffusion current will be shown to inhibit the formation of the image charge distribution so that the barrier lowering is reduced relative to the perfect conductor case. The reduction in the image charge lowering will be quantified by the effective image charge, e_{eff}. We will find that in general it approaches the full electronic charge at carrier densities greater than 10^{12} cm^{-2}, while tending to zero at low densities. In the majority unipolar problem, the formation of a depleted hole in the sheet charge will further inhibit the development of an image charge, resulting in a barrier lowering that becomes independent of the electric field above a minimum field strength.

3.1. Introduction.

Consider first the unipolar well where the escaping charge is of opposite polarity. For example, if an electron is placed before a sheet of positively charged holes, the holes will be attracted towards the electron. This is referred to as the minority unipolar case. A steady state will be reached when the drift current due to the presence of the external charge is balanced by the diffusion current resulting from the non-uniform carrier distribution. Since in this case the distribution is produced by accumulating charge, in the quasi-static approximation there is no limitation on the amount of charge that can be assembled in the image distribution. Consequently, in the absence of diffusion we would obtain the perfect conductor result, regardless of the carrier density.

The escape of a carrier from a unipolar charge sheet of opposite polarity has only limited relevance to practical situations. For example, the escape of the last few electrons from an optically generated electron-hole plasma in a quantum well, where the holes are still abundant, will have little effect on the overall escape characteristics of the well.

However, since the only significant difference between this and the ideal conductor problem is the finite carrier density, it allows us to more closely examine the role of the diffusion current. As the drift current is proportional to the carrier density while the diffusion current depends only on its derivative, as the sheet carrier density decreases, the role of the diffusion current should be accentuated.

Consider now a unipolar well where the escaping charge is of the same sign as the well charge, i.e.: a majority carrier. This would correspond to a doped quantum well or to photogenerated carriers in an intrinsic well when only the slower escaping species remains. In this case, the presence of the escaping charge will push the sheet carriers away to produce a depletion of the well carrier distribution. We refer to this as the majority unipolar case. Again, a steady state is attained when the drift and diffusion currents are equal and opposite. If the charge is close enough, the field will be sufficient to completely deplete the available carrier density and form a hole in the sheet charge. As a result, the effective image charge is limited at short distances by the finite carrier density in the well. This would in fact occur more readily in the absence of diffusion so that even if diffusion were omitted, the perfect conductor solution would break down in the majority unipolar problem.

The bipolar well is the most general case and is of particular relevance to a photogenerated electron-hole plasma in a doped or intrinsic quantum well. In this case both accumulation and depletion occur. It is not immediately obvious how the image charge will be divided between the two species or whether a depleted hole will be formed as in the majority unipolar case. In fact, we will find that a depleted region is never formed, even at the lowest carrier densities considered.

3.2. Calculating the Image Charge Effect in a Quantum Well.

3.2.1. The drift-diffusion equations.

The classical description of the carrier motion in a semiconductor is given by the drift-diffusion equation,

$$\nabla \cdot \left(\mathbf{j}_{drift} + \mathbf{j}_{diff} \right) = -\bar{e} \frac{\partial n}{\partial t} . \tag{3.2}$$

As an analytic solution for the carrier distribution does not exist, Eq. (3.2) will be solved

using the numerical technique of finite-differences (Press, 1992). The drift and diffusion currents are given by

$$\mathbf{j}_{drift} = \bar{e}\mu n \mathscr{E} \tag{3.3}$$

and

$$\mathbf{j}_{diff} = -\bar{e} D_n \nabla n \tag{3.4}$$

respectively, where μ is the mobility, D_n is the diffusion coefficient, and $\bar{e}$ is the charge on the carriers in the charge sheet including the sign. In the unipolar case, this can be the same or opposite to the charge on the escaping carrier. In the bipolar system, there will be two sets of current equations, coupled via the electric field. For non-degenerate carrier densities, the mobility and diffusion coefficients are related by the Einstein relations

$$D_n = \frac{\mu k_B T}{e}. \tag{3.5}$$

Since the problem possesses cylindrical symmetry, circular cylindrical coordinates are used and the charge sheet is chosen to lie in the plane defined by z = 0. This is illustrated in Fig. 3.1. Substituting Eqs. (3.3)-(3.5) in Eq. (3.2) with $\bar{e}n$ replaced by σ, the sheet charge density, gives the result

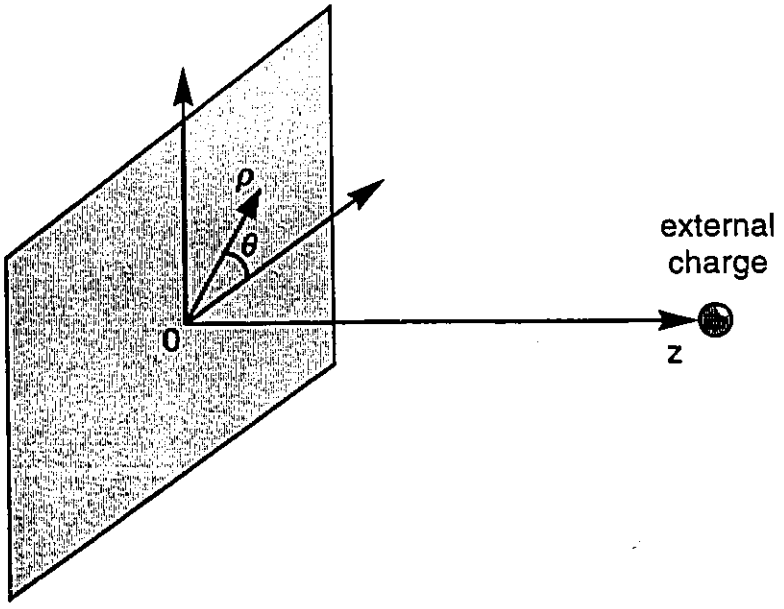

Fig. 3.1: Coordinate scheme used in the image charge simulations. The shaded region represents the plane of the quantum well.

$$\frac{\partial \sigma(\rho)}{\partial t} = \frac{1}{\rho}\frac{\partial}{\partial \rho}\left[\mu\sigma(\rho)\mathcal{E}_\rho(\rho) - \frac{\mu k_B T}{e}\left(\rho\frac{\partial \sigma(\rho)}{\partial \rho}\right)\right] \tag{3.6}$$

where the origin is chosen to lie in the plane at the point directly opposite the escaping charge. The condition for steady state is

$$\frac{\partial \sigma(\rho)}{\partial t} = 0. \tag{3.7}$$

Note that applying Eq. (3.7) to Eq. (3.6) sets the left side of Eq. (3.6) equal to zero and hence causes the dependence on the mobility to cancel. Since at steady state both the electron and hole currents must vanish, this will be true in the bipolar case as well.

Eq. (3.6) is then the working equation for the simulation. The condition for convergence is Eq. (3.7) which implies that this is the quasi-static approximation, as discussed in the previous chapter. The assumption is that the response of the carriers in the sheet is very fast on the time-scale of the motion of the escaping charge. As the escaping carriers will be dominated by those with just enough energy to escape, this is a reasonable approximation.

3.2.2. Details of the calculation.

The radial symmetry in the plane of the charge sheet permits the use of concentric circular rings as charge bins. This scheme is illustrated in Fig. 3.2. The central radius of the i^{th} bin is located at R_i, while the inner and outer boundaries are at ρ_{i-1} and ρ_i respectively. When compared with the usual cartesian grid, the use of circular bins provides much greater coverage for a manageable number of bins. To further improve the coverage, the width of the rings expands as R increases. This scheme is permissible because the slope in the charge distribution decreases at large ρ, so that the details of the charge distribution are mostly confined to the region near the origin.

At very large ρ, it is assumed that the charge distribution is unaffected by the escaping charge. Hence, the charge sheet is divided into two sections: small ρ, where the sheet is divided into bins, and large ρ, where the sheet is treated as a single, fixed bin.

At each of the bins the charge density is evaluated according to Eq. (3.6). The currents are evaluated at the boundaries between the bins so that the change in σ_i is given by

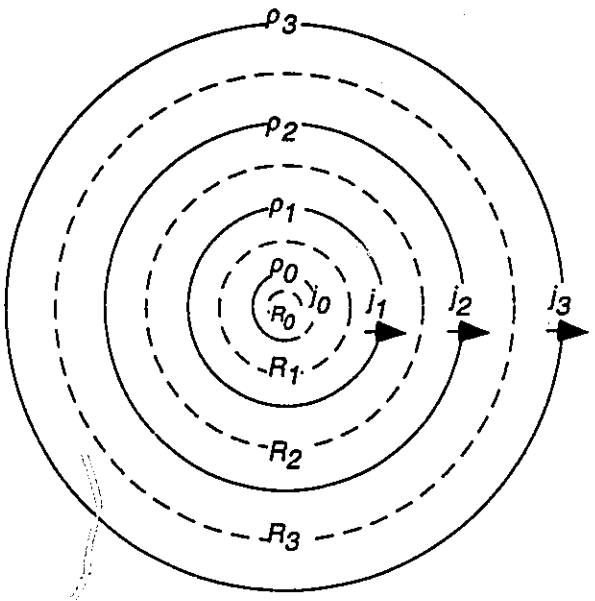

Fig. 3.2: Concentric rings/bins used in image charge simulations. Charge densities, σ_i, are calculated at the R_i's and the fields and currents are calculated at the ring boundaries, ρ_i.

$$\sigma_i(t+\Delta t)=\sigma_i(t)+\left[\frac{1}{R_i dR_i}\left(\rho j_{tot,i}-\rho_{i-1}j_{tot,i-1}\right)\right]\Delta t \tag{3.8}$$

where dR_i is the thickness of the i^{th} ring as defined by

$$dR_i=\rho_i-\rho_{i-1}. \tag{3.9}$$

The total current density, $j_{tot,i}$, is the sum of the drift and diffusion currents at ρ_i. The drift current density is calculated according to

$$j_{drift,i}=\mu\,\overline{\sigma(\rho_i)}\,E_i \tag{3.10}$$

where $\overline{\sigma(\rho_i)}$ is the average charge density at the boundary ρ_i and is approximated by

$$\overline{\sigma(\rho_i)}=\sigma_i+\left(\frac{\sigma_{i+1}-\sigma_i}{R_{i+1}-R_i}\right)\frac{dR_i}{2}. \tag{3.11}$$

The diffusion current density is calculated as

$$j_{diff,i}=-\frac{\mu k_B T}{e}\left(\frac{\sigma_{i+1}-\sigma_i}{R_{i+1}-R_i}\right). \tag{3.12}$$

To evaluate the electric field at ρ_i requires an expression for the electric field due to a ring of charge Q_i with a radius R_i. This is given by the series solution (Smythe, 1939)

$$\mathscr{E}^{\sigma}(\rho_i)=\begin{cases}\left(\dfrac{Q_i}{4\pi\varepsilon R_j^2}\right)\displaystyle\sum_{n=0}^{\infty}(2n+1)\left(\frac{\rho}{R_j}\right)^{-(2n+2)}\left[\frac{1\cdot 3\ldots(2n-1)}{2\cdot 4\ldots 2n}\right]^2, & \rho>R_j \\ \left(\dfrac{Q_i}{4\pi\varepsilon R_j^2}\right)\displaystyle\sum_{n=0}^{\infty}(2n)\left(\frac{\rho}{R_j}\right)^{(2n-1)}\left[\frac{1\cdot 3\ldots(2n-1)}{2\cdot 4\ldots 2n}\right]^2, & \rho<R_j\end{cases} \tag{3.13}$$

To reduce computation time, these values are calculated once at the beginning of the program and stored as a matrix, M_{ij}, such that

$$\mathscr{E}_i^{\sigma}=\sum_j^N M_{ij}Q_j \tag{3.14}$$

where N is the number of bins and the charge in the jth bin, Q_j, is given by

$$Q_j=\sigma_j(2\pi R_j dR_j). \tag{3.15}$$

The total field is obtained by adding the field due to the external charge,

$$\mathscr{E}_i^{q}=\frac{\bar{e}}{4\pi\varepsilon}\frac{\rho}{\left(\rho^2+z^2\right)^{3/2}}, \tag{3.16}$$

to the sheet field given by Eq. (3.14).

The basic algorithm is as follows. The sheet charge distribution, $\sigma(\rho)$, is initialized to some estimate of the equilibrium charge distribution. This is usually chosen to be the distribution given by the perfect conductor solution. The electric fields and currents are calculated at the boundaries, ρ_i. The change in charge density is then calculated for each of the bins, according to Eq. (3.6). Changes in the sign of the charge density are not permitted, so in cases where the calculated change in charge density exceeds the existing density, the out-going current is adjusted to make the density in the bin go exactly to zero. The entire procedure is repeated until convergence is attained.

The number of iterations required to reach convergence will depend on the time

increment, *dt*. This cannot be made arbitrarily large as the simulation rapidly becomes unstable. In fact, there will be an upper limit, determined by the ring spacings and the mobility, above which the program will always become unstable, no matter how small the carrier densities or currents. Therefore *dt* must be kept to a small value; 10^{-20} s was found to be the upper limit for the parameters used.

The natural criteria for convergence is for the relative change in the charge in each bin (i.e.: the current density divided by the charge density) to fall below some arbitrary cutoff. However, it turns out that the bins at large ρ have a much smaller effect on the potential energy of the escaping charge than the bins at small ρ. Furthermore, due to their increased widths it takes longer for these bins to reach equilibrium. Since the objective of the simulation is to calculate the potential energy of the escaping charge as a function of distance from the charge sheet, convergence can be assumed when the relative change in the calculated potential per iteration falls below some arbitrary limit. This limit was set at one part in 2×10^9 per iteration.

The potential energy of the external charge is calculated by adding the potential energies due to each of the rings. For a charge $\bar{e}$ at a distance z from a ring of radius R_i, containing a total charge Q_i, the potential energy is given by

$$V(z)=-\frac{\bar{e}}{|\bar{e}|}\frac{Q_i}{4\pi\varepsilon}\frac{1}{\left(R_i^2+z^2\right)^{1/2}}. \tag{3.17}$$

However, this is derived for the case where the charges in the ring are held fixed as the external charge is moved in from infinity. In the actual problem, these charges are mobile and are assembled into the ring as the charge is brought in. As a result, half of the work done in assembling this configuration is performed on the charges in the ring, the other half on the external charge. Therefore, to calculate the potential energy of the external charge alone, it is necessary to divide the result (3.17) by two.

Given the potential energy as a function of z, the distance from the sheet, the barrier lowering can be determined by calculating the total potential energy profile for different electric fields. The barrier lowering is then obtained by evaluating

$$\Delta\varphi_b(\mathscr{E})=E_b-\max\left(V_{im}(z)-e\mathscr{E}z\right) \tag{3.18}$$

where $V_{im}(z)$ is the image charge potential calculated as described in the preceding paragraph.

3.3 Results.

In this section the results of the image charge simulations will be presented for the three possible scenarios: an escaping minority carrier (minority unipolar), an escaping majority carrier (majority unipolar), and escape from a bipolar well. The first case is of the least practical importance but serves to illustrate the impact of the diffusion current on the image charge formation. The second case corresponds to the escape from doped unipolar wells or the escape of the slower species from a photogenerated electron-hole plasma in a quantum well. The third is the most general case, where both electrons and holes are present in different proportions. Calculations will be presented for carrier densities ranging from 10^{10} cm^{-2} to 10^{13} cm^{-2}. The diffusion current is shown to substantially reduce the degree of image charge formation, and hence the amount of barrier lowering, in all three cases. We will find that in general, the image charge lowering can be described by the perfect conductor equation, Eq. (2.46), where the charge on the free carrier (and hence the image) is replaced by an effective charge that approaches e, the charge on the electron, at high carrier densities. In the majority unipolar case, the image charge distribution is limited by the finite sheet carrier density so that above a certain electric field, the barrier lowering becomes independent of the field. The cutoff field between the field-dependent and field-independent regimes is proportional to the carrier density, and above the cutoff, the barrier lowering exhibits a power law dependence on the carrier density. In an intrinsic unipolar well, the field due to the free charge in the well is always greater than the cutoff field, so that the barrier lowering is independent of the applied bias.

3.3.1. The oppositely charged unipolar well (minority unipolar).

To isolate the effects of the diffusion current on image charge formation, the situation where the sheet charge and the escaping charge are of opposite polarity was considered. As the image charge distribution is formed by accumulating sheet charge, the depletion that occurs in both the majority unipolar and bipolar cases is absent. Therefore, any differences in the image potential with respect to the perfect conductor solution will be due entirely to the diffusion current.

Simulations were performed following the procedure described in the previous section for well carrier densities ranging from 10^{10} cm^{-2} to 10^{13} cm^{-2}. The only parameter used in the calculation is the relative permittivity, ε_r, where the approximate GaAs value of 11 is assumed for the relative permittivity. A value for the mobility is also assumed,

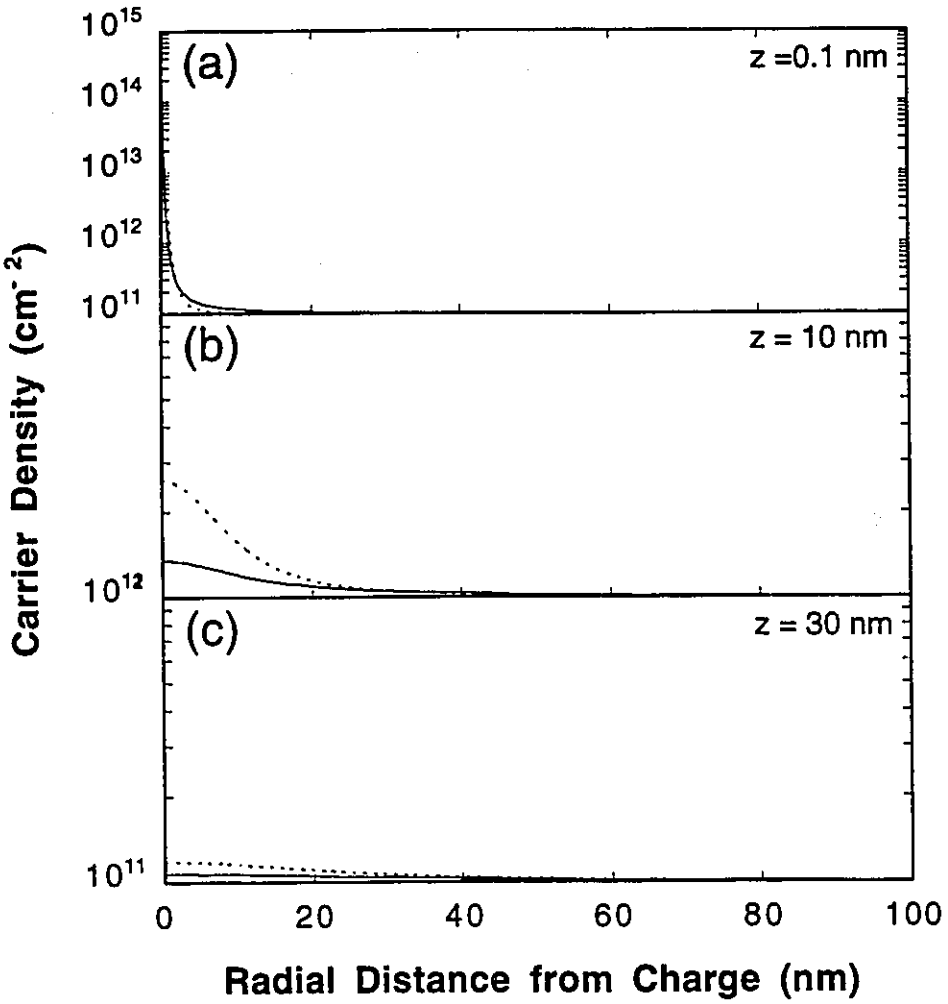

Fig. 3.3: Calculated sheet charge distributions for an escaping minority carrier at distances of (a) 0.1 nm, (b) 10 nm, and (c) 30 nm from a unipolar quantum well. The solid curves give the simulation results while the dotted curves correspond to the perfect conductor solution.

however its actual value is unimportant to the equilibrium solution since it cancels out between the drift and diffusion currents.

Fig. 3.3 shows the calculated sheet carrier distributions as a function of the radial in-plane coordinate (ρ) for an external charge at distances, z, of (a) 0.1 nm, (b) 10 nm, and (c) 30 nm from the well. The unperturbed carrier density is 10^{11} cm^{-2}. For comparison, the image charge distributions in the perfect conductor case are shown by the dotted curves. At all distances, the simulation results lie below those calculated for the perfect conductor. Since these would be obtained by omitting the diffusion term from the simulation, Fig. 3.3 shows that the diffusion current significantly reduces the image charge distribution.

Fig. 3.4 displays the calculated image charge potentials for sheet carrier densities of

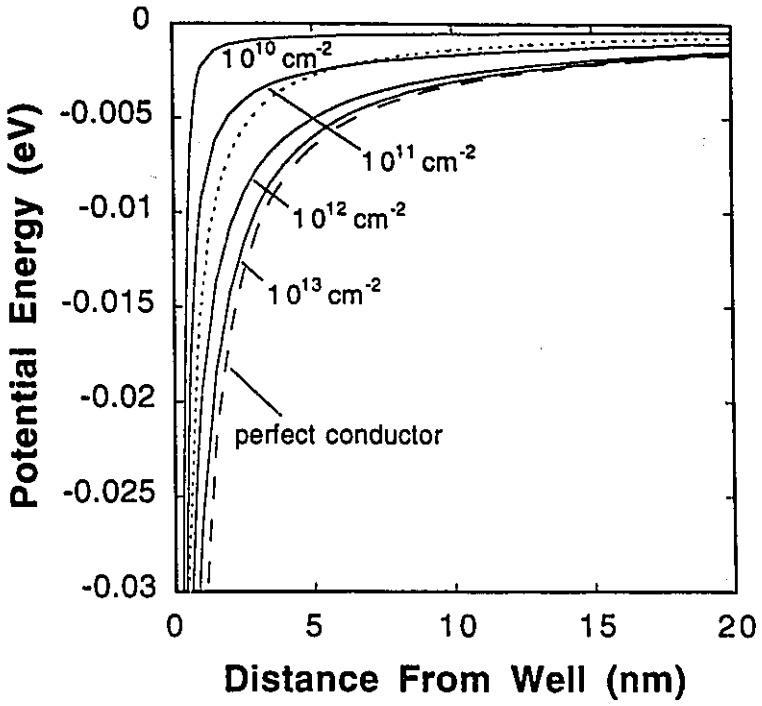

Fig. 3.4: Image charge potentials calculated by the minority unipolar simulation. The dashed curve is the potential obtained in the perfect conductor approximation while the dotted curve is a fit to the 10^{11} cm^{-2} data according to Eq. 3.19. As the carrier density is increased, the potential functions approach the perfect conductor result. At low carrier densities, the potential energy differs from the ideal result by as much as 700%.

between 10^{10} and 10^{13} cm^{-2}. For comparison, the dashed curve displays the perfect conductor result. As expected, the latter calculation produces the deepest potential while the minority unipolar curves become increasingly shallow as the carrier density decreases. This is a result of the reduction in accumulated image charge due to the diffusion current, since its relative importance increases as the carrier density decreases.

While the form of the potential is similar to that found in the perfect conductor case, it does not have the same inverse dependence on the position, z. The best fit to the 10^{11} cm^{-2} data for a function of the form

$$V(z) = -\frac{A}{z} \tag{3.19}$$

where A is a fitting parameter, is shown by the dotted line in Fig. 3.4. The discrepancy is primarily due to the rapid downward curvature at small z. At these distances, the carrier density near the centre of the distribution becomes large so that the effect of the diffusion current is weakened and the behaviour becomes more like that of the ideal conductor.

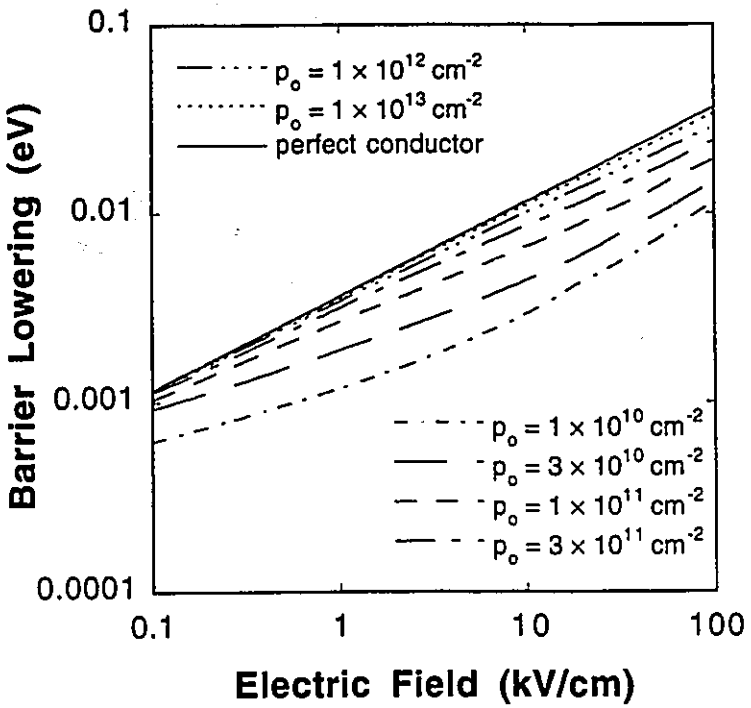

Fig. 3.5: Image charge barrier lowering as a function of the total electric field for minority unipolar case. Curves are shown for carrier densities between 10^{10} and 10^{13} cm^{-2}, and for the perfect conductor solution. The discrepancy between the drift-diffusion result and the perfect conductor solution increases with decreasing carrier density.

From the potential functions, we obtain the barrier lowering as a function of the total field. These are shown in Fig. 3.5 for sheet carrier densities of between 10^{10} and 10^{13} cm^{-2}. For comparison, the perfect conductor solution is also given. The simulation results lie below the perfect conductor values for all of the carrier densities considered. However, as the density increases, the curves shift toward the drift-only solution, with very little difference remaining at 10^{13} cm^{-2} (<8% at 100 kV/cm). These results indicate that at the high concentrations commonly found in doped semiconductors, the perfect conductor solution is still applicable. At lower densities, less than 10^{11} cm^{-2}, the discrepancy between the drift-diffusion and perfect conductor solutions increases significantly.

Although the simulation results do not obey the square root dependence exhibited by the perfect conductor result given by Eq. (2.47), particularly at low carrier densities and small electric fields, it is still instructive to fit the data and compare the results with the perfect conductor equations. It will then be possible to define an effective charge which will allow us to continue to use the perfect conductor equations to estimate the image charge lowering. In Fig. 3.6, the calculated data have been fitted to functions of the form

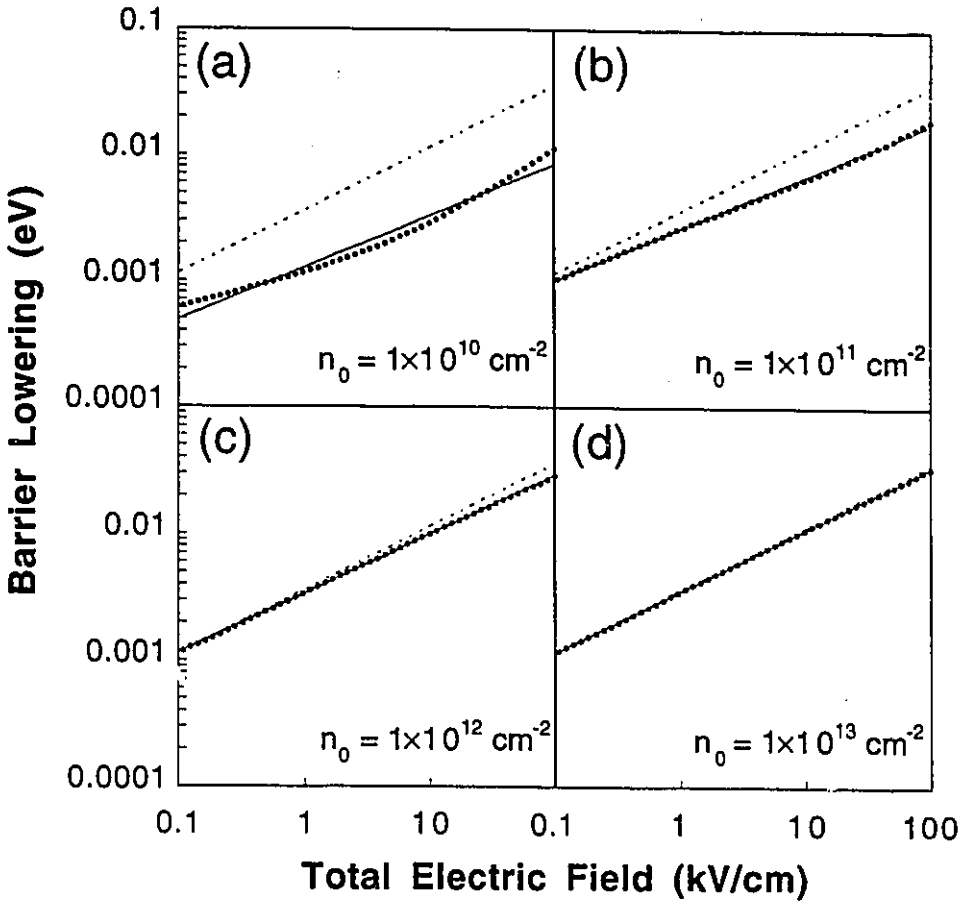

Fig. 3.6: Image charge lowering as a function of the total electric field for the minority unipolar case. The The solid lines are fits to the calculated data to a square root power law while the dotted curves are the perfect conductor results. The fits improve at higher carrier densities, although even at the lowest density considered the error is less than 10% over this range of electric fields.

$$\Delta\phi = A\,\mathcal{E}^{1/2} \tag{3.20}$$

where A is the fitting parameter. The fits are quite good at high densities with differences of less than 0.4 meV relative to the calculated data. The agreement deteriorates at 10^{10} cm^{-2}, however the differences remain less than 1 meV. Comparing the fitted coefficients A to the ideal value given by

$$\left(\frac{e}{4\pi\varepsilon}\right)^{1/2} \tag{3.21}$$

we obtain the effective charges plotted in Fig. 3.7. Error bars obtained from the fits to the

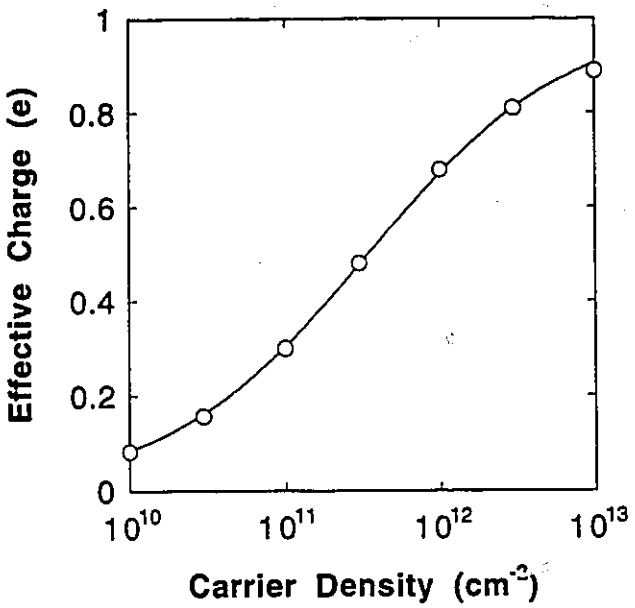

Fig. 3.7: Effective charges as a function of the sheet carrier density as obtained from fits to the minority unipolar barrier lowering curves. Error bars that reflect the uncertainties in the fits to the barrier lowering curves as inFig. 3.6. are contained within the symbols.

barrier lowering data are contained within the symbols. The solid line shows a best fit to the data described by the equation

$$e_{eff}=\frac{1}{1+5.54\times 10^{7} n^{-0.673}} \tag{3.22}$$

where the effective charge is given in units of e, the electronic charge, and the carrier density, n, is given in cm^{-2}. The effective charge can then be used to estimate the barrier lowering according to

$$\Delta\phi=\left(\frac{e_{eff}}{4\pi\varepsilon}\right)^{1/2}\mathscr{E}^{1/2}. \tag{3.23}$$

Note that while the fits to the barrier lowering data are poor at low carrier densities and small fields, in these regimes the lowering is of the order of an meV or less and hence the resultant error in calculated thermal escape rates will be negligible.

3.3.2. The similarly charged unipolar well (majority unipolar).

To perform the majority unipolar calculation, the only required change to the previous simulation was the sign of the escaping charge. Again, carrier densities between 10^{10} cm^{-2} and 10^{13} cm^{-2} were considered, using a relative permittivity of 11.

Fig. 3.8 shows the calculated sheet charge distributions where the diffusion current is included (solid curve) and omitted (dotted curve). These are given for external charge distances of (a) 0.1 nm, (b) 10 nm, and (c) 30 nm from the surface, where the unperturbed carrier density is 10^{11} cm^{-2}. Note that since the sheet carriers and the escaping carrier are of the same polarity, the image charge manifests itself by depleting the sheet charge

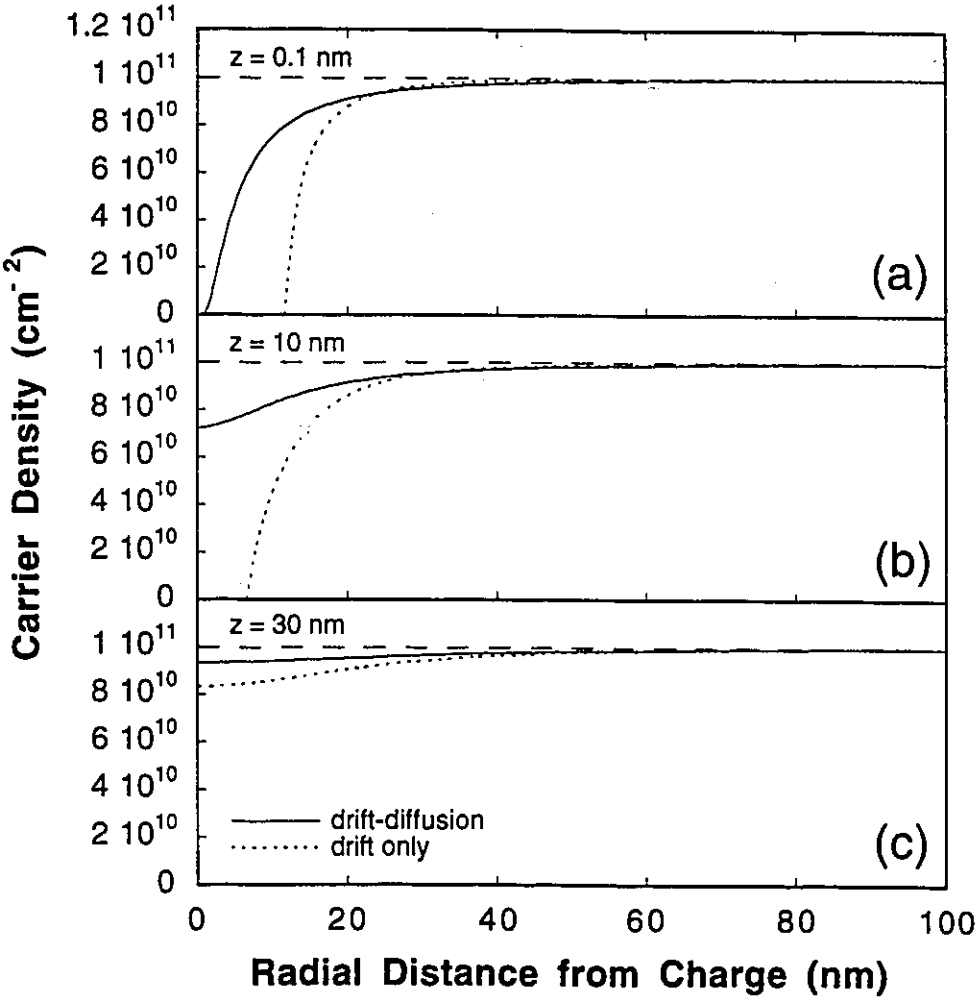

Fig. 3.8: Sheet charge distributions calculated with (solid) and without (dotted) the diffusion current for an escaping majority carrier at a) 0.1 nm, b) 10 nm , and c) 30 nm from the surface of a unipolar quantum well. The unperturbed carrier density is 10^{11} cm^{-2} and is represented by the dashed line. The diffusion current inhibits the accumulation of image charge resulting in a shallower depletion of the sheet carriers.

distribution. As seen in the minority unipolar results, the diffusion current causes a dramatic reduction in the amount of sheet charge depletion. In Fig. 3.8 (b) there is already a region completely depleted of charge in the drift-only result while the drift-diffusion curve shows only 28% depletion at the centre of the distribution. At this carrier density, depletion occurs in the drift-diffusion simulation only for $z < 0.8$ nm, compared with 11.5 nm in the drift-only simulation. This further illustrates the importance of including the diffusion component when solving for the image charge distribution.

By subtracting the background carrier density, we obtain the actual image charge distribution responsible for the image potential. In Fig. 3.9 image charge distributions for a sheet density of 10^{11} cm^{-2} and an external charge at a distance of 10 nm from the surface are shown as calculated for the perfect conductor, the minority unipolar, and the majority unipolar cases. We see that there is a significant difference between the results obtained from the two unipolar drift-diffusion simulations. Since a depleted hole in the sheet charge has not yet formed in the majority unipolar case at this distance, the only difference between the two calculations is that in one the image charge is produced by depleting the carriers, while in the other it is via accumulation. Since the magnitude of the drift current depends on the carrier density, it will be larger in the minority simulation where the carrier density is always greater than the background value, whereas in the majority case it is always less. Therefore, the effect of the diffusion current is stronger in the majority

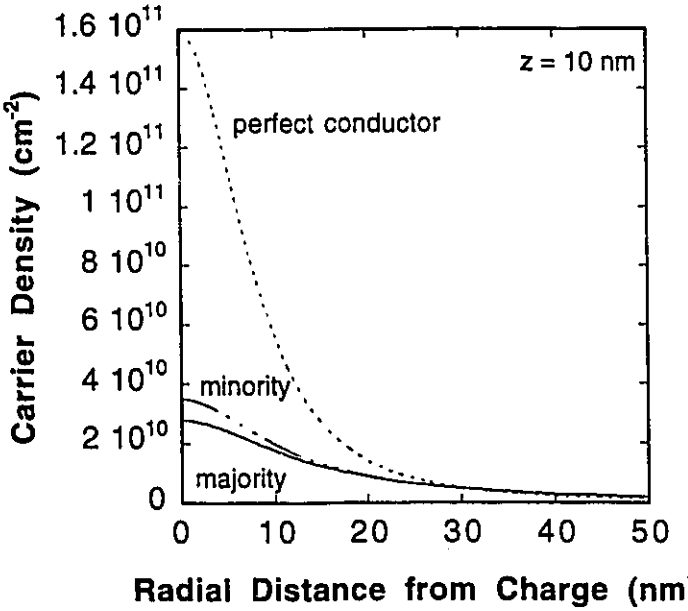

Fig. 3.9: Comparison of the image charge carrier distributions obtained from the perfect conductor (dotted), minority unipolar (dash-dotted), and majority unipolar (solid) calculations. The background sheet carrier density is 10^{11} cm^{-2} and the external charge is 10 nm from the well layer.

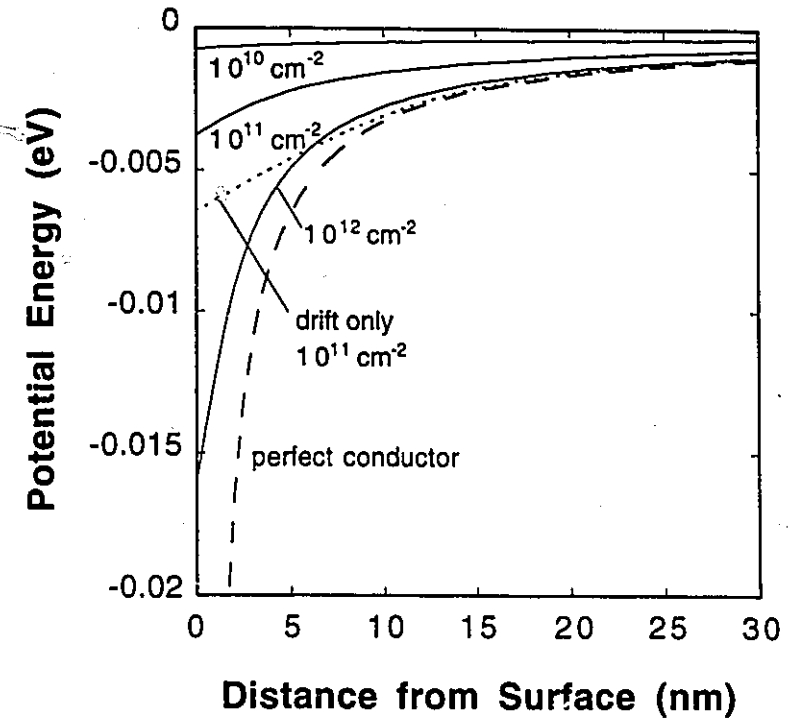

Fig. 3.10: Calculated image potentials for carrier densities of 10^{10}, 10^{11}, and 10^{12} cm^{-2} for a majority carrier escaping from a unipolar quantum well. Also shown are the potentials obtained from the perfect conductor solution (dashed) and the drift-only simulation (dotted) for a carrier density of 10^{11} cm^{-2}.

unipolar simulation than in the minority unipolar simulation, resulting in the reduced image charge distribution. Of course, the perfect conductor approximation produces the largest image charge distribution since it does not include the diffusion current.

Graphs of the majority unipolar image potential for different well carrier densities are shown in Fig. 3.10. The reductions in the image charge distributions produce shallower potential wells. At higher sheet densities, the effect of the diffusion current decreases and the potential profile shifts towards the ideal conductor result. Note that the drift-diffusion curves deviate from the perfect conductor prediction at all distances whereas the drift-only result, as shown by the dotted curve, deviates only when the external charge is close enough to deplete through the sheet. The deviation in both cases is due to a reduction in the image charge distribution, however in the drift-only case this results solely from the limitation of the finite sheet charge density.

When the potential energy functions for the majority unipolar simulation in Fig. 3.10 are compared with those obtained from the minority unipolar simulation in Fig. 3.4, we find that the rapid downward curvature at small z is present only in the minority unipolar data. This reflects the limitations of generating the image charge

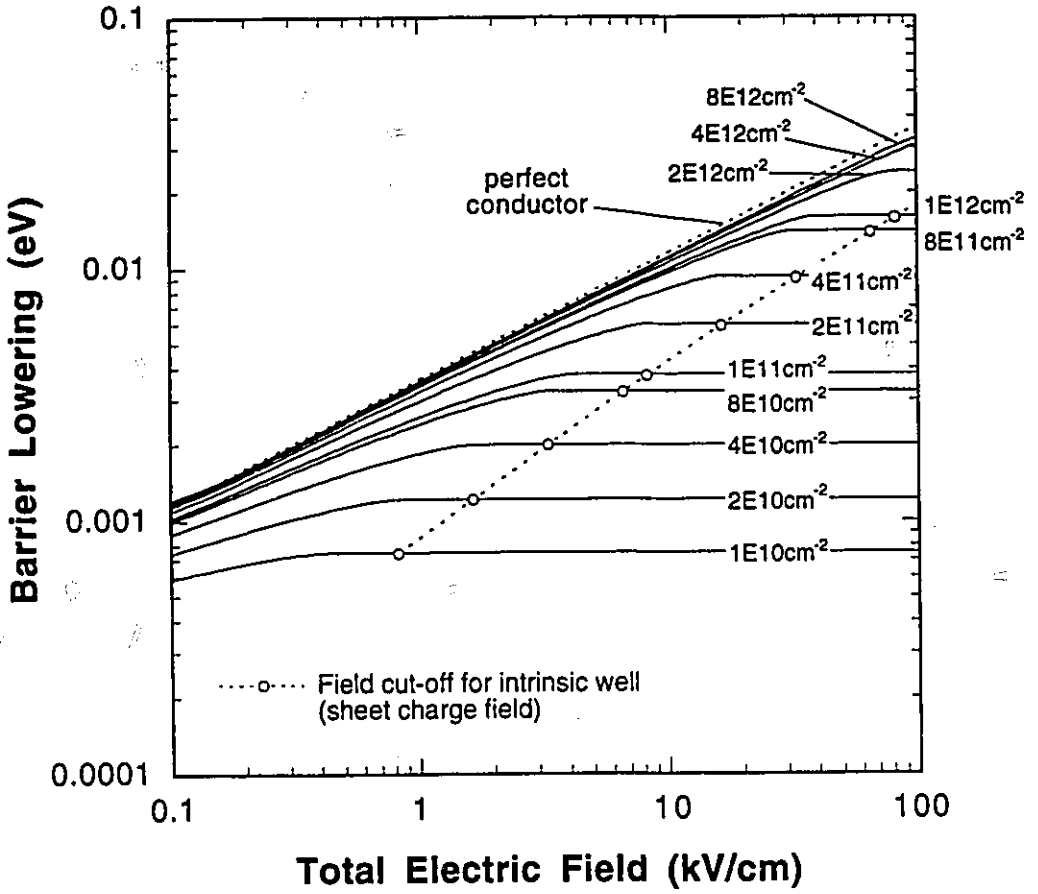

Fig. 3.11: Calculated majority unipolar image charge barrier lowering as a function of the total electric field. Each curve corresponds to a different carrier density. The dashed curve represents the minimum field due to the sheet charge density in the case of a unipolar intrinsic well. The intersection of the dashed curve with any of the barrier lowering curves gives the field due to the sheet charge density alone.

distribution by depleting the sheet carrier density. The high peak carrier densities which produce the large potential energies in the minority unipolar simulation simply cannot be attained in the majority unipolar case. Although this will have a significant effect on the barrier lowering at higher field strengths, at low fields there will be little difference between the two unipolar simulation results.

Fig. 3.11 shows the calculated image charge lowering as a function of the electric field. This field will include contributions due to the net charge density in the well, which in the case of a unipolar intrinsic well is simply the carrier density. If the well is doped then the ionized dopants must be considered also. Any externally applied field will be *in addition* to this charge sheet field and hence it represents a lower limit to the total field at the well. The corresponding well potential is illustrated in Fig. 3.12 for (a) zero applied field

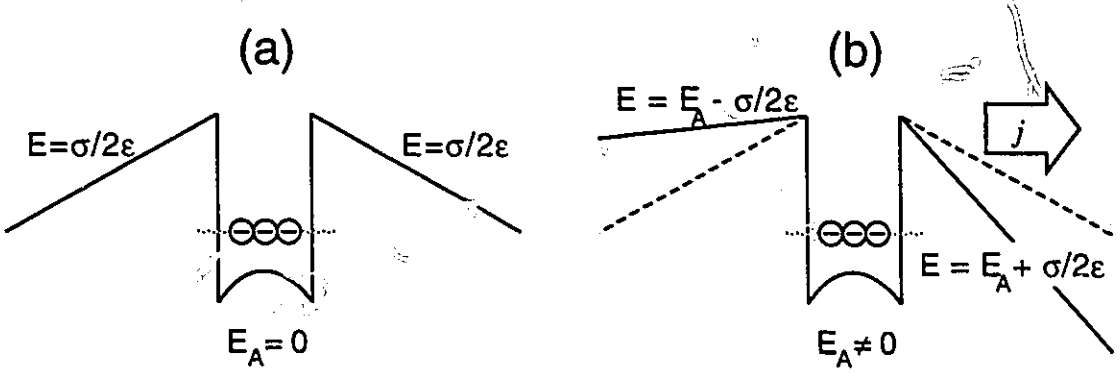

Fig. 3.12: The minimum field due to the net charge density in the well. a) In the absence of an external field, the net charge in the well produces a field of magnitude $\sigma/2\varepsilon$. b) The external field, E_A, is then added to the charge field, E_σ, so that the total field is given by $E_\sigma + E_A$.

and (b) a non-zero applied field. In the direction of escape, the charge sheet field adds to the applied field. The dashed curve in Fig. 3.11 indicates the strength of the charge sheet field as a function of the carrier density for the intrinsic well. It is interpreted as follows: the intersection of the dashed curve with any of the barrier lowering curves marks the minimum field for that particular carrier density in a *unipolar intrinsic* well (where there are no dopants to compensate any of the free charge). In all cases the dashed curve lies within the flat portion of the barrier lowering curve where it is independent of the total field. This implies that in intrinsic unipolar wells the majority carrier barrier lowering is *always independent of the field* and depends only on the carrier density. This is in stark contrast to the perfect conductor result where the barrier lowering contains a square root dependence on the total field.

The origin of the field-independent behaviour is the reduced image charge formation, in particular due to the limited depletion of the finite sheet charge density. In the perfect conductor case, the image charge distribution diverges at its centre as the external charge approaches the surface. This results in a sharp downward curvature in the potential energy profile. The smaller image charge obtained in the simulation produces a much gentler curvature. This is illustrated in Fig. 3.13 where the total potential energy profiles for the drift-diffusion and perfect conductor cases are shown for an absolute field of 50 kV/cm. Where the perfect conductor solution forms a peak at a distance of 2.55 nm from the surface, in the drift-diffusion case the peak occurs at the surface. Since the potential maximum will also be located there at larger fields, the barrier lowering is independent of the total field for values greater than some minimum value. It turns out that for all carrier densities considered, the sheet charge field lies above this minimum. Fig. 3.14 is a plot of the field dependence cutoff, above which the barrier lowering is field

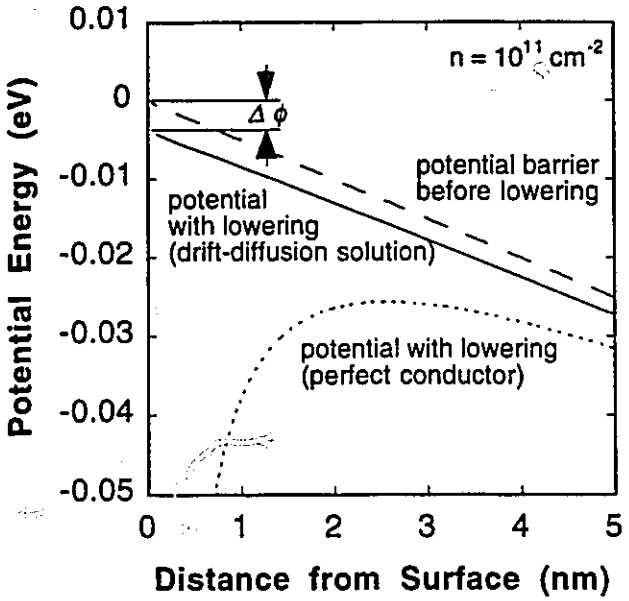

Fig. 3.13: Total potential energy profile for an external charge in the field of its image in a 50 kV/cm electric field for the majority unipolar drift-diffusion (solid) and perfect conductor (dashed) solutions. The dashed-dotted line represents the barrier in the absence of image charge formation. The maximum in the potential profile occurs at the surface for the drift-diffusion result as compared to the peak formed at z = 25 nm in the perfect conductor case. This results in a barrier lowering that is independent of the electric field.

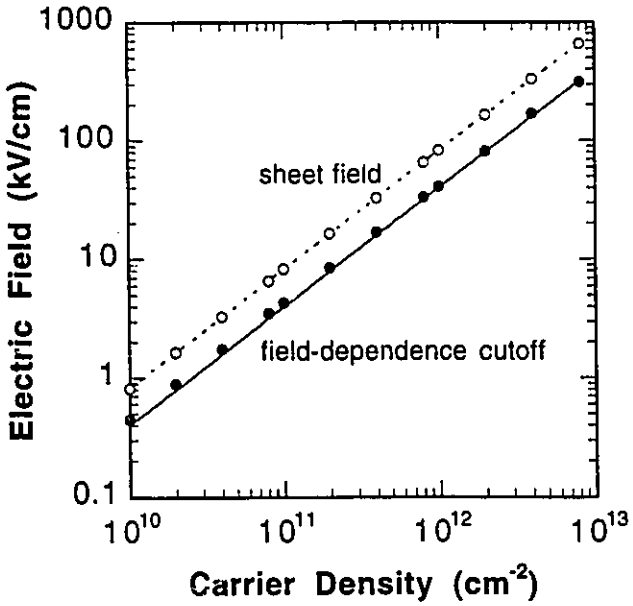

Fig. 3.14: Sheet field cutoff (open) and sheet field (filled) as a function of the sheet carrier density; the solid line is linear fit to the cutoff data. The field cutoff marks the transition between the field-dependent and field-independent regimes in the majority unipolar case. Since the cutoff line lies below the sheet field line, barrier lowering is always independent of the applied field in an intrinsic unipolar quantum well for the case of majority carrier escape.

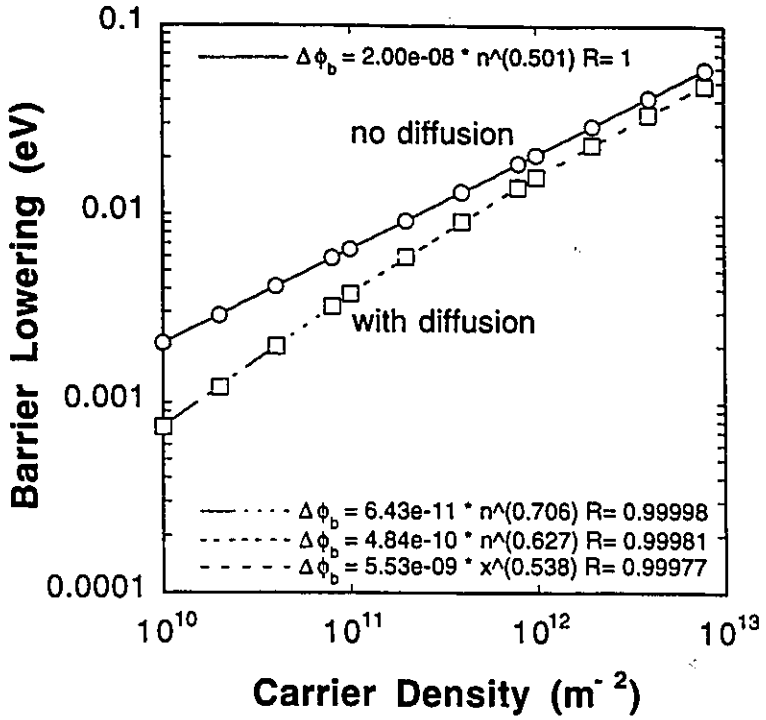

Fig. 3.15: Majority unipolar barrier lowering as a function of the sheet carrier density. While the drift-only data fits what is very nearly a square root law, the drift-diffusion data is best described by applying the power law fit in sections. The exponent varies from 0.7 at low densities to nearly 1/2 at the higher densities.

independent. The solid line is a fit to the data which shows that the cutoff field is proportional to the carrier density, where the constant of proportionality is $(4.10 \pm 0.01)\times10^{-11}$ kV•cm, with the carrier density given in cm^{-2} and the cutoff field in kV/cm. Also shown is the sheet field, which lies above the cutoff for all carrier densities.

Fig. 3.15 shows the field independent barrier lowering as a function of the carrier density for a unipolar intrinsic well. Also shown is the same result for the drift-only simulation. The reduced image charge formation due to the influence of the diffusion current produces a smaller barrier lowering. The solid line describes the fit to the drift-only data to a power law where the exponent is very nearly 1/2. A comparable fit to the drift-diffusion data can only be achieved if the power law is applied in sections, where the exponent decreases from 0.7 at low carrier densities to approach the value of 0.5, as obtained in the drift-only data, at high carrier densities. The excellent fit to the drift-only data by the square root equation suggests that an analytical derivation is possible. However, such a form has not been determined to date.

While the field-independent description given above would always apply in the case

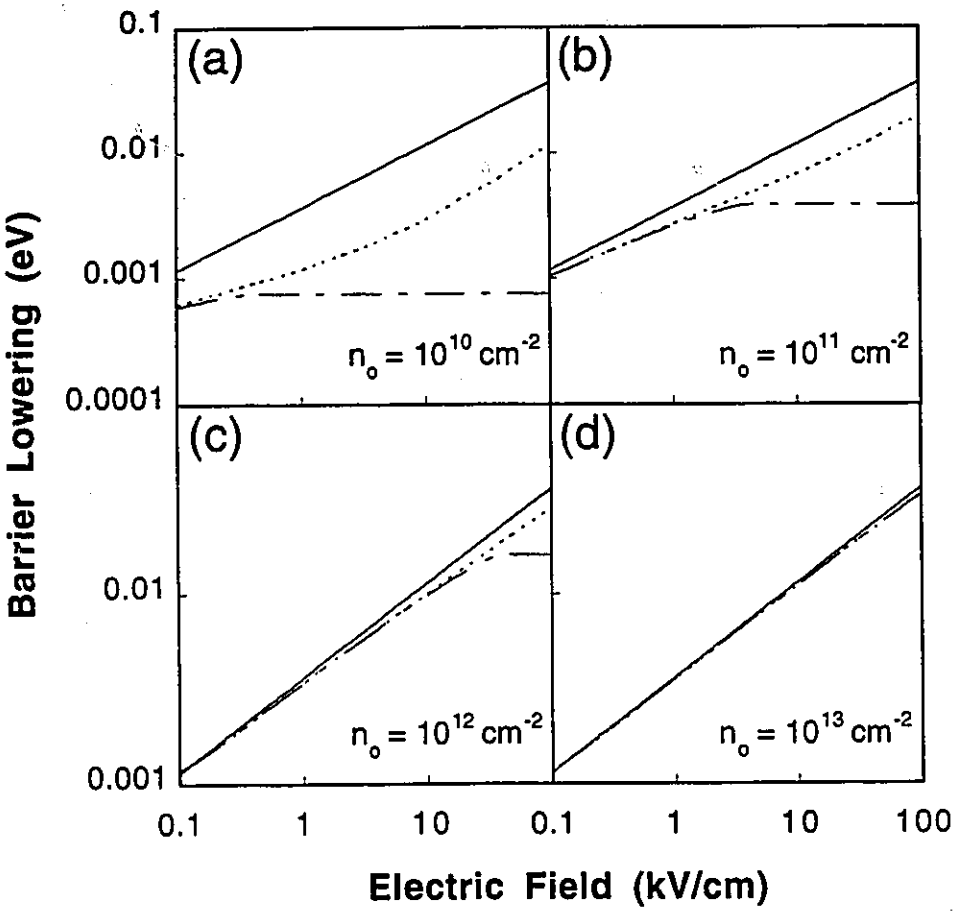

Fig. 3.16: Image charge barrier lowering calculated for the majority unipolar case (dash-dotted) compared with the result obtained from the minority unipolar simulation (dotted) for carrier densities of (a) 10^{10} cm^{-2}, (b) 10^{11} cm^{-2}, (c) 10^{12} cm^{-2}, and (d) 10^{13} cm^{-2}. The solid curves give the perfect conductor result. Within the field-dependent regime, the depletion results closely follows the accumulation curves.

of undoped unipolar quantum wells, in the presence of dopants or other ionized impurities, the sheet field may be reduced or even entirely compensated. Within the field dependent regimes, Fig. 3.16 shows that the behaviour is similar to that obtained for the minority unipolar case, deviating only near the field-independent regimes. Fig. 3.17 presents the field dependent image charge lowering for carrier densities of (a) 10^{12} cm^{-2} and (b) 10^{13} cm^{-2} fitted to the square root law of Eq. (3.20). The effective charges obtained from similar fits are plotted in Fig. 3.18 along with those obtained for the minority unipolar simulation. At higher carrier densities, where the fits are much better, the effective charges are similar, the majority values being slightly smaller than the minority results. This reflects the slight reduction in the image charge distribution noted earlier in Fig. 3.9. It is apparent from Fig. 3.18 that the carrier dependence of the effective charge differs between

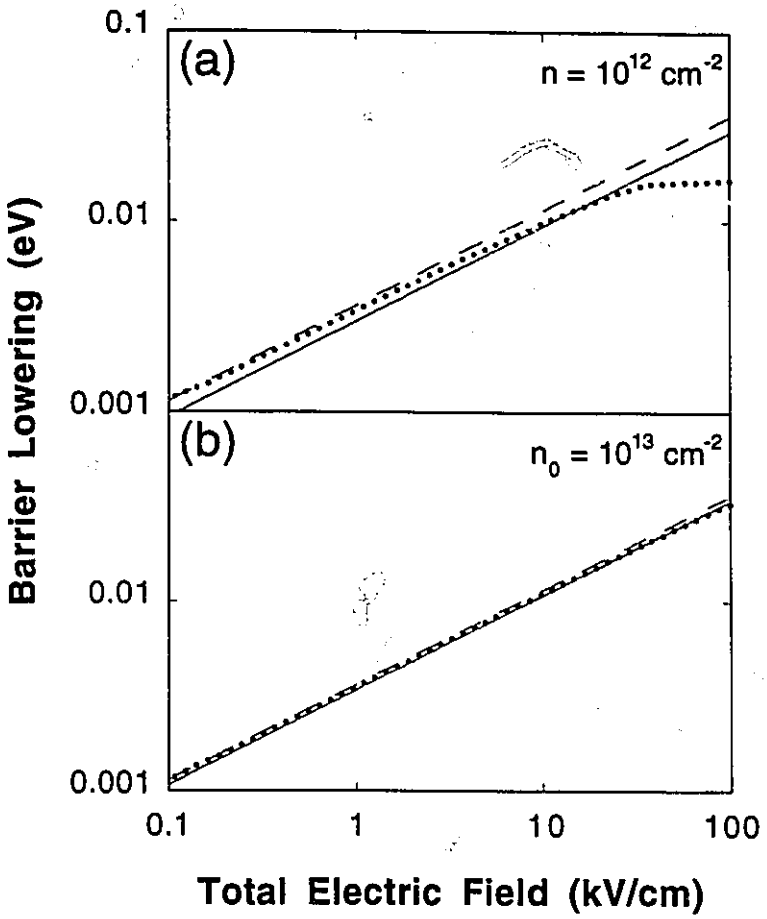

Fig. 3.17: Square root fits (solid lines) to the barrier lowering in the field independent regime for the majority unipolar case for carrier densities of (a) 10^{12} cm^{-2} and (b) 10^{13} cm^{-2}. The dashed lines give the perfect conductor lowering for comparison. At the lower carrier density, where the field-independent cutoff occurs at a lower electric field strength, the fit is degraded by an increase in curvature as the cutoff is approached.

the two simulations. The majority unipolar values are well described by

$$e_{eff} = -0.558 + (4.99 \times 10^{-2}) \ln n, \tag{3.24}$$

where again, the effective charge is in units of the electronic charge and sheet carrier density, n is given in units of cm^{-2}. Unfortunately, the analysis could not be extended to low carrier densities where the barrier lowering was predominantly field-independent.

It is apparent from Fig. 3.11 that for a unipolar quantum well, majority image charge lowering should be included only if the carrier density is greater than approximately 10^{11} cm^{-2}. At smaller densities, the depletion of the charge sheet prevents any substantial barrier lowering from occurring. However, at higher carrier densities the perfect conductor

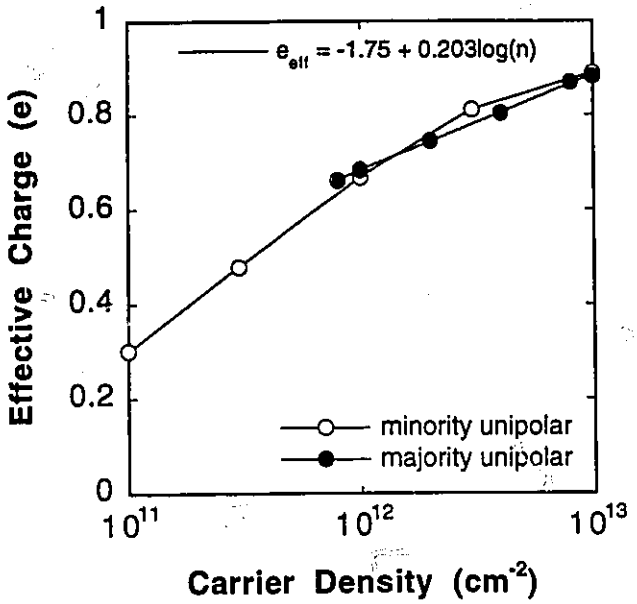

Fig. 3.18: Effective image charge for the majority unipolar case as a function of carrier density. Applies only if the total electric field is less than the cutoff field, as given inFig. 3.14.

solution becomes a reasonable approximation. It is suggested that for total fields below the cutoff, as given by the proportionality constant of $(4.10 \pm 0.01)\times10^{-11}$ kV·cm, the perfect conductor solution be applied with an effective charge as given by Eq. (3.24). For total fields greater than the cutoff, the field independent formula should be used as given in Fig. 3.15.

3.3.3. The bipolar quantum well.

The calculation of the bipolar sheet response to the presence of an external charge is performed by combining the programs for majority and minority carrier escape. In this case, two complete sets of charge distributions and currents must be simultaneously calculated, where the two systems are coupled via the electric field. Otherwise, the approach is identical to those taken in the unipolar simulations.

Fig. 3.19 shows the calculated sheet carrier distributions for the case of an escaping electron at distances of (a) 0.1 nm, (b) 10 nm and (c) 30 nm, where the electron (solid curves) and hole (dotted curves) densities in the sheet are both 10^{11} cm^{-2}. The external electron causes a depletion in the electron population while the holes are accumulated. In contrast to the majority unipolar simulation, the electron density does not go to zero at the centre, even when the external electron is only 1 Å from the surface. This remains true

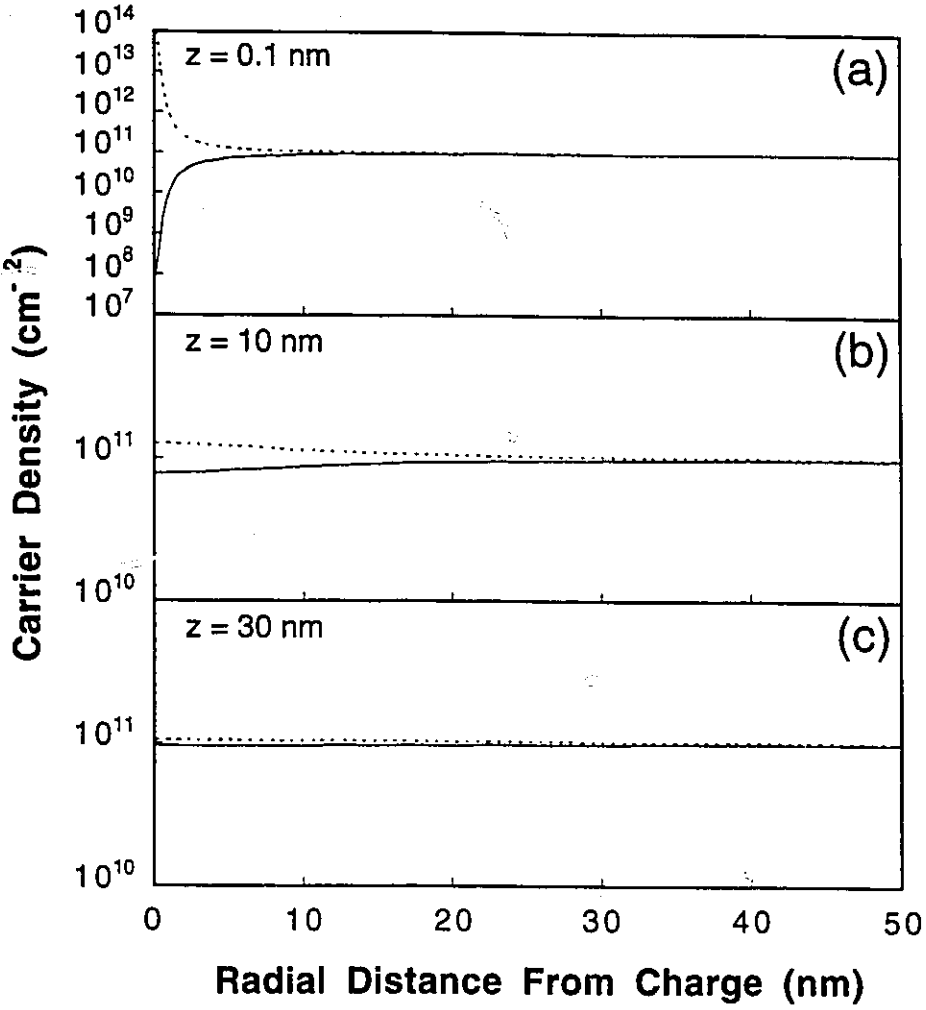

Fig. 3.19: Image charge distributions in a bipolar quantum well for equal electron and hole carrier densities of 10^{11} cm^{-2}. These are shown for an escaping electron at distances of (a) 0.1 nm, (b) 10 nm and (c) 30 nm. In contrast to the depletion simulation, even when the external electron is 1 Å from the surface the electron sheet is not depleted through at the centre.

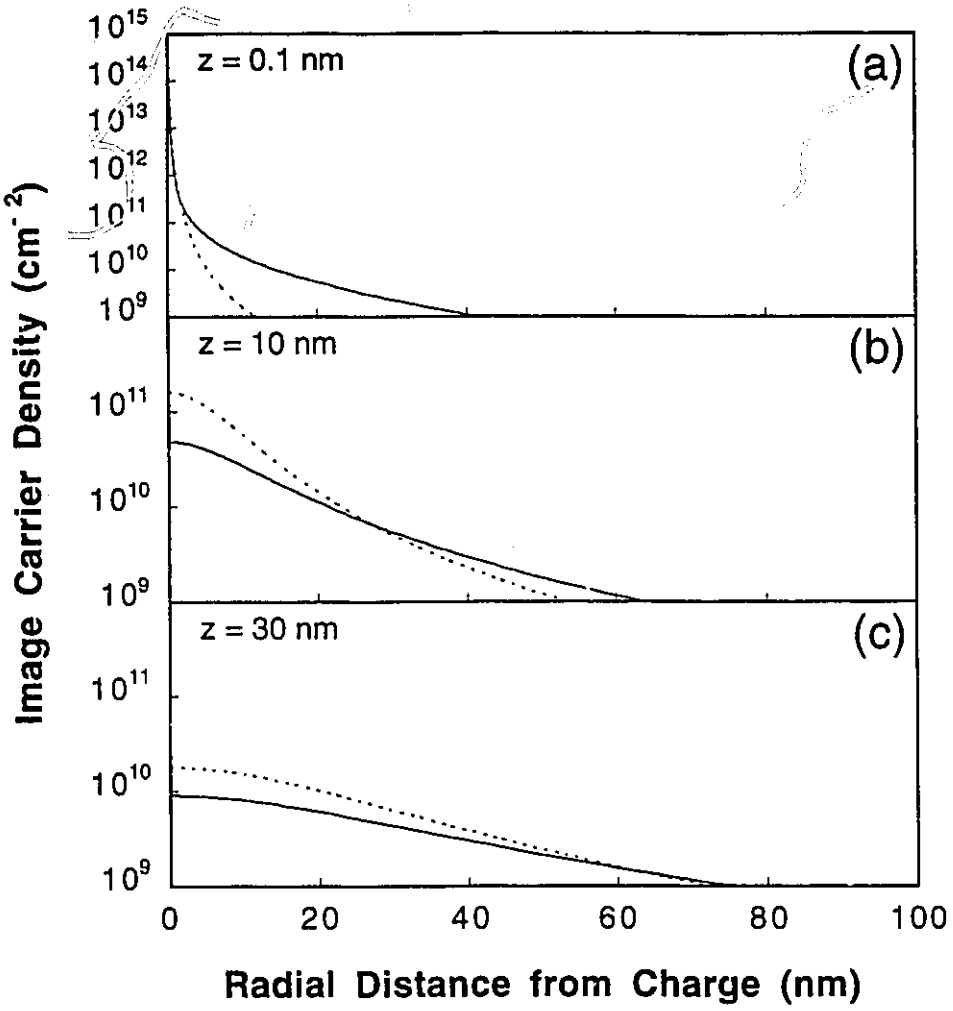

Fig. 3.20: Calculated total image carrier densities for a bipolar quantum well with equal electron and hole densities of 10^{11} cm^{-2}. These are shown for an escaping electron at distances of (a) 0.1 nm, (b) 10 nm and (c) 30 nm. The solid curves show the simulation results while the dotted curves give the perfect conductor solutions. The peak in the distribution is reduced in the drift-diffusion curves as a result of the diffusion current.

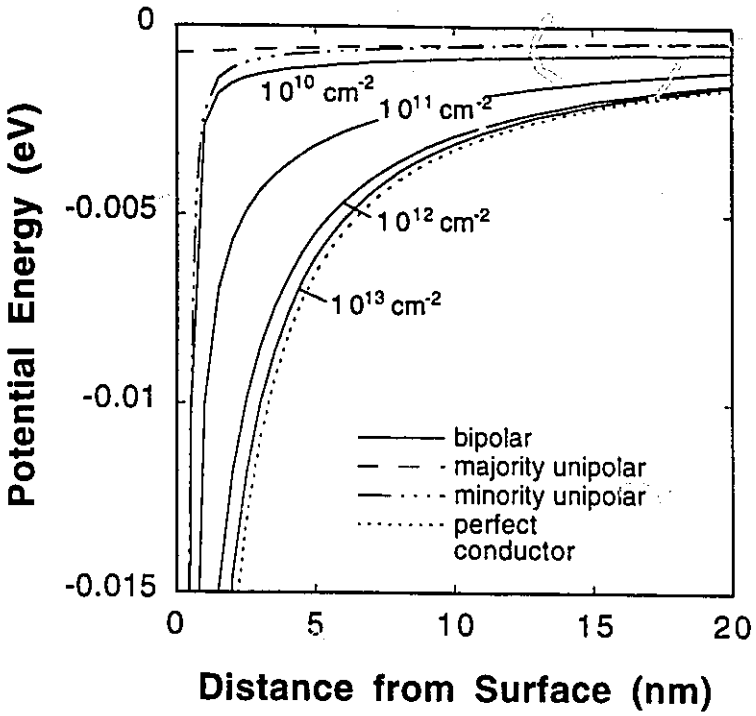

Fig. 3.21: Calculated image charge potentials for equal electron and hole carrier densities of 10^{10}, 10^{11}, 10^{12}, and 10^{13} cm^{-2}. The majority and minority unipolar results for a carrier density of 10^{10} cm^{-2} are represented by the dashed and dashed-dotted curves respectively. The dotted curve shows the perfect conductor result.

even at the lowest carrier densities considered.

The total image charge density is obtained by adding the amount of accumulated hole charge to the depleted electron charge. These are shown in Fig. 3.20 for the same three external charge distances considered in Fig. 3.19. At all distances the calculated distributions (solid curves) have lower peaks and gentler slopes than the perfect conductor results (dotted curves). This is due to the diffusion current that is omitted from the perfect conductor treatment.

The image charge potentials obtained from the calculated image carrier densities are shown in Fig. 3.21 for equal electron and hole carrier densities of 10^{10}, 10^{11}, 10^{12}, and 10^{13} cm^{-2}. As the carrier densities increase the potential curves move downwards to approach the perfect conductor result shown by the dotted curve. Also shown for comparison are the majority unipolar (dashed curves) and minority unipolar (dashed-dotted curves) results for carrier densities of 10^{11} cm^{-2}. The flat behaviour of the majority simulation is overshadowed by the contribution of the hole accumulation. In fact, the bipolar results closely resemble the minority results in form, although the potential wells are deeper in the bipolar case, as expected due to the greater total carrier density.

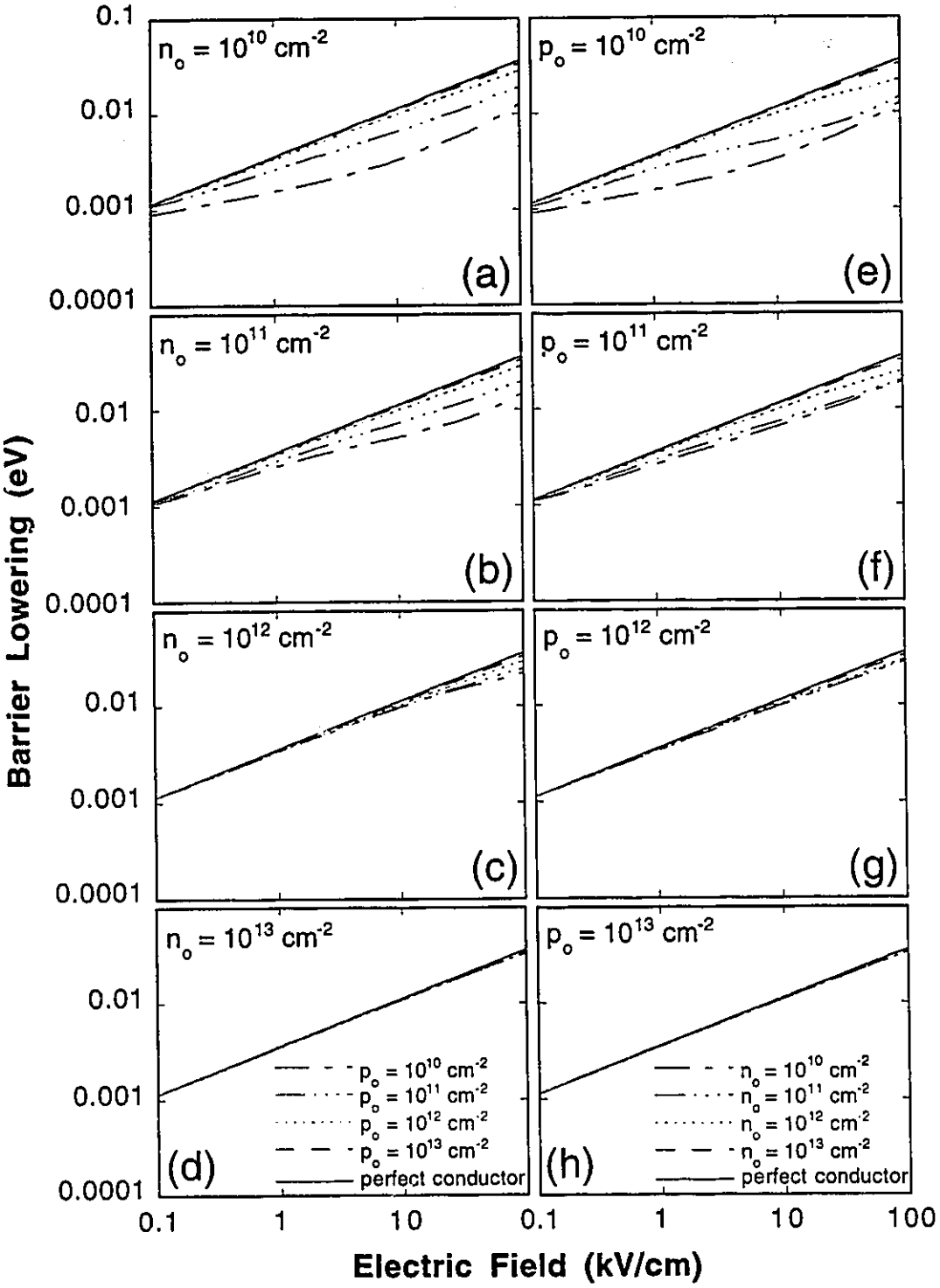

Fig. 3.22: Calculated barrier lowering for an electron escaping from a bipolar quantum well with electron densities of (a) 10^{10}, (b) 10^{11}, (c) 10^{12}, and (d) 10^{13} cm^{-2} and hole densities of (e) 10^{10}, (f) 10^{11}, (g) 10^{12}, and (h) 10^{13} cm^{-2}. In each graph, curves are shown for the full range of populations for the other carrier species. The perfect conductor solution (solid line) is a good approximation at high densities, but deteriorates below 10^{12} cm^{-2}.

Fig. 3.22 shows the calculated image charge lowering as a function of the total electric field for the full range of carrier densities considered. Fig. 3.22 (a)-(d) give the barrier lowering for *electron* densities of 10^{10}, 10^{11}, 10^{12}, and 10^{13} cm^{-2}, while (e)-(h) give the results for *hole* densities covering the same range. In each case, the curves are given for densities of the other carrier species between 10^{10} and 10^{13} cm^{-2}. This presentation format was chosen to fully exhibit the separate influences of the electron and hole densities on the image charge lowering. It is obvious from (d) and (h) that if either of the carrier species is abundant, on the order of 10^{13} cm^{-2}, the perfect conductor solution is a good approximation. The agreement deteriorates substantially at the lower total carrier densities where the difference can be greater than 70% at high fields. As expected from the minority and majority unipolar results, the accumulating hole population produces a greater barrier lowering effect than the depleting electrons. This is reflected by the more substantial barrier lowering observed in the constant hole density ((e)-(h)) plots than in the constant electron ((a)-(d)) plots.

To quantify the image charge effect in the bipolar drift-diffusion simulation, square root fits were applied to the barrier lowering curves to determine the effective image charges. Fig. 3.23 shows the fits for equal electron and hole carrier densities of (a) 10^{10} cm^{-2}, (b) 10^{11} cm^{-2}, (c) 10^{12} cm^{-2}, and (d) 10^{13} cm^{-2}. Similar to the minority unipolar case, the fits are very good at higher carrier densities but deviate at low populations. Again, the resultant error is not significant since the discrepancy is primarily at low fields where the barrier lowering is of the order of an meV. Fig. 3.24 shows the effective image charges as a function of the hole density for each of the four electron densities considered. The open circles represent the results from the minority unipolar simulation. Note that for an electron density of 10^{10} cm^{-2} the effective charges are almost identical to the minority results except at the smallest hole density. This indicates that a small electron population has little effect on the image charge lowering. The inset to Fig. 3.24 shows the same data plotted against the total carrier density in the well. The general behaviour is similar to that observed in the minority unipolar simulation, as illustrated by the fitted curves. The solid curve corresponds to the bipolar data and is described by the equation

$$e_{eff} = \frac{1}{1 + 1.95 \times 10^{8} (n+p)^{-0.581}} \tag{3.25}$$

while the dotted curve is a fit to the minority unipolar data and was determined previously to be given by Eq. (3.19). Note that in Eq. (3.25), n and p are the electron and hole

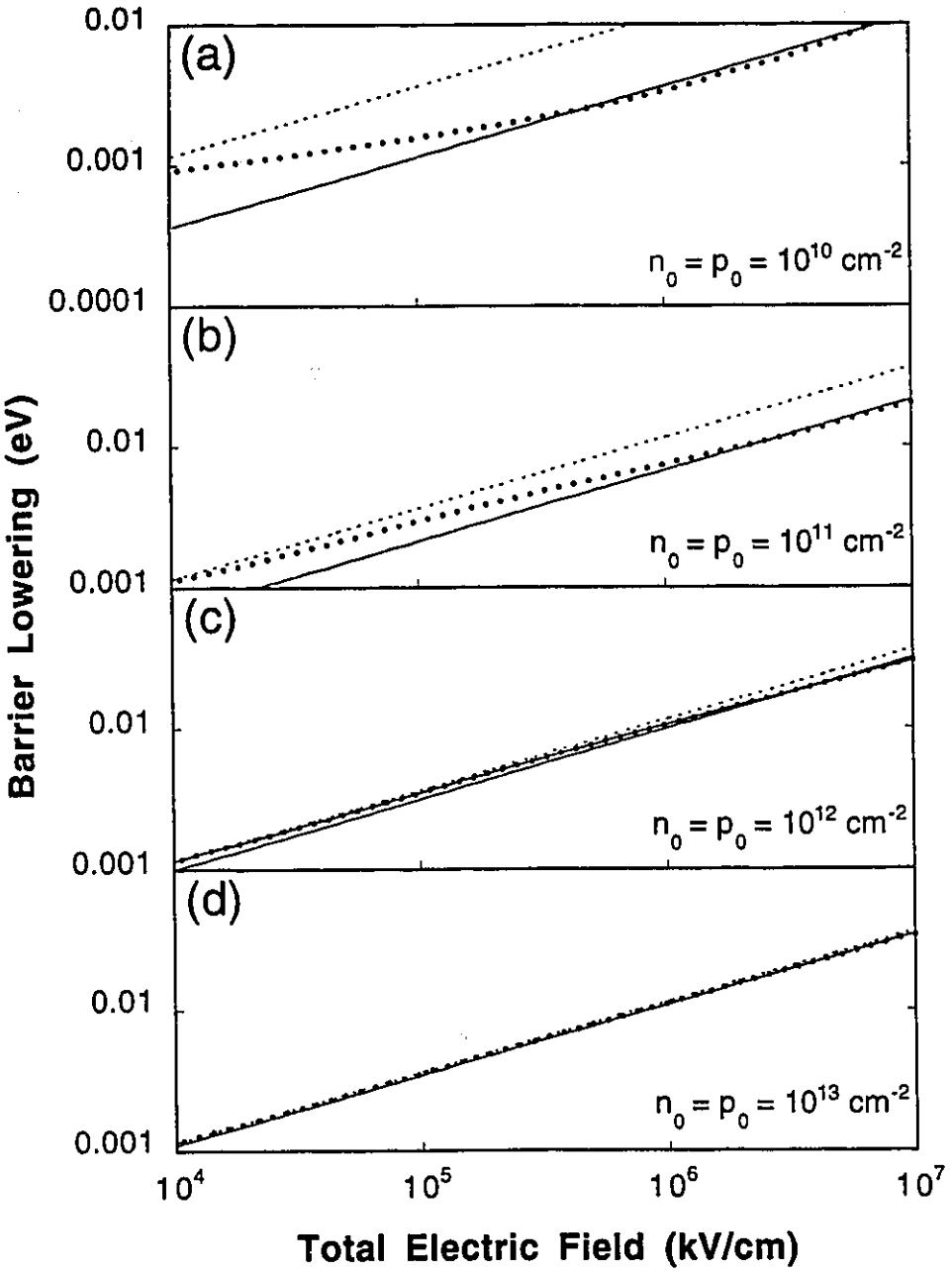

Fig. 3.23: Square root fits (solid line) to the calculated bipolar barrier lowering for equal electron and hole densities of (a) 10^{10}, (b) 10^{11}, (c) 10^{12}, and (d) 10^{13} cm^{-2}. The dotted line shows the perfect conductor result. At the lower carrier densities the fit becomes poor at small fields, however the actual barrier lowering is small in this regime.

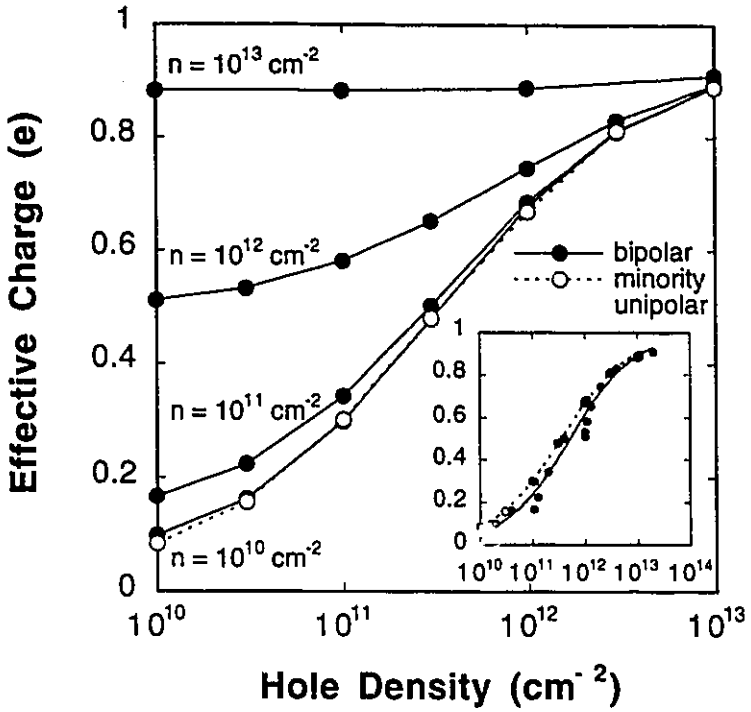

Fig. 3.24: Effective charge plot as a function of the hole population for an electron escaping from a bipolar quantum well. The open circles give the minority unipolar result for comparison. The inset shows the same points plotted against the total carrier density in the well. The solid curve shows a fit to the bipolar data while the dotted curve is a fit to the minority data which are shown in open circles. The bipolar data points that fall below the fitted curve correspond to situations where the electron density is greater than the hole density.

densities given in units of cm^{-2}. The points that lie below the fitted curve correspond to situations where the electrons outnumber the holes. It is not surprising that the bipolar results approach the minority unipolar values when the hole population makes up a significant portion of the total carrier density since the minority unipolar simulation is identical to the bipolar case when the electron density tends to zero.

To summarize the bipolar image charge effect, as with the unipolar simulations, a carrier density of 10^{13} cm^{-2} is sufficient to make the perfect conductor solution a good approximation. At lower carrier densities, the effective charge given by Eq. (3.25) or extrapolated from Fig. 3.24 can be used in Eq. (3.23) to calculate the barrier lowering. While at low total carrier densities the deviation from the ideal case can be substantial, the remaining barrier reduction is still significant.

3.4. Summary of Drift-Diffusion Simulation Results.

In this chapter, the image charge distributions in unipolar and bipolar quantum wells have been determined numerically in the quasi-static approximation, including both accumulation and depletion of the sheet charge. For the first time, the effects of the diffusion current have been included and shown to produce significant reductions in the amount of barrier lowering, particularly at low carrier densities. The majority unipolar case gave the largest deviations from the perfect conductor calculation, mostly due to the formation of a depleted hole in the sheet charge. This results in a *field-independent* behaviour that is in stark contrast to the usual square root dependence. The field-independent barrier lowering obeys what is essentially a power law dependence on the carrier density, where the exponent tends to 1/2 at higher carrier densities. If the diffusion current is omitted from the simulation, the exponent is almost exactly 1/2. In *intrinsic* unipolar quantum wells, the net charge of the free carriers in the well generates an electric field in addition to any externally applied fields. It turns out that this field lies within the field-independent regime for all carrier densities so that the barrier lowering is always field independent. However, if there are sufficient ionized dopants within the well to compensate the free charge, then the field-dependent behaviour will apply.

For the bipolar and minority unipolar situations, the barrier lowering remains field dependent since the possibility of accumulating charge removes the limitation encountered in the majority unipolar simulation. In this case, the deviation of the barrier lowering relative to the ideal case was quantified by deriving *effective image charges* from square root fits to the barrier lowering as a function of the total electric field. These can then be used in the ideal conductor equation for the barrier lowering. Although the agreement becomes poor at low total carrier densities and low fields, this results in only minimal errors since the actual barrier lowering is small in this regime anyways.

It has been shown that in all three scenarios, at high carrier densities, the effective image charge approaches the electronic charge so that the barrier lowering can be substantial. However, we will find in the following chapter that barrier lowering effects do not have the impact on thermionic emission expected from conventional theories (Schneider and Von Klitzing, 1988), (Moss, 1994). As a result, it appears that image charge lowering will only have a significant effect on thermionic emission calculations in a limited number of situations.

Chapter 4: Electron-Phonon Scattering From 2D To 3D States.

As shown in chapter 2, in the high field regime the thermal escape from a quantum well subband is determined by the thermal distribution of the carriers within the subband and the scattering rate into continuum states. In order to predict the thermionic emission time it is therefore necessary to calculate this scattering time.

In this chapter a first principles calculation of the electron-phonon 2D-to-3D scattering rate based on Fermi's Golden Rule will be presented. First, the properties of phonons in semiconductors will be briefly reviewed. A general formula for calculating electron-phonon scattering will then be given, followed by a detailed description of each of the components in the rate expression: the initial and final state wavefunctions, the final state density of states, and the interaction Hamiltonians. Finally, the evaluation of the total 2D-to-3D scattering rates will be outlined.

While it is almost universally assumed that polar optical phonon scattering dominates the electron scattering in III-V materials, there is reason to doubt that this will hold true in all situations. In particular, at low temperatures the large energy of the optical phonons will result in very small phonon populations and the more abundant low energy acoustic phonons may then take over. This effect is observed in high purity epitaxial bulk GaAs (Stillman, 1976) and 2D in-plane mobilities (Price, 1980) where the acoustic phonon processes become important below ~100 K. To investigate this possibility, piezoelectric and deformation potential scattering by acoustic phonons will be included along with the polar optical phonons.

Results will be presented for GaAs/AlGaAs wells of various widths and depths,

with initial calculations comparing the different scattering processes. This will reveal that polar optical phonon scattering dominates even at low temperatures due to the effective reduction in the barrier height by an amount equal to the phonon energy. Calculations for different well widths and depths will show that the scattering function and hence the thermionic emission rate are strongly affected by the presence of continuum resonances near the top of the well potential. Attempts at replicating the full calculation by fitting the scattering function to either step-functions or Fermi-Dirac-type functions will be presented, with the Fermi-Dirac approximation consistently improving upon the step-function approximation. In both cases, the fitting parameters will depend on the well configuration and hence more work is required to produce an analytic parameterization of the thermionic emission time.

While similar calculations have been performed previously (Shorthose, 1989), (Liang and Lent, 1990), (Rosencher, 1994), (Tsai, 1994a, 1994b), only Shorthose *et al* (1989) and Rosencher *et al* (1994) explicitly included the effects of a transverse electric field. In both cases, they only gave results for a particular device structure and did not clearly present the details of their calculation. Furthermore, in the latter the results are presented in such a way that they cannot be applied to the thermionic emission calculations described in Chapter 2. The calculations presented here represent the first calculation to include the acoustic phonon processes, and the most comprehensive attempt at formulating a scheme for simplified calculations of the thermionic emission time in the presence of an electric field.

4.1. Basic Properties of Phonons in Semiconductors.

For free electrons in semiconductor heterostructures there are four main types of scattering: phonon, defect, alloy or interface roughness, and carrier-carrier scattering. For low to moderate carrier densities, carrier-carrier scattering can be neglected. Both alloy and interface scattering are important only for high carrier densities, low temperatures and/or narrow wells (Walukiewicz, 1984). In high purity samples, in particular undoped epitaxial layers, impurity scattering only becomes important near liquid nitrogen temperatures (E. E. Mendez, 1986), (Weisbuch, 1991). So at room temperature, the electron-phonon interaction dominates the electron scattering (Price, 1980), (Ridley, 1982), (Weisbuch, 1991).

In this section, I will present a very brief review of the properties of phonons (for a

more detailed treatment, see for example, Ashcroft and Mermin (1976)). Phonons are quanta of the vibrational excitations in a solid, analogous to photons as quanta of the electromagnetic field. The description is derived from the harmonic approximation for the motion of the ions in a crystal lattice.

Each neighbouring pair of ions can be considered to form a simple harmonic oscillator. However, because every ion is coupled to each of its neighbours, all of the oscillators in the crystal are coupled together. As a result, the vibrational excitations can be very complex. Fortunately, it is possible to choose a set of coordinates such that the vibrational modes are uncoupled; these are referred to as the *normal coordinates* and the resulting vibrational modes are called the *normal modes*. In this coordinate system, each of the normal modes can be described by an independent harmonic oscillator.

From the quantum mechanical treatment of the harmonic oscillator, the energy eigenvalues of the normal modes are given by

$$E_{n,q} = \hbar\omega_q\left(n_q + \tfrac{1}{2}\right), \tag{4.1}$$

where ω_q is the frequency of the normal mode that has been excited. Since the excitation energies are discrete, the system is said to be quantized and the lattice vibrations are considered to be a collection of particles each carrying energy $\hbar\omega_q$. These particles are called phonons. The quantum number n_q, then gives the occupation or number of phonons in the mode of frequency ω_q.

The motion of the ions resulting from a particular phonon can be described by a plane wave of wavevector, **q**, and polarization, **a**. In a crystal with a single atom basis, there are three possible polarizations for each wavevector: one longitudinal and two transverse. Each contributes a separate branch to the ω vs. q, or *dispersion*, relationship. In a crystal with a two-atom basis, as in the zinc-blende or diamond structures, there are six solutions or branches in the dispersion relation. These are illustrated in Fig. 4.1. The lower three branches, which are also present in the case of the single atom basis, are called the acoustic branches while the upper three are the optical branches. The optical branch again contains one longitudinal and two transverse modes. In general, the acoustic branch is approximated as having a linear dispersion, corresponding to a constant sound velocity, v_s. The optical branch is treated as having no dispersion, with a constant frequency, ω_0. The atomic displacement at the lattice point **R** is the sum of the displacements due to each of the individual modes and is therefore a sum of plane waves. The displacement at **R** is written as (Ridley, 1993)

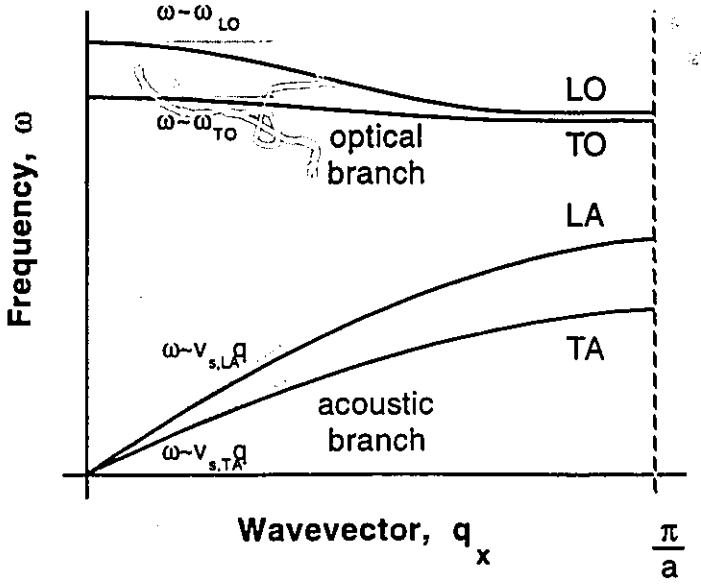

Fig. 4.1: Schematic illustration of typical phonon dispersion curves in a zinc blende or diamond structure semiconductor. For small wavevectors, the acoustic branches can be approximated as having a linear dispersion (i.e. constant sound velocity) while the optical branches are modelled by flat dispersion relationships. These are indicated by the grey lines near $q_x = 0$.

$$\mathbf{u}(\mathbf{R}) = \frac{1}{\sqrt{N}} \sum_{\mathbf{q}} \left(\Omega_{\mathbf{q}} \mathbf{a}_{\mathbf{q}} e^{i\mathbf{q}\cdot\mathbf{R}} + \text{c.c.} \right), \tag{4.2}$$

where $\Omega_{\mathbf{q}}$ is the normal coordinate, $\mathbf{a}_{\mathbf{q}}$ is the polarization vector of the mode, $\mathbf{q}$ is the wavevector and N is the number of unit cells in the crystal. The abbreviation c.c. indicates the complex conjugate of the first term. This displacement will form the basis for evaluating each of the different types of electron-phonon interactions.

It should be pointed out that in the following derivations bulk phonons will be assumed. This is an approximation since in a quantum well structure, the material interfaces confine not only electrons, but phonons as well (Huang and Zhu, 1988), (Rücker, 1992). This gives rise to new modes such as confined, guided and interface modes whose displacements are not described by the bulk expression (4.2). However, detailed studies have shown that electron-phonon scattering rates calculated with microscopic models for the confined and interface modes lie between the results obtained from bulk phonon calculations for the well and barrier materials (Rücker, 1992). For wells greater than ~50 Å in width, the microscopic calculations are within 10% of those using bulk phonons characteristic of the well material, while for narrower wells they approach the

results obtained using bulk barrier phonons. Since the objective of these calculations is to determine the overall escape times to within the precision of the material parameters, etc., the accuracy obtained using bulk expressions for the phonons should be adequate.

4.2. Electron-Phonon Scattering in Semiconductors.

The scattering rate from a particular electronic state (labelled by the subscript i) is given by perturbation theory in the form of Fermi's Golden rule

$$W_i = \frac{2\pi}{\hbar} \int |\langle \Psi_f | H_{e\text{-}ph} | \Psi_i \rangle|^2 \delta(E' - E)\, dS_f, \tag{4.3}$$

where Ψ_i and Ψ_f are the initial and final state wavefunctions respectively, including both the electron and phonon states, $H_{e\text{-}ph}$ is the electron-phonon interaction Hamiltonian, E_i and E_f are the initial and final state energies respectively, dS_f is the final state density of states, and the integration is over all possible final states.

For electron-phonon transitions, the wavefunction is comprised of an electronic component and a phonon component. In general, the electrons are described by Eq. (2.2), the modified Bloch functions, while the phonon system is described most succinctly by the occupation numbers of each of the modes, identified by branch and wavevector. This format takes advantage of the orthogonality of the spatial wavefunctions of the phonon modes while allowing us to make use of the creation and annihilation operators from the simple harmonic oscillator.

The exact form of the interaction Hamiltonian will depend on the particular electron-phonon scattering process, however in all cases, it will be a function of the ionic displacements. This is because the perturbations in electronic energy result from the relative motions of the ions. Therefore, the general interaction Hamiltonian will be proportional to Eq. (4.2), differing in each case by some coupling coefficient.

4.2.1. The wavefunctions.

We begin by writing out the wavefunctions for the initial and final states. As described in Chapter 2, in the envelope function approximation the electronic wavefunction in the quantum well is

$$\psi(\mathbf{r})=\frac{1}{\sqrt{L_x L_y}}e^{i\mathbf{k}_{\parallel}\cdot\mathbf{r}_{\parallel}}\phi_n(z), \tag{4.4}$$

where the $_{\parallel}$ subscript refers to the in-plane (xy-plane) components and $\phi_n(z)$ is the z-component as calculated using Airy functions. The final state wavefunction will have exactly the same form, differing only in that $\phi_n(z)$ will not be confined to the well layer.

The normalization of the z-component of the wavefunction is critical since it will strongly affect the value of the matrix element. We consider that the system is placed in an artificial 'box' where the dimensions of the box are eventually taken to infinity. The normalization condition is given by the integral

$$\int_{-\infty}^{\infty}|\phi(z)|^2 dz=1. \tag{4.5}$$

In this case, most of the integral is performed over large negative z. The asymptotic forms for the Airy and Bairy functions at large negative z_j, where z_j is given by Eq. (2.7), are (Abromowitz, 1964)

$$\begin{aligned} Ai(z_j)&=M(-z_j)\cos\left[\theta(-z_j)\right] \\ Bi(z_j)&=M(-z_j)\sin\left[\theta(-z_j)\right] \end{aligned} \tag{4.6}$$

where

$$M^2(-z_j)\cong\frac{1}{\pi}z_j^{-\frac{1}{2}}\sum_0^{\infty}\frac{(-1)^k}{12^k k!}2^{3k}\left(\frac{1}{2}\right)_{3k}(2z_j)^{-3k} \tag{4.7}$$

and

$$\theta(-z_j)\cong\frac{1}{4}\pi-\frac{2}{3}z_j^{\frac{3}{2}}\left[1-\frac{5}{4}(2z_j)^{-3}+\frac{1105}{96}(2z_j)^{-6}-\frac{82825}{128}(2z_j)^{-9}+\ldots\right]. \tag{4.8}$$

For large, negative z_j, the envelope function (2.9) can then be written as

$$\phi_j(z_j)\cong\sqrt{C_j^2+D_j^2}\,M(-z_j)\cos\left[\theta(-z_j)-\tan^{-1}\left(\frac{D_j}{C_j}\right)\right] \tag{4.9}$$

To perform the integration in Eq. (4.5) the integral is divided into two sections: large, negative z and smaller values of z, i.e.: in the quantum well region. The two regions meet at some arbitrary but finite point, z_0, giving

$$\int_{-L_z}^{\infty} |\phi_j(z_j)|^2 dz = \int_{-L_z}^{z_0} |\phi_j(z_j)|^2 dz + \int_{z_0}^{\infty} |\phi_j(z_j)|^2 dz \tag{4.10}$$

where L_z is the size of the artificial box beyond which the wavefunction vanishes. The asymptotic form in Eq. (4.9) will be employed in the first term while the second term will retain the full expressions. Since the potential barrier slopes upward on the positive z side of the well, the wavefunction vanishes for large positive z, and the second term remains finite. It is expected that the first term will scale with the integration length, L_z. Then in the limit that L_z goes to infinity, the second term, containing the contributions near the quantum well, will be negligible.

For the large, negative z integration, the leading, non-constant, terms in the expansions (4.7) and (4.8) dominate. As a result, the integral is transformed into

$$\int_{-L_z}^{z_0} |\phi_j(z_j)|^2 dz = \int_{-L_z}^{z_0} \frac{1}{\pi} z_j^{-\frac{1}{2}} \cos^2\left[\frac{2}{3} z_j^{\frac{3}{2}} - \zeta_j\right] dz. \tag{4.11}$$

This can be separated into a sinusoidal term and a power law term by making the substitution

$$\cos^2(u) = \frac{1}{2}[1 + \cos(2u)]. \tag{4.12}$$

Since the sinusoidal term is damped by a factor $z^{-1/2}$ it will generate a finite contribution which will depend only on the value of z_0. The integral then reduces to

$$\int_{-\infty}^{z_0} |\phi_j(z_j)|^2 dz = \frac{1}{2\pi} \int_{-L_z}^{z_0} z_j^{-\frac{1}{2}} dz + \vartheta(z_0) \tag{4.13}$$

where $\upsilon(z_0)$ is the damped sinusoidal contribution. Substituting for z_j from Eq. (2.7) and integrating gives

$$\int_{-\infty}^{z_0} |\phi_j(z_j)|^2 dz = \frac{1}{\pi}\left(\frac{L_z}{\alpha_j e \mathscr{E}}\right)^{\frac{1}{2}} + \vartheta(z_0) \tag{4.14}$$

where

$$\alpha_j = \left[\frac{2m_j^*}{(e\hbar\mathscr{E})}\right]^{\frac{1}{3}}. \tag{4.15}$$

Since all other terms in the complete integral, Eq. (4.10), are finite and depend only on the value of z_0, the $L_z^{1/2}$ term will dominate in the large L_z limit. Therefore the full normalization constant for $\phi_j(z)$ is

$$\sqrt{C_j^2 + D_j^2}\left[\frac{L_z}{\pi^2 \alpha_j e\mathscr{E}}\right]^{\frac{1}{4}} \tag{4.16}$$

independent of the choice of z_0.

Fig. 4.2 illustrates that as the normalization length becomes large, the asymptotic form derived above is in good agreement with the result obtained from numerical integration of the full wavefunction, with differences of less than 1%. As a result, the simple form in Eq. (4.16) can be used for the normalization of the wavefunction without significant loss of accuracy.

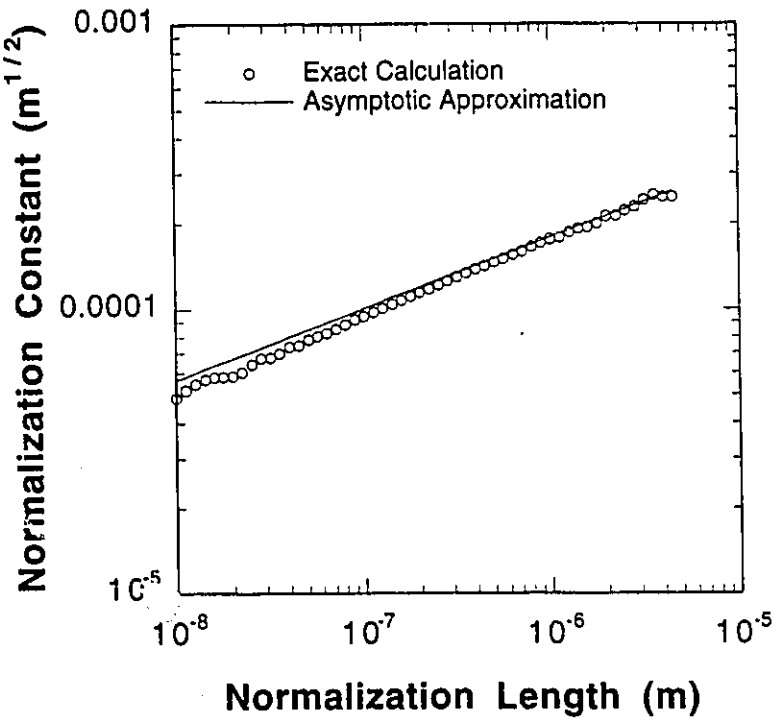

Fig. 4.2: Comparison of exact normalization constant from numerical integration with the asymptotic approximation as a function of the normalization length.

The phonon wavefunction is represented by

$$\varphi=\sum_{q,b}\left|n_{q,b}(\omega_{q,b})\right\rangle, \tag{4.17}$$

such that

$$\left\langle n_{q,b}(\omega_{q,b})\right|\Omega_{q^*,b^*}\left|n_{q',b'}(\omega_{q',b'})\right\rangle=\left(\frac{\hbar}{2\,\overline{M}\,\omega_{q,b}}\right)^{\frac{1}{2}}\delta_{q,q'\pm q^*}\,\delta_{b,b'\pm b^*} \times\left[\sqrt{n_{q,b}(\omega_{q,b})}\;\delta_{n',n-1}+\sqrt{n_{q,b}(\omega_{q,b})+1}\;\delta_{n',n+1}\right] \tag{4.18}$$

where the unprimed symbols correspond to the initial state, and the primed to the final state. The subscript b refers to the phonon branch, and $n_{q,b}$ is the occupation of the mode with wavevector $\mathbf{q}$, in the b^{th} branch. $\overline{M}$ is the unit cell reduced mass and is given by

$$1/\overline{M}=1/M_1+1/M_2 \tag{4.19}$$

where M_1 and M_2 are the masses of the two atoms that make up the basis of the unit cell. In the last bracket of Eq. (4.18), the first term applies to the absorption of a phonon, the second term to emission. For simplicity, this occupation factor is written as

$$N^{\pm}(\omega_{q,b})=n_{q,b}(\omega_{q,b})+\frac{1}{2}\pm\frac{1}{2} \tag{4.20}$$

where the upper sign refers to emission and the lower sign to absorption.

The total wavefunction is then given by

$$\Psi_{k_t,n}(\mathbf{r})=\frac{1}{\sqrt{L_x L_y}}e^{i\mathbf{k}_{\parallel}\cdot\mathbf{r}_{\parallel}}\phi_n(z)\sum_{q,b}\left|n_{q,b}(\omega_{q,b})\right\rangle. \tag{4.21}$$

4.2.2. The summation over final states.

As shown in Eq. (4.4), the electronic wavefunction in the plane of the quantum well consists of plane waves. The area in k-space associated with each plane wave state is $(2\pi)^2/(L_xL_y)$ the inverse of which gives the k-space density of states. To sum over all of the plane wave states, we then integrate over

$$2\frac{L_x L_y}{(2\pi)^2} dk_x dk_y \tag{4.22}$$

where the factor of 2 reflects the two possible spins of the electrons.

Similarly, the phonons are also described by plane wave states and so the summation over all phonon states is performed by integrating over

$$\frac{L_x L_y L_z}{(2\pi)^3} dq_x dq_y dq_z = \frac{V}{(2\pi)^3} q_{\|} dq_{\|} dq_z d\theta \tag{4.23}$$

where V is the volume of the crystal.

The only remaining contribution is due to the summation over the electronic states in the z-direction. Since the $\phi_n(z)$ are not plane wave states, the preceding approach cannot be applied. Instead, the quantum well is considered to sit in an infinite triangular well as depicted schematically in Fig. 4.3. This is the same approach used in the normalization treatment presented in the preceding section. In this approximation, the quantum well is treated as a small perturbation on the triangular well such that the density of states is not

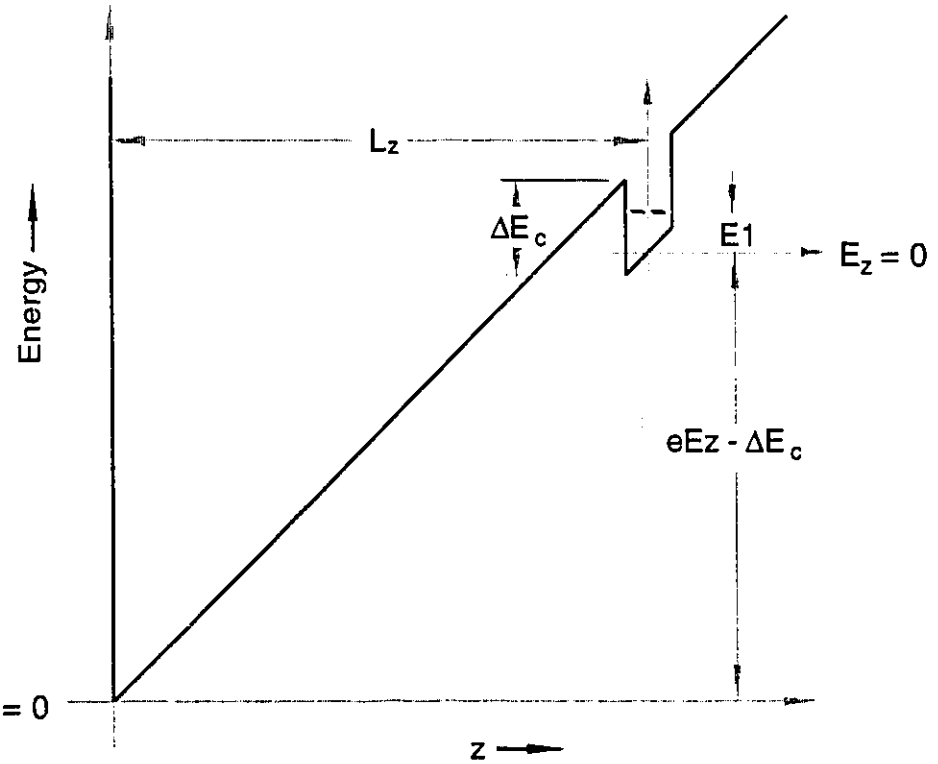

Fig. 4.3: Schematic illustration of the quantum well in the infinite triangular well approximation.

significantly affected. For a triangular well at large energies, E_n, the energy eigenvalues are given by (Weisbuch, 1991)

$$E_n \cong \left(\frac{\hbar^2}{2m}\right)^{\frac{1}{3}} \left(\frac{3\pi e \mathscr{E}}{2} n\right)^{\frac{2}{3}} \tag{4.24}$$

where n is the quantum number labelling each quantized state. The density of states is defined as the number of states between energy E and $E+dE$. Since n is the only quantum number, it essentially counts states, permitting the density of states to be written as

$$g(E) = \frac{\partial n}{\partial E} \tag{4.25}$$

Solving for n in Eq. (4.24) and performing the differentiation in Eq. (4.25) yields

$$g_z\left(E_z'\right) = \frac{1}{\pi e \mathscr{E}} \left(\frac{2m}{\hbar^2}\right)^{\frac{1}{2}} \left(E_z'\right)^{\frac{1}{2}}. \tag{4.26}$$

The E_z' in this equation is referenced to the bottom of the triangular well. To apply to the quantum well system, it must be shifted to the energy zero for the quantum well as shown in Fig. 4.3. This requires the transformation

$$E_z' = E_z - \Delta E_c + e \mathscr{E} L_z \tag{4.27}$$

where ΔE_c is the conduction band offset between the well and barrier materials, and the primed energy is relative to the bottom of the triangular well, the unprimed relative to the centre of the well. In the limit that L_z is large, the last term in Eq. (4.27) dominates and Eq. (4.26) becomes

$$g_z(E_z) = \left(\frac{2m}{\pi^2 \hbar^2 e \mathscr{E}}\right)^{\frac{1}{2}} L_z^{\frac{1}{2}} \tag{4.28}$$

This is the density of states for the continuum energy levels in a quantum well system in an electric field. Hunt (1992) arrives at the same result following a slightly different approach, however the same approximations are applied. Note that the artificial normalizing length or box size, L_z, will cancel with the L_z factor in the normalization

constant, as desired. Thus the full expression for dS_f is

$$dS_f = 2\frac{L_x L_y}{(2\pi)^2} dk_x dk_y \left(\frac{2m}{\pi^2 \hbar^2 e \mathscr{E}}\right)^{\frac{1}{2}} L_z^{\frac{1}{2}} dE_z \frac{V}{(2\pi)^3} d\mathbf{q} \tag{4.29}$$

4.2.3. The general electron-phonon scattering rate.

As pointed out earlier, the interaction Hamiltonian in each case will depend on the displacement, $\mathbf{u}(\mathbf{R})$, as given by Eq. (4.2). Therefore, the general Hamiltonian is written as

$$H_{e-ph} = C_{q,b} \sum_{q,b} \left\{ \Omega_{q,b} \mathbf{a}_q e^{i\mathbf{q}\cdot\mathbf{R}} + \text{ c.c.} \right\} \tag{4.30}$$

We can directly evaluate the matrix element up to this coupling coefficient $C_{q,b}$. The phonon contribution is evaluated according to Eq. (4.18). The x and y components of the electron wavefunctions combine with the plane wave component in the Hamiltonian of Eq. (4.30) to produce integrals of the form

$$\left| \int_{-L_x/2}^{L_x/2} \frac{1}{L_x} \exp\left[i\left(k_x' - k_x \pm q_x\right)x \right] dx \right|^2 = 2\pi\delta\left(k_x' - k_x \pm q_x\right) \tag{4.31}$$

which contains the requirement for conservation of crystal momentum. A similar result cannot be derived for the z-component since the initial and final states are not simple plane waves. For now, we define the function $G_{n',n}(q_z)$ as

$$G_{n',n}(q_z) = \int_{-L_z}^{\infty} \phi_{n'}(z) e^{iq_z z} \phi_n(z) dz \tag{4.32}$$

Combining equations (4.18), and (4.29)-(4.32) in Eq. (4.3) yields the general form for the electron-phonon scattering rate in a quantum well system:

$$W(k) = \frac{2\pi}{\hbar} \int \left(\frac{\hbar}{2\overline{M}\,\omega_{q,b}}\right) C_{q,b}^2 \left|G_{n',n}(q_z)\right|^2 2dk_x dk_y \left(\frac{2m}{\pi^2\hbar^2 e\mathscr{E}}\right)^{\frac{1}{2}} L_z^{\frac{1}{2}} dE_z \frac{V}{(2\pi)^3}$$
$$\times q_1 dq_1 dq_z d\theta \delta\left(k_x' - k_x \pm q_x\right) \delta\left(k_y' - k_y \pm q_y\right) \delta\left(E_{n',k_x',k_y'} - E_{n,k_x,k_y} \pm \hbar\omega_{q,b}\right) \tag{4.33}$$

where the upper signs refer to emission and the lower signs to absorption, and the unprimed variables refer to the initial state and the primed to the final state.

The next step is to determine the interaction Hamiltonian for each of the different mechanisms: polar scattering by longitudinal optical phonons, and deformation potential and piezoelectric scattering by acoustic phonons. In polar semiconductors such as GaAs and InP, polar optical phonon scattering is generally the most important process for both 2D-to-2D and bulk scattering, except at low temperatures where acoustic phonons become important (Mendez, 1986). A similar transition was expected in these calculations, however, it will turn out that the polar optical phonon scattering dominates in all regimes.

4.3. Polar Optical Phonon Scattering.

The electron-polar longitudinal optical (LO) phonon interaction results from the polarization of the unit cell due to the motion of the oppositely charged ions in the unit cell. The basic derivation of the interaction Hamiltonian as given by Ridley (1993) will be outlined below.

For an optical phonon where the two basis atoms move in opposite directions, the polarization of the unit cell is then just

$$\mathbf{P}(\mathbf{R}) = \frac{e^* \mathbf{u}(\mathbf{R})}{V_o}, \tag{4.34}$$

where V_o is the volume of the unit cell, e^* is the magnitude of the effective ionic charge and the displacement $\mathbf{u}(\mathbf{R})$ is given by Eq. (4.2). The effective ionic charge reflects the polarizability of the ion. At high frequencies the heavy ionic cores cannot respond to the field so that only the deformation of the electronic clouds contributes. At low frequencies both contributions are present. Therefore, the ionic contribution alone is given by the difference between the high and low frequency polarizations. It can be shown that (Ridley, 1993)

$$(e^*)^2 = \frac{\overline{M}\, V_0 \omega_0^2 \varepsilon_0^2}{\varepsilon_p} \tag{4.35}$$

where

$$\frac{1}{\varepsilon_p}=\left(\frac{1}{\varepsilon_\infty}-\frac{1}{\varepsilon_s}\right), \tag{4.36}$$

and ε_s and ε_∞ are the static and high frequency dielectric constants respectively.

The interaction Hamiltonian is given by the Coulomb energy of the free electron, and can be written as

$$H_{e-ph}=\int \rho(\mathbf{R})\varphi(\mathbf{R})\mathrm{d}\mathbf{R}, \tag{4.37}$$

where $\rho(\mathbf{R})$ is the free charge distribution and $\varphi(\mathbf{R})$ is the electrostatic potential due to the polarization. The electric field associated with the polarization is

$$\mathscr{E}(\mathbf{R})=-\frac{\mathbf{P}(\mathbf{R})}{\varepsilon_o} \tag{4.38}$$

which can then be substituted into the integral (4.37) after the following transformation

$$\begin{aligned} H_{e-ph} &= \int [\nabla\cdot\mathbf{D}(\mathbf{R})]\,\varphi(\mathbf{R})\mathrm{d}\mathbf{R} \\ &= -\int \mathbf{D}(\mathbf{R})\cdot\nabla\varphi(\mathbf{R})\mathrm{d}\mathbf{R} \\ &= \int \mathbf{D}(\mathbf{R})\cdot\mathscr{E}(\mathbf{R})\mathrm{d}\mathbf{R}, \end{aligned} \tag{4.39}$$

to give

$$H_{e-ph}=-\frac{1}{\varepsilon_o}\int \mathbf{D}(\mathbf{R})\cdot\mathbf{P}(\mathbf{R})\mathrm{d}\mathbf{R}. \tag{4.40}$$

The electric displacement, $\mathbf{D}(\mathbf{R})$, due to the free charges, neglecting screening effects, is given by

$$\mathbf{D}(\mathbf{R})=-\nabla\left(\frac{\bar{e}}{4\pi|\mathbf{r}-\mathbf{R}|}\right) \tag{4.41}$$

where $\bar{e}$ is the charge on the free carrier, including its sign, and $\mathbf{r}$ is its position. By substituting Eqs. (4.2), (4.34), and (4.41) in Eq. (4.40) and integrating we obtain

$$H_{e-ph}=-\frac{1}{\sqrt{N}}\frac{\bar{e}e^{*}}{V_o\varepsilon_o}\sum_{q}\frac{1}{q}\left[\Omega_q e^{iq\cdot R}+\ c.c.\ \right]. \tag{4.42}$$

The effective charge is given by Eqs. (4.35) and (4.36). This is the interaction Hamiltonian for polar optical phonons where screening effects have been neglected.

The total transition rate from the state $\Psi_{n,k}$ is obtained by determining $C_{q,b}$ from Eqs. (4.30) and (4.42), and substituting in Eq. (4.33), to give the result

$$W(k)=\frac{2e^2\omega_0}{\varepsilon_p}\frac{N^{*}(\omega_0)}{(2\pi)^3}\left(\frac{2m}{e\mathscr{E}\hbar^2}\right)^{\frac{1}{2}}L_z^{\frac{1}{2}}\int\frac{q_{\|}}{q_{\|}^2+q_z^2}\left|G_{n',n}(q_z)\right|^2 dE_z' d\mathbf{k}_{\|}' dq_{\|} d\theta dq_z$$
$$\times\,\delta\left(\mathbf{k}_{\|}'-\mathbf{k}_{\|}\pm\mathbf{q}_{\|}\right)\delta\left(E_{n',k_{\|}'}-E_{n,k_{\|}}\pm\hbar\omega_0\right) \tag{4.43}$$

where the subscript $_{\|}$ refers to components in the *xy*-plane.

4.4. Deformation Potential Scattering by Acoustic Phonons.

Deformation potential scattering is due to the local fluctuations of the band edge energy generated by the strain induced by acoustic vibrations. Unlike polar optical phonon scattering discussed above or piezoelectric scattering, which will be covered next, it can take place in any semiconductor since it does not require a polar basis. The basic form for the interaction is given by (Ridley, 1993)

$$H_{e-ph}=\sum_{ij}\Xi_{ij}S_{ij} \tag{4.44}$$

where the Ξ_{ij} are the elements of the deformation potential tensor and the S_{ij} are the strain components as defined by

$$S_{ij}=S_{ji}=\frac{1}{2}\left(\frac{\partial u_i}{\partial x_j}+\frac{\partial u_j}{\partial x_i}\right) \tag{4.45}$$

where $\mathbf{R}(x_1, x_2, x_3)$ is the position vector of the unit cell. The S_{ij} can be determined from Eq. (4.2) for the displacement, $\mathbf{u}(\mathbf{R})$,which upon substitution in Eq. (4.30) gives

$$H_{e-ph}=\frac{1}{2\sqrt{N}}\sum_{q}\left\{i\Omega_q e^{iq\cdot R}\left[\sum_{ij}\Xi_{ij}\left(a_i q_j+a_j q_i\right)\right]+\text{c.c.}\right\} \tag{4.46}$$

Since shear strains do not affect the electronic energies in Γ valleys (Ridley, 1993), only the $i = j$ terms will contribute and Eq. (4.46) reduces to

$$H_{e-ph}=\frac{1}{2\sqrt{N}}\sum_{q}\left\{i\Omega_q e^{iq\cdot R}\Xi_d \mathbf{a}\cdot\mathbf{q}+c.c.\right\} \tag{4.47}$$

where Ξ_d is the deformation potential for hydrostatic compression or dilation. The dot product between **a** and **q** allows only longitudinal modes to contribute.

Comparing Eq. (4.47) with Eq. (4.30) to obtain $C_{\mathbf{q},b}$, and substituting in Eq. (4.33) gives the total scattering rate from the state $\Psi_{n,k}$ as

$$\begin{aligned}W(k)=&\frac{\Xi_d^2}{2\rho_m v_{s,l}}\frac{1}{(2\pi)^2}\left(\frac{2m}{e\mathscr{E}\hbar^2}\right)^{\frac{1}{2}}L_z^{\frac{1}{2}}\int q_{\|}\sqrt{q_{\|}^2+q_z^2}\,|G_{n',n}(q_z)|^2 N^{\pm}(\omega_{q,b})\\&\times dE_z' d\mathbf{k}_{\|}' dq_{\|} dq_z d\theta\,\delta\left(\mathbf{k}_{\|}'-\mathbf{k}_{\|}\pm\mathbf{q}_{\|}\right)\delta\left(E_{n',k_{\|}'}-E_{n,k_{\|}}\pm\hbar\omega_{\mathbf{q},b}\right)\end{aligned} \tag{4.48}$$

where the substitutions

$$\rho_m=\frac{N\overline{M}}{V} \tag{4.49}$$

and

$$\omega_q=v_{s,l}q \tag{4.50}$$

have been made.

4.5. Piezoelectric Scattering by Acoustic Phonons.

In polar crystals whose crystal structure lacks inversion symmetry, such as wurtzite or zinc blende, shear strains are accompanied by the generation of a macroscopic electric field. The electron-phonon interaction is then via the piezoelectric fields generated by the shear strains induced by acoustic phonons.

The polarization due to the piezoelectric effect is given by (Ridley, 1993)

$$P_i=\frac{1}{\varepsilon_r}\sum_{jk}h_{ijk}S_{jk} \tag{4.51}$$

where h_{ijk} are the elements of the piezoelectric tensor, S_k are the elements of the strain tensor as given by Eq. (4.45) and ε_r is the relative dielectric permittivity. In zinc blende crystals, there is only one independent piezoelectric constant (Nye, 1957) and in reduced notation (see Appendix A for a description)

$$\mathbf{h}=\begin{bmatrix} 0 & 0 & 0 & h_{14} & 0 & 0 \\ 0 & 0 & 0 & 0 & h_{14} & 0 \\ 0 & 0 & 0 & 0 & 0 & h_{14} \end{bmatrix}. \tag{4.52}$$

The zeros in the first three columns indicate that only shear strains generate piezoelectric fields.

As for the polar optical phonon, the basic interaction is given by Eq. (4.40) where the electric displacement **D** is given by Eq. (4.41) and the polarization **P** is given above. To perform the integration, the transformation

$$\begin{aligned} \int \mathbf{D}(\mathbf{R})\cdot\mathbf{P}(\mathbf{R})d\mathbf{R} &= \int \left[\nabla \varphi_e(\mathbf{R})\right]\cdot\mathbf{P}(\mathbf{R})d\mathbf{R} \\ &= \int \varphi_e(\mathbf{R})\left[\nabla\cdot\mathbf{P}(\mathbf{R})\right]d\mathbf{R} \end{aligned} \tag{4.53}$$

is applied, where $\varphi_e(\mathbf{R})$ represents the potential at **R** due to the free charge at **r**. The $(\nabla\bullet\mathbf{P})_x$ component yields

$$(\nabla\cdot\mathbf{P})_x=-\sum_q \frac{h_{14}}{\varepsilon_r\sqrt{N}}\left\{\left(a_y q_z+a_z q_y\right)q_x\Omega_q e^{iq\cdot R}+\ c.c.\right\} \tag{4.54}$$

with similar results for the remaining directions. Recombining the three components and performing the integration, we obtain

$$H_{e-ph}=-\frac{\bar{e}h_{14}}{\varepsilon_r\varepsilon_0\sqrt{N}}\sum_q\left\{2\left(a_x\beta\gamma+a_y\alpha\gamma+a_z\alpha\beta\right)\Omega_q e^{iq\cdot R}+c.c.\right\} \tag{4.55}$$

where α, β, γ are the direction cosines relative to the crystal axes for the phonon wavevector as given by

$$q_x=q\alpha,\ q_y=q\beta,\ q_z=q\gamma \tag{4.56}$$

and q is the magnitude of the phonon wavevector.

The full expression for the transition rate is then

$$W(k)=\left(\frac{eh_{14}}{\varepsilon_r\varepsilon_0}\right)^2\frac{1}{\rho_m v_s}\frac{2}{(2\pi)^2}\left(\frac{2m^*}{e\mathscr{E}\hbar^2}\right)^{\frac{1}{2}}L_z^{\frac{1}{2}}\int 4(a_x\beta\gamma+a_y\alpha\gamma+a_z\alpha\beta)^2\frac{|G_{n',n}(q_z)|^2}{q}$$
$$\times N^{\pm}(\omega_{q,b})\,d\mathbf{k}_1'dE_z'd\mathbf{q}\delta\left(\mathbf{k}_1'-\mathbf{k}_1\pm\mathbf{q}_1\right)\delta\left(E_{n',k_1'}-E_{n,k_1}\pm\hbar\omega_{q,b}\right) \tag{4.57}$$

where the substitution given by Eq. (4.49) for the mass density has been made. The presence of the direction cosines indicates that this process is anisotropic and will depend on the polarization of the mode. It is therefore necessary to perform some averaging to retain tractability. In particular, we wish to average over the plane of the well, i.e.: over α and β.

For longitudinal modes, the polarization vector and the wavevector are parallel. Therefore

$$a_1=\alpha,\ a_2=\beta,\ a_3=\gamma \tag{4.58}$$

and the angular dependence reduces to

$$(3\alpha\beta\gamma)^2 \tag{4.59}$$

By noting that $\alpha=(\alpha^2+\beta^2)^{1/2}\cos\theta$ and $\beta=(\alpha^2+\beta^2)^{1/2}\sin\theta$ where θ is the angle in the xy-plane, the average of Eq. (4.59) over the x-y plane is calculated to be

$$\left\langle(3\alpha\beta\gamma)^2\right\rangle=\frac{9}{8}\left(\alpha^2+\beta^2\right)^2\gamma^2=\frac{9}{8}\left(1-\gamma^2\right)^2\gamma^2. \tag{4.60}$$

For transverse modes, the wavevector and the two polarization vectors form an orthogonal system. The angular dependence for each of the modes can be determined by formulating the transformation matrix between the crystal axes and the axes defined by the wavevector and polarizations. This gives for the combined angular dependence of both transverse modes (see Appendix B for a detailed derivation)

$$\alpha^2\beta^2+\beta^2\gamma^2+\alpha^2\gamma^2-\left(3\alpha\beta\gamma^2\right) \tag{4.61}$$

The average of the second term was already determined to be Eq. (4.59). Averaging the first term over the *xy*-plane gives

$$\begin{aligned}\left\langle \alpha^2\beta^2+\beta^2\gamma^2+\alpha^2\gamma^2 \right\rangle &= \frac{1}{8}\left(\alpha^2+\beta^2\right)\left(\alpha^2+\beta^2+8\gamma^2\right) \\ &= \frac{1}{8}\left(1-\gamma^2\right)\left(1+7\gamma^2\right)\end{aligned} \tag{4.62}$$

If not for the difference in v_s between the longitudinal and transverse modes, all of the modes could be combined in a single expression where the angular dependence would be given by Eq. (4.61). However, the difference is significant and so we obtain two expressions, one for the longitudinal mode and another for the two transverse modes.

Replacing the direction cosines by the wavevector components and noting that $q_{\|}/q = (\alpha^2 + \beta^2)^{1/2}$ we obtain for the angular dependence of the longitudinal mode, averaged over the plane of the well,

$$\frac{9}{8}\frac{q_{\|}^4 q_z^2}{q^6}. \tag{4.63}$$

Substituting this into Eq. (4.57) for the total transition rate gives for longitudinal modes

$$\begin{aligned}W(k) = \left(\frac{eh_{14}}{\varepsilon_r\varepsilon_0}\right)^2 \frac{1}{\rho_m v_{s,l}} \frac{2}{(2\pi)^2}\left(\frac{2m^*}{e\mathscr{E}\hbar^2}\right)^{\frac{1}{2}} L_z^{\frac{1}{2}} \int \frac{9}{2}\frac{q_{\|}^5 q_z^2}{\left(q_{\|}^2+q_z^2\right)^{7/2}} \left|G_{n',n}(q_z)\right|^2 N^{\pm}(\omega_{q,b}) \\ \times d\mathbf{k}_{\|}' dE_z' dq_{\|} dq_z d\theta \delta\left(\mathbf{k}_{\|}' - \mathbf{k}_{\|} \pm \mathbf{q}_{\|}\right) \delta\left(E_{n',k_{\|}'} - E_{n,k_{\|}} \pm \hbar\omega_{q,b}\right).\end{aligned} \tag{4.64}$$

For the combined transverse modes, the angular dependence is

$$\frac{8q_{\|}^2 q_z^2 + q_{\|}^4}{8q^4} - \frac{9}{8}\frac{q_{\|}^4 q_z^2}{q^6} \tag{4.65}$$

which yields a transition rate given by

$$\begin{aligned}W(k) = \left(\frac{eh_{14}}{\varepsilon_r\varepsilon_0}\right)^2 \frac{1}{\rho_m v_{s,t}} \frac{2}{(2\pi)^2}\left(\frac{2m^*}{e\mathscr{E}\hbar^2}\right)^{\frac{1}{2}} L_z^{\frac{1}{2}} \int \left\{\frac{\left(8q_z^2+q_{\|}^2\right)q_{\|}^3}{2\left(q_{\|}^2+q_z^2\right)^{5/2}} - \frac{9q_{\|}^5 q_z^2}{2\left(q_{\|}^2+q_z^2\right)^{7/2}}\right\} \\ \times \left|G_{n',n}(q_z)\right|^2 N^{\pm}(\omega_{q,b}) d\mathbf{k}_{\|}' dE_z' dq_{\|} dq_z d\theta \delta\left(\mathbf{k}_{\|}' - \mathbf{k}_{\|} \pm \mathbf{q}_{\|}\right) \delta\left(E_{n',k_{\|}'} - E_{n,k_{\|}} \pm \hbar\omega_{q,b}\right)\end{aligned} \tag{4.66}$$

4.6. Evaluation of the 2D-to-3D Scattering Rates.

To calculate the transition rates in Eqs. (4.43), (4.48), (4.64), and (4.66) requires integrating over each of the degrees of freedom: k_x', k_y', E_n', q_x, q_y, and q_z. Furthermore, the function $G_{n',n}(q_z)$ includes an integration over z. Some of these degrees of freedom are removed by the delta functions that impose conservation of energy and in-plane momentum. The elimination of k_x' and k_y', the integration over the direction of $\mathbf{q}$ in the xy-plane, and the resultant limitations on E_n' are essentially the same in all three cases. However, the approaches for the optical and acoustic processes will eventually diverge due to the differences in the dispersion relations and the functional dependences on $q_{||}$ and q_z.

The reduction of the degrees of freedom follows the approach of Liang and Lent (1990). Conservation of the in-plane momentum gives

$$k_{||}'^2 = k_{||}^2 + q_{||}^2 \pm 2k_{||}q_{||}\cos\theta \tag{4.67}$$

where θ is the angle between $\mathbf{k}_{||}$ and $\mathbf{q}_{||}$ and the upper sign is for emission and the lower sign is for absorption. Assuming parabolic bands, conservation of energy gives

$$E_{n'} + \frac{\hbar^2 k_{||}'^2}{2m^*} - E_n - \frac{\hbar^2 k_{||}^2}{2m^*} \pm \hbar\omega_{\mathbf{q},b} = 0 \tag{4.68}$$

where E_n and $E_{n'}$ are the energy solutions for the envelope functions of the initial and final states respectively. Combining Eqs. (4.67) and (4.68) by eliminating $k_{||}'$ yields

$$\left(E_q + E_{n'} - E_n \pm \hbar\omega_{\mathbf{q},b}\right) \pm 2\sqrt{E_q E_k}\cos\theta = 0 \tag{4.69}$$

where

$$E_q = \frac{\hbar^2 q_{||}^2}{2m^*}, \quad E_k = \frac{\hbar^2 k_{||}^2}{2m^*}. \tag{4.70}$$

By defining

$$\eta \equiv E_q + E_{n'} - E_n \pm \hbar\omega_{\mathbf{q},b}, \tag{4.71}$$
$$\kappa \equiv 2\sqrt{E_q E_k},$$

Eq. (4.69) can be re-written as a delta function containing the entire θ-dependence. As a result, the $d\theta$ integration gives for both absorption and emission

$$2\int_0^{\pi}\delta(\eta\pm\kappa\cos\theta)\,d\theta=\frac{2}{\sqrt{\kappa^2-\eta^2}}. \tag{4.72}$$

This imposes the restriction on E_n'

$$E_{min}<E_n'<E_{max} \tag{4.73}$$

where

$$\begin{aligned}E_{\min}&=E_n-E_q\mp\hbar\omega_{q,b}-2\sqrt{E_kE_q}=-(\eta+\kappa)+E_n'\\E_{\max}&=E_n-E_q\mp\hbar\omega_{q,b}+2\sqrt{E_kE_q}=-(\eta-\kappa)+E_n'\end{aligned} \tag{4.74}$$

The right-hand side of Eq. (4.72) can be re-written as

$$\frac{2}{\sqrt{\kappa^2-\eta^2}}=\frac{2}{\sqrt{(E_{max}-E_n')(E_n'-E_{min})}} \tag{4.75}$$

For polar optical phonon scattering, the approximation $\omega_{q,b}=\omega_0$ is assumed. The integration over $q_{||}$ is then limited by the requirement that E_{max} must be greater than E_{start}, where E_{start} is an arbitrary lower cutoff generally chosen to be sufficiently larger than E_n, the initial state energy, to exclude scattering into the ground state resonance. The choice of E_{start} becomes less obvious when there are multiple subbands and the highest resonance is near the top of the well. This will be discussed in detail in §4.7.12. For the upper limit on the $q_{||}$ integration, we obtain

$$\begin{aligned}q_{max}&=\sqrt{\frac{2m}{\hbar^2}}\left[\sqrt{E_k}+\sqrt{E_k+(E_n-E_{start}\mp\hbar\omega_0)}\right]\\&=k_{||}+\sqrt{k_{||}^2+\frac{2m}{\hbar^2}(E_n-E_{start}\mp\hbar\omega_0)}\,.\end{aligned} \tag{4.76}$$

For emission there is an added restriction on $k_{||}$

$$k_{\parallel}^2 > \left[\frac{2m^*}{\hbar^2}\left(\hbar\omega_0 - E_n + E_{start}\right)\right] \tag{4.77}$$

which arises due to conservation of energy. This states that the initial free (in-plane) kinetic energy must be greater than the sum of the increase in the z-direction energy state and the energy of the emitted phonon.

The remaining integral then has the form

$$W\left(n,k_{\parallel}\right) \propto \int_0^{q_{max}} q_{\parallel} dq_{\parallel} \int_{\min(E_{min},E_{start})}^{E_{max}} \frac{dE_n'}{\sqrt{\left(E_{max}-E_n'\right)\left(E_n'-E_{min}\right)}} \int_0^{\infty} dq_z \frac{\left|G_{n,n'}(q_z)\right|}{q_{\parallel}^2+q_z^2}. \tag{4.78}$$

Note that the occupation factor $N^{\pm}(\omega_0)$ is left out of the integration since it does not depend on q_z or $q_{\parallel}$.

For acoustic phonons, the dispersion is assumed to be linear such that $\omega_{q,b} = v_s q$. This changes the energy conservation relation (4.68) to

$$E_{n'} + \frac{\hbar^2 k_{\parallel}'^2}{2m} - E_n - \frac{\hbar^2 k_{\parallel}^2}{2m} \pm \hbar v_s \left(q_z^2+q_{\parallel}^2\right)^{\frac{1}{2}} = 0 \tag{4.79}$$

Following the same procedure as for the optical phonons, we again arrive at Eq. (4.75) for the evaluation of the integral over θ where E_{min} and E_{max} are now given by

$$\begin{aligned} E_{min} &= E_n - E_q \mp \hbar v_s \left(q_z^2+q_{\parallel}^2\right)^{\frac{1}{2}} - 2\sqrt{E_k E_q} = -(\eta+\kappa) + E_{n'} \\ E_{max} &= E_n - E_q \mp \hbar v_s \left(q_z^2+q_{\parallel}^2\right)^{\frac{1}{2}} + 2\sqrt{E_k E_q} = -(\eta-\kappa) + E_{n'} \end{aligned} \tag{4.80}$$

Since q_z now appears in E_{min} and E_{max}, Eqs. (4.80) cannot immediately be solved for $q_{\parallel}$ to determine its limits. Instead, q_z is considered first. By requiring $E_{max} > E_{start}$, we obtain for emission and absorption respectively

$$\begin{aligned} q_z^2 &< \left(\frac{1}{\hbar v_s}\right)^2 \left[2\sqrt{E_k E_q} + E_n - E_q - E_{start}\right]^2 - q_{\parallel}^2 \equiv \left(q_{z,max}^{emm}\right)^2 \\ q_z^2 &> \left(\frac{1}{\hbar v_s}\right)^2 \left[E_q - E_n - 2\sqrt{E_k E_q} + E_{start}\right]^2 - q_{\parallel}^2 \equiv \left(q_{z,min}^{abs}\right)^2 \end{aligned} \tag{4.81}$$

For absorption, since the actual lower limit on q_z is min(0, $q_{z,min}^{abs}$), Eq. (4.81) places no restriction on the values of $q_{||}$. For emission, we require that $q_z^2 > 0$. This leads to the quadratic inequality

$$q_{||}^2+\frac{2m^*}{\hbar^2}\left(\hbar v_s-\frac{\hbar^2 k_{||}}{m}\right)q_{||}+\frac{2m^*}{\hbar^2}\left(E_{start}-E_n\right)<0 \tag{4.82}$$

which gives the following condition on $q_{||}$

$$q_{||,min}^{emm}<q_{||}<q_{||,max}^{emm} \tag{4.83}$$

where

$$\begin{aligned} q_{||,min}^{emm} &= -\left(\frac{m^* v_s}{\hbar}-k_{||}\right)-\sqrt{\left(\frac{m^* v_s}{\hbar}-k_{||}\right)^2+\frac{2m^*}{\hbar^2}\left(E_n-E_{start}\right)}\,, \\ q_{||,max}^{emm} &= -\left(\frac{m^* v_s}{\hbar}-k_{||}\right)+\sqrt{\left(\frac{m^* v_s}{\hbar}-k_{||}\right)^2+\frac{2m^*}{\hbar^2}\left(E_n-E_{start}\right)}\,. \end{aligned} \tag{4.84}$$

The final expression for the integrations for acoustic phonon scattering via the deformation potential is

$$\begin{aligned} W^r\left(n,k_{||}\right) \propto \int_{q_{||,min}}^{q_{||,max}} dq_{||} \int_{\min(E_{min},\,E_{start})}^{E_{max}} \frac{dE_n'}{\sqrt{\left(E_{max}-E_n'\right)\left(E_n'-E_{min}\right)}} \\ \times \int_{q_{z,min}}^{q_{z,max}} dq_z q_{||}\sqrt{q_{||}^2+q_z^2}\,\left|G_{n,n'}(q_z)\right| N^*\left(v_s\sqrt{q_{||}^2+q_z^2}\right) \end{aligned} \tag{4.85}$$

where the limits on $q_{||}$ apply only to emission; for absorption the integration is from 0 to ∞. The limits for q_z are as given by Eq. (4.81) where for emission, $q_{z,max}$ is ∞, and for absorption, $q_{z,min}$ is 0. Note that since the phonon energy depends on the magnitude of the wavevector, the occupation factor must be included in the integration.

Finally, the corresponding expressions for piezoelectric scattering are

$$W(n,k_{\parallel}) \propto \int_{q_{\parallel,min}}^{q_{\parallel,max}} dq_{\parallel} \int_{\min(E_{min},E_{start})}^{E_{max}} \frac{dE_n'}{\sqrt{(E_{max}-E_n')(E_n'-E_{min})}} \times \int_{q_{z,min}}^{q_{z,max}} dq_z \frac{9q_{\parallel}^5 q_z^2}{(q_{\parallel}^2+q_z^2)^{7/2}} |G_{n,n'}(q_z)| N^{\pm}\left(v_s\sqrt{q_{\parallel}^2+q_z^2}\right) \quad (4.86)$$

for longitudinal modes and

$$W(n,k_{\parallel}) \propto \int_{q_{\parallel,min}}^{q_{\parallel,max}} dq_{\parallel} \int_{\min(E_{min},E_{start})}^{E_{max}} \frac{dE_n'}{\sqrt{(E_{max}-E_n')(E_n'-E_{min})}} \times \int_{q_{z,min}}^{q_{z,max}} dq_z q_{\parallel} \left\{ \frac{(8q_{\parallel}^2 q_z^2+q_{\parallel}^4)}{(q_{\parallel}^2+q_z^2)^{5/2}} - \frac{9q_{\parallel}^4 q_z^2}{(q_{\parallel}^2+q_z^2)^{7/2}} \right\} |G_{n,n'}(q_z)| N^{\pm}\left(v_s\sqrt{q_{\parallel}^2+q_z^2}\right) \quad (4.87)$$

for transverse modes.

This completes the evaluation of the scattering rates for polar optical phonon scattering, and deformation potential and piezoelectric scattering by acoustic phonons. Piezoelectric and deformation potential scattering by optical phonons have been omitted as they will be negligible compared to the polar process. As we will see in the following sections, polar LO phonon scattering will also dominate over both acoustic phonon processes.

4.7. Results.

Calculations were performed for a variety of GaAs/AlGaAs well configurations as a function of the electric field to examine the general behaviour of the escape rate under different conditions. A 60 Å wide symmetric GaAs/$Al_{0.20}Ga_{0.80}As$ well was considered first to examine in detail the results of the scattering calculations. Thermionic emission times were then calculated and compared to the simplified expression given by Eq. (2.39). While this approximation gave rough agreement, it was found that a Fermi-Dirac function was much more successful at reproducing the results of the complete calculation. The dependence of the scattering rate and thermionic emission rate on the well width and depth was investigated briefly where both single and multiple subband wells were considered. Finally, calculations were performed for an asymmetric well and compared to measured

electron escape times reported by Cavaillès *et al* (1992).

4.7.1. The 60Å symmetric $GaAs/Al_{0.20}Ga_{0.80}As$ well.

This well configuration was chosen to be the generic testbed due to its relatively high barriers (162 meV) and single confined subband. The absence of higher subbands removes the complication of thermally-assisted tunnelling, while the high barriers retain sharp bound state resonances even under large fields. The material parameters used in the calculations are listed in Table 4.1 and the potential profile is shown in Fig. 4.4. Also indicated in the figure are the range of final state energies considered and the overlap function integration limits, z_{max} and z_{min}. The latter were chosen such that the lower z limit (z_{min}) corresponded to the intercept of the ground state energy with the barrier potential, while the upper z limit (z_{max}) was set to 3/4 of the absolute value of z_{min}. In this approximation the initial state wavefunction is set to zero in above-barrier regions of space to reflect the fact that initially, the particle is localized within the well. On the positive z side, since the wavefunction is damped as it penetrates the rising potential barrier, the

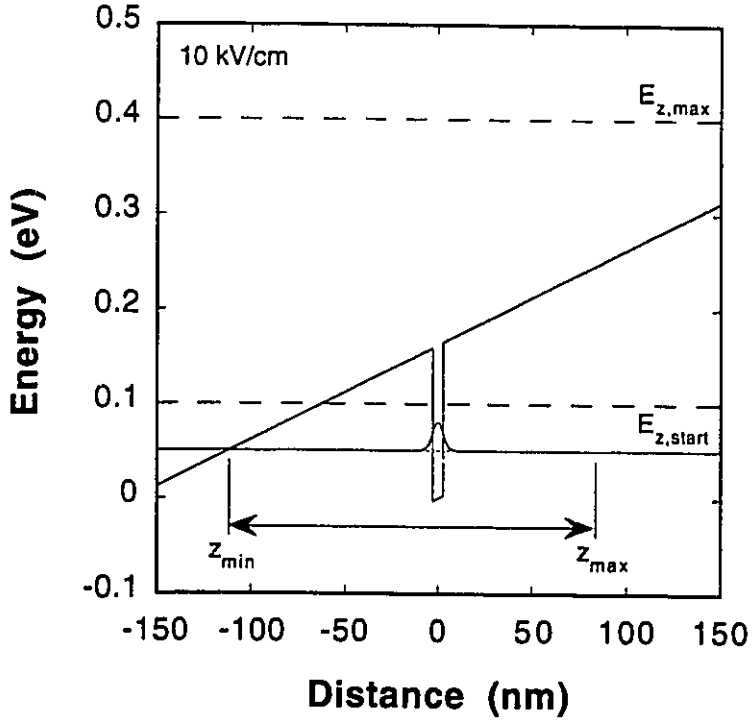

Fig. 4.4: Illustration of the potential profile for the 60 Å $GaAs/Al_{0.20}Ga_{0.80}As$ quantum well in a 10 kV/cm electric field. The final state energy range considered is indicated by the shaded region, while the limits of integration, z_{max} and z_{min} are indicated by the arrow. The lower limit is given by the intersection of the bound state energy and the barrier potential while the upper limit is arbitrarily set to 3/4 of the absolute value of the lower limit. The energy zero is at the midpoint of the bottom of the well.

wavefunction becomes negligibly small and the integration can be cutoff arbitrarily. A distance of 3/4 of the negative z limit should be more than adequate to allow the wavefunction to vanish. The lower energy limit, $E_{z,start}$ (= E_{start}), is chosen such that it is sufficiently removed from the confined state to omit intrasubband scattering. This is straightforward in cases where the uppermost subband is well removed from the top of the well, however, as the separation is reduced, it becomes increasingly difficult to distinguish between confined and unconfined states. This will be encountered in §4.7.10-§4.7.12 in relation to narrow, shallow and multiple subband wells. The upper limit, $E_{z,max}$, is chosen to be at least $5k_BT$ above the barrier height at 300 K, so that contributions from energies greater than $E_{z,max}$ will be negligible. Unless otherwise indicated, all calculations presented in §4.7.2 through §4.7.5 were performed using these parameters.

TABLE 4.1: Material parameters used in the GaAs/$Al_xGa_{1-x}As$ quantum well scattering calculations.

Parameter	Value
Lattice constant, a (Å)	5.653
Crystal density, ρ (gm/cm^3)	5.360
Piezoelectric constant, h_{14} (C/m^2)	0.160
Static dielectric constant, ε_s	13.18
High frequency dielectric constant, ε_∞	10.89
Deformation potential, Ξ_d (eV)	7.0
LO-phonon energy, $\hbar\omega_0$ (eV)	0.03625
Sound velocity, TA phonons, $v_{s,TA}$ (m/s)	2.99×10^{3} †
Sound velocity, LA phonons, $v_{s,LA}$ (m/s)	5.11×10^{3} †
Effective mass, GaAs, m^* (m_0)	0.067
Effective mass, $Al_{1-x}Ga_xAs$, m^* (m_0)	0.067 + 0.083 x
Conduction band offset (eV)	0.65†† ΔE_g = 0.811 x

all values taken from Adachi (1985) except

†Price (1991)
††Zhu (1993), Drummond (1985)

4.7.2. The overlap function, $G_{n,n}(q_z)$.

The overlap function, $G_{n,n}(q_z)$, as given by Eq. (4.32), is common to all three types of scattering. Fig. 4.5 (a) shows a contour plot of the overlap function calculated for the 60 Å testbed well in a 5 kV/cm electric field. For final state energies below the barrier edge, the overlap function falls rapidly to zero, while decreasing slowly for increasing energy above the barrier edge. The width of the overlap function in the q_z direction reflects the momentum uncertainty in both the initial and final states due to the presence of the

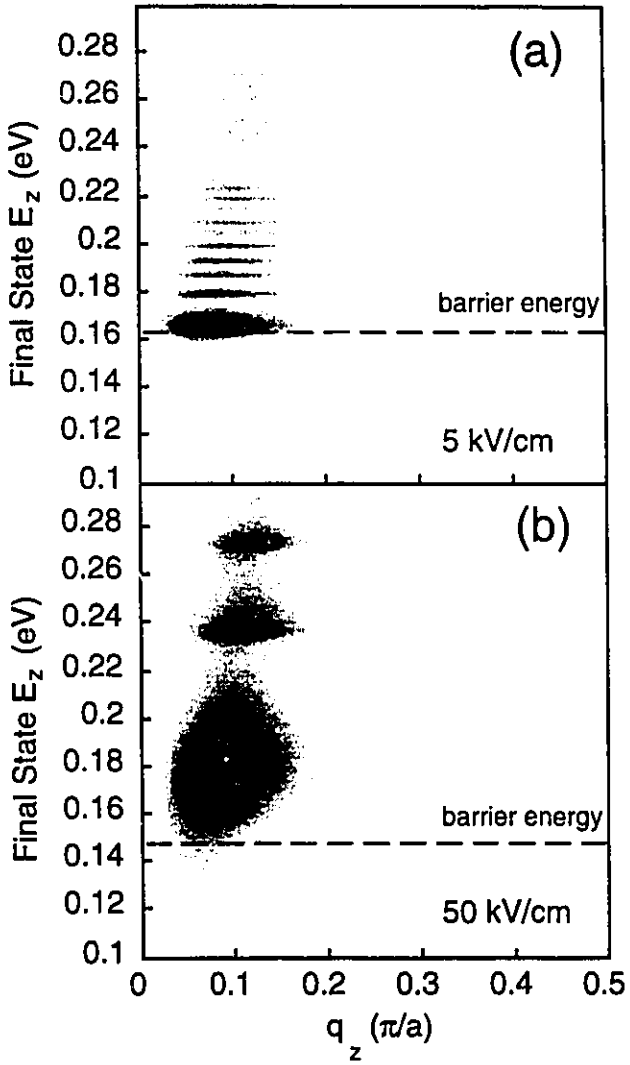

Fig. 4.5: Contour plots of the overlap function $G_{n,n'}(q_z)$ for a 60 Å GaAs/$Al_{0.20}Ga_{0.80}As$ quantum well in (a) 5 kV/cm and (b) 50 kV/cm electric fields as a function of q_z and E_z'. Darker regions correspond to larger values of $G_{n',n}$. At higher fields the peaks broaden considerably and extend to energies below the barrier edge. Note that the barrier energy is lower at 50 kV/cm due to the well inclination as described in §2.5.2.

perpendicular electric field and, for the initial state, the confining potential well. In the absence of the field, the final state is a plane wave with a well-defined momentum, while the initial state retains a momentum width due to the quantum confinement that would again result in a broadening of the overlap function. For a bulk process with no electric field, both initial and final states have well defined momenta and, as for the in-plane direction described in §4.2.3, the overlap reduces to a delta function which gives the momentum conservation condition. Hence, the width of the overlap function falls to zero. In Fig. 4.5 (b), the electric field is increased to 50 kV/cm, lowering the potential barrier as described in §2.5.2. Due to the increased penetration of the 3D final state wavefunction through the triangular tip of the barrier potential, the abrupt rise in the overlap function at the barrier energy is smeared and now extends to much lower energies.

Oscillations in the final state energy direction are visible in both the low and high

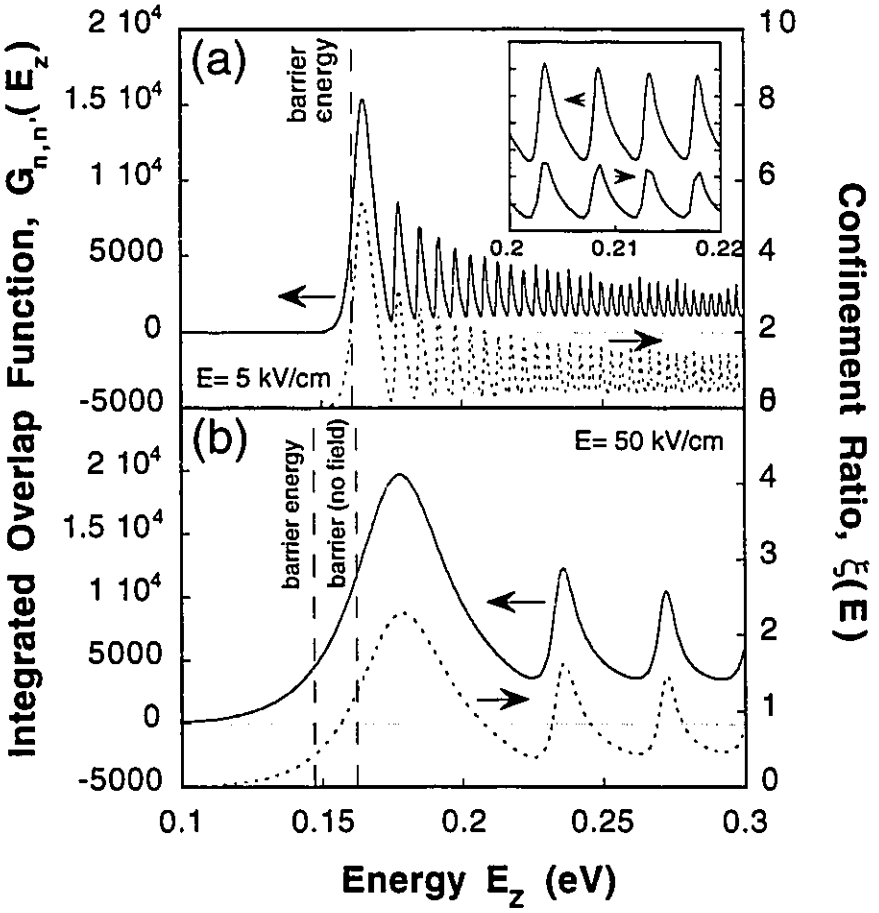

Fig. 4.6: The overlap function, $G_{n,n'}(q_z)$, vs. E_z integrated over q_z for electric fields of (a) 5 kV/cm and (b) 50 kV/cm. The dotted curve shows the corresponding confinement ratio, $\xi(E_z)$, revealing that the oscillations in the overlap are due to above-barrier resonances in the final state wavefunction. The inset to (a) more clearly illustrates this for the high frequency oscillations that occur at low electric fields. The vertical dashed lines indicate the potential barrier energies; the electric field produces a 15 meV shift in (b).

field contour plots. This is more clearly illustrated in Fig. 4.6, where the contour plots in Fig. 4.5 have been integrated over q_z. As illustrated by comparison with the confinement ratio, $\xi(E)$, the peaks correspond to above-barrier resonances, characterized by increased amplitude within the well region. The width of the resonances increases with increasing electric field, so that fewer peaks appear at high fields. Similar characteristics have been reported previously in relation to the 1D density of states above a quantum well (Trzeciakowski and Gurioli, 1991).

4.7.3. 2D-to-3D scattering rates: polar optical phonons.

Once the overlap function has been calculated, the individual scattering rates can be determined according to the algorithms described in §4.6. Fig. 4.7 shows the calculated 2D-to-3D electron scattering rates via polar optical phonon scattering for the GaAs/AlGaAs 60 Å quantum well testbed as a function of the initial state in-plane energy, E_k. Since the perpendicular energy, E_z, is essentially quantized, E_k corresponds to the free kinetic energy

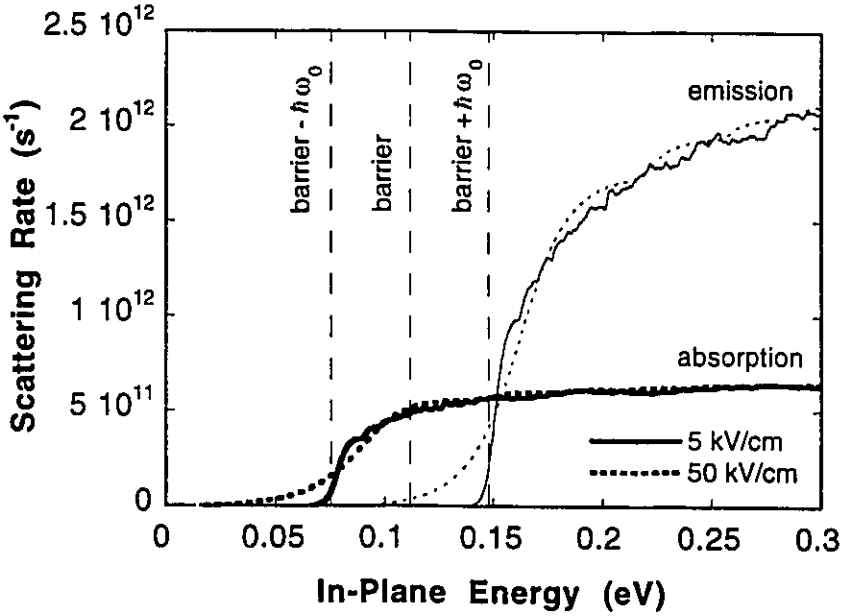

Fig. 4.7: The 2D-to-3D electron scattering rate via polar optical phonon scattering for the 60 Å GaAs/AlGaAs testbed well at 300 K. The solid curves give the low field (5 kV/cm) results while the dotted curves represent the high field (50 kV/cm) results. The heavier curves give the rates for phonon absorption while the lighter ones correspond to phonon emission. The onset of scattering is shifted in energy relative to the barrier edge by an amount equal to the LO phonon energy, where phonon absorption produces a shift to lower energy and emission shifts the scattering to higher energy. The vertical dashed lines indicate the barrier energy at zero field, the outer lines indicating the effective raising or lowering of the barrier by an amount equal to the phonon energy. At 50 kV/cm, all three would be shifted to lower energies by 15 meV.

of the confined electron. The most striking feature of these curves is the shift in the onset of scattering relative to the barrier energy. For LO phonon *absorption*, electrons can scatter out of the well as soon as their kinetic energy is within $\hbar\omega_0$, the LO phonon energy, of the barrier energy. Conversely, electrons scattering into 3D states via LO phonon *emission* must acquire greater than $\hbar\omega_0$ above the barrier energy prior to undergoing the transition.

The difference in the magnitude of the scattering rate between absorption and emission is primarily due to the occupation factor given by Eq. (4.20). While for both emission and absorption this contains a stimulated term proportional to the number of phonons present, for emission there is also a constant spontaneous term. The curves in Fig. 4.7 were calculated for a phonon temperature of 300 K, where $k_BT \approx 26$ meV. Since $\hbar\omega_0 \approx 36$ meV, the phonon occupation, as given by the Bose-Einstein distribution, will be less than unity. Therefore, the spontaneous emission term will dominate the thermionic emission rate. As shown in Fig. 4.8, the scattering rates without the occupation factors are very similar in magnitude.

There are some subtle features in the scattering curves of Fig. 4.7. The high frequency noise is spurious and is due to the difficulty in integrating over the rapid

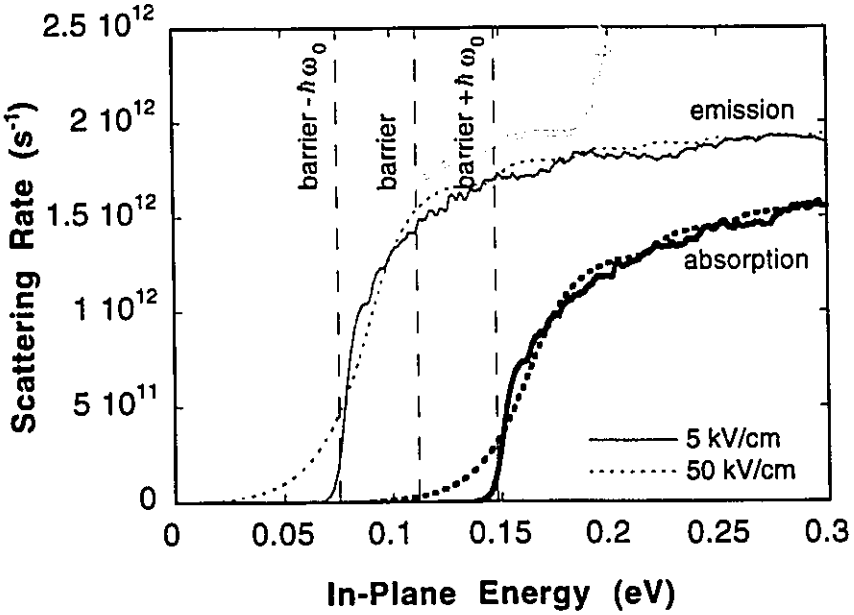

Fig. 4.8: The 2D-to-3D electron scattering rate via polar optical phonon scattering for the 60 Å GaAs/AlGaAs testbed well, where the phonon occupation factors have been set to unity for both emission and absorption. The solid curves give the low field (5 kV/cm) results while the dotted curves represent the high field (50 kV/cm) results, and the heavier curves correspond to phonon absorption, the lighter ones to phonon emission. There is only a small difference in the magnitudes of the scattering rates between emission and absorption. The vertical dashed lines indicate the barrier energy at zero field, the outer lines indicating the effective raising or lowering of the barrier by an amount equal to the phonon energy. At 50 kV/cm, all three would be shifted to lower energies by 15 meV.

oscillations in the overlap function. At high fields, where the oscillation period is longer, the noise disappears. In all cases, it can be eliminated by increasing the resolution of the integrations. However, as this does not significantly alter the general shape or magnitude of the curves but dramatically increases the computation time, the stepsize was not decreased any further. The soft steps visible in the 50 kV/cm scattering rate correspond to the peaks in the overlap function. As discussed earlier, these arise due to resonances in the 3D final states. They are not as visible in the low field curve where the oscillation frequency is much higher.

Finally, the principal effect of the electric field is to smear the onset of scattering so that a tail extends to energies below the barrier, while just above the barrier, the scattering is reduced slightly. The shift in the scattering edge expected from the linear barrier lowering term of Eq. (2.43) is *not* observed. As seen in the overlap function calculations, the low energy tail is due in part to the increased penetration of the 3D states through the triangular tip of the barrier potential. Both of these results will be considered in greater detail in §4.7.8. The magnitude of the scattering rate at energies well above the barrier edge is unaffected by the electric field.

4.7.4. 2D-to-3D scattering rates: longitudinal acoustic phonons via the deformation potential.

Fig. 4.9 shows the 2D-to-3D electron scattering rates via deformation potential scattering by longitudinal acoustic phonons for the GaAs/AlGaAs testbed well. In contrast to the curves for polar optical phonon scattering, there is little difference between the emission and absorption curves and the shift in energy is almost non-existent. This is a result of the lower energy of the acoustic phonons. Recall that the acoustic phonons were treated as having a linear dispersion given by Eq. (4.49), so that small q phonons have small energies. Fig. 4.10 shows that the scattering rate is dominated by phonons with $q_{\|} \approx 0.11\ \pi/a$ and $q_z \approx 0.09\ \pi/a$ which corresponds to a phonon energy of ~2.8 meV. Considering that the escaping electrons have initla kinetic energies of ~110 meV, the phonon energy will have little effect on the initial and final state conservation of energy. Nonetheless, there is a ~4.2 meV shift between the emission and absorption scattering rates, which corresponds to roughly twice the phonon energy. Also, the small phonon energy results in a large phonon occupation factor so that the stimulated term dominates over the spontaneous term in the emission occupation factor. As a result, the spontaneous term produces only a small difference in the magnitude of the scattering rates between

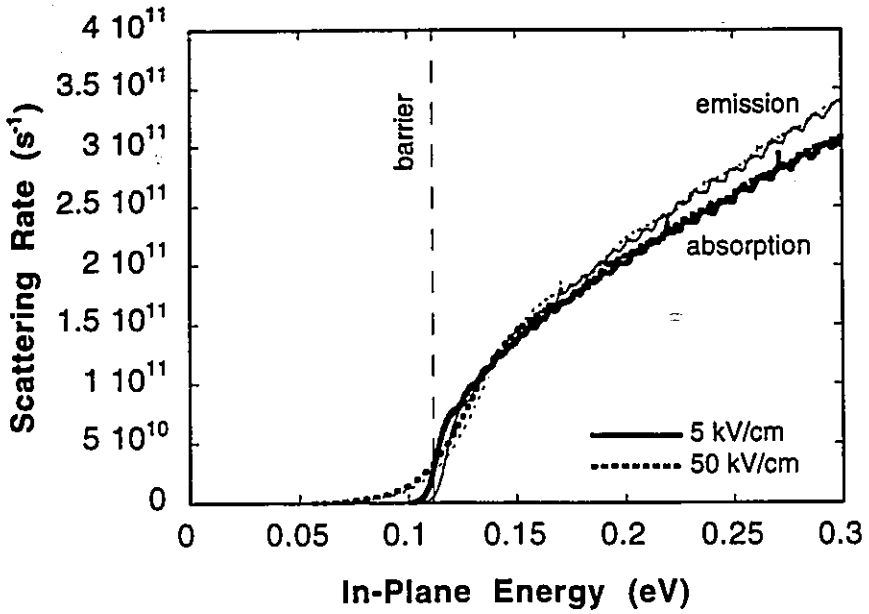

Fig. 4.9: The 2D-to-3D electron scattering rate via longitudinal acoustic phonon deformation potential scattering for the 60 Å GaAs/AlGaAs testbed well. The solid curves give the low field (5 kV/cm) results while the dotted curves represent the high field (50 kV/cm) results. The heavier curves give the rates for phonon absorption while the lighter ones correspond to phonon emission. Due to the small energy carried by the acoustic phonons, there is little separation between the emission and absorption curves. Note that the barrier energy given by the vertical dashed line is for zero field only; at 50 kV/cm, it would be shifted to lower energy by 15 meV.

emission and absorption.

The subtle step-like features observed in the LO phonon scattering calculations are also seen in the deformation potential curves. These are again attributed to resonances in the final state wavefunction. The field-induced smearing of the scattering function noted in the polar LO phonon result is also present in the deformation potential calculation. It is illustrated by the dotted curve in Fig. 4.9 representing the scattering rate at an electric field strength of 50 kV/cm and is again attributed to increased penetration through the barrier by the 3D final state wavefunction.

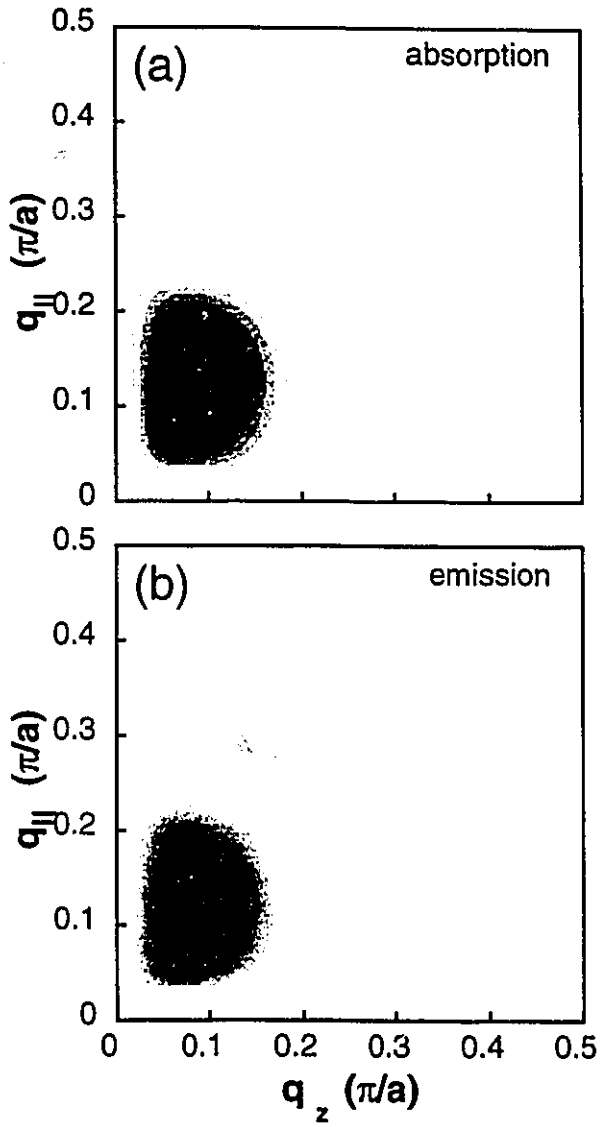

Fig. 4.10: Contour plot of the deformation potential scattering rate versus the perpendicular (q_z) and in-plane ($q_{||}$) phonon wavevector components for (a) absorption and (b) emission. Darker regions correspond to higher scattering rates. In both cases, the contours are centred about a total q of approximately $0.14\pi/a$ which corresponds to a phonon energy of ~2.8 meV.

4.7.5. 2D-to-3D scattering rates: longitudinal and transverse acoustic phonons via piezoelectric coupling.

Fig. 4.11 shows the calculated 2D-to-3D electron scattering rates via the piezoelectric effect for longitudinal acoustic phonons; transverse acoustic phonons are considered in Fig. 4.12. Both sets of curves are very similar to those obtained for deformation potential scattering by acoustic phonons: the low phonon energy produces only a small difference between the emission and absorption processes. However, where the deformation potential curves increase linearly beyond 150 meV, the piezoelectric curves more closely resemble the rounded step-functions of the polar LO phonon scattering. This can be attributed to the similarities in the interaction Hamiltonians between the piezoelectric and polar optical processes, while the deformation potential scattering has very different origins.

When the magnitudes of the scattering rates are compared, it is found that the transverse acoustic phonons dominate over the longitudinal modes, due in part to the smaller sound velocity associated with these branches. As seen previously, the scattering curve extends down to energies below the barrier at high fields. Also visible are the step-like features arising from the final state resonances.

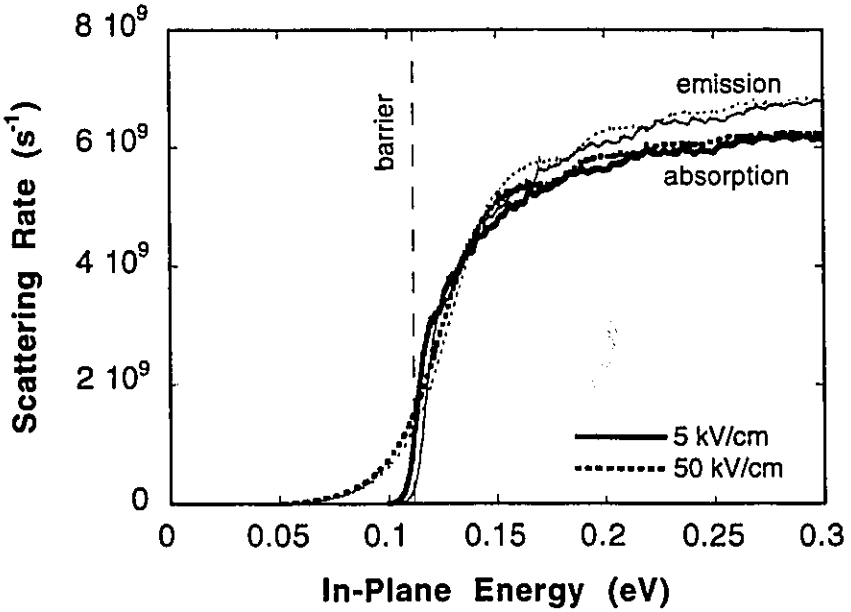

Fig. 4.11: The 2D-to-3D electron scattering rate via longitudinal acoustic phonon piezoelectric scattering for the 60 Å GaAs/AlGaAs testbed well. The solid curves give the low field (5 kV/cm) results while the dotted curves represent the high field (50 kV/cm) results. The heavier curves give the rates for phonon absorption while the lighter ones correspond to phonon emission. Note that the barrier energy given by the vertical dashed line is for zero field only; at 50 kV/cm, it would be shifted to lower energy by 15 meV.

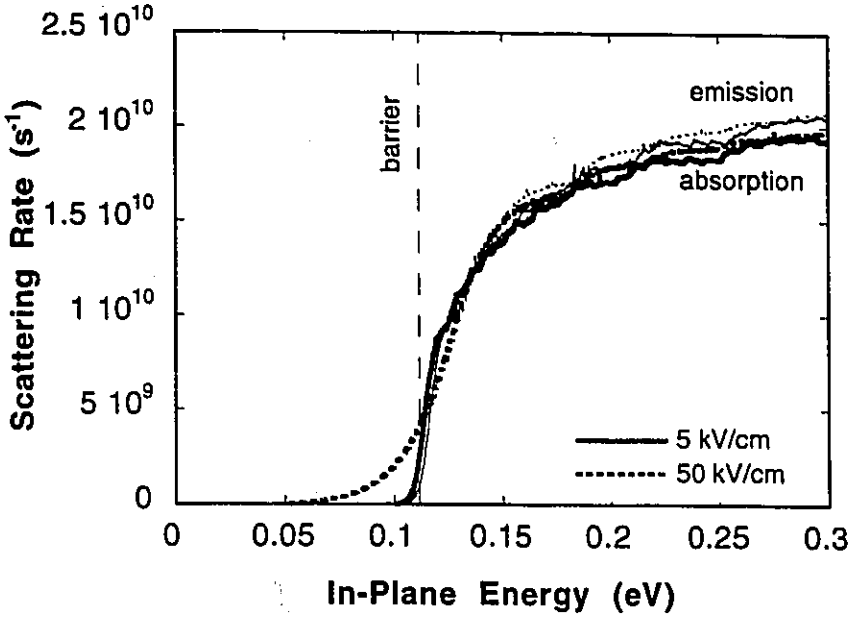

Fig. 4.12: The 2D-to-3D electron scattering rate via transverse acoustic phonon piezoelectric scattering for the 60 Å GaAs/AlGaAs testbed well. The solid curves give the low field (5 kV/cm) results while the dotted curves represent the high field (50 kV/cm) results. The heavier curves give the rates for phonon absorption while the lighter ones correspond to phonon emission. Note that the barrier energy given by the vertical dashed line is for zero field only; at 50 kV/cm, it would be shifted to lower energy by 15 meV.

4.7.6. 2D-to-3D scattering rates: summary.

Fig. 4.13 compares the scattering rates for each of the different processes, where longitudinal and transverse acoustic modes have been kept separate for the piezoelectric interaction. For simplicity, the emission and absorption rates have been combined so that there is a single curve for each scattering process. The phonon temperature is 300 K for all curves. It is apparent that polar optical phonons will dominate the 2D-to-3D scattering rate at room temperature. This was expected, due to the greater coupling constant for this process. LO phonon absorption will be further assisted by the effective reduction in the barrier height by the LO phonon energy, $\hbar\omega_0$, while for acoustic phonon processes this effect is negligible. To summarize Fig. 4.13, we can list the scattering processes in order of importance as follows: polar optical phonon, longitudinal acoustic phonon via the deformation potential, transverse acoustic phonon via piezoelectric coupling, and longitudinal acoustic phonon via piezoelectric coupling.

Fig. 4.14. depicts the same calculations as Fig. 4.13. but for a phonon temperature of 30 K. As a result of the reduced phonon occupation factors, all of the scattering rates

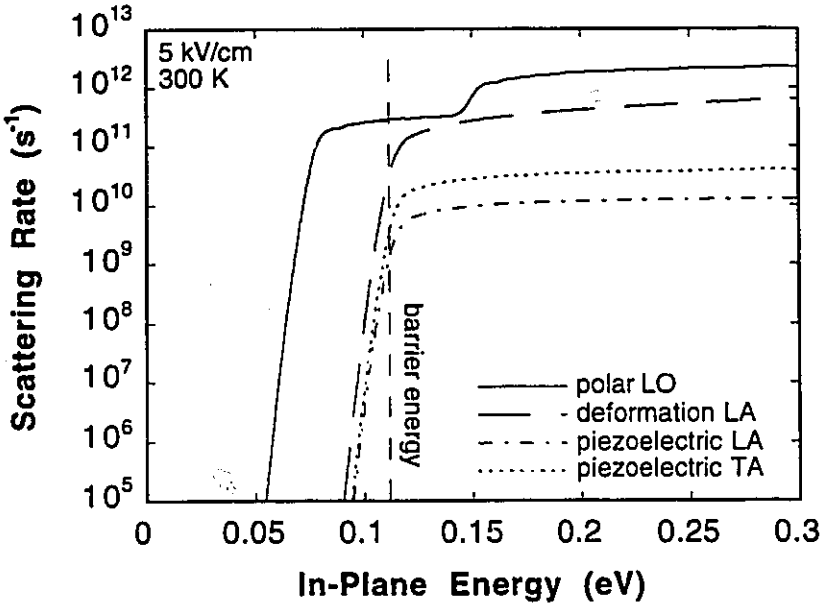

Fig. 4.13: The 2D-to-3D electron scattering rates given by each of the different phonon scattering mechanisms for the 60 Å GaAs/AlGaAs testbed well in a 5kV/cm electric field. The emission and absorption results have been combined for each curve. The phonons are characterized by a temperature of 300 K. Note that the barrier energy given by the vertical dashed line is for zero field only; at 50 kV/cm, it would be shifted to lower energy by 15 meV.

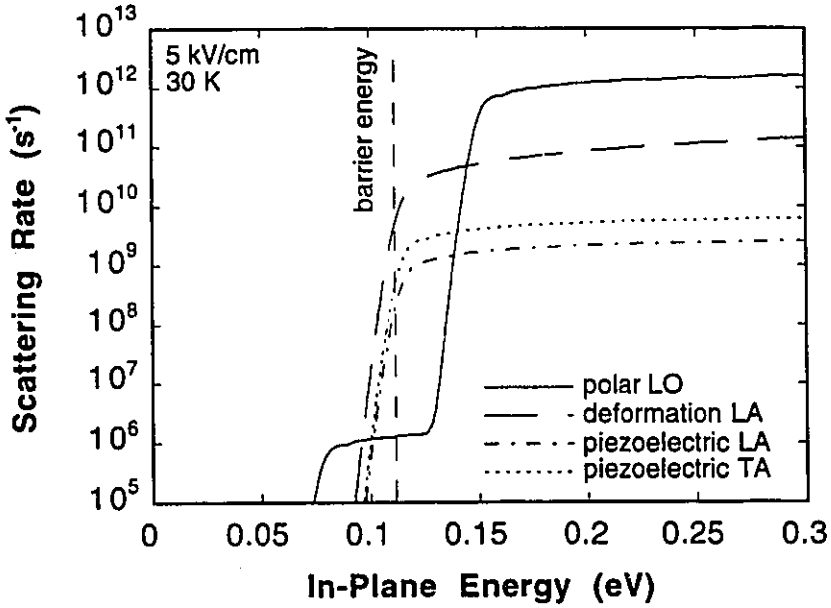

Fig. 4.14: The 2D-to-3D electron scattering rates given by each of the different phonon scattering mechanisms for the 60 Å GaAs/AlGaAs testbed well. The emission and absorption results have been combined for each curve. The phonons are characterized by a temperature of 30 K. Note that the barrier energy given by the vertical dashed line is for zero field only; at 50 kV/cm, it would be shifted to lower energy by 15 meV.

are inhibited at lower temperature. In particular, LO phonon absorption is decreased by 5 orders of magnitude due to the relatively large LO phonon energy. This was expected to essentially eliminate LO phonon absorption at low temperatures, however, this will turn out not to be the case.

4.7.7. Electron thermionic emission rates.

The scattering rates calculated in the previous section can be used to calculate the electron thermionic emission time according to Eq. (2.38). The total scattering rate, $1/\tau_s(E)$, is obtained by adding the curves for each of the different scattering mechanisms, including both emission and absorption. The emission times are plotted in Fig. 4.15 for several electric field strengths as a function of temperature. It is assumed that the electron and phonon gases are at the same temperature, with the electron distribution calculated according to Fermi-Dirac statistics, the phonon distribution according to Bose-Einstein statistics. An electron density of 10^{10} cm^{-2} is assumed throughout. The behaviour is as expected for a thermally activated process: fast at high temperatures, slower at lower temperatures. It is interesting to note that by room temperature, the thermionic emission

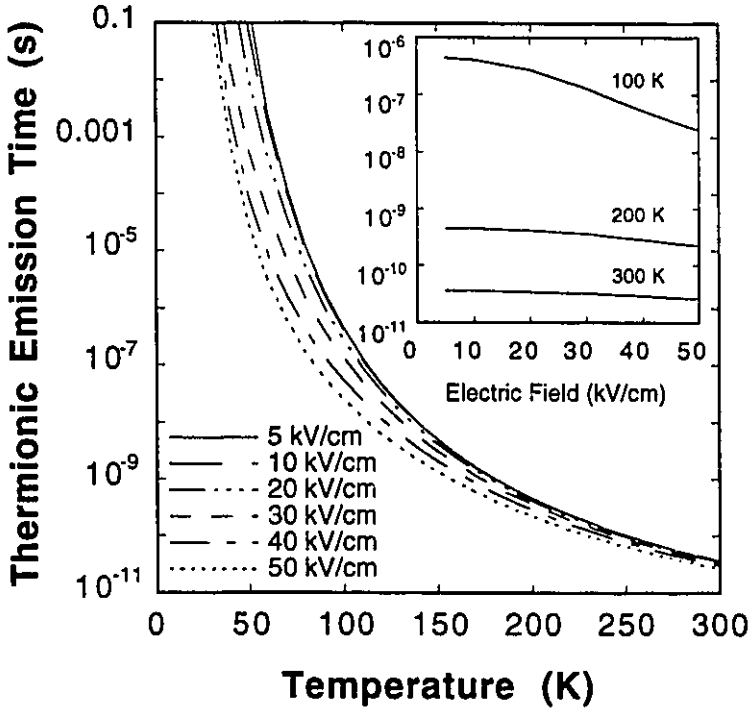

Fig. 4.15: Calculated thermionic emission times for the 60 Å GaAs/AlGaAs testbed well as a function of temperature and for several electric fields. The shorter escape times correspond to greater electric field strengths. The inset illustrates the increased field sensitivity at lower temperatures.

time is on the order of *30 picoseconds*, despite a barrier height that is more than four times k_BT. The separation between curves corresponding to different electric field strengths is a result of the smearing effect in the scattering functions. In the inset to Fig. 4.15, we see that the effect of the electric field increases at lower temperatures. At high temperatures, the electron distribution is more spread out so that the smeared portion of the scattering function makes up a smaller fraction of the accessible scattering events. This is illustrated schematically by Fig. 4.16 (a). At low temperatures, this region dominates the electron scattering, as shown in Fig. 4.16 (b), so that the effects of the electric field are enhanced.

To determine which of the scattering mechanisms governs the electron escape from the well, the contributions due to each of the different mechanisms are shown in Fig. 4.17. This reveals that *LO phonon absorption dominates at all temperatures*. This is despite the fact that at low temperatures the infinitesimal LO phonon density results in a very small absorption rate, as seen earlier in Fig. 4.14. However, since an electron can absorb an LO phonon once it is within $\hbar\omega_0$ from the top of the barrier, the potential barrier is effectively

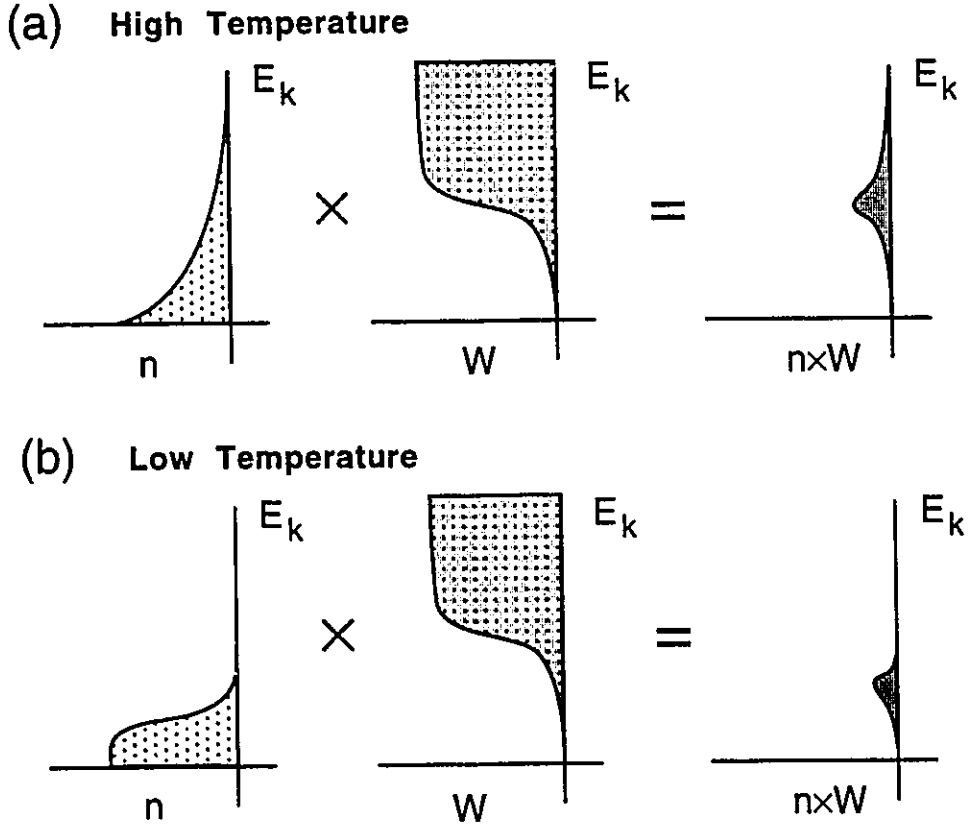

Fig. 4.16: Schematic illustration of the effect of smearing in the scattering function at (a) high temperature and (b) low temperature. At high temperature, the electron distribution extends well above the onset of the scattering function, while at low temperatures only the transition region contributes significantly to the scattering. As a result, the electric field has a greater impact on the emission rate at low temperatures.

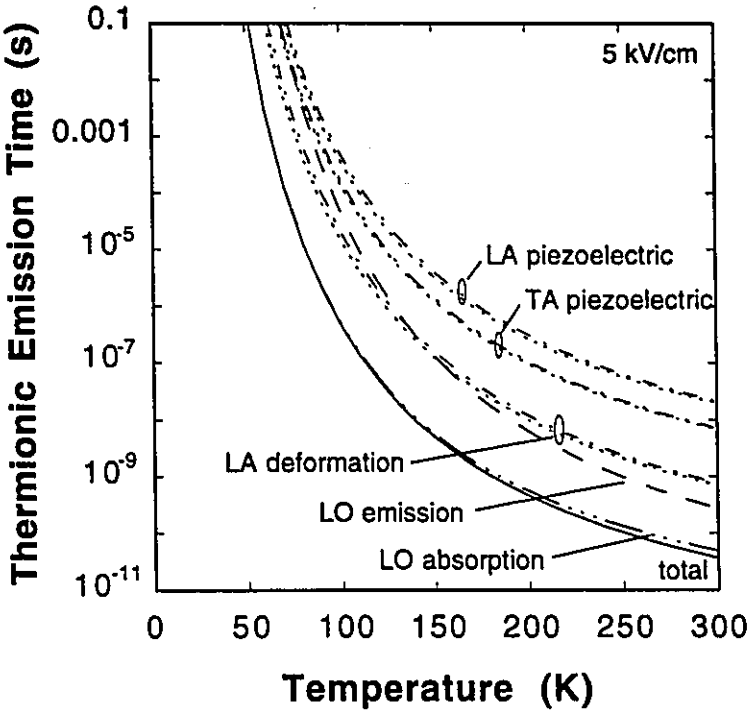

Fig. 4.17: Comparison of the emission times for the different scattering processes as a function of temperature. The solid curve is the total escape rate. LO phonon absorption dominates at all temperatures, while piezoelectric scattering is weakest.

lowered by an amount equal to $\hbar\omega_0$. In other words, although it costs 36 meV to excite an LO phonon to be available for absorption, 36 meV in electron energy is saved and the two effects cancel. To illustrate this effect, consider the simplification where both the electron and phonon occupation factors are given by Boltzmann distributions. Then the thermionic emission rate given by Eq. (2.39) can be written as

$$\frac{1}{\tau_{TE}} = \frac{e^{-\hbar\omega_0/k_BT}}{\tau_s'} e^{-(\Delta E-\hbar\omega_0)/k_BT} \tag{4.88}$$

where it has been adapted to the case where there is only a single confined state and τ'_s is the average electron-LO phonon scattering rate with the LO phonon occupation factor for absorption shown explicitly. It is apparent from Eq. (4.88) that the $\hbar\omega_0$ terms cancel leaving

$$\tau_{TE} = \tau_s' e^{-\Delta E/k_BT} \tag{4.89}$$

so that the effect of the phonon occupation is removed. Consequently, LO phonon absorption remains the dominant mechanism at low temperatures.

As demonstrated by Eq. (4.89), this will further simplify the approximate thermionic emission expression in Eq. (2.39), where originally the temperature dependence of the scattering time was hidden within $\tau_s(E)$. Obviously, $\tau_s(E)$ is *not* temperature independent, as illustrated by comparing Figures 4.13 and 4.14. However, this dependence is due entirely to the phonon occupation factor, which we now find cancels with the barrier lowering term in the electron occupation factor.

4.7.8. The effect of a transverse electric field.

As the scattering calculations were performed in the presence of a transverse electric field we can examine in some detail how it affects the scattering rate. As mentioned previously, we expected that the electric field would shift the scattering to lower energies in accordance with the linear barrier lowering term described in §2.5.2. However, this does not turn out to be the case. Instead, the scattering edge is smeared such that a tail extends below the barrier while the midpoint of the scattering edge remains fixed. For energies just above the barrier, the scattering is reduced relative to the low field case, then rises slowly so that away from the barrier energy, the magnitude of the scattering rate is unaffected by the electric field.

The low energy tail of the scattering rate indicates that substantial scattering is possible at energies below the barrier. This is the result of the penetration of the final state wavefunctions through the triangular tip of the barrier, as seen in Fig. 4.18. Meanwhile, the shape of the wavefunction does not change dramatically between 20 meV below the top of the barrier and 20 meV above, characterized primarily by a smooth increase in amplitude within the well region. As a result, the overlap function rises gradually, starting below the potential barrier energy. This is in stark contrast to the abrupt rise at the top of the barrier expected classically which has generally been applied to quantum well systems (Schneider, 1988), (Moss, 1994).

The preceding result also allows us to speculate on the significance of image charge lowering. This effect has been omitted from these calculations since it would involve solving for the wavefunctions in the potentials derived in the previous chapter, which varied with the carrier density. Considering that these are non-analytic potentials that would break the 2D symmetry of the problem, this would constitute a formidable problem. Nonetheless, we can speculate on how the scattering rate and hence the emission rate

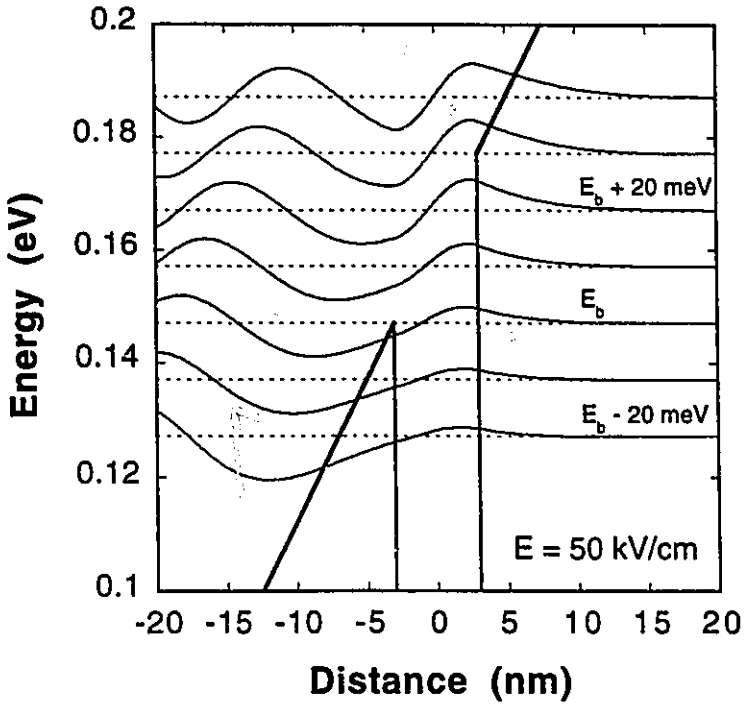

Fig. 4.18: Final state wavefunctions near the top of the barrier for the 60 Å GaAs/AlGaAs testbed well in a 50 kV/cm electric field. For energies even 20 meV below the barrier energy, the wavefunction easily penetrates into the well region. Within the well region, the wavefunction amplitude varies slowly over this energy range, resulting in a smeared scattering function in contrast with the abrupt transition expected classically.

would be affected. The image potential will in general round off the top of the triangular barrier. As seen in Fig. 4.18, at energies 20 meV below the tip of the potential barrier, the wavefunction penetrates into the well with a ~50-75% reduction in amplitude relative to energies just above the barrier. In comparison, even if we assume the perfect conductor solution, at the same field strength of 50 kV/cm the image charge lowering would be 26 meV. While this will produce a similar increase in wavefunction amplitude within the well, it will not result in the dramatic increases in scattering rate expected from the classical picture. As a result, the effects of image charge lowering will be weakened, affecting primarily the low energy tail of the scattering function. This is in addition to the reductions in image charge lowering described in the previous chapter. At high temperatures, where the details of the low energy tail have less of an impact on the thermionic emission time, the effect of image charge lowering will be small. At low temperatures, it should have a more significant effect, particularly at high carrier densities. In either case, its impact will be reduced relative to that expected from conventional calculations of the thermionic emission time (eg.: Schneider (1988), Moss (1994)). Further calculations are required to obtain a

more quantitative estimate of the effects of image charge lowering on the thermionic emission time.

4.7.9. Simplified calculations of the electron thermionic emission rate.

For designers who require thermionic emission times to predict the performance of their devices, the procedure presented in the preceding sections is far too involved. However, as was outlined in §2.4, an analytic expression is derivable in the situation where the scattering function can be approximated as a constant, independent of the in-plane energy, with an effective barrier height, i.e.: a step function. We will find that this approximation is frequently degraded by sloping or roundness in the scattering function. As a result, a more complex approximation will also be considered where the scattering rate is fitted to a Fermi-Dirac function. While this form is more successful at reproducing the results of the full calculation, it requires two extra parameters and cannot be integrated analytically. It is hoped that these approximate forms will provide the framework for developing a simple system for calculating the scattering-based thermionic emission time. This would require mapping the dependence of the fitting parameters on the well characteristics. Once this has been accomplished, the thermionic emission time for any arbitrary structure could be calculated using the appropriate parameter values and either the step-function or Fermi-Dirac approximations for the scattering function, thus by-passing the complex calculations presented earlier in this chapter. While the dependence of the fitting parameters on the well configuration will be briefly investigated in §4.7.10-4.7.12, the complete characterization will be left to future work.

Since the total scattering rate is dominated by polar optical phonon scattering, all other phonon scattering processes are omitted. LO phonon emission adds the term

$$\frac{1}{\tau_{TE}} = \frac{1+e^{-\hbar\omega_0/k_BT}}{\tau'_{s,emm}} e^{-(\Delta E+\hbar\omega_0)/k_BT} \tag{4.90}$$

to Eq. (4.89), where the 1 enters to include spontaneous emission. This gives for the total thermionic emission time

$$\begin{aligned}\frac{1}{\tau_{TE}} &= \frac{1}{\tau'_{s,\,abs}} e^{-(\Delta E/k_BT)} + \frac{1+e^{-\hbar\omega_0/k_BT}}{\tau'_{s,emm}} e^{-(\Delta E+\hbar\omega_0)/k_BT} \\ &= \left[\frac{1}{\tau'_{s,abs}} + \frac{1}{\tau'_{s,emm}} e^{-\hbar\omega_0/k_BT} + \frac{1}{\tau'_{s,emm}} e^{-2\hbar\omega_0/k_BT}\right] e^{-(\Delta E/k_BT)}\end{aligned} \tag{4.91}$$

where *emm* and *abs* refer to phonon emission and absorption respectively and the primes indicate that the scattering times do not include the phonon occupation factors.

We are now faced with the task of determining the average scattering times and the effective barrier heights[1]. Since the scattering curves do not have abrupt onsets, but instead feature gradual transitions characterized by widths that increase with the electric field, it is not obvious how to calculate the average. In particular, it is not clear where to begin averaging. In Fig. 4.19 the LO phonon absorption scattering functions for the standard testbed well are shown for (a) low and (b) high field. The straight lines represent the step-function approximations calculated where the low energy cutoffs to the averaging were set to 1% (light) and 25% (heavy) of the maximum scattering rate. That is, the averaging was performed over energies where the scattering function was greater than 1% (or 25%) of the

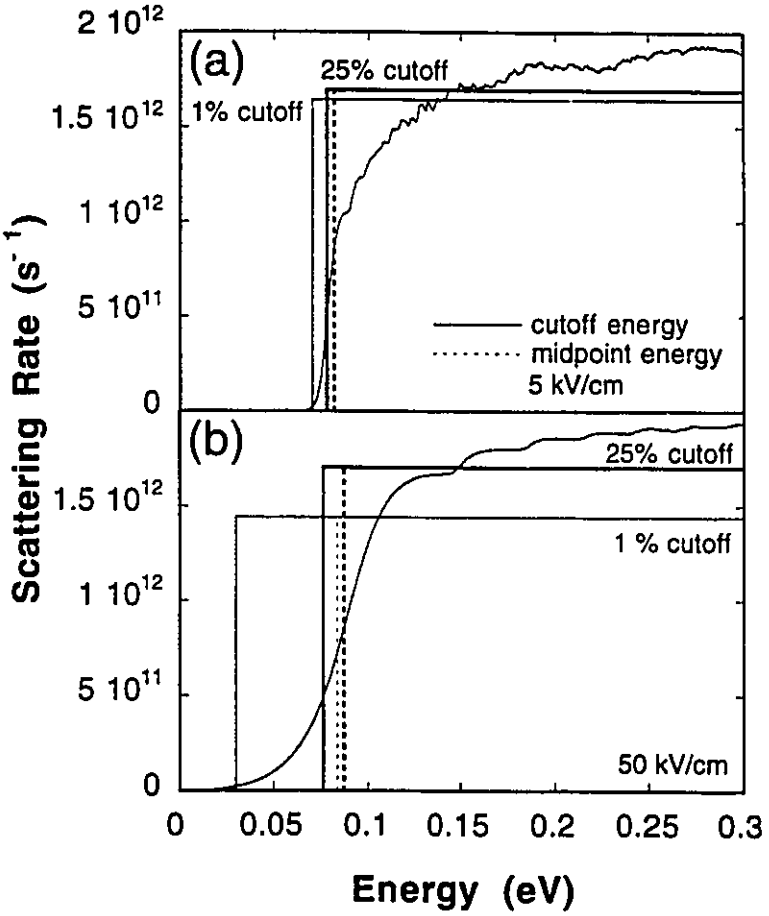

Fig. 4.19: Illustration of the calculated average scattering times for cutoffs of 1% (light) and 25% (heavy) for electric fields of (a) 5 kV/cm and (b) 50 kV/cm. The solid lines mark the cutoff energies and the dotted lines the midpoint energies. The differences between the 1% and 25% values increase at higher field.

[1]Note that the *effective barrier height* is determined from the onset of the 2D-to-3D scattering function, while the *potential barrier height* is the height of barrier potential relative to the subband minimum.

maximum value of the scattering function, within the energy range considered (0-300 meV). This point will be referred to as the *low energy cutoff*. At the lower field, there is only a slight difference between the two step functions. However, at 50 kV/cm, there is a 47 meV difference in the cutoff energy and the average scattering rate rises by 21% from 1.4E12 to 1.7E12 s^{-1}. The disparity between the two results is due to the low energy tail in the high field scattering function and reflects how poorly the step function applies in this regime.

Also shown in the figure are the *midpoint* lines (dotted) indicating where the scattering function is equal to half the average value. Interestingly, it is only marginally affected by the choice of cutoff criteria. As seen in Fig. 4.20 (a), the midpoint value is also roughly independent of the electric field. This observation supports the earlier appraisal

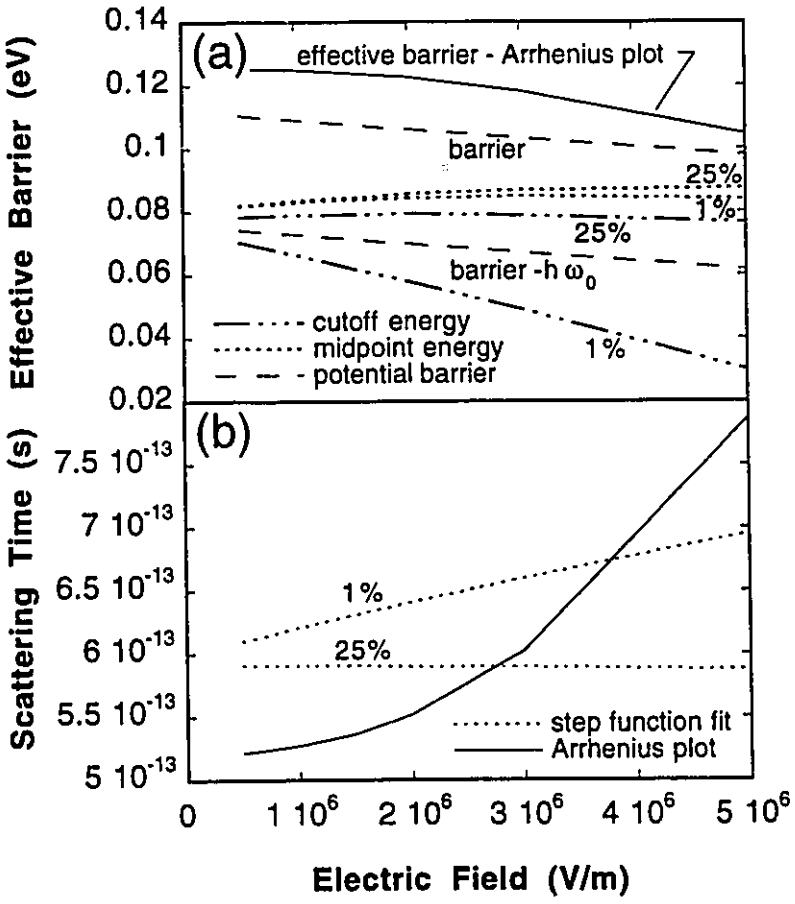

Fig. 4.20: (a) Cutoff (dash-dotted) and midpoint (dotted) energies for 1% and 25% criteria and effective barrier heights obtained from Arrhenius plots (solid) of the calculated thermionic emission rates as a function of the electric field. The short dashes give the barrier height and the barrier height minus the phonon energy for comparison. While the 1% cutoff energy shows a strong bias dependence, the midpoint energy is essentially unaffected. (b) The average scattering rates obtained from the step-function fit (dotted) and from the Arrhenius plots (solid). Neither cutoff criteria accurately reproduces the Arrhenius results.

that the scattering function does not shift to lower energies with the electric field. Meanwhile, the cutoff energy does exhibit a strong bias dependence which reflects the smearing of the scattering function edge. In Fig. 4.20 (b), the average scattering rates obtained from the 1% and 25% analyses are shown by the dotted curves. While the expected field-independent behaviour is observed in the 25% cutoff data, it is not seen in the 1% case where a greater percentage of the smeared region is included in the average.

If we consider only LO phonon absorption, then in the case where there is only a single confined state the simplified Eq. (2.39) reduces to Eq. (4.89). The parameters τ' and ΔE_{eff} can then be obtained from an Arrhenius plot, as demonstrated in Fig. 4.21. While the plots are linear at low fields, at higher fields, some curvature is evident, reflecting the degradation of the fit to the step-function approximation. The results of the Arrhenius plots are given by the solid curves in Fig. 4.20. The linear behaviour expected in the effective barrier height is not observed, nor is the average scattering time independent

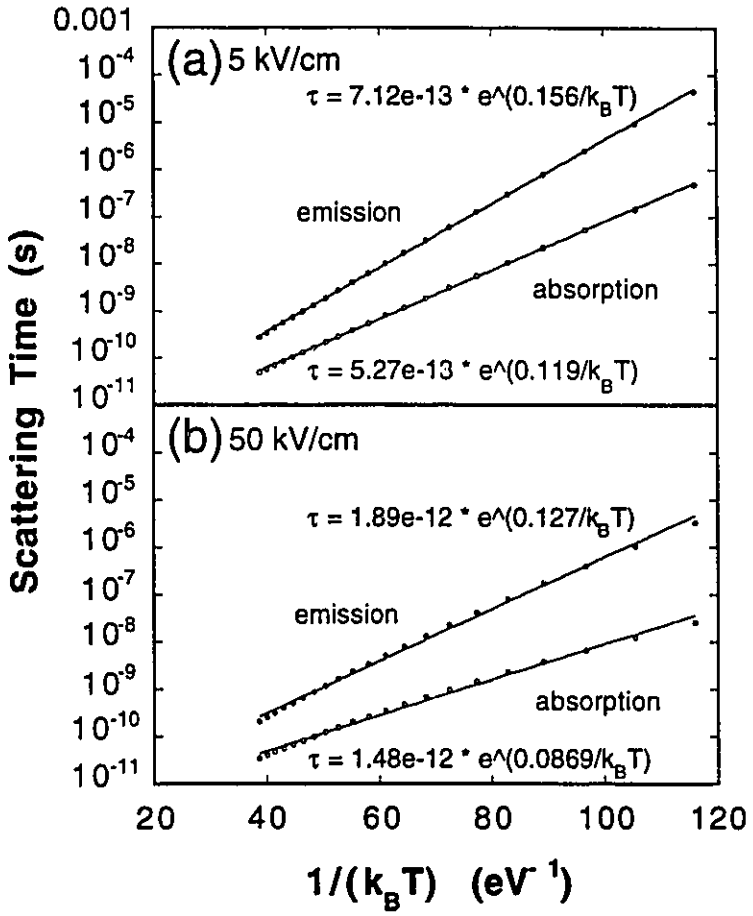

Fig. 4.21: Arrhenius plots of the calculated thermionic emission times from the 60 Å GaAs/AlGaAs testbed well for electric fields of (a) 5 kV/cm and (b) 50 kV/cm. The data is linear over the full temperature range in the low field case but displays some curvature at 50 kV/cm.

of the field. Note that as predicted by Eq. (4.89), the barrier height obtained from the Arrhenius plot is not $E_b - \hbar\omega_0$, but $\sim E_b$.

Obviously, the step-function approximation is rather poor in the presence of an electric field. A better fit is obtained with a Fermi-Dirac-type function,

$$W(E_k) = \frac{W_o}{1 + \exp\left(\frac{E_b - E_k}{\delta E}\right)} \tag{4.92}$$

as shown in Fig. 4.22. In this case, there is good agreement both at low fields, as in Fig. 4.22 (a), and high fields, shown in Fig. 4.22 (b). Fig. 4.23 shows the behaviour of the fitting parameters, W_o, E_b, and δE as a function of the electric field. Both the average scattering rate, W_o, and the barrier energy E_b (the equivalent to the Fermi energy in Eq. (4.92)), are roughly independent of the field. The only field dependence enters

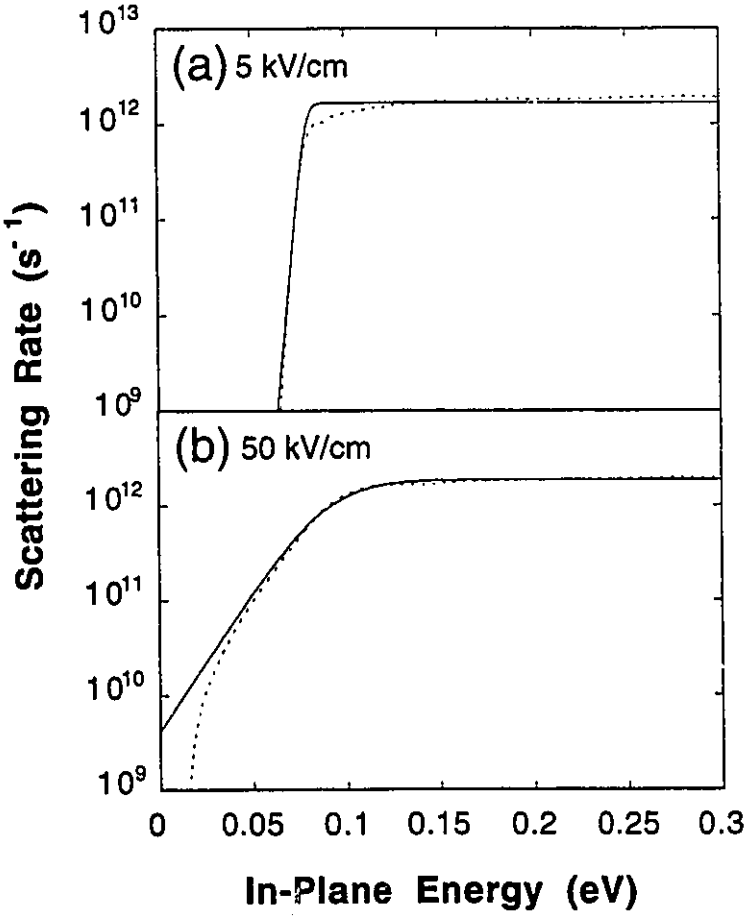

Fig. 4.22: Fermi-Dirac fit to the LO phonon absorption scattering function for the 60 Å GaAs/AlGaAs testbed well in a (a) 5 kV/cm and (b) 50 kV/cm electric field. The fit improves at higher field however there is a low energy cutoff in the scattering function that is not reproduced by the Fermi-Dirac function.

through the transition width, δE (the equivalent to the thermal energy). The transition width varies linearly with the electric field as demonstrated by the fitted lines in Fig. 4.23, and there is little difference between the emission and absorption parameters.

We now have two approximations to consider in trying to recreate the results of the full calculation of the thermionic emission rate. The first is the step-function approximation. The most desirable approach would express the entire field dependence in the barrier height. The obvious choice for the average scattering time is then the average value obtained from the 25% criteria. Choosing an effective barrier height is more difficult. We know that the emission rate should increase with increasing field so that the barrier height must decrease with the field. This rules out both midpoint curves and the cutoff

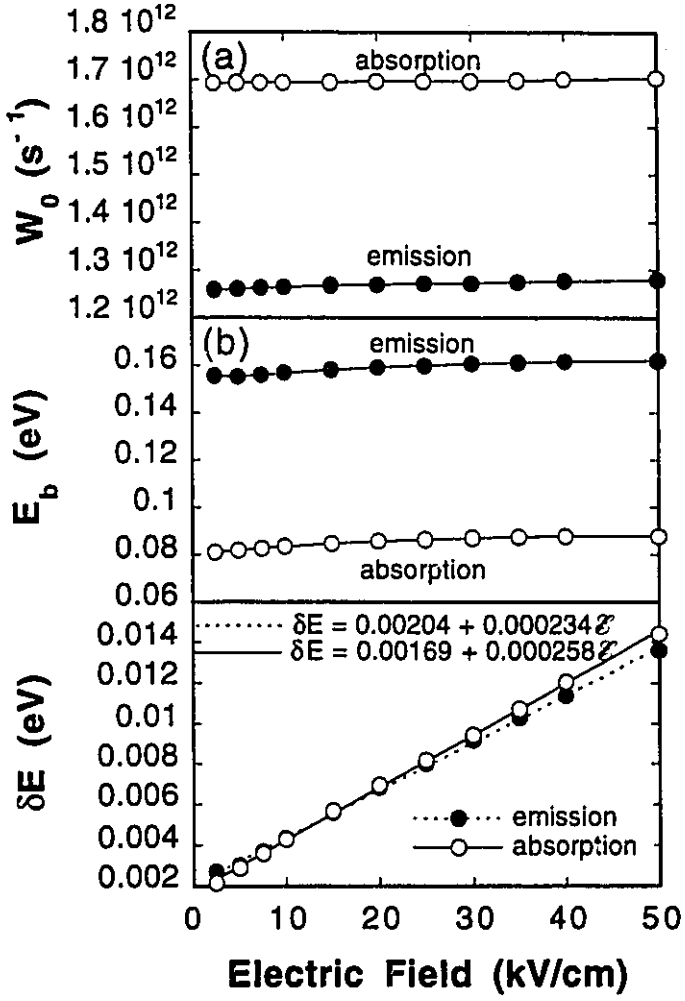

Fig. 4.23: The fitting parameters for the scattering function: (a) W_o, (b) E_b, and (c) δE versus the electric field, where the filled circles represent emission and the open circles absorption. While both the average scattering rate, W_o, and the barrier energy E_b are roughly independent of the field, the transition width, δE varies linearly with the field, as shown by the fitted lines.

energy according to the 25% criteria. It turns out that the 1% low energy cutoff decreases too strongly with the electric field, leaving only the actual potential barrier as a reasonable estimate of the effective barrier height. The field dependence is included by the linear term due to the well inclination as given by Eq. (2.42) to give the dashed curves in Fig. 4.24. Surprisingly, for small fields the agreement is reasonable, particularly near room temperature where the difference is less than 10%. At higher fields, the differences increase substantially. In both cases, the agreement can be improved by averaging the emission and absorption E_b values and substituting it for the zero field effective barrier height. This accounts for the fact that the scattering does not begin abruptly at the barrier edge, so that the effective barrier is ~10 meV higher than the potential barrier. The linear

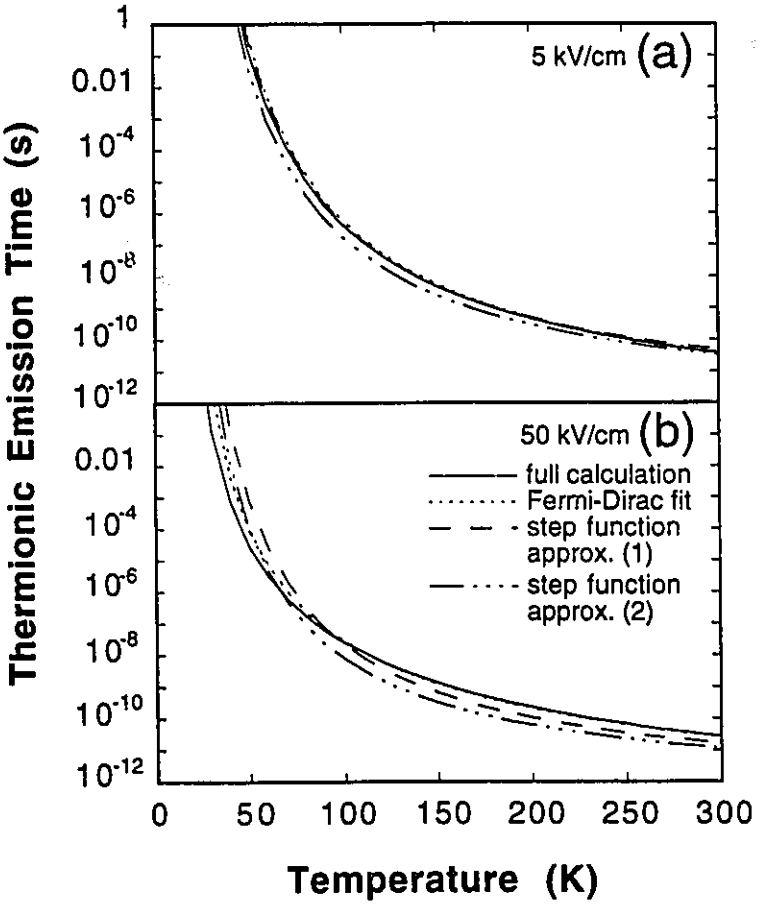

Fig. 4.24: Comparison of the electronic thermionic emission times calculated using the full scattering treatment (solid), the Fermi-Dirac fit (dotted), and the step-function approximation (dashed and dash-dotted) at (a) 5 kV/cm and (b) 50 kV/cm. The two curves for the step function approximation correspond to (1) estimating the effective barrier height as the average of the E_b values obtained for the LO phonon emission and absorption curves and (2) the height of the potential barrier. Both at low and high fields, the average E_b value gives better agreement. At low fields, there is good agreement for both the Fermi-Dirac and step-function approximations, particularly near room temperature where the difference is less than 10%. At higher fields, however, the step-function approximation breaks down.

barrier lowering term is included as before to give the dash-dotted curves in Fig. 4.24. As noted earlier, the edge of the scattering function does not shift to lower energies with increasing fields, but instead broadens, producing a low energy tail. As a result, the linear term overestimates the effect of the electric field, as seen in Fig. 4.25. The error is more pronounced at higher temperatures, where the low energy tail in the scattering function has less of an impact on the full calculation.

Using the Fermi-Dirac fits to the scattering functions we are forced to numerically integrate Eq. (2.39). Since the average scattering rate, W_0, and the barrier energy, E_b, are roughly independent of the electric field, we can use fixed average values for all fields. The transition width, δE, varies linearly with the field, so that with two parameters, i.e.: the slope and the intercept, we can reproduce the field dependence of the scattering function. In summary, the entire scattering function can be reproduced at any field using four parameters. The phonon occupation factors can be removed as in Eq. (4.91) if the barrier energies, E_b, are shifted appropriately. However, since this calculation requires a numerical integration anyways, it is just as easy to explicitly include the phonon occupation. The results are shown by the dotted curves in Figs. 4.24 and 4.25. It is

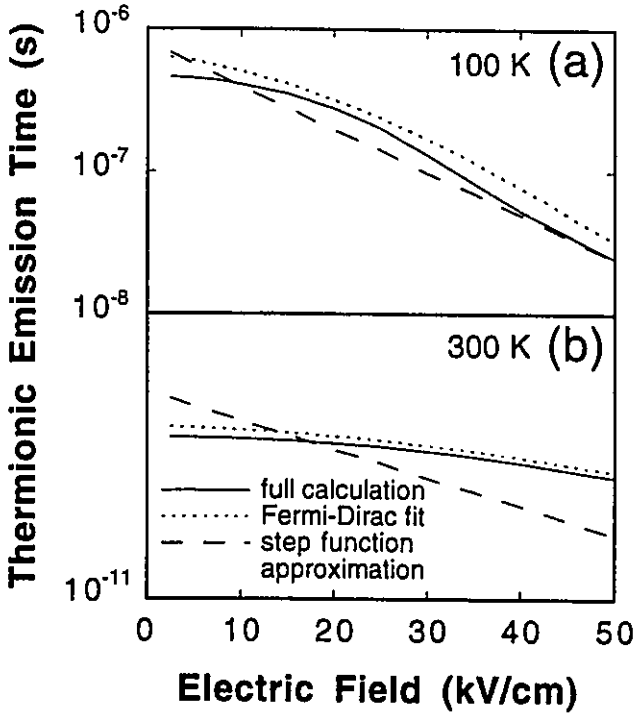

Fig. 4.25: Comparison of the electronic thermionic emission times calculated using the full scattering treatment (solid), the Fermi-Dirac fit (dotted), and the step-function approximation (dashed) at (a) 100 K and (b) 300 K. Although both approximations give reasonable agreement with the full calculation at low temperatures, the room temperature plot reveals that the linear barrier lowering term in the simple expression overestimates the effect of the electric field.

immediately apparent that this approximation for the scattering function is much better over the full range of electric fields and temperatures. The difference is in most regimes less than 5%. Of course, there is a higher cost for this accuracy in terms of the complexity of the calculation and the number of parameters.

To summarize this section, simplified calculations of the thermionic emission rate based on step-function and Fermi-Dirac approximations for the scattering function have been compared. The purpose of these approximate forms is to provide a framework for the development of a parameterization scheme that would allow quick calculations of the thermionic emission times without requiring the full scattering calculation outlined in §4.3-4.6. Despite the fact that the step function is a poor approximation at high fields, and that the linear barrier lowering was used to imitate the effects of the low energy tail of the scattering function, this approximation yielded reasonable results. It would be suitable for quick estimates of escape times at room temperature. For good agreement over the full temperature and bias range, the parameterized Fermi-Dirac fit should be employed. In this case, the difference from the full calculation is less than 5% under almost all conditions. Unfortunately, this approach suffers from the increased complexity of a numerical integration, and requires four parameters instead of two. Nonetheless, it represents a significant reduction in complexity relative to the full calculation.

4.7.10. Well width dependence.

The preceding calculations dealt exclusively with a 60 Å $GaAs/Al_{0.2}Ga_{0.8}As$ quantum well. By changing the width of the well, the initial and final states will both be altered, thereby influencing the scattering and thermionic emission rates. In this section, the variation of the scattering rate with the well width will be briefly explored. Since it was shown in the previous section that the scattering rate is dominated by LO phonon emission and absorption, only these processes will be included.

Fig. 4.26. shows the LO phonon absorption rates for $GaAs/Al_{0.20}Ga_{0.80}As$ wells with widths of 50 Å, 55 Å, 60 Å, and 65 Å. For narrower widths, the bulk phonon approximation begins to break down (Rücker, 1992) and for wider wells, higher energy confined states appear, introducing complications which will be dealt with separately. The first thing to notice in the figure is that for the narrowest well the scattering function is quite rounded, but becomes increasingly abrupt as the width increases. This reflects the proximity of a continuum resonance near the top of the well. In fact, at 65 Å, there is a second loosely confined state in the well. For the narrower widths this resonance moves

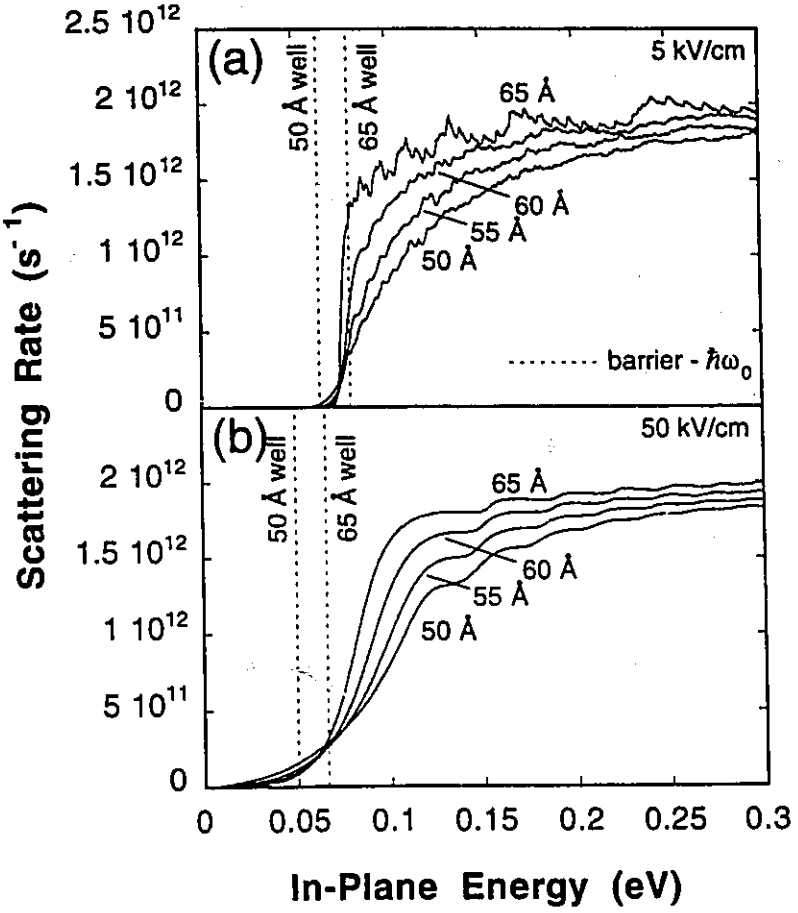

Fig. 4.26: LO phonon absorption rates for GaAs/$Al_{0.20}Ga_{0.80}As$ wells with widths of 50 Å, 55 Å, 60 Å, and 65 Å in electric fields of (a) 5 kV/cm and (b) 50 kV/cm. The vertical dotted lines indicate the potential barrier heights for the narrowest (50 Å) and widest (65 Å) wells. At a well width of 65 Å, a second quasi-bound state just appears at the barrier energy, resulting in the sharp rising edge in the scattering rate. As the well width decreases, the influence of this resonance moves to higher energies so that the edge of the scattering function becomes more rounded. Note also that at higher energies the scattering rates converge.

further into the continuum, as demonstrated by the confinement ratio plotted in Fig. 4.27.

As a consequence of the differences at the edge of the scattering function, the effective barrier height does not really shift with the well width as expected; since the confined state energy drops as the well widens, the potential barrier height increases with the well width. This is shown by the dotted vertical lines in Fig. 4.26, revealing a shift of more than 15 meV between the widest and narrowest wells. However, as we will see, the effective barrier *decreases* with the well width. This, in combination with the increased magnitude of the scattering function, will result in shorter room temperature thermionic emission times for the wider wells despite the greater barrier height. As we will see in considering multi-subband wells, the same effect will lead to an oscillatory emission rate as

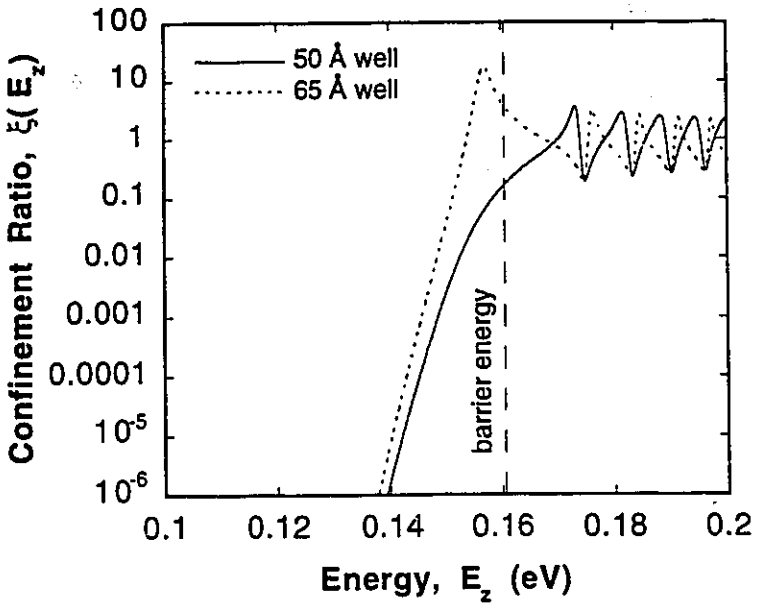

Fig. 4.27: Confinement ratio near the barrier energy for the 50 Å (solid) and 65 Å (dotted) quantum wells. The wider well has a resonance just below the barrier energy, while for the narrower well, the next resonance is ~12 meV above the barrier energy. This produces a more rounded rising edge in the scattering function for the narrower well, as seen in Fig. 4.26.

a function of the well width.

The scattering curves were fitted to Fermi-Dirac functions as before and can be characterized by the four parameters E_b, W_0, and the intercept and slope of the δE vs. $\mathscr{E}$ dependence, δE_0 and $d(\delta E)/d\mathscr{E}$. These are presented in Fig. 4.28. The average scattering rates, W_0, shown in Fig. 4.28 (a) increase linearly with the well width for both emission and absorption. The slopes of the fitted lines shown in the figure are nearly identical at 2.1×10^{10} and 1.9×10^{10} s^{-1} $Å^{-1}$ for absorption and emission respectively. The linear dependence on the well width can be attributed to the enhanced contribution of the low-lying continuum resonance. The phonon wavevectors involved will also change slightly as the energy scales shift due to the drop in the subband energy, however this will have a minor effect.

The behaviour of the effective barrier height, E_b, as a function of the well width is displayed in Fig. 4.28 (b) by the filled circles. The potential barrier height is shown by the open circles. The effective barrier height is actually larger for the *narrower* wells due to the slow onset of the scattering function. It coincides with the potential barrier height only when a resonance is present at the top of the well to produce a sharp rising edge in the scattering function. In general, the effective barrier height is greater than the potential barrier.

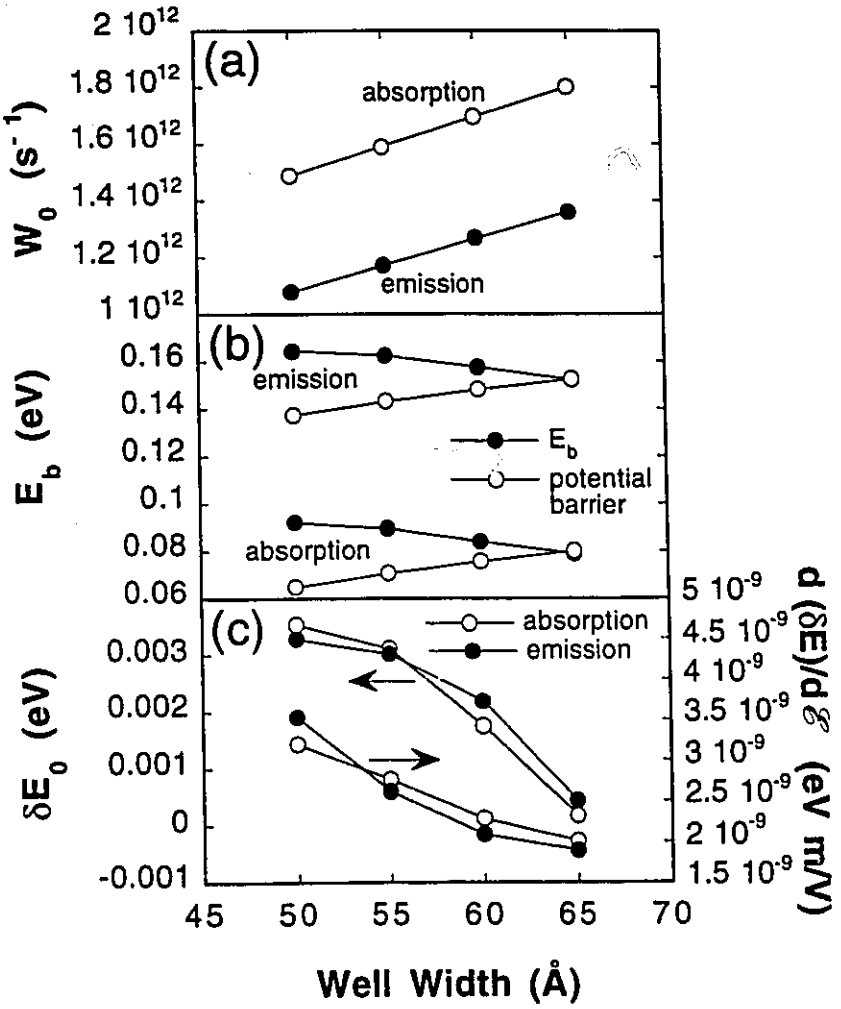

Fig. 4.28: The (a) average scattering rate, W_0, (b) effective barrier height, E_b, and (c) field dependence parameters of the transition width, δE, obtained from Fermi-Dirac fits to the scattering function. The effective barrier heights actually decrease while the potential barriers increase with the well width. The average scattering rates increase linearly with the well width, with slopes of 2.1×10^{10} and 1.9×10^{10} s^{-1}Å^{-1} for absorption and emission respectively. The fit parameters for the transition width decrease with the well width reflecting the rounding of the scattering function edge as the first continuum resonance rises further above the well. The emission and absorption curve exhibit nearly identical behaviours.

Linear fits to the transition width, δE, were performed to give the slope and intercept parameters shown in Fig. 4.28 (c). As observed for the testbed well, there is little difference between the emission and absorption values. Both the slope and the intercept decreased for increasing well width, reflecting the increasing sharpness in the onset seen in Fig. 4.26.

In Fig. 4.29 the low field (5 kV/cm) thermionic emission times calculated for the four widths are compared. As stated earlier, the shortest times are generated by the widest

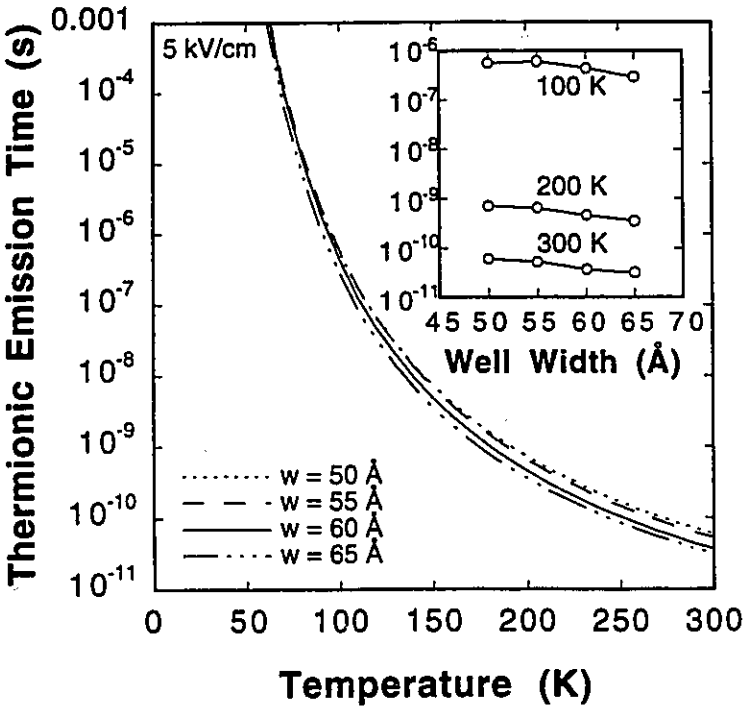

Fig. 4.29: Thermionic emission times calculated for GaAs/$Al_{0.20}Ga_{0.80}As$ wells with 50 Å, 55 Å, 60 Å, and 65 Å widths at a field strength of 5 kV/cm. The inset shows the emission times versus well width for temperatures of 100 K, 200 K, and 300 K. Despite the fact that the narrower wells have lower potential barriers, the shortest emission times are obtained from the widest well.

wells where the resonance is closest to the top of the well, although the differences between structures are small. Similar to the behaviour seen in the bias dependent curves for the 60 Å testbed well, the differences increase at lower temperature where the details of the onset of the scattering function become more important.

This is an interesting result. Conventional calculations of the thermionic emission times (Schneider, 1988), (Moss, 1994) would produce values that increase with increasing well width as a result of the higher potential barriers. However, the assumptions that the basic communication between the well and continuum states is unaffected by the well width, or that the effective barrier height is equal to the potential barrier height, are inaccurate. As a result, the detailed calculations give a well width dependence that is in direct contradiction with the conventional or classical theories.

The situation is different at higher fields, as shown in Fig. 4.30, where the thermionic emission times at a field strength of 50 kV/cm are compared. Now at low temperatures, the order is reversed with the narrowest well having the shortest escape time. At room temperature, the widest well is still the fastest, as at low fields. The difference

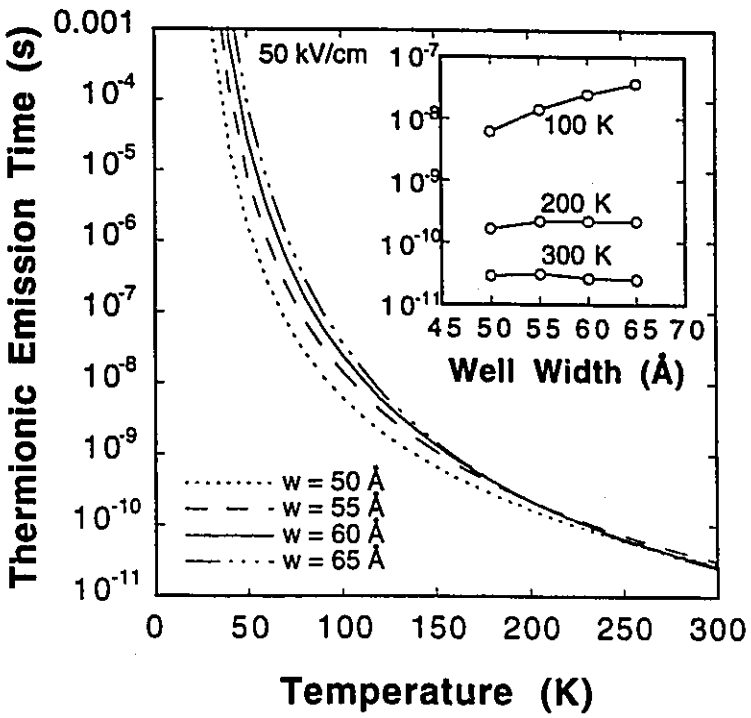

Fig. 4.30: Thermionic emission times calculated for GaAs/$Al_{0.20}Ga_{0.80}As$ wells with 50 Å, 55 Å, 60 Å, and 65 Å widths at a field strength of 50 kV/cm. The inset shows the emission times versus well width for temperatures of 100 K, 200 K, and 300 K. At low temperatures, the narrowest wells produce the shortest emission times as a result of the low energy tail in the scattering function extending to lower energies.

between the low and high field behaviour can be attributed to the low energy tail arising from the penetration of the final state wave function through the barrier potential. Although the edge of the scattering function remains sharper and the scattering rate generally higher in the wider well, the low energy tail extends to lower energies in the narrower well. Since at low temperatures the electron distribution is less spread out, the low energy tail dominates the emission rate and so the narrow wells have faster emission times.

Fig. 4.31 compares the thermionic emission times for the narrow 50 Å well calculated using the Fermi-Dirac function (dotted) and the step-function (dashed) approximations with the full calculation (solid). It is immediately apparent that the step-function approximation is not appropriate in this case. The Fermi-Dirac function provides much better agreement, although it worsens at the lower field strength due to the more rounded scattering function. As shown in Fig. 4.32 (a), the Fermi-Dirac function is unable to reproduce the full curve at 5 kV/cm but performs much better at 50 kV/cm, as seen in Fig. 4.32 (b). The roundness of the scattering function is also the cause of the large discrepancy in the step-function approximation at all fields. At high fields, there is

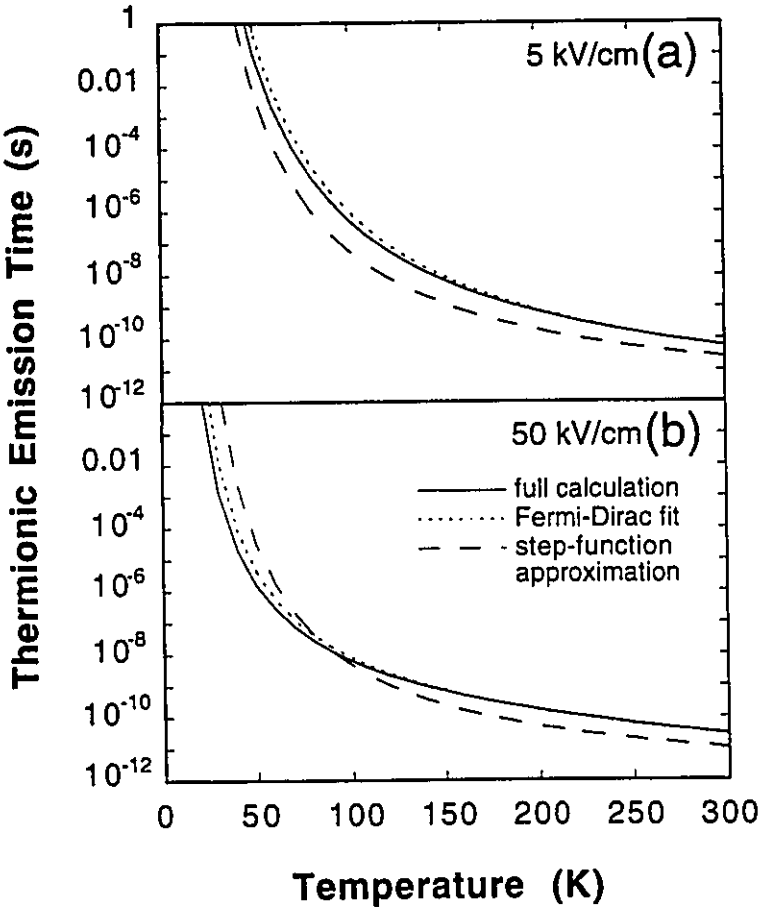

Fig. 4.31: Thermionic emission times for the 50 Å $GaAs/Al_{0.2}Ga_{0.8}As$ well calculated according to the step function (dashed) and Fermi-Dirac function (dotted) approximations compared with the full calculations (solid) for electric fields of (a) 5 kV/cm and (b) 50 kV/cm. While the Fermi-Dirac function gives good agreement at both low and high fields, the step-function approximation performs poorly in both cases. This reflects the poor fit to the step-function due to the roundness of scattering function.

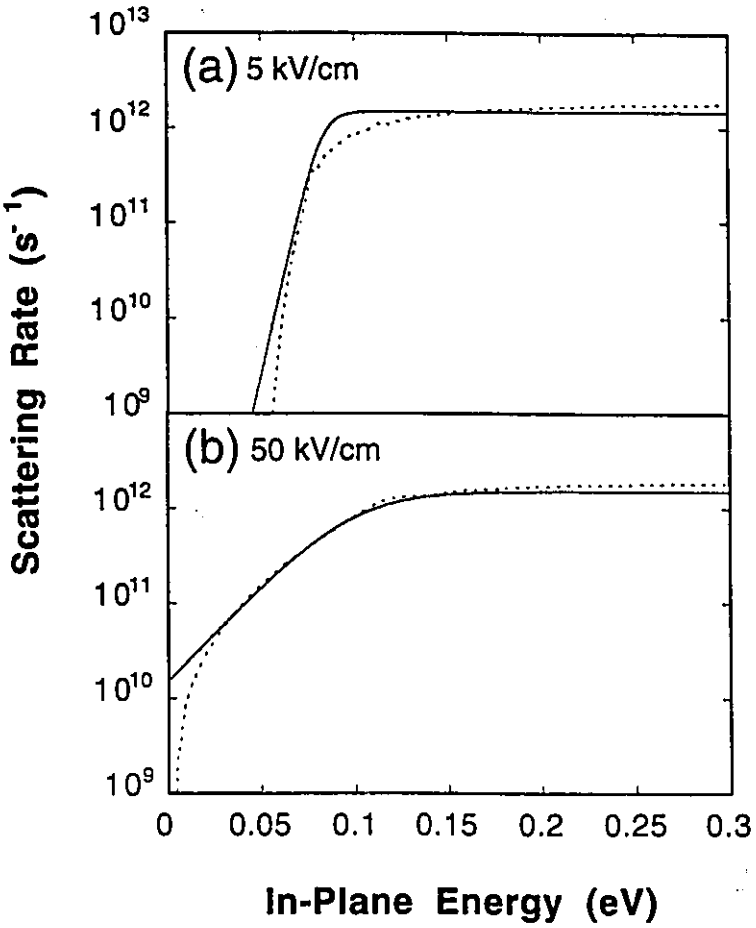

Fig. 4.32: Fermi-Dirac function fits to the LO-phonon scattering functions for the 50 Å GaAs/AlGaAs well for electric fields of (a) 5 kV/cm and (b) 50 kV/cm. The agreement is poor at low biases due to rounding of the scattering function's rising edge. This results in larger discrepancies between the Fermi-Dirac function approximation and the full calculation of the thermionic emission time at low fields.

additional broadening of the transition width leading to even greater differences relative to the full calculation. We can conclude from Figs. 4.24, 4.25 and 4.31 that both the step-function and Fermi-Dirac approximations are more accurate when there is a resonance near the top of the well.

4.7.11. Barrier height dependence.

As seen in the previous section, changing the well width has a significant effect on the scattering function, particularly at the onset of scattering. The sharply rising edge seen in the wider wells was attributed to the presence of a resonance at the top of the well. Similar conditions can be obtained by varying the depth of the well while keeping the width

constant. This is accomplished by varying the Al content in the barriers, while leaving the GaAs well layer unchanged. In this section, the effects of varying the well depth on the scattering rate will be investigated. As before, only LO phonon scattering will be considered.

Fig. 4.33 shows the scattering functions for Al mole concentrations in the barriers of 14%, 16%, 18%, and 20% for electric field strengths of (a) 5 kV/cm and (b) 50 kV/cm. The well thickness is kept constant at 60 Å. In contrast to the dependence on well width, there is a significant energy shift in the scattering function as the barrier height is reduced. Moreover, the increase in smearing in shallower wells is less noticeable, despite the fact that the first continuum resonance moves from just above the well for 20% Al barriers, to

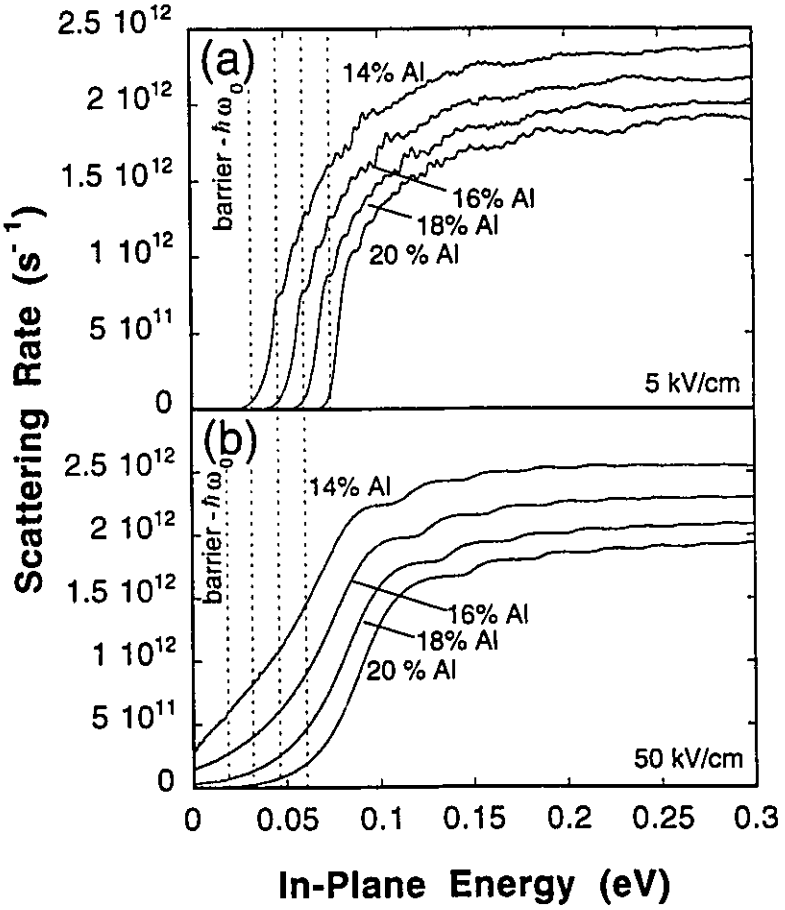

Fig. 4.33: LO phonon absorption rates for 60 Å GaAs/$A_xGa_{1-x}As$ wells where the Al content in the barriers ranges from 14% to 20%, in electric fields of (a) 5 kV/cm and (b) 50 kV/cm. The dotted vertical lines represent the potential barrier heights for the different well depths. In contrast to the well width dependence, the curves scale upwards as the well depth decreases, and the effect of the continuum resonance is less noticeable. At high fields, the tail in the scattering rate for the shallowest well falls more abruptly than the others. This is evidence that the low energy cutoff to the integration excluded some 2D-to-3D scattering events.

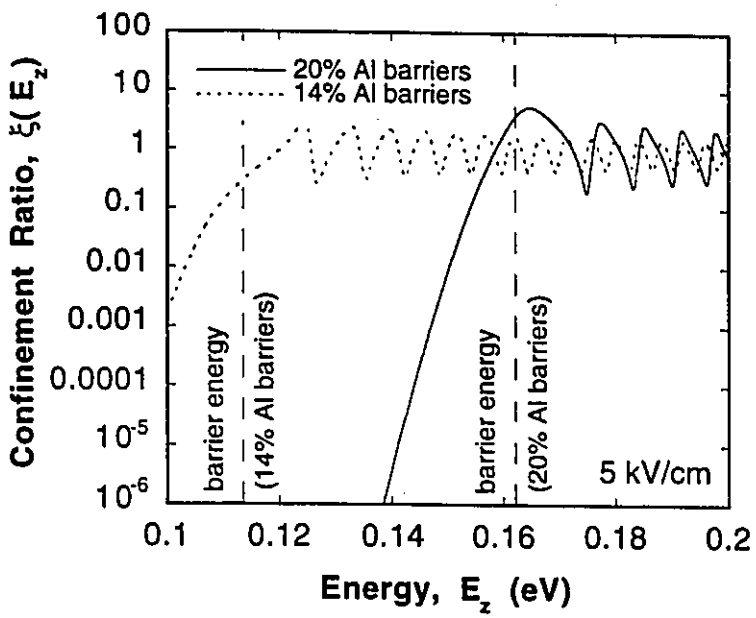

Fig. 4.34: The confinement ratio near the barrier energy for 60 Å $GaAs/Al_xGa_{1-x}As$ wells with 14% (dotted) and 20% (solid) Al content in the barriers. The first continuum resonance moves from just above the barrier energy in the 20 % Al well to 11 meV above the barrier for the 14% Al well.

11 meV above the barrier energy for 14 % Al content. This is illustrated by the confinement ratio plotted in Fig. 4.34.

At high field, shown in Fig. 4.33 (b), it appears that for the shallower wells the low energy tail in the scattering function is artificially attenuated by the minimum E_z cutoff, E_{start} (see §4.6). This is especially noticeable in the 14% Al well where the low energy tail falls more rapidly than the slow, asymptotic descent exhibited by the other curves. This indicates that some 2D-to-3D scattering events are not being included, the result of choosing E_{start} too far from the subband minimum. In cases where the resonance is so broad that it is difficult to distinguish between resonance states and penetrating 3D states, it becomes impossible to avoid either excluding some 2D-to-3D scattering as described above, or including some 2D-to-2D scattering in the 2D-to-3D scattering rate. We will return to this problem in the following section on multi-subband wells.

The average scattering rate is plotted in Fig. 4.35 (a) and decreases monotonically as the well becomes deeper. Unlike in the well width dependence, the effect of the low-lying continuum resonance is overshadowed by the increase in the energy difference between the subband minimum and the final states. That is, the origin of the decrease lies primarily in the integration over the phonon wavevector.

Fig. 4.35 (b) shows the effective barrier height (filled circles) as obtained from the

Fermi-Dirac fits to the LO phonon scattering function, compared with the potential barrier heights. Both increase linearly with the well depth, although the effective barrier height rises more slowly than the potential barrier height as a result of the increased smearing for shallower wells. Again note that the effective barrier height is always greater than the potential barrier height.

In Fig. 4.35 (c) the fitting parameters for the transition width, δE, both decrease with the well depth. This behaviour has the same origins as the well width dependence, resulting from the proximity of the first continuum resonance to the top of the well. As the

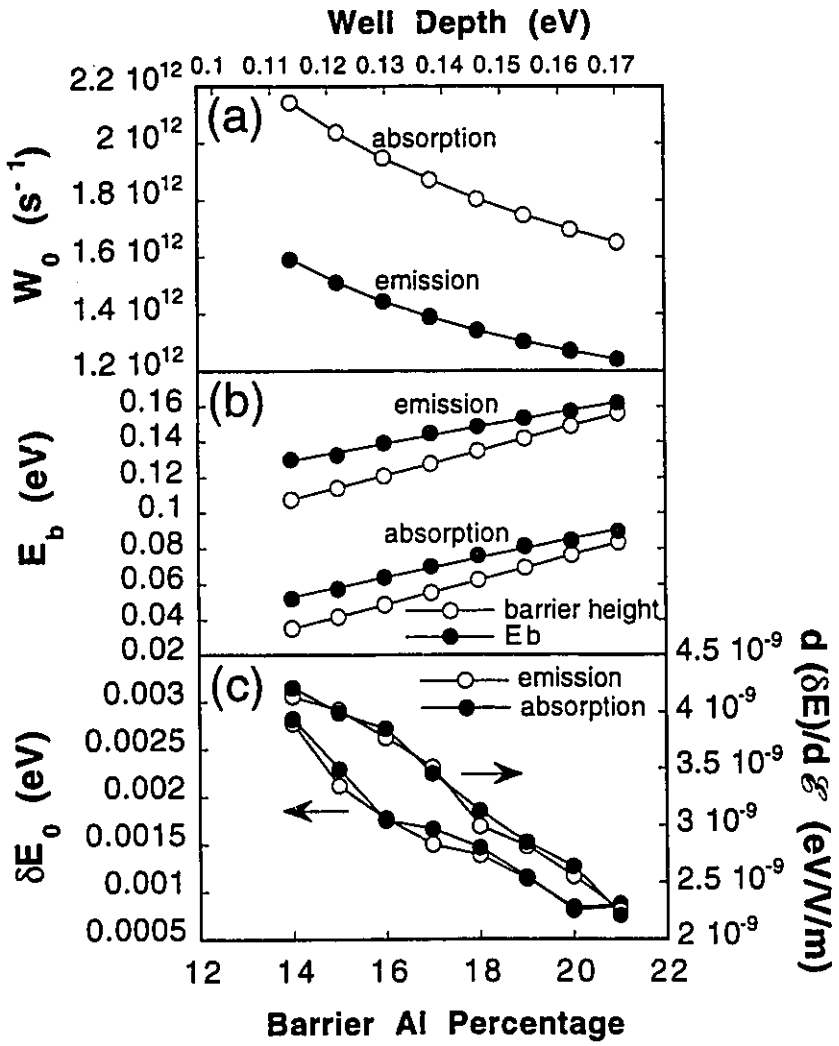

Fig. 4.35: The (a) average scattering rate, W_0, (b) effective barrier height, E_b, and (c) field dependence parameters of the transition width, δE, obtained from Fermi-Dirac fits to the scattering function as a function of the well depth. The average scattering rates decrease smoothly with the well depth. The effective barrier heights increase linearly with the well depth, although not at the same rate as the potential barriers. Both fit parameters for the transition width decrease with the well depth reflecting the rounding of the scattering function edge as the first continuum resonance rises further above the well. The emission and absorption curves exhibit nearly identical behaviour.

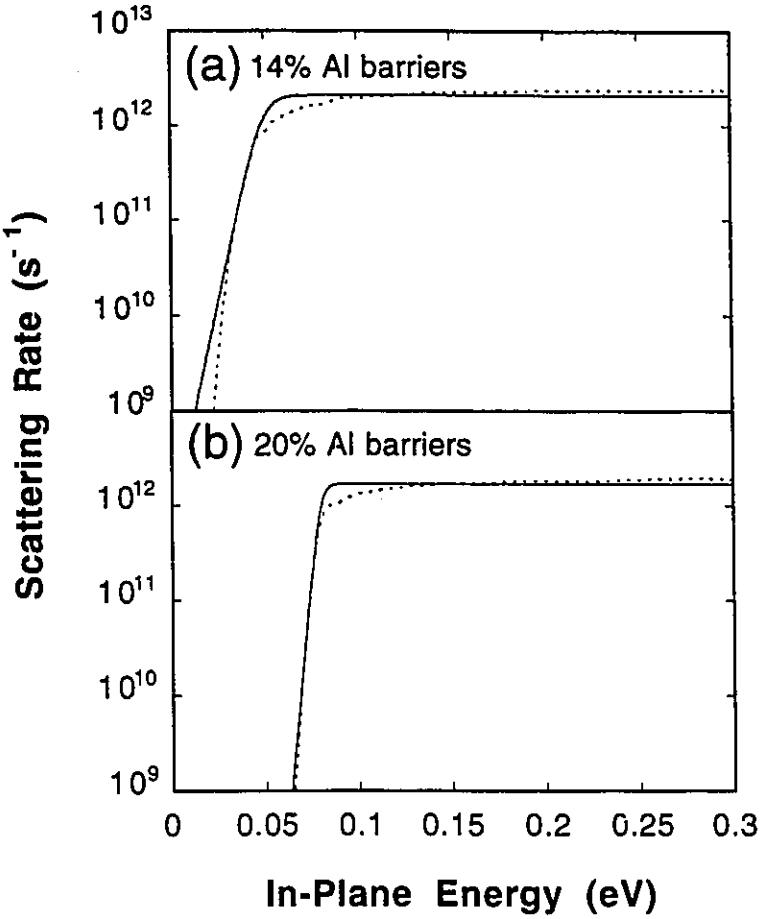

Fig. 4.36: Fermi-Dirac function fits (solid curve) to the LO-phonon scattering function (dotted curve) for 60 Å $GaAs/Al_xGa_{1-x}As$ wells with barrier Al contents of (a) 14% and (b) 20%. The fit for the shallower wells is degraded by the increased curvature near the edge of the scattering function.

well depth decreases, the resonance rises further above the barrier energy, causing the scattering function to become more rounded.

The scatter in the δE fitting parameters reflects the difficulty in fitting the scattering function to the Fermi-Dirac function, particularly for the shallower wells. As shown in Fig. 4.36 (a), the fit worsens considerably due to the increased curvature at the onset of scattering. This same difficulty was observed for the narrow $GaAs/Al_{0.2}Ga_{0.8}As$ wells. Furthermore, the values plotted in Fig. 4.35 (c) are obtained from linear fits to the Fermi-Dirac fitting parameters; i.e.: these points are the result of two successive fitting procedures. As such, they are mostly intended to give a feel for the behaviour of the scattering function as the depth of the well is varied.

Fig. 4.37 shows the calculated thermionic emission times for barrier Al mole concentrations of 14% (dash-dotted), 16% (dashed), 18% (dotted), and 20% (solid) under

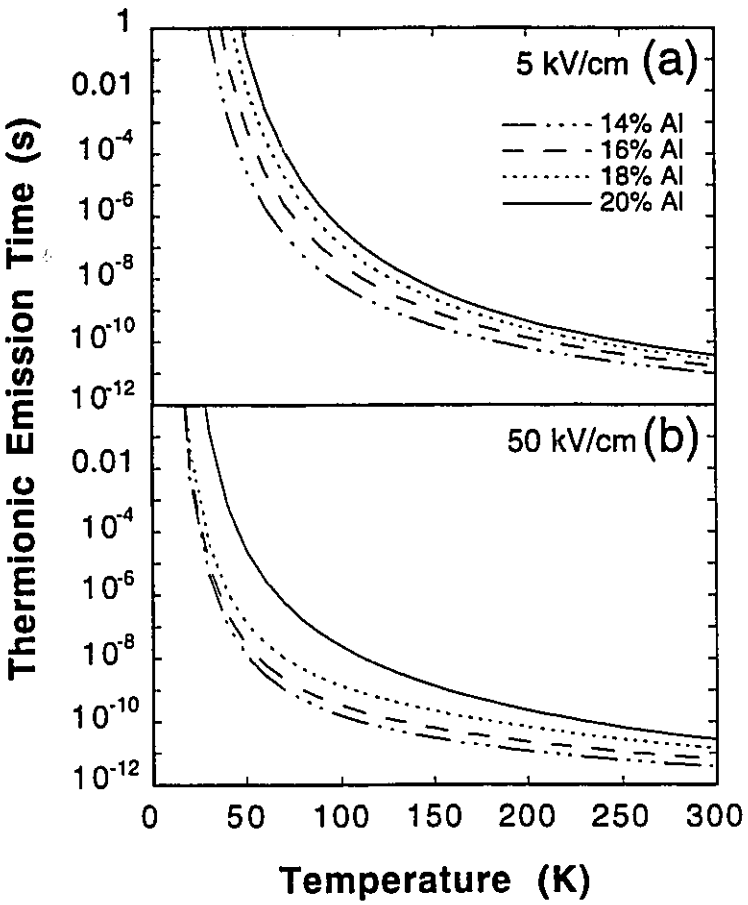

Fig. 4.37: Thermionic emission rates calculated for 60 Å $GaAs/Al_xGa_{1-x}As$ wells with barrier Al mole concentrations of 14% (dash-dotted), 16% (dashed), 18% (dotted), and 20% (solid) in electric fields of (a) 5 kV/cm and (b) 50 kV/cm. As expected, the shallowest wells have the shortest escape times.

fields of (a) 5 kV/cm and (b) 50 kV/cm. As expected, the shallower wells have shorter escape times due to the lower effective barrier and higher average scattering rate. This is true at both low and high fields, however while the curves have the same shape and are evenly spaced at low field, at high field the curves from the shallower wells bunch together at low temperature. This is due in part to the fact that at low temperatures the electron distribution is compressed so that the escape rate is dominated by the low energy tail in the scattering function that results from the wavefunction penetration of the potential barrier. The average scattering rate then becomes less important, particularly for the shallower wells where the transition is less abrupt to begin with. Furthermore, the artificial attenuation of the scattering function within the low energy tail that plagues the shallower wells lessens the differences between the scattering rates at low energies. As a result, the variation in emission rate as a function of the well depth diminishes at low temperatures.

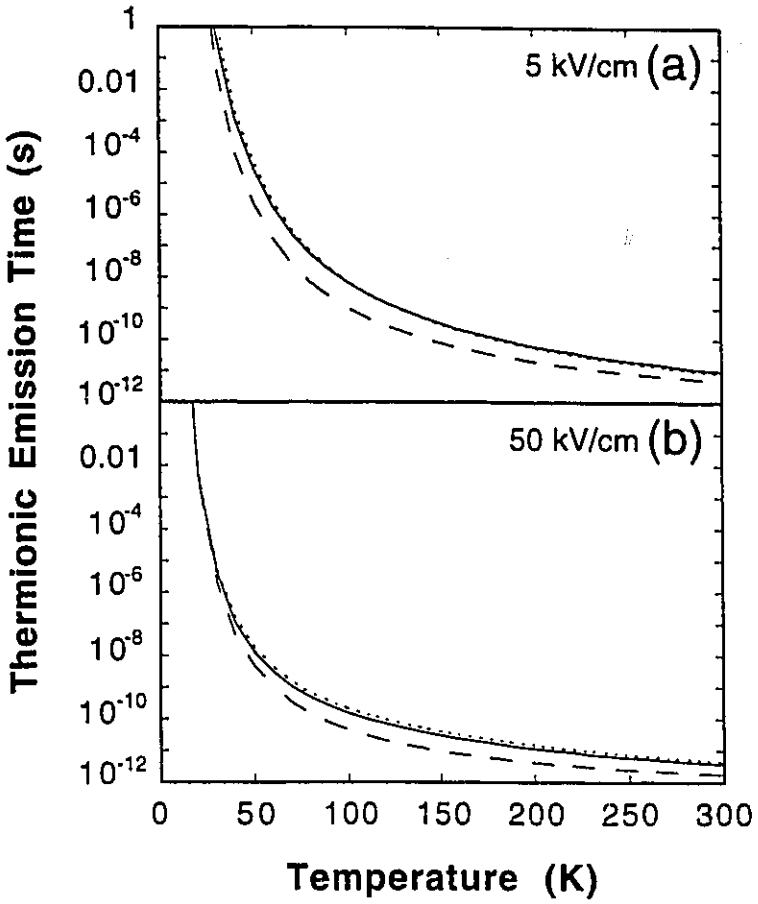

Fig. 4.38: Comparison of thermionic emission times calculated according to the Fermi-Dirac function (dotted) and step-function approximations (dashed) for the LO-phonon scattering function for the 60 Å $GaAs/Al_{0.14}Ga_{0.86}As$ well in electric fields of (a) 5 kV/cm and (b) 50 kV/cm. The solid curve is from the full calculation.

Fig. 4.38 compares the thermionic emission times calculated using the Fermi-Dirac function and step-function approximations for the scattering function with the times generated by the full calculation. These are shown for the shallowest well, with barrier Al concentrations of 14%, in electric fields of (a) 5 kV/cm and (b) 50 kV/cm. Just as for the well width variation, the step function approximation fails to reproduce the results of the full calculation due to the increased curvature in the scattering function. On the other hand, the Fermi-Dirac function approximation does give good agreement, particularly at low fields.

We have seen that the step-function and particularly the Fermi-Dirac approximations are capable of reproducing the full calculation over a range of well configurations. Furthermore, the fit parameters displayed clear trends in relation to the well width and

depth, however only a small region of the well parameter space has been explored. A more complete characterization is necessary to fully determine the behaviour of the scattering function fit parameters. This should then provide the framework for developing a method for quickly calculating the thermionic emission times.

4.7.12. Multiple subbands.

As seen in the two previous sections, the 60 Å $GaAs/Al_{0.2}Ga_{0.8}As$ well is roughly the deepest, widest well for which there is only a single confined subband. If either the width or depth is increased slightly a second loosely confined subband appears within the well. In this case, the problem of calculating the 2D-to-3D scattering rate in the presence of an electric field becomes more complicated. The main difficulty stems from determining what constitutes scattering into a 3D state as opposed to a 2D state. This is simple enough in the absence of an electric field, since all confined subbands have well defined energies in the z-direction. In this case, one need only begin integrating at an energy slightly greater than the upper subband minimum to avoid 2D-to-2D intersubband scattering (in fact, since only confined states are found at energies less than the barrier energy, one need only integrate from the barrier energy up). However, in the presence of an electric field, the confined subbands are broadened into energy resonances. If the final state energy, E_z', is within the resonance associated with a confined subband, then this should be considered 2D-to-2D scattering. The difficulty is in determining whether the final state is sufficiently outside the energy resonance to be considered 3D. This problem was first encountered in the previous section with respect to shallow wells.

Consider the confinement ratio, $\xi(E_z)$, for a 100 Å $GaAs/Al_{0.2}Ga_{0.8}As$ well as shown in Fig. 4.39 for both low (solid) and high (dotted) fields. At low fields the upper confined subband has an extremely narrow resonance so that the cutoff for 3D states can be chosen almost arbitrarily close to the resonance peak. At the higher field, the resonance broadens considerably such that in the region between the resonance peak and the above barrier resonances, there is only a mild decrease in the confinement ratio. In this case, a reasonable choice for the 3D cutoff would be in the vicinity of the local minimum in the confinement ratio. This is indicated by the arrow in the inset to Fig. 4.39 where the region of interest has been expanded.

As the well is widened further, a third subband will become confined near the top of the well. The combination of the subband width and its proximity to the 3D continuum makes it difficult to establish a reasonable cutoff between subband states and penetrating

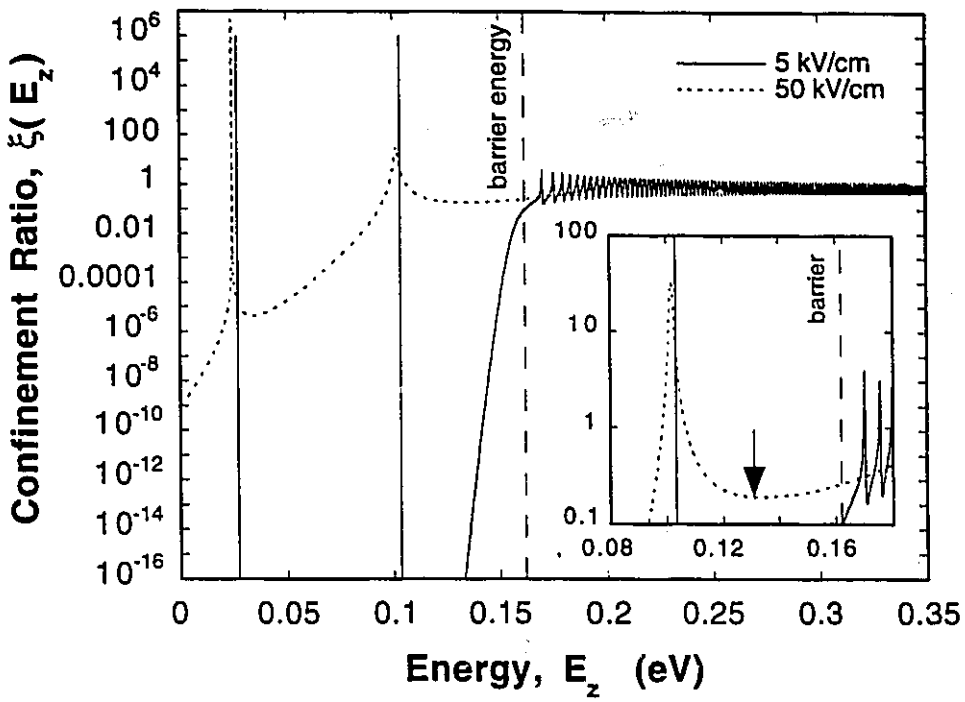

Fig. 4.39: Confinement ratio for a 100 Å $GaAs/Al_{0.2}Ga_{0.8}As$ well in an electric field of 5 kV/cm (solid) and 50 kV/cm (dotted). The dashed line indicates the barrier energy. The inset shows a closeup of the region between the upper subband and the continuum. The arrow indicates the local minimum in the confinement ratio which marks the boundary between 2D and 3D states.

3D states. If the upper subband is very loosely bound, as is the case for the 65 Å $GaAs/Al_{0.2}Ga_{0.8}As$ well, then it will have an extremely short lifetime, on the order of 100 fs. In this case, we can consider the state to be unbound and include scattering into this subband as part of the 2D-to-3D scattering rate. However, for situations where the lifetime of the upper subband is of the order of the scattering rate, this approximation breaks down. Simply using the local minimum as the cutoff will likely exclude scattering events that are 2D-to-3D, artificially cutting off the low energy tail in the scattering function. This effect will be observed in the calculations for the 95 Å wells presented in the next section. In this case, a satisfactory procedure for calculating the total 2D-to-3D scattering rate in the presence of an electric field could not be found. Results have been presented in the literature where it appears that they have covered a broad range of well widths that contain multiple subbands. However, either the effects of an electric field were not included (Liang and Lent, 1990), (Tsai, 1994a, 1994b) or, if included, the upper subband was treated as a 3D state or, more precisely, the upper state was considered to be in equilibrium with the continuum (Rosencher, 1994).

To investigate, briefly, the behaviour of the scattering rate as the well width is increased to include a second subband, calculations were performed for GaAs/$Al_{0.2}Ga_{0.8}As$ wells with widths of 100 Å, 110 Å and 120 Å. As in the case of the 65 Å well, the 120 Å well contains a very loosely bound (third) state right at the top of the well. These widths were chosen because the upper (second) subband is well below the barrier energy. Nonetheless, in the 100 Å well the upper subband was shallow enough for the broadening of the resonance width to limit the electric field to less than 30 kV/cm.

The scattering functions retain the general features seen in the single subband calculations, with the onset becoming sharper as the well width is increased. In Fig. 4.40, the effective barrier heights (open symbols) are compared to the potential barriers (filled symbols) for widths of 50 Å to 120 Å. For those greater than 65 Å wide, there are two confined subbands, each with its corresponding effective barrier height and potential barrier. As in the single subband case, the effective barriers for both the ground and upper subbands decrease with increasing well thickness, despite the fact that the potential barrier increases. This is again attributed to the proximity of a continuum resonance to the top of the well.

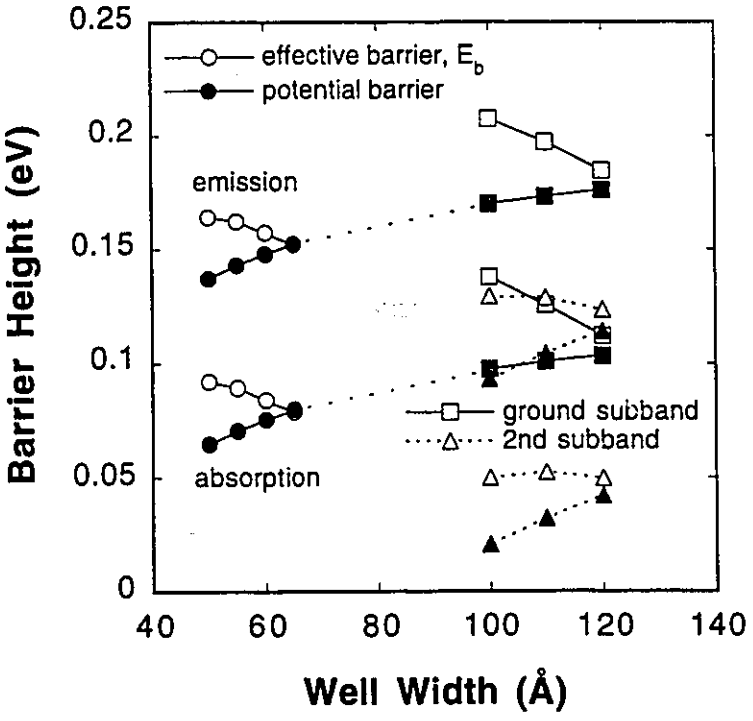

Fig. 4.40: The effective barrier heights (open) and potential barriers (filled) for GaAs/$Al_{0.20}Ga_{0.80}As$ wells as a function of the well width. For widths greater than 65 Å and less than 120 Å, there are two confined subbands, each with its own barrier heights. In all cases, the effective barrier height decreases with increasing well width in contrast with the potential barrier which increases as the well widens.

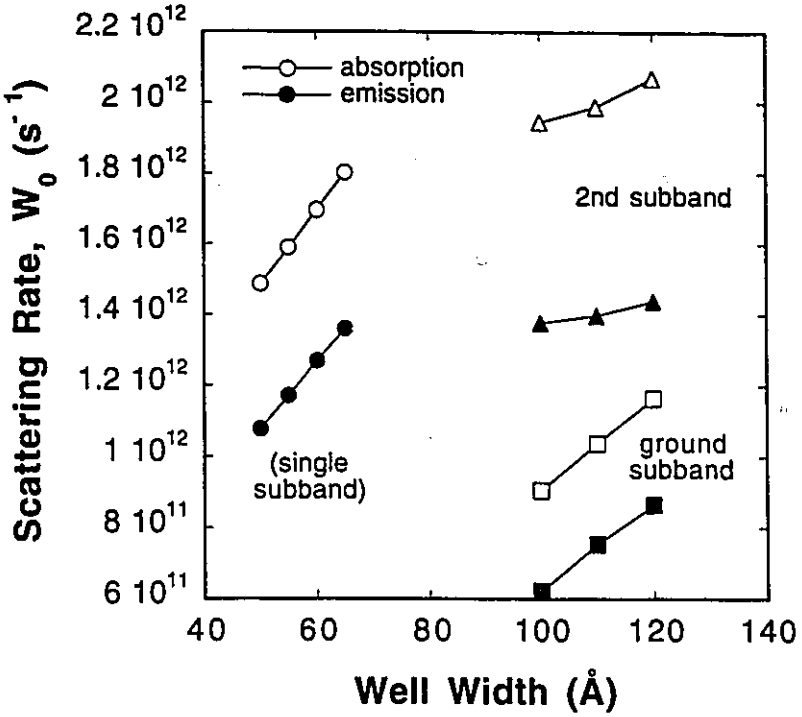

Fig. 4.41: The average scattering rate as a function of the well width for GaAs/$Al_{0.20}Ga_{0.80}As$ wells. The scattering rate increases with the well width in all cases.

Fig. 4.41 shows the average scattering rates as a function of the well width. In all cases, the scattering rate increases with the well width. As a combined result of the increasing scattering rate and decreasing effective barrier height, the thermionic emission time decreases with well width, until a higher subband is strongly confined to the well. This is demonstrated in Fig. 4.42 where, following confinement of the upper subband at widths greater than 65 Å, the thermionic emission time increases before resuming its downward trend. This is analogous to the oscillatory behaviour that has been theoretically predicted in quantum well carrier capture rates (Brum, 1986a, 1986b), (Sotirelis and Hess, 1994) and, more recently, observed experimentally (Blom, 1993a, 1993b), (Fujiwara, 1995). We can expect that if the width is increased beyond 120 Å, there should be another jump in the emission time. A previous emission calculation performed in the absence of electric fields showed the emission time *increasing* with the well width and *decreasing* abruptly when a new subband became confined (Tsai, 1994a, 1994b). However, simple, normalized plane waves were employed as the final state wavefunctions, and as a result, the enhanced amplitudes that characterize continuum resonances were absent from their calculations.

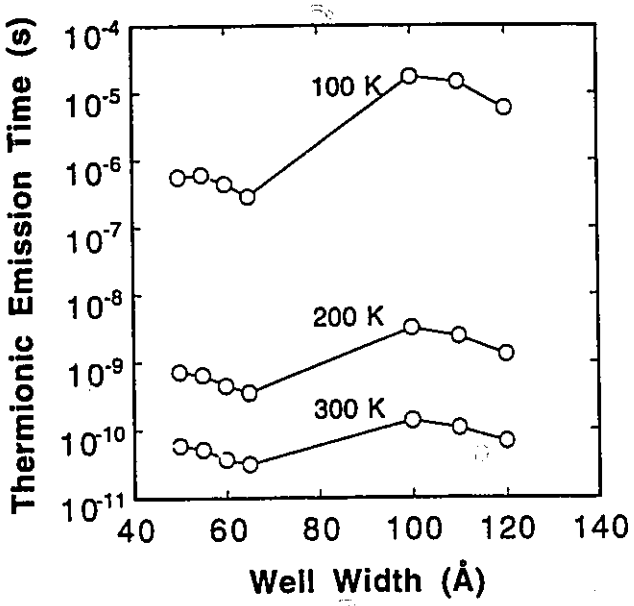

Fig. 4.42: Calculated thermionic emission times for GaAs/$Al_{0.20}Ga_{0.80}As$ wells as a function of well width, at temperatures of 100 K, 200 K, and 300 K, in a 5 kV/cm electric field. The thermionic emission time decreases with increasing well width until a higher subband becomes confined to the well.

We can only speculate on the behaviour between well widths of 65 Å and 100 Å, as this marks the region where the broadness of the upper confined subband interferes with the 2D-to-3D scattering calculation. In the zero field calculation of Tsai *et al* (1994a, 1994b), the emission time changes abruptly when a new upper subband is confined. In the presence of an electric field, because the distinction between confined and unconfined states is blurred, the drop in emission rate will be softened. The precise behaviour of the curve will depend on what we choose to consider thermionic emission as opposed to thermally-assisted tunnelling.

4.7.13. Summary of dependence on well configuration.

In the preceding sections I have investigated how the thermionic emission calculation is affected by changes in the well parameters. As the well width is varied, the sharpness of the scattering function is determined by the proximity of a continuum resonance with respect to the top of the well. As a result, although a wider well will have a larger potential barrier, the effective barrier is decreased. When combined with a scattering rate that increases with the well thickness, this generates thermionic emission times that decrease with increasing well width, opposite to what one would expect from conventional

thermionic emission theories. Similar trends in the sharpness of the scattering function were observed as the well depth was varied, however, the changes in the barrier height resulting from the variations in the barrier composition dominated. As a result, the effective barrier heights increased with the well depth. The scattering rate also increased with well depth resulting in slower thermionic emission times for deeper wells, as expected. Finally, the case of multiple subbands was considered by treating $GaAs/Al_{0.2}Ga_{0.8}As$ wells between 100 Å and 120 Å wide. The LO phonon scattering functions retained the same general characteristics described above so that the thermionic emission time decreased with increasing well width. However, in going from a single subband to two subbands, the emission time initially increased when the upper subband became strongly confined within the well. As the well was widened further and a third resonance approached the top of the well, the emission time resumed its downward trend. Similar behaviour is expected each time a new subband appears in the well. Unfortunately, the difficulties encountered when treating scattering in the presence of loosely bound upper subbands prevented the calculation of 2D-to-3D scattering rates and thermionic emission times within the transition region.

The two approximation schemes for the scattering function that were first presented in relation to the 60 Å $GaAs/Al_{0.2}Ga_{0.8}As$ well were also applied to the various well configurations. Both approximations suffered as the lowest continuum resonance moved away from the top of the well, causing the scattering function to become increasingly rounded. Nonetheless, they should provide a useful framework for developing a parameterization scheme that would allow quick calculations of the thermionic emission time. This is left to future work.

4.7.14. Case Study: 95 Å $Al_{0.2}Ga_{0.8}As/GaAs/Al_{0.4}Ga_{0.6}As$ asymmetric well.

The reason for choosing this particular well configuration is that it has been fabricated and studied by Cavaillès *et al* (1992), where they measured the electron and hole escape rates using the pump-probe technique. This is one of the few published works where the separate contributions of the electrons and holes have been clearly identified, allowing comparison with the detailed calculations of this thesis. Furthermore, it presents an opportunity to examine how an asymmetric barrier affects the scattering rates. We begin, then, by comparing the calculations for the symmetric well and the asymmetric well.

Fig. 4.43 shows the calculated envelope functions and energies in the 95 Å asymmetric well. There are two confined states, with the second 52 meV below the top of

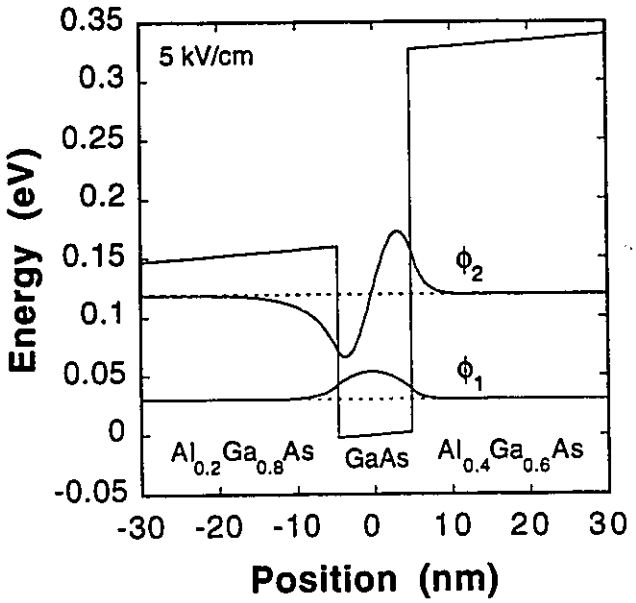

Fig. 4.43: Calculated energies and envelope functions for confined states in a 95 Å asymmetric $GaAs/Al_xGa_{1-x}As$ well.

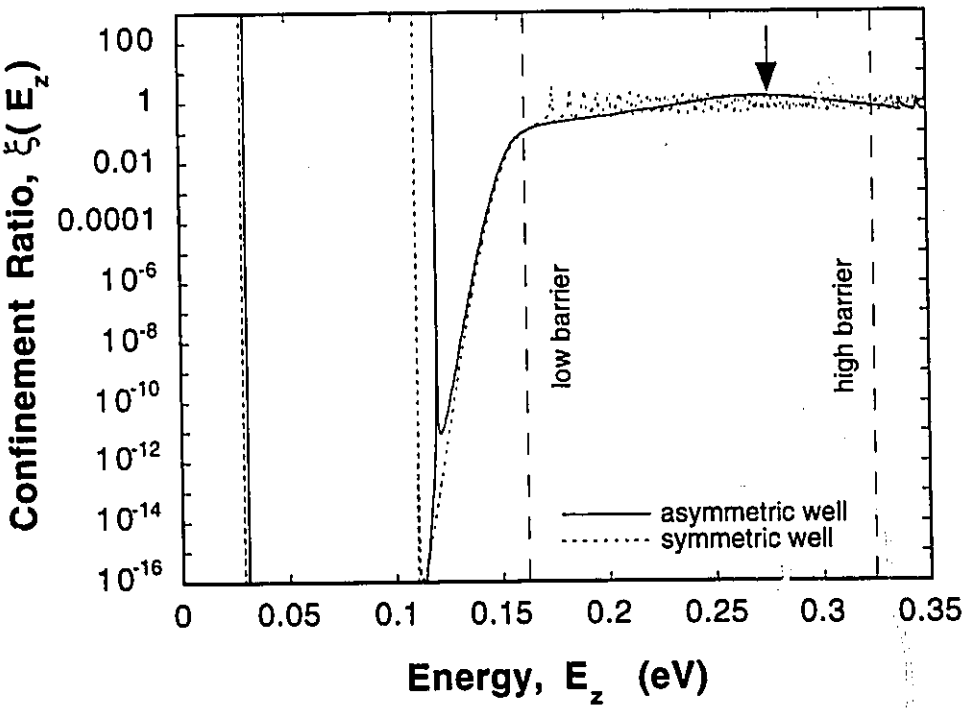

Fig. 4.44: Confinement ratio, $\xi(E_z)$, for the symmetric ($Al_{0.20}Ga_{0.80}As$ barriers - dotted) and asymmetric ($Al_{0.20}Ga_{0.80}As/GaAs/Al_{0.40}Ga_{0.60}As$ - solid) 95 Å well in a 5 kV/cm electric field. The arrow indicates the single broad peak in the asymmetric well confinement ratio for energies above the low barrier and below the high barrier. The vertical dashed lines indicate the energies of the low and high barriers.

the lower barrier. The difficulties discussed in §4.7.12 will only become important at the higher fields. Fig. 4.44 compares the confinement ratios for the symmetric and asymmetric wells. The presence of the high barrier produces a slight increase in the energies of the confined subbands due to the increased confinement. More interesting however is the removal of the high frequency oscillations for energies greater than the smaller barrier as seen in the asymmetric well. Instead, a single, extremely broad resonance is centred at the arrow. The overlap integral will be characterized by similar features and hence the scattering rates should differ between the two wells, despite the similarities in configuration.

Fig. 4.45 shows the electron-LO phonon scattering rate from the ground subband of both the symmetric (dotted) and asymmetric wells (solid) in a 5 kV/cm electric field. At most energies, the asymmetric rate is suppressed relative to the symmetric rate. This can be attributed to the removal of the above-barrier resonances by the presence of the high barrier. Incidentally, this also eliminates the noise seen in the symmetric curve. The logarithmic scale was chosen to reveal the behaviour below the barrier, where it can be seen that the two curves are very similar, with the asymmetric rate slightly greater than the symmetric rate.

The electron-LO phonon scattering rates from the ground state under high field

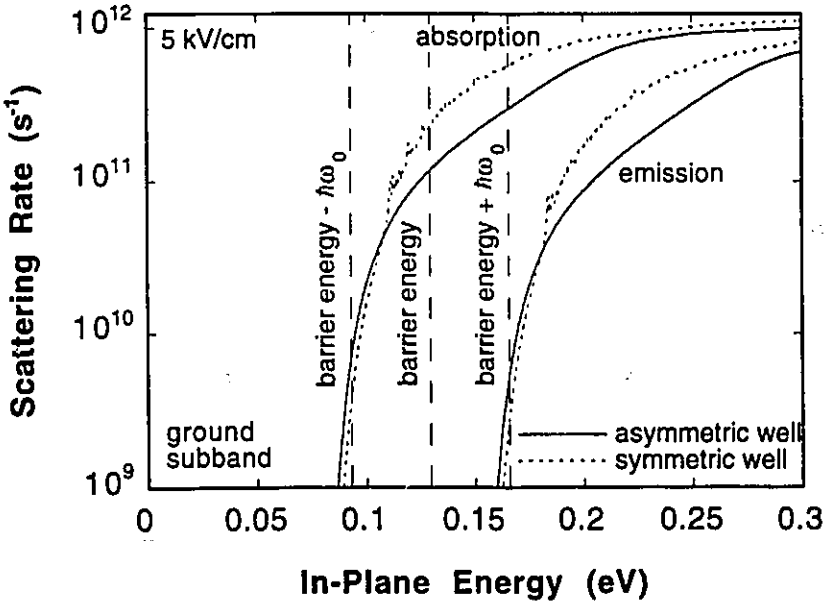

Fig. 4.45: 2D-to-3D electron-LO phonon scattering rates from the ground subband of the symmetric (dotted) and asymmetric (solid) 95 Å GaAs/AlGaAs quantum wells. Above the barrier the asymmetric scattering rate is inhibited relative to the symmetric rate but below the barrier they merge. The vertical dashed lines indicate the energy of the low barrier, the outer lines representing the effective raising or lowering of the barrier by an amount equal to the phonon energy.

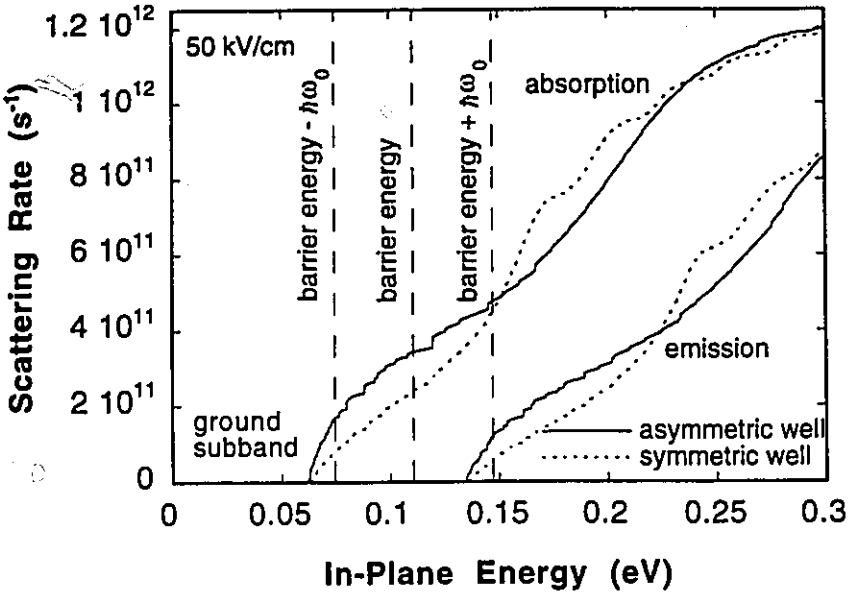

Fig. 4.46: 2D-to-3D LO phonon scattering rates from the ground subband of the symmetric (dotted) and asymmetric (solid) 95 Å GaAs/AlGaAs quantum wells in a 50 kV/cm electric field. For energies below the barrier, the asymmetric rate is greater, while just above the symmetric rate is faster. The vertical dashed lines indicate the energy of the low barrier, the outer lines representing the effective raising or lowering of the barrier by an amount equal to the phonon energy.

(50 kV/cm) are presented in Fig. 4.46. The symmetric results are given by the dotted curves while the asymmetric case is represented by the solid curves. As seen previously, the curves are smeared by the electric field. In the low energy tail the differences between the two wells become enhanced; we will find that this dominates the relative emission rates at low temperatures. It is important to note that the abrupt cutoff to the scattering rate at 0.063 eV for absorption and 0.136 eV for emission is artificial, resulting from the choice of the low energy cutoff, E_{start}, imposed to exclude scattering into the second subband. At this field strength the lifetime of the upper subband is less than a picosecond, so that thermally-assisted tunnelling will dominate the escape anyways.

From the LO-phonon scattering curves, the thermionic emission times from the well have been calculated and are presented in Fig. 4.47 for both the symmetric (dotted) and asymmetric (solid) wells. At low fields, the emission rate from the asymmetric well is slower due to the suppression of the scattering rate. The relative decrease is similar to the difference in scattering rates; roughly 35% throughout the temperature range. At high fields, the enhancement of the asymmetric rate within the low energy tail results in a faster asymmetric emission rate. Since the relative increase in the asymmetric scattering rate occurs at low energies where the electron population is greater, the effect on the emission

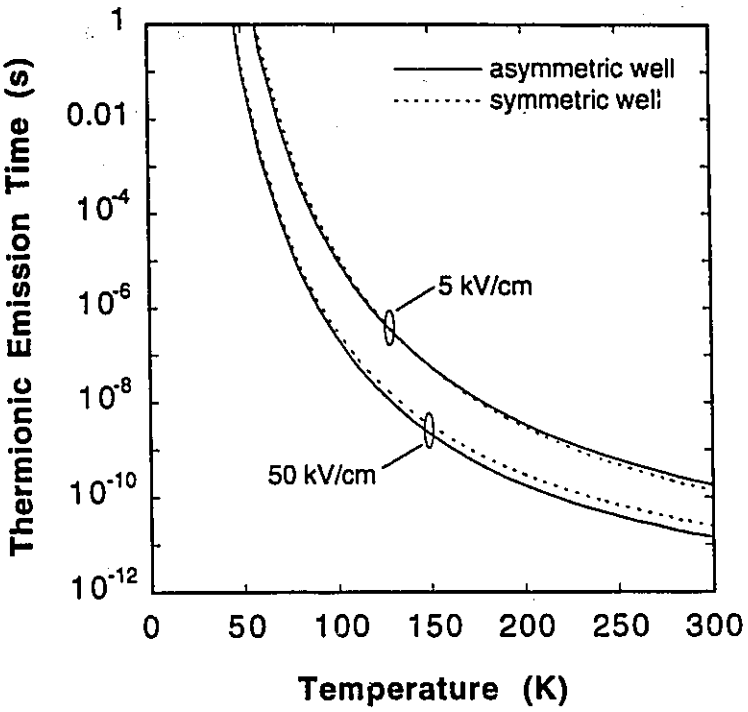

Fig. 4.47: Calculated thermionic emission times for the symmetric (dotted) and asymmetric (solid) 95 Å GaAs/AlGaAs quantum wells for electric fields of 5 kV/cm and 50 kV/cm. For low fields the symmetric well has the faster escape rate while for high fields the order is reversed.

time is substantial. The calculated values for high fields are less accurate, however, as the low energy tail in the scattering function is artificially limited, as described previously. It is expected that if this restriction could be avoided, the emission times for both structures would decrease further.

As stated earlier, the asymmetric structure has been studied experimentally by Cavaillès *et al* (1992). Using the pump-probe technique, they measured the electron escape times from the well as a function of bias at room temperature. In Fig. 4.48 the measured data points (open circles) are compared with the calculated escape time (solid curve). Also shown are the individual escape times calculated for each of the various mechanisms: thermionic emission (dashed), thermally-assisted tunnelling (dotted), and tunnelling (dash-dotted). At electric fields greater than 30 kV/cm, the escape is dominated by thermally-assisted tunnelling, although at the largest fields tunnelling becomes significant. Below 30 kV/cm, thermionic emission takes over. Note that the thermionic emission calculation was not attempted beyond 70 kV/cm due to the difficulties described in this and the preceding section. To facilitate the calculation of the overall escape rate, the 70 kV/cm value was extrapolated out to 100 kV/cm. This should not result in any significant errors

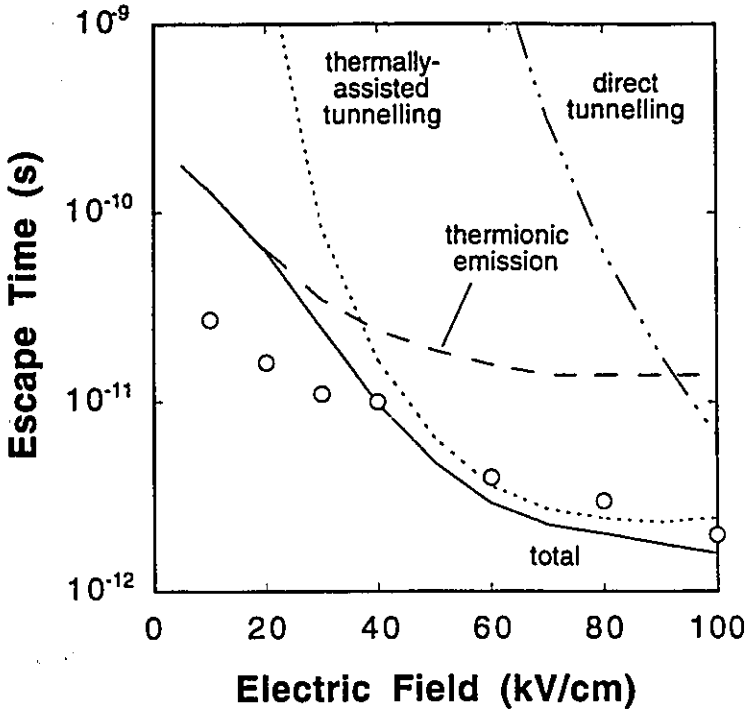

Fig. 4.48: Measured electron escape times (open circles) from a 95 Å $Al_{0.20}Ga_{0.80}As/GaAs/Al_{0.40}Ga_{0.60}As$ quantum well compared with calculated values. The individual escape times via the various mechanisms are also shown: thermionic emission (dashed), thermally-assisted tunnelling (dotted), and tunnelling (dash-dotted). The overall escape rate is given by the solid curve.

since the thermally-assisted tunnelling and tunnelling rates are almost an order of magnitude faster than thermionic emission in this region.

Within the thermally-assisted tunnelling regime, the difference between the measured and calculated values is less than 50%. Although the calculation appears to underestimate the measured times at 8-10 kV/cm, it is likely that the measurement is in fact limited by the resolution of the measurement system. While the authors claim a resolution of 1 ps, this is probably an overestimation considering that the pulse width of the excitation laser is given as 0.6-1 ps. Within the thermionic emission regime, the calculated times are 3-5 times slower than the measured values. This is in contrast to the oft-used Schneider-Von Klitzing (1988) result, which gives values that are ~2 times *faster* than the measured times. Interestingly, using the low field result of Eq. 2.35, the thermionic emission times are well reproduced (Moss, 1994). In fact, Fig. 5 of Moss (1994) shows good agreement between the calculated and measured escape times at all fields. However, it appears that this is due to an inaccuracy in the calculation of the thermally-assisted tunnelling time, where beyond 60 kV/cm it becomes *slower* as the field strength increases. This is the

result of assuming that the 2D states are in equilibrium with the 3D states above the well. Since the potential barrier is lowered by the field according to Eq. (2.42), the bulk-like 3D density of states is also assumed to begin at this lower energy. As a result, the fraction of carriers in the 3D states increases. The reduction in the subband occupation factor dominates over the shortened tunnelling lifetime so that the thermally-assisted tunnelling time increases with the electric field. Considering that in a field of 70 kV/cm the tunnelling lifetime of the upper subband is 70 fs and it takes just 45 fs for an electron initially at rest to ballistically travel twice the width of the well, it seems unlikely that the 3D states are in equilibrium with the 2D states. The more accurate calculation would apply the carrier distribution to the 2D states only, as described in §2.6. This approach was used in Fig. 4.48. With these thermally-assisted tunnelling times, the agreement in Moss (1994) would degrade substantially at high fields. Similarly, if the thermionic emission times generated by the scattering calculation of this work were lowered to agree with the measured data at low fields, the total escape times at high field would then be too short by 4-5 times.

If both the thermally-assisted tunnelling and thermionic emission times had disagreed with the measured data by roughly the same amount, or at least in the same direction, we could have easily attributed the discrepancy to the barrier height or to the effective mass. Unfortunately, the disagreement at low fields indicates that the calculated thermionic emission times are slow, since this is the only process that contributes in this regime. Meanwhile, at high fields the calculated thermally-assisted tunnelling time must be underestimated since the addition of a thermionic emission time in agreement with the low field values would produce a total escape time that is shorter than observed. So we require sources of error that will cause one process to become slower while the other becomes faster.

Consider first the thermally-assisted tunnelling calculation. There are two main assumptions built into this theory. The first is that of thermal equilibrium within the 2D subbands. Obviously, as the tunnelling times become very short, this assumption breaks down. The limiting process is then the repopulation of the upper subband via intersubband scattering. While this would slow the thermally-assisted tunnelling process as desired, it would have a similar effect on the thermionic emission process, contrary to what is observed. The second assumption is that of parabolic bands. In bulk GaAs the effective mass increases with k (Rössler, 1984) so that the subband energies will be increasingly overestimated at higher k values (Chen and Andersson, 1991). A rough correction using an effective mass from Chen and Andersson (1991) to recalculate the subband energy and

tunnelling lifetime increases the thermally-assisted tunnelling time by a factor of ~2. Adding this correction to Fig. 4.48 improves the agreement throughout the thermally-assisted tunnelling regime. Meanwhile, the energy of the ground state will also be lowered, but by a smaller amount, so that the net effect will be the lowering of the upper state. Non-parabolicities should also be expected in the in-plane effective masses of the quantum well due to the confining potential of the well (Ekenberg, 1989). An increasing effective mass will result in a greater density of states at higher energies, leading to shorter thermionic emission times, however the thermally-assisted tunnelling time would also decrease. The relative changes between the two mechanisms would depend on the exact behaviour of the effective masses. Obviously, including the effects of realistic band structures is a somewhat complicated issue and it is difficult to predict how the overall escape rates will be affected. Nonetheless, the omission of non-parabolicities in the calculations will introduce significant errors in both the thermionic emission and thermally-assisted tunnelling calculations.

There are other possible sources of error in the calculated thermionic emission times, although some can be disregarded. Consider first the accuracy of the electron-LO phonon scattering calculation. Bulk phonons were used even though it is known that the phonon structure is in fact modified by the quantum well. However, this was shown to be accurate to within 10% for wells of similar width (Rücker, 1992). Furthermore, the confined phonons produced *smaller* scattering rates than the bulk phonons (Rücker, 1992), (Ridley, 1994), which would lead to slower thermionic emission rates. It was noted in reference to Fig. 4.46 that the artificial restriction on the final state energy causes an underestimation of the escape rate, however this only occurs at large fields. As can be seen in Fig. 4.48, the discrepancy actually worsens as we approach flat band. One possible source of the inaccuracy lies in the 3D density of states. Recall that the derivation presented in §4.2.2 neglected the presence of the quantum well. Detailed attempts at calculating the continuum density of states in the presence of a quantum well have been reported (Trzeciakowski and Gurioli, 1991), (Austin and Jaros, 1985) where the *change* in the 1D density of states due to the quantum well structure was determined. Trzeciakowski and Gurioli (1991) showed that while the density of states is not affected below the top of the well, it oscillates at energies above the well. Similar to the behaviour observed in the overlap function in §4.7.2, the peaks in the density of states oscillations correspond to continuum resonances, where the period of oscillation increases with the electric field. This effect would increase the contributions of the continuum resonances to the scattering rate, thus lowering the thermionic emission time.

As discussed in §4.7.8, the effects of image charge lowering have been omitted from these calculations due to the difficulty of solving for the wavefunctions in the presence of the image potentials derived in the previous chapter. However, in this case we can show that this is a reasonable approximation. The carrier density in these experiments was estimated at ~10^{10} cm^{-2} where the effective image charge is ~0.1e. The resultant image charge barrier lowering at a field of 30 kV/cm is then ~6 meV. At room temperature, this would produce only a minor increase in the thermionic emission rate, much less than the required factor of ~3-5.

We next examine the physics behind the calculation. The assumption that the carrier immediately leaves the vicinity of the well upon scattering into a continuum state would underestimate the escape time, contrary to what is observed. The only significant possibility that remains is that LO-phonon scattering is not the dominant scattering mechanism. Since the other important phonon scattering processes were also considered in this work and found to be insignificant relative to the polar optical phonon process, a completely different mechanism must be considered. Carrier-carrier scattering can be ruled out in this case because the experiments were performed at low densities, on the order of 10^{10} cm^{-2}. The two most probable mechanisms are then impurity and interface roughness scattering. Both will be sample dependent and hence difficult to calculate without a more detailed knowledge of the material quality. However, considering that at room temperature LO phonon scattering is expected to dominate (Walukiewicz, 1984), it is unlikely that either of these processes could produce the required 3-5 times increase in the escape rate.

Alternatively, some of the error will be contained within the experimental points themselves. As mentioned earlier, at high fields where the escape time approaches 1 ps, the system resolution becomes important. Furthermore, the electron escape times are extracted from a complicated five parameter fit to the experimental data where it is assumed that the decay of the exciton saturation component is equal to the electron escape rate. Obviously, this is not a direct measurement of the electron escape time and is therefore susceptible to errors. In the next chapter, experimental data from time-resolved photoconductivity measurements performed on strained InGaAsP/InP multiple quantum well laser structures will be presented. While in principle the analysis of this experiment is much simpler than for the pump-probe measurement, the device parasitics restricted the analysis to the holes. Unfortunately, as the deviations from parabolic bands in this case are much worse than in the asymmetric GaAs/AlGaAs sample, the discrepancies between the measured and calculated escape times are magnified.

Further checks of this calculation are hampered by the lack of suitable experimental

data in the literature. While there are many papers reporting carrier sweepout times in quantum well structures, few of them clearly identify the separate contributions of electrons and holes, making comparisons difficult. Similar theoretical calculations have been reported, however, again comparisons are not straightforward. Shorthose *et al* (1989) calculated the LO-phonon-mediated escape rates from a 50 Å InGaAs/InP quantum well in an electric field (they referred to this process as 'phonon-assisted tunnelling') and obtained emission rates between 500 ps at 30 kV/cm to 0.2 ps at 150 kV/cm. Considering that the well depth was assumed to be 250 meV, giving a barrier height of ~175 meV (assuming an effective mass of 0.041 m_e), the high field times appear to be too short. Indeed, they find that the thermal escape rate is greater than the direct tunnelling rate even at fields of 175 kV/cm. This is probably due to the fact that they do not truncate the bound state wavefunction at the barrier edge as described in §4.7.1, but include contributions from unconfined regions of the initial state wavefunction. Hence, as the field increases, and the initial state becomes less confined, the overlap with continuum states increases due to contributions from outside the well. This leads to an unrealistically short thermionic emission time at high fields. As a result, their times are consistently shorter than those obtained in this work; at 30 kV/cm we obtain a value of 4 ns as compared to their 500 ps. The difference should be less at lower fields and if we extrapolate their curves to 5 kV/cm, we obtain a value of 3 ns which compares favourably with the 4.7 ns calculated according to the approach of this thesis. Liang and Lent (1990) calculated the 2D-to-3D electron-LO-phonon scattering rates (they did not complete the thermionic emission calculation) from unbiased GaAs/AlGaAs quantum wells and their results are similar in magnitude to those presented here. Tsai *et al* (1994a, 1994b) performed similar calculations for unbiased $In_{0.3}Ga_{0.7}As$/GaAs wells, obtaining an escape time of roughly 15 ps for a 50 Å well. However, they do not include the effects of continuum resonances and they assume that the initial and final states are in thermal equilibrium. Furthermore, they do not give the material parameters used in the calculation and it appears that the value assumed for the effective mass is much smaller than that given by a linear interpolation between the InAs and GaAs values. As a result, an attempt at reproducing their results was not possible. Finally, Thibaudeau and Vinter (1994) calculated the LO-phonon mediated time constant to compare with impedance spectroscopy measurements performed on a biased GaAs/$Al_{0.22}Ga_{0.78}As$ quantum well. Unfortunately, this time constant does not directly correspond to the thermionic emission time but describes the exchange of electrons between the well and continuum states where the respective quasi-Fermi levels are equal.

In summary, the measured escape times from a 95 Å asymmetric GaAs/$Al_xGa_{1-x}As$

have been compared with the calculations described in this thesis. While there is good agreement at high fields where thermally-assisted tunnelling is dominant, at low fields the thermionic emission time is overestimated by the LO-phonon scattering calculation by a factor of ~3-5. However, for good agreement throughout the field range, both the thermionic emission time and the thermally-assisted tunnelling time must be adjusted. The discrepancy is attributed primarily to two factors: the omission of band non-parabolicities and the assumption that the quantum well does not affect the final state density of states. Contributions from impurity or alloy scattering processes are unlikely to produce this substantial an error. Finally, some of the discrepancy can be attributed to uncertainties in the experimental data points themselves, in particular due to the complexity of the analysis.

4.8. Summary.

In this chapter calculations of the 2D-to-3D electron-phonon scattering rates from quantum wells in an electric field have been presented. The results from a 60 Å $GaAs/Al_{0.2}Ga_{0.8}As$ well revealed that polar optical phonon scattering dominates over deformation potential and piezoelectric scattering by acoustic phonons at all temperatures and biases. Unlike in bulk or 2D-to-2D scattering, optical phonon absorption remains dominant even at low temperatures due to lowering of the effective barrier by an amount equal to the phonon energy. The application of a perpendicular electric field was found to smear the onset of the scattering function such that a low energy tail extends below the barrier energy. However, the scattering function as a whole *does not shift* with the lowered potential barrier as expected. This leads to the speculation that the effects of image charge lowering will be weak; further calculations are needed to quantitatively determine its impact on the thermionic emission rate. The full thermionic emission calculation was compared with simplified forms that approximated the LO phonon scattering function as either step-like or as a Fermi-Dirac type function. The latter was quite successful at reproducing the detailed approach while the simpler step-function was found to provide reasonable agreement near room temperatures and small fields. These approximate forms should provide a framework for the development of a simple but accurate calculation of the thermionic emission times from arbitrary quantum wells.

The dependence of the scattering rate on the well width and depth was examined briefly. The proximity of a continuum resonance to the top of the well determined the sharpness of the scattering function edge. This was quantified by the transition width, δE,

of the Fermi-Dirac fit, decreasing as the well thickness increased until a new subband was confined to the well. The more abrupt scattering functions resulted in effective barrier heights that decreased for wider wells, despite the rise in the potential barrier height. Meanwhile, the average scattering rate increased with the well thickness so that the emission rate also increased. This is opposite to the behaviour expected from classical theories of thermionic emission. As the well depth was varied, the effects of the first continuum resonance were again observed in the rising edge of the scattering function. However, in this case, they were small in comparison with the changes in the potential barrier height. As a result, the effective barrier height increased with the potential barrier. The scattering rate and the emission rate both decreased with increasing well depth, as expected classically. The preceding examinations were restricted to well configurations where only a single subband was confined to the well. In situations where multiple subbands are confined to the well, it becomes difficult to differentiate between scattering into continuum states as opposed to the broad resonances of upper subbands. This was only resolved satisfactorily in situations where the highest subband was sufficiently below the top of the well, or where it was so loosely confined that its lifetime was much shorter than the scattering time. Calculations were also performed for a set of well widths that resulted in two confined states, revealing characteristics similar to the single subband case. An oscillatory dependence on well width similar to that observed in quantum well carrier capture times was observed in the thermionic emission times.

Finally, an asymmetric well and symmetric well were compared. In the asymmetric well, the high barrier suppressed the scattering rate for energies just above the low barrier resulting in a 35% reduction in the thermionic emission time at low fields. At high fields, the emission times were reversed due to an enhancement in the scattering rate for energies below the barrier edge in the asymmetric case. The calculated times for the asymmetric well were compared to measured escape times as obtained from pump-probe measurements performed by Cavaillès *et al* (1992). While the measured escape times were well-reproduced within the thermally-assisted tunnelling regime (> 30 kV/cm), at low fields, the calculated thermionic emission times were 3-5 times too slow. The discrepancy between measured and calculated times is attributed primarily to the effects of band non-parabolicities and the omission of resonances in the continuum density of states. Other scattering processes not included here may also contribute to the 2D-to-3D scattering rate, however, they are expected to have only a minor effect on the calculated thermionic emission times. Finally, the discrepancy may be partially due to uncertainties in the experimental escape times arising from the complexity of the data analysis.

Chapter 5: Experimental Determination of Quantum Well Carrier Escape Rates.

In the preceding chapters, theoretical descriptions of the escape processes from semiconductor quantum wells were given. In this chapter, I will present an experimental determination of carrier escape rates from a strained InGaAsP/InP multiple quantum well (MQW) laser structure by time-resolved photoconductivity (PC). The first half of the chapter will describe the measurement technique and the experimental apparatus. The second half will contain the results of measurements performed on the strained InGaAsP/InP multiple quantum well sample. Finally, the measured escape times will be compared with those calculated using the methods described in the preceding chapters.

5.1. Time-Resolved Photoconductivity (PC): Introduction.

As described in the first chapter, photogenerated electron-hole pairs can relax by recombining within the quantum well or by escaping the well potential and recombining elsewhere. Carriers escaping from a well situated within the depletion region of a *p-n* or *p-i-n* junction will be swept to the contacts by the electric field. By connecting the contacts through an external circuit, we allow a photocurrent to flow, the measurement of which is the basis of the photoconductivity (PC) experiment. If the carriers are generated by a short pulse of light, the decay of the photocurrent corresponds to the escape rate from the well, provided that the transit time through the intrinsic region is short relative to the escape time and parasitics do not limit the response. This is the *time-resolved* PC experiment.

The main advantage of time-resolved PC is the simplicity of the analysis; in most regimes of interest, the escape lifetime is obtained directly from the decay of the photocurrent signal. However, in practice, it is more difficult to achieve the time resolutions that can be routinely provided by all-optical experiments such as pump-probe or up-conversion photoluminescence, where the resolution is limited primarily by the width of the excitation pulse. The high-speed limitations in electrical measurements are generally the combined result of the current measurement system (e.g.: an oscilloscope) and parasitics in the sample and sample mount. While oscilloscopes with 7 ps risetimes are currently available, the 50 Ω impedance of the circuit requires capacitances on the order of 100 fF for comparable RC time constants. Depending on the device structure, this can be difficult to achieve. Furthermore, microwave transmission lines are required throughout the circuit to transport the high frequency signals without introducing broadening or oscillations. Impedance mismatches must also be avoided, as they introduce further distortions in the signal. Despite these difficulties and limitations, time-resolved PC remains the most direct measurement of the carrier escape rates from quantum wells.

As the current measurement already requires electrical contacts to the sample, it is a relatively simple matter to apply an external bias. This provides control of the internal electric field. As described earlier, the tunnelling rate rises almost exponentially with the electric field, while the thermionic emission rate increases only slightly. Conversely, by performing experiments in a temperature-controlled environment the temperature sensitivity of the thermal escape processes is revealed, while the tunnelling rate is essentially unaffected. By varying these two parameters, it is generally possible to isolate one or the other escape mechanism, and hence measure the tunnelling or thermionic emission time. This becomes less clear when there are multiple confined subbands as the thermally assisted tunnelling process exhibits both the field dependence of tunnelling and the temperature sensitivity of thermionic emission.

5.2. Measurement Apparatus.

To perform time-resolved PC, two principal pieces of equipment are required. The first is a pulsed light source, usually a laser. The second is a high speed electrical measurement system, the simplest and most common of which is the sampling oscilloscope. Furthermore, microwave transmission lines and circuit elements are required to accommodate the high frequency signals.

5.2.1. Pulsed light source: gain switched diode laser.

The light source used in these experiments was a gain-switched diode laser. Gain switching is achieved by applying a large current pulse to a diode laser. The pulse must be short enough so that only one relaxation oscillation is excited, on the order of 0.1-1 ns. With this technique, 20 ps pulsewidths can routinely be achieved (Lau and Yariv, 1985), with pulses as short as 4 ps reported (Nagarajan, 1989).

The diode used in these experiments was a 1.3 μm Mitsubishi InGaAsP/InP laser with a 10 mA threshold current. This was driven by an Avtech pulse generator, which in turn was triggered by a programmable pulse generator driven at a repetition rate of 1 MHz. A DC power supply was also required to pre-bias the laser slightly below threshold.

The main drawback of the gain-switched diode laser is its low output power. Even at the relatively high repetition rate of 1 MHz, the average power output was less than a nanowatt. The signal generated in the samples was just sufficient to measure without preamplification.

An attempt was made to measure the pulse width of the diode laser using a high speed New Focus 1.3 μm detector. This revealed that while the pulse itself was on the order of a few hundred picoseconds, it was difficult to measure accurately due to the extensive time jitter. When averaged, the pulse appeared to be almost a nanosecond wide. However, as the measurements that will be discussed concentrated on the long portion of the photocurrent response where the time scales are generally longer than a nanosecond, this should not affect the analysis. As a check, measurements were also performed using the 100 ps pulses from a Nd:YAG laser. The PC responses obtained using this light source were no faster than with the diode laser.

5.2.2. High speed current measurements.

While it is relatively easy to excite carriers with short pulses of light, it is somewhat more difficult to extract them from the active region and measure that escape rate externally. The first requirement is a means of measuring the photocurrent with a time resolution on the order of tens of picoseconds. This is most easily accomplished with a digital sampling oscilloscope. In these experiments, a Tektronix CSA 803 communications signal analyzer mainframe was used, with SD-24 and SD-32 sampling heads giving bandwidths of 20 GHz and 50 GHz respectively. As the signals obtained in these experiments were limited to >500 ps by device parasitics, the 20 GHz head was used in all measurements.

This bandwidth corresponds to a minimum risetime of 18 ps. The mainframe is computer controllable via a GPIB parallel interface, allowing control of all front panel functions as well as permitting transfer of data, ie.: traces, to the computer. The traces were averaged either 128 or 256 times by the oscilloscope prior to transfer.

5.2.3. Microwave transmission lines.

The high frequencies contained in the PC responses require microwave transmission lines to carry the signal between the device and the sampling head. For frequencies up to 20 GHz, high quality coaxial cable with SMA connectors is adequate; for higher frequencies either K-connectors or V-connectors must be used. The standard impedance of the transmission lines is 50 Ω, and any deviations from this impedance will partially reflect the signal. The reflections appear as a series of notches or bumps in the oscilloscope trace that have the same basic shape as the original response. The number and amplitude of the reflections depends on the magnitude of the mismatch, while their relative position in the signal depends on the location of the impedance mismatch in the circuit.

The sensitivity of the system to impedance mismatches was demonstrated by the fact that significant reflections could be produced by improperly tightened SMA cable connectors. Some reflections were unavoidable, as with the bias-tee used to apply a DC voltage to the sample; this device always presented a small impedance mismatch. To keep these reflections away from the main part of the response, three feet of 50 Ω coaxial cable were used to distance the bias-tee from the sampling head. This placed the reflection at approximately 12 ns following the peak of the signal.

The bias-tee was necessary to apply a DC bias to the sample without placing the DC circuit elements in the high frequency path. It is a simple device composed of an inductor and a capacitor, as illustrated in Fig. 5.1. The inductor isolates the DC supply from the AC circuit which is coupled in via the capacitor. The DC coupled measurement circuit employed in these experiments is shown in Fig. 5.2. Here the device under test is connected to the bias-tee on one end and the oscilloscope on the other. The DC supply is connected to the inductor, while the capacitor is grounded via a 50 Ω termination. The AC current path is shown by the arrow. Note that the total resistance in the circuit, excluding the device under test itself, is 100 Ω as opposed to 50 Ω. This is an unfortunate drawback to this configuration as it doubles the RC time constant due to the parasitic capacitances in the circuit. The 3dB frequency response of the bias-tee used in these experiments was 100 kHz to 50 GHz.

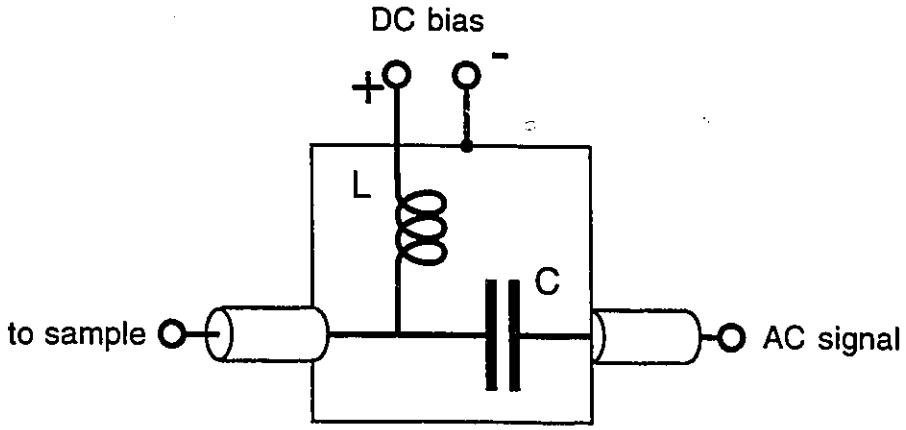

Fig. 5.1: Bias-tee. The inductor isolates the DC circuit elements from the AC circuit which is coupled via the capacitor.

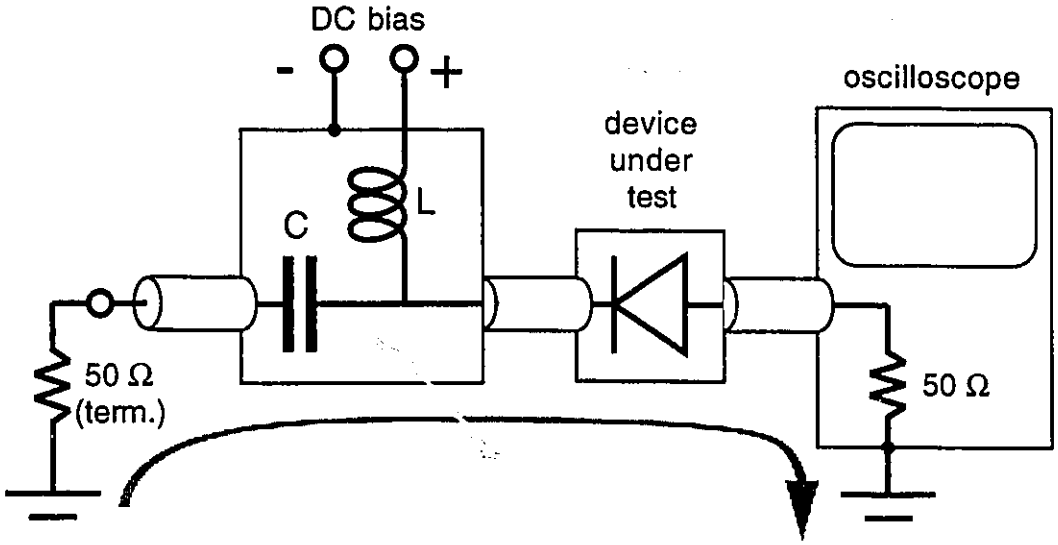

Fig. 5.2: DC coupled bias-tee configuration. All of the sample current passes through the 50 Ω termination within the oscilloscope. The AC circuit is completed by terminating the capacitor in 50 Ω. The grey arrow indicates the AC current flow.

5.3. Sample/Mount Requirements.

Perhaps the greatest difficulty in performing high speed electrical measurements is extracting the actual device response and delivering it to the scope without degradation. This places stringent requirements on the sample, the sample mount and the transmission line to the sampling head. In particular, stray or parasitic capacitances and inductances must be minimized. Impedance mismatches must also be avoided.

5.3.1. Device parasitics.

For any semiconductor structure, the contact layers and/or metal pads or lines will introduce parasitic capacitances. In the *p-i-n* laser structure, the *p* and *n* contacts form a parallel plate capacitor so that the device capacitance is given approximately by

$$C_{dev}=\frac{\varepsilon A}{d} \tag{5.1}$$

where ε is the dielectric constant in the intrinsic region, A is the area of the smaller contact, and d is the thickness of the intrinsic region. In the above it is assumed that the depletion of the contacts is negligible, as are any edge effects which may result from the finite size of the contacts or from one contact being smaller than the other. To minimize this capacitance it is necessary to keep at least one of the contacts small. In a properly made ridge waveguide structure, the ridge makes up the entire top contact and so it is possible to have a very small capacitance. However, as we will see, this is not always easy to achieve in practice.

The dominant parasitic inductance in a mounted sample comes from the wirebond(s) connecting the device to the transmission line. This is minimized by keeping the wirebond as short as possible, as the inductance scales with the length. It was found that lengths of <2mm were required to prevent the appearance of significant oscillations or broadening in the signal.

5.3.2. Sample mounts.

The InGaAsP/InP lasers were mounted on DC mounts, as illustrated in Fig. 5.3. The high frequency signal was extracted by bringing the centre conductors of two SMA connectors as close to the sample as possible. This is shown in Fig. 5.4. A wirebond is

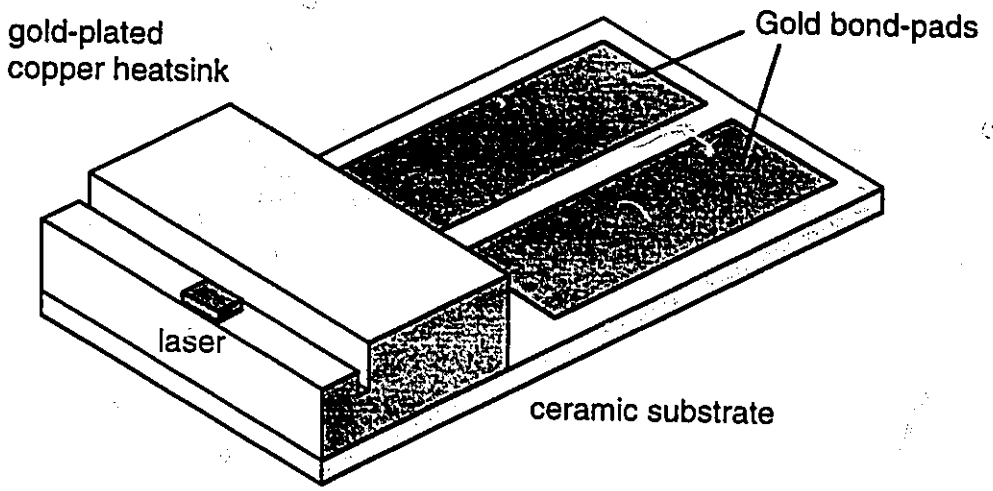

Fig. 5.3: InGaAsP/InP laser mount. The cleaved laser is mounted on the front ledge of the gold-plated copper heatsink which is in turn secured to a ceramic substrate with two gold contact pads. Since the substrate is conducting in these devices, one of the contacts is made via the gold plated heatsink while the other requires a wirebond to the top metallization of the device.

made to the top contact of the laser and then attached to the centre conductor of one of the SMA connectors with silver paste. The device itself was bonded to a gold-plated copper heatsink, providing contact to the *n*-type substrate. The copper block was then electrically connected to the centre conductor of the other SMA jack with silver paste. While this arrangement obviously included some significant impedance mismatches, the parasitic capacitance of the device itself limited the response to ~1 ns so that the reflections due to the mount were on too short a timescale to be observed.

5.4. The Time-Resolved Photoconductivity Setup.

The individual elements described in the preceding sections were assembled to form a high-speed, time-resolved PC measurement setup, as illustrated in Fig. 5.5. The sample was mounted within a vacuum chamber so that measurements could be performed at low temperatures. Two different cryostats were used. The first employed a closed-cycle liquid helium refrigerator which could reach temperatures from 45 K up to room temperature. The main disadvantage of this system was that the vibrations from the compressor could not be fully isolated from the sample stage. Due to the extreme sensitivity of the optical alignment into the waveguide, these vibrations produced intolerable amounts of noise in the oscilloscope signal. As a result, measurements could not be made with the compressor running but were instead performed as the sample warmed up after the compressor was

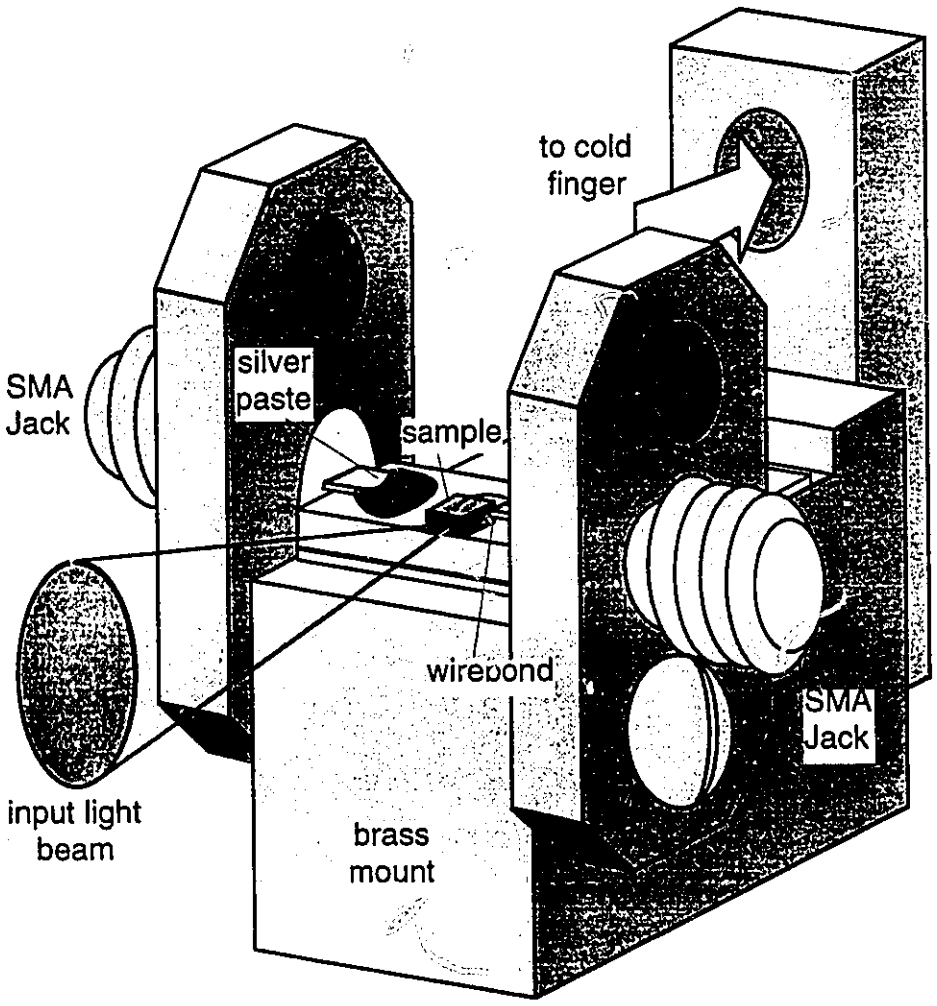

Fig. 5.4: InGaAsP laser sample holder. The laser mount is fastened to the brass block using silver paste. Electrical contact to the device is via the wirebond to the top contact while the substrate is accessed through the gold-plated copper block. Optical access is via the front facet.

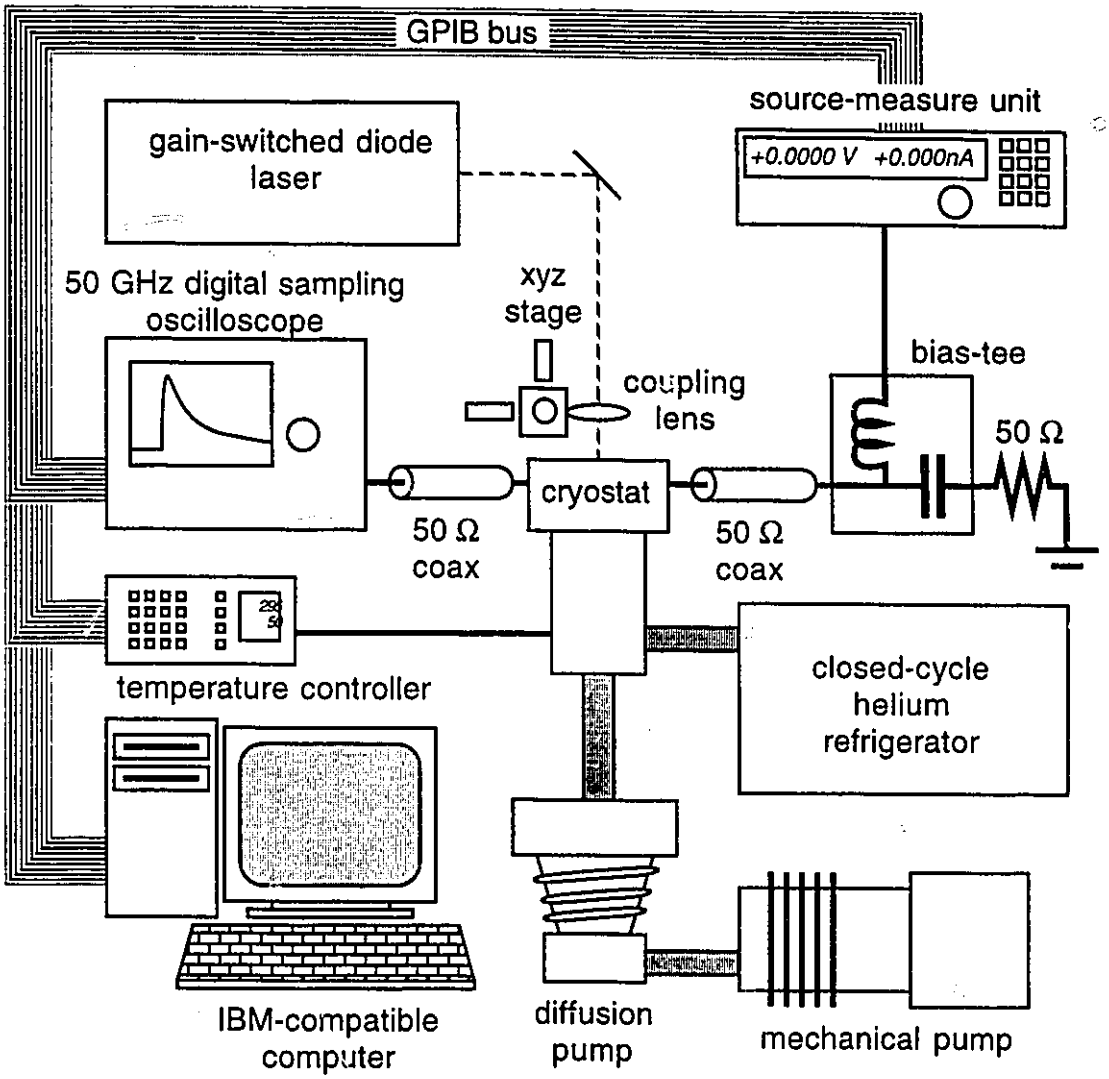

Fig. 5.5: Time-resolved photoconductivity measurement system. The light from the gain switched diode laser is coupled into the sample mounted in the cryostat. The photocurrent is extracted with the aid of a bias-tee and measured on the sampling oscilloscope. The temperature controller, oscilloscope, and SMU are computer-controlled via the GPIB bus.

alignment into the waveguide, these vibrations produced intolerable amounts of noise in the oscilloscope signal. As a result, measurements could not be made with the compressor running but were instead performed as the sample warmed up after the compressor was turned off. This added some uncertainty to the results since the temperature was continuously changing, however, the thermal drift during any measurement was never more than 2 or 3 K.

The second system was introduced later to resolve this problem of thermal drift. It has a liquid nitrogen cooled cryostat where the sample is mounted on a cold finger which extends from a reservoir of liquid nitrogen. Depending on the spacer used to separate the heater and sample stage from the nitrogen reservoir, the stage can reach temperatures as low as 80 K, with a range of approximately 170 K. In both systems, temperature control was provided by a Lakeshore temperature controller. This system was assembled after the time-resolved PC measurements had been performed and was used only for the current-voltage measurements.

The light from the gain-switched diode laser was steered towards the cryostat and coupled into the sample using a lens mounted on an *xyz* translation stage. The focal length of the lens was chosen to be as short as possible to provide the smallest spot size and hence the most efficient coupling into the waveguide. In these experiments, because the sample was mounted within a cryostat, the working distance of the lens was limited by the separation between the sample and the optical access window. As a result, the shortest focal length allowed was between 50 and 75 mm.

The electrical connections to the sample were made via microwave vacuum feedthroughs and standard flexible coaxial cables with SMA connectors inside and out. The electrical circuit was assembled according to the DC coupled circuit of Fig. 5.3, where the photocurrent traces were measured by the Tektronix digital sampling oscilloscope. The bandwidth of the measurement system was limited by the SMA connectors to 18.5 GHz.

The DC supply used in the experiments was a Keithley 238 source-measure unit (SMU). This is an extremely versatile piece of equipment that sources voltage or current from 100 μV to 100 V or 100 fA to 1 A, while simultaneously measuring the voltage or current with sensitivities of 10 μV and 10 fA respectively. The measurement capabilities were used to simultaneously measure photocurrent while the oscilloscope was taking traces. It is also computer-controllable via a GPIB interface allowing the computer to set the voltage and read the measured currents.

The sampling oscilloscope, SMU, and temperature controller were controlled by a desktop computer via an IEEE-488 interface bus. This permitted automation of the

measurement routines and downloading of the data including the sampled traces, the DC currents and the sample temperatures. The measurement routines were written in Microsoft QuickBASIC and allowed user-defined measurement scans, data storage, and included some crude graphics. Measured data were stored in ASCII formatted files to allow easy transfer to other programs or operating systems.

5.5. Test structures: Strained InGaAsP/InP Multiple Quantum Well Laser Structure.

Carrier sweepout rates in reverse-biased quantum well laser structures were first studied in detail by Moss *et al* (1992a, 1992b) in a GaAs/AlGaAs single quantum well GRaded INdex Separate Confinement Heterostructure (GRINSCH) ridge-waveguide laser. They found that despite being optimized for efficient electron and hole *capture*, the escape times were as short as 25 ps in reverse bias. The combination of a fast response and ~100% internal quantum efficiency in a reverse biased laser structure has implications for the monolithic integration of lasers, detectors, and modulators (via the QCSE).

The strained laser structure studied in this thesis was grown by Dr. Norbert Puetz at Bell-Northern Research in Nepean, Ontario, for Dr. John Evans as part of his doctoral thesis (1994). It was one of a series of four structures which were nominally identical save for the composition of the three quantum wells in the active region. These four structures were also studied by this author and reported previously (Takasaki, 1992, 1993); the material and laser characteristics of the samples will be summarized here.

Of the four structures described in the previous work, only the sample with 1.2% tensile strained wells will be studied here. The reason for this choice will be made clear at a later stage. The active region consists of three 63 Å $In_{0.36}Ga_{0.64}As$ quantum wells separated by 100 Å $In_{0.87}Ga_{0.13}As_{0.29}P_{0.71}$ barriers. The well region is flanked by 700 Å of barrier material followed by a 700 Å $In_{0.92}Ga_{0.08}As_{0.17}P_{0.83}$ step-index confinement region. Both the barrier and confinement regions are lattice-matched to the *n*-InP substrate, and the entire active region is intrinsic. Between the confinement region and the top *p*-InP contact there is a 50 Å InGaAs etch-stop layer that forms a narrow quantum well at the interface; there is no corresponding layer at the *n*-InP interface. The zero-bias bandstructure is illustrated in Fig. 5.6, where the band-bending at the contact layers has been omitted.

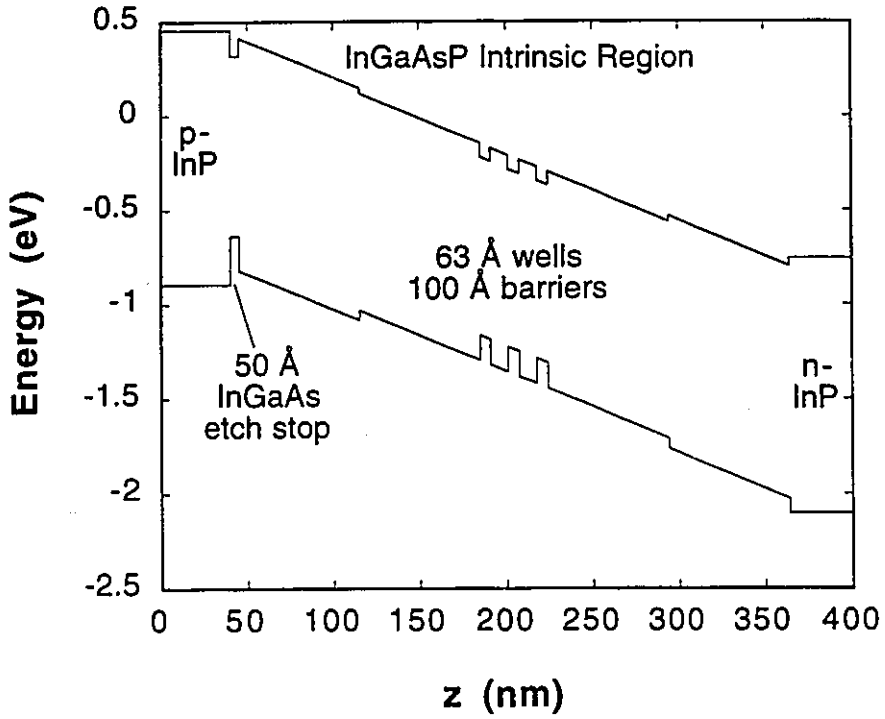

Fig. 5.6: Band structure of 1.2% tensile strained InGaAsP/InP multiple quantum well laser structure under 0 V external bias. Band bending at the InP interfaces has been omitted for simplicity. A conduction band offset of 35% was assumed. Shaded areas indicate doped regions.

5.5.1. Material characteristics.

Samples from this wafer were studied by transmission electron microscopy (TEM) to confirm layer thicknesses and investigate material quality. The resultant images were presented previously (Takasaki, 1992). While no defects were visible, indicating good material quality, the images did reveal that the well thickness was 63 Å, as opposed to the specified 55 Å. This resulted in a shift in the photoluminescence wavelength from the desired 1.30 μm to 1.39 μm.

Devices from this wafer were processed into ridge-waveguide laser structures; no special processing steps were required for the time-resolved photoconductivity experiments. The ridge is formed by etching two trenches through the *p*-InP contact layer down to the InGaAs etch-stop, leaving a 2 μm rib. An SiN_2 dielectric layer isolates the top metallization from all surfaces except for the top of the ridge. The device structure is schematically illustrated in Fig. 5.7. Samples were then cleaved into 250 μm, 500 μm and 1000 μm cavity lengths. The lasing characteristics were described previously where a

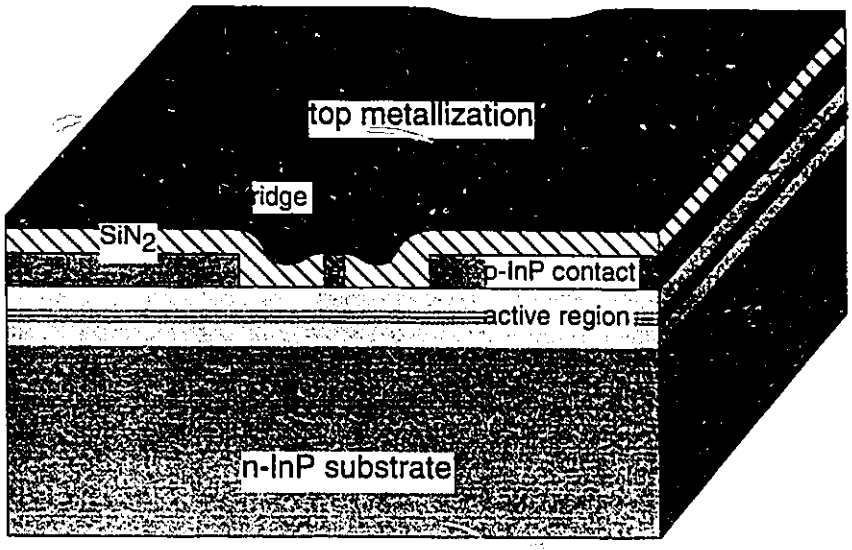

Fig. 5.7: Schematic illustration of the ridge-waveguide structure. The entire active region is intrinsic. Not to scale.

typical lasing threshold for a 500 μm cavity length was approximately 20 mA (Takasaki, 1992).

As discussed previously in this chapter, the time-resolved photoconductivity experiment requires a small device capacitance to minimize the RC time constant. The smallest devices, with 250 μm cavity lengths, had capacitances of approximately 10 pF. This combined with the 100 Ω series resistance of the two terminations in the AC circuit shown in Fig. 5.2 gives an RC time constant of 10 ns. Recall that the device capacitance in a *p-i-n* structure can be modelled as a parallel plate capacitor where the area is given by the smaller contact. In a ridge-waveguide structure, this should correspond to the ridge alone, however this is inconsistent with the observed capacitance. Two explanations are possible. Either the dielectric is not thick enough, so that the entire top surface acts as the top plate in parallel with the ridge, or there is a conductive path linking the ridge to the contact material outside the trenches. The InGaAs quantum well at the InP interface would be filled with holes supplied by the contact dopants and as a result could fulfill this role. Both of these possibilities are consistent with the observed capacitance. In any case, the measurements were limited to 1 ns resolution by the RC time constant.

The devices were mounted on gold-plated copper heat sinks which were in turn mounted on ceramic carriers. A wirebond contacted the top-side metallization while the substrate was accessed via the gold surface of the copper heat sink. These were then mounted within the cold chamber as described in the previous sections.

5.6. Experimental Results.

5.6.1. Current-voltage characteristics.

Current-voltage characteristics of the strained InGaAsP/InP MQW laser structure were measured as a function of temperature and are plotted in Fig. 5.8. Points were taken over a voltage range of -11 V to 1 V, in 0.1 V steps, for sample temperatures of 110 K, 150 K, 200 K, 250 K, and 300 K. Note that negative voltages correspond to reverse biases. As these measurements were carried out in the liquid N_2 cryostat, the lowest accessible temperature (with that particular set of spacers) was 110 K. Reverse breakdown is gradual, but can be considered to occur at reverse biases greater than -8 V at all temperatures.

5.6.2. Time-resolved photoconductivity.

Time-resolved photoconductivity measurements were performed over a temperature range of 50 K to 300 K and applied biases of -5 V to 1 V. The room temperature results

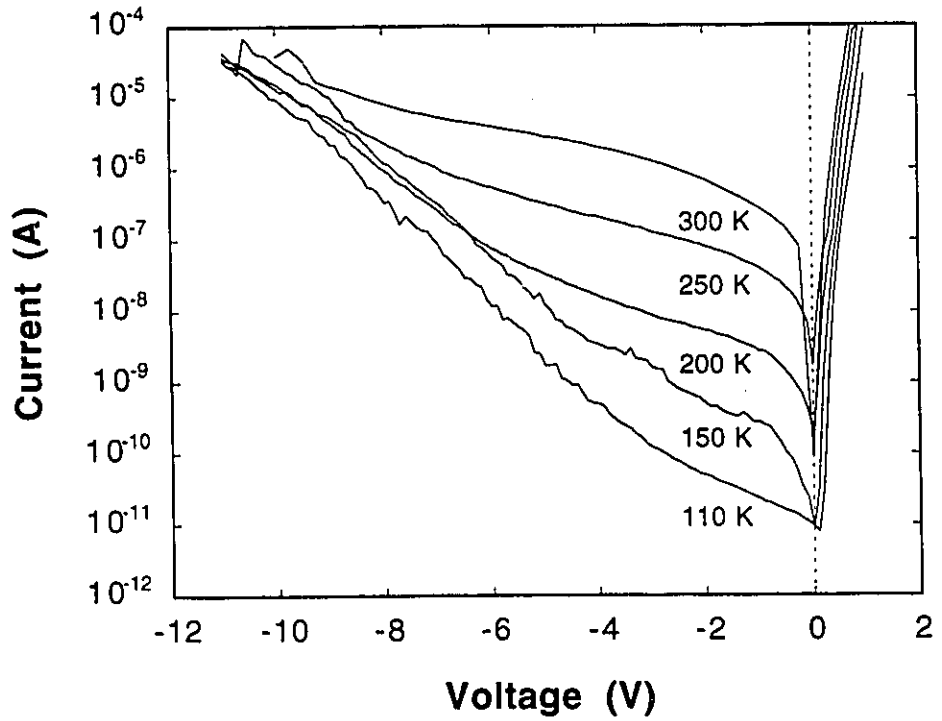

Fig. 5.8: Current-voltage characteristics of 1.2% tensile strained InGaAsP/InP MQW laser structure. Curves are given for sample temperatures of 110 K, 150 K, 200 K, 250 K, and 300 K. Breakdown occurs between -8 V and -10 V at all temperatures.

were reported previously (Takasaki, 1993) and will be summarized briefly here. When plotted on a logarithmic scale, the photocurrent decay was characterized by not one but two time constants, as illustrated in Fig. 5.9. The slow time constant was on the order of 10 ns while the fast time constant was approximately 1 ns. The origin of the two-component decay was shown to be due to the separate escape of electrons and holes from the active region (Takasaki, 1993). The fast component was attributed to the electrons, due to their lighter effective masses and shallower potential wells, while the slow component was assigned to the holes.

Since the fast response was limited by the RC time constant under many situations, we will concentrate instead on the holes. The hole escape times as a function of temperature are presented in Fig. 5.10 for applied biases of -0.5 V, 0.0 V, and 0.5 V. For larger reverse biases, the measured decay time was limited by the RC time constant. The strong temperature dependence observed in the 0.0 V and 0.5 V data indicates that in forward bias, the escape is dominated by a thermal process. At -0.5 V, a similar temperature dependence is observed between 100 K and 200 K, while below 100 K the escape time is flat. It appears that in this case, there is a transition between tunnelling at low temperatures and thermal escape at higher temperatures. It remains to be determined if the thermal process is thermionic emission or thermally-assisted tunnelling. Above ~200 K the response flattens at all biases, indicating that the response is limited by parasitics.

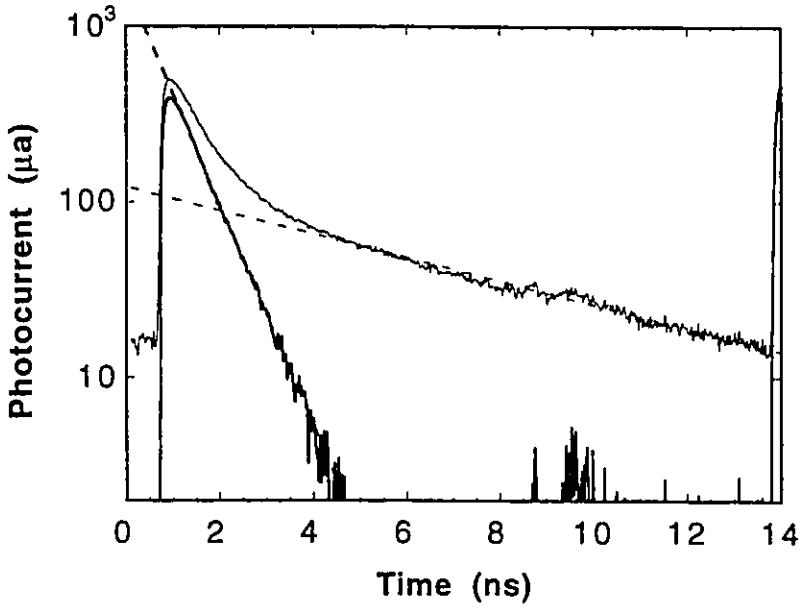

Fig. 5.9: Time-resolved photoconductivity trace showing two exponential decays. The slow time constant is on the order of 10 ns and is attributed to the holes escape, while the fast time constant is on the order of 1 ns and is attributed to the electrons.

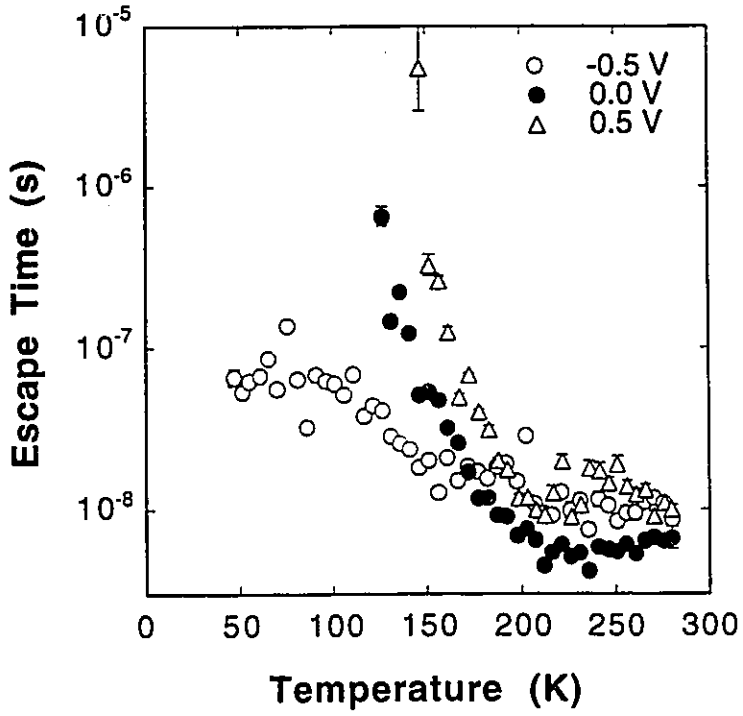

Fig. 5.10: Measured hole escape times in a 1.2% tensile strained InGaAsP/InP MQW laser structure as a function of temperature, for applied biases of -0.5 V, 0.0 V and 0.5 V. For larger reverse biases the decay time is limited by the RC time constant. The 0.0 V and 0.5 V data exhibit a strong temperature dependence indicating a thermally-activated process, while at -0.5 V tunnelling appears to dominate below ~100 K. Above 200 K, the temperature independent behaviour is due to parasitic limitations.

The traditional approach to analyzing thermally activated processes is the Arrhenius plot. Unfortunately, in cases where there are more than one subband, the expression (2.39) does not lend itself to the usual τ vs. $1/k_BT$ plot, and in the valence band there are always at least two subbands, one each for the light and heavy holes. Fortunately, the energy separation between the first two subbands is large enough that at low temperatures, the exponential term arising from the occupation of the ground state dominates the summation. In this case, the equation reduces to

$$\tau_{TE} = \frac{m_1^* e^{\Delta E_{1,eff}/k_b T}}{\left(\sum_i \frac{m_i^*}{\tau_{s,i}}\right)} \tag{6.1}$$

which is of the form necessary for an Arrhenius plot. Such plots were made for the bias and temperature regimes where the escape was obviously thermally activated. These are shown in Fig. 5.11. for biases of (a) 0.0 V, (b) 0.25 V, (c) 0.5 V, and (d) 0.75 V. Also

shown are the fitted lines whose slopes give the activation energy, while the intercepts correspond to the constant term consisting of the effective masses and scattering times.

The activation energies obtained from the Arrhenius plots can be compared to calculated values of the potential barrier heights. Since the presence of strain does not significantly alter the effective mass in the z-direction, bulk values can be used to calculate the subband energies (Hensel and Feher, 1963), (Foreman, 1994). The valence band offset is also required, however there remains some dispute over which determination is most accurate. Reported values range from 40% to 75% of the total bandgap difference (Forrest, 1984), (Uomi, 1990), (Soucail, 1990), (Nag, 1991), (Koteles, 1993), (Queisser, 1994), although the majority of studies now indicate that the band offset is in the

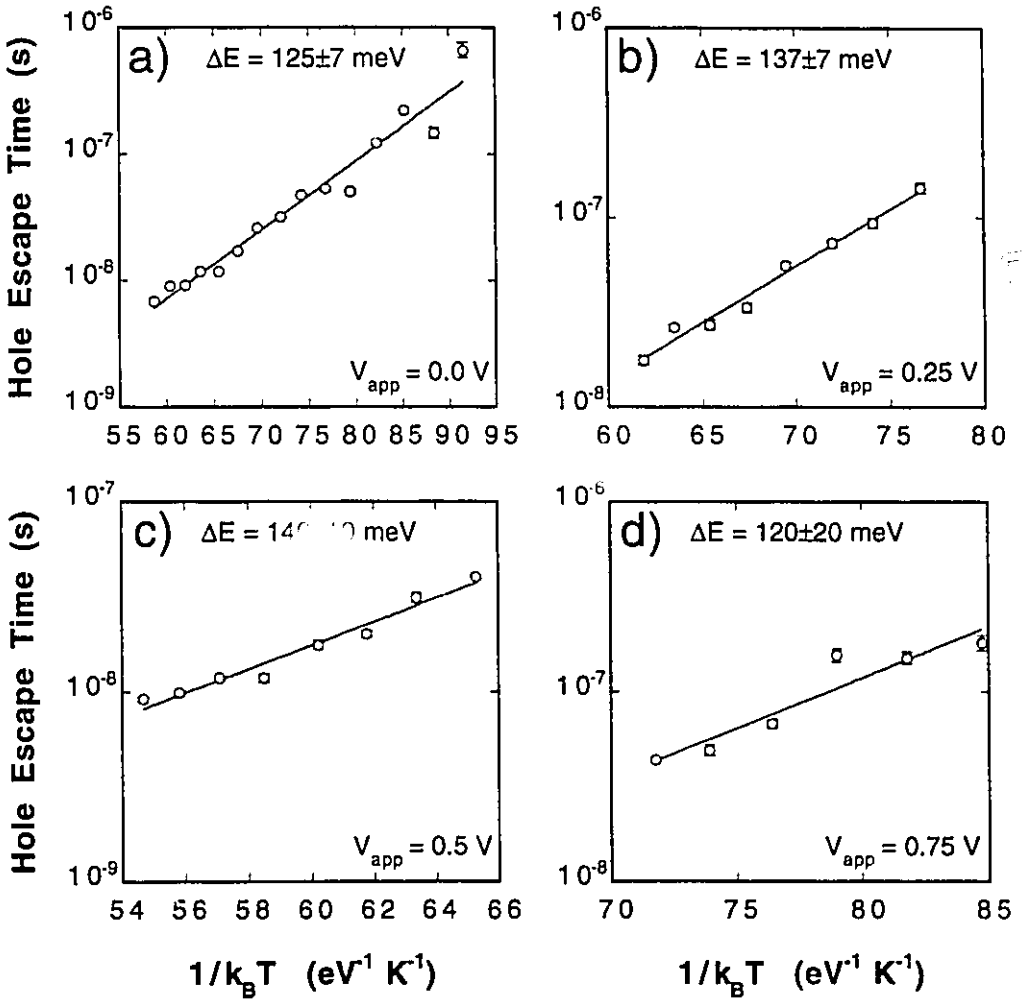

Fig. 5.11: Arrhenius plots of the hole escape time for the strained InGaAsP/InP MQW laser structure for biases of (a) 0.0 V, (b) 0.25 V, (c) 0.5 V, and (d) 0.75 V. The slopes give the barrier height while the average scattering times can be derived from the intercepts.

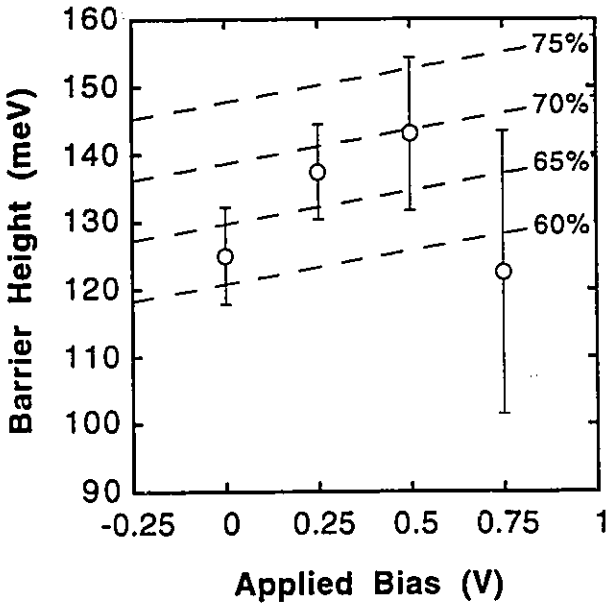

Fig. 5.12: Measured barrier heights obtained from Arrhenius plots. The dashed lines give the calculated potential barrier heights assuming valence band offsets of 60%, 65%, 70%, and 75%. A band offset between 65% and 70% is indicated. Note that the large error bars on the 0.75 V data point reflect the poor signal-to-noise as the PC signal weakens near flat-band conditions.

neighbourhood of 60-75% (Uomi, 1990), (Queisser, 1994). Fig. 5.12 shows the measured effective barrier heights compared with the calculated potential barrier heights (dashed lines) based on valence band offsets of 60%, 65%, 70%, and 75%, where the linear barrier lowering term has been added. The barrier lowering was included to approximate the field dependence observed in the Arrhenius plots of the calculated thermionic emission times. As shown in Fig. 4.20 (a), the activation energies from the calculated emission times lie some 10 meV above the lowered potential barrier, decreasing smoothly, but non-linearly, with the electric field. The magnitude of this offset will depend on the well width and depth due to the variations in the rising edge of the scattering function. Adding 10 meV to each dashed line in Fig. 5.12 would essentially shift each of the labels upwards, such that the 75% line would correspond to 70%, the 70% line to 65%, etc. Obviously, the error bars permit a range of valence band offsets; however, a value of between 65% and 70% gives the best agreement with the data. Including the 10 meV offset shifts the range to 60-65%, so for now we will assume a value of 65%. We will find that this particular choice of band offset also gives excellent agreement with the calculated tunnelling escape times.

We can now perform calculations of the escape times from the well and compare them with the measured values. The relevant material parameters for the quantum well are

given in Table 5.1, including the bulk effective masses and band gaps. Since the quantum well material is an alloy of InAs and GaAs, these parameters were obtained by linear interpolation of the InAs and GaAs values. Based on the 65% valence band offset, the subband energies were calculated, where it was assumed that the wells are isolated. This is a reasonable approximation due to the 100 Å thickness of the barriers. The presence of tensile strain in the wells shifts the light and heavy hole energies so that the $k = 0$ degeneracy is lifted (Hensel and Feher, 1963). In essence, the light and heavy holes sit in different potential energy wells that are spatially coincident. The energy shifts of the band edge energies were calculated by Evans (1994), however he calculated the well depths based on a 60% valence band offset. These were corrected to the 65% valence band offset to give a light hole well 195.9 meV deep while the heavy hole well has a depth of 92.8 meV. To calculate the thermionic emission and thermally-assisted tunnelling times, the in-plane effective masses are required. These were calculated according to the theory of Chuang (1991) using the Luttinger parameters given by Landolt-Börnstein (1987). The effective masses at the subband minima are given in Table 5.2, along with the subband energies. The hole band structure in the parabolic approximation is illustrated in Fig. 5.13.

TABLE 5.1: Bulk material parameters for the strained InGaAsP/InP multiple quantum well laser.

Parameter	Value
Lattice constant (barrier), a (Å)	5.869
Well band gap, E_g (eV)	0.946[†]
Barrier band gap, E_g (eV)	1.15[†]
Static dielectric constant, ε_s	13.89
High frequency dielectric constant, ε_∞	11.38
LO phonon energy, $\hbar\omega_0$ (eV)	0.03386
Light hole effective mass, quantum well, $m^*_{LH,w}$ (m_0)	0.0532[†]
Heavy hole effective mass, quantum well $m^*_{HH,w}$ (m_0)	0.4676[†]
Light hole effective mass, barrier, $m^*_{LH,b}$ (m_0)	0.0773[†]
Heavy hole effective mass, barrier $m^*_{HH,b}$ (m_0)	0.7194[†]

all values from Landolt-Börnstein (1987).

[†]calculated by Evans (1994).

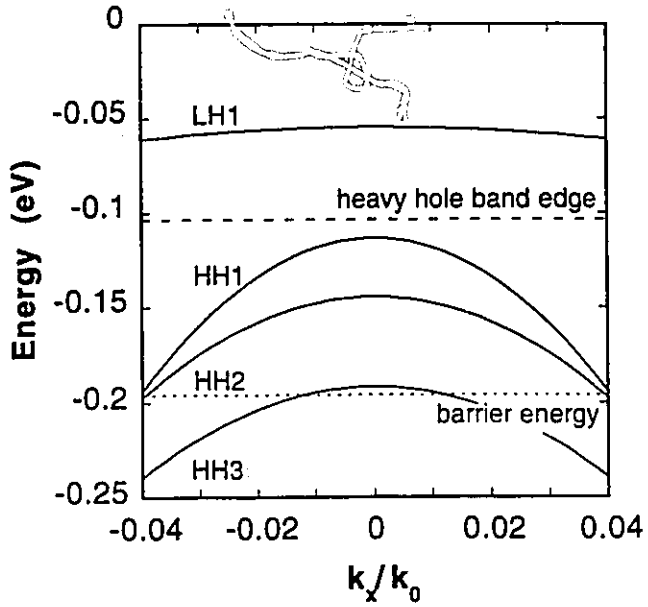

Fig. 5.13: Calculated band structure for the tensile strained InGaAs quantum well. The presence of tensile strain shifts the light hole band up in energy, while the heavy hole band moves down. The subbands are assumed to be parabolic and the effective masses at the subband minima were calculated according to the theory of Chuang (1991). The energies are relative to the bottom of the light hole well. The dashed line indicates the bottom of the heavy hole well and the dotted line marks the barrier energy for both light and heavy holes.

TABLE 5.2: Calculated hole energies and effective masses at the subband minima for the strained InGaAsP/InP multiple quantum well laser. Effective masses were calculated according to the theory of Chuang (1991).

	LH1	HH1	HH2
Energy (eV)	0.054	0.113	0.144
Effective mass, m^* (m_0)	0.271	0.0215	0.0328

The assumption of parabolic bands is typically much poorer in the valence band than the conduction band due to the intermixing of the many hole subbands (Foreman, 1994). In this particular case however, the tensile strain actually reduces the degree of intermixing by lowering the light hole well while raising the heavy hole well. This makes the ground state a light hole (LH) state which actually has a large in-plane effective mass (Hensel and Feher, 1963), (Eppenga, 1987). The upper subbands are heavy hole (HH) states with small in-plane effective masses. As a result, the calculated valence band structure shown in Fig. 5.13 contains almost no instances of the subband crossings that would lead to large non-parabolicities (Weisbuch, 1991). It is because of the expected

reduction in non-parabolicities that this structure was chosen for the experiments. For both compressively strained and unstrained wells, the ground subband is a heavy hole subband with a small in-plane effective mass. This narrow subband will inevitably intersect a higher energy light hole subband which has a heavier in-plane mass. This is illustrated schematically in Fig. 5.14.

Fig. 5.15 shows the calculated (lines) and experimental (points) overall escape times for the strained InGaAsP/InP MQW laser structure under applied biases of -0.5, 0.0 V, and 0.5 V. In the calculations, the electric field across the well was calculated by assuming that all of the voltage is dropped across the 3165 Å of intrinsic material. The total voltage is the sum of the applied bias and the 1.2 V built-in potential of the junction. The qualitative agreement is reasonable, with the transition to tunnelling at low temperatures in the -0.5 V data well-reproduced. However, there are substantial quantitative differences. Within the thermally activated regimes, the calculated escape times are an order of magnitude too fast at 0.0 V, and almost two orders of magnitude too fast at 0.5 V. Furthermore, the shift with applied bias seen in the measured data is almost entirely absent from the calculated curves. The latter effect can be attributed to the presence of loosely bound subbands near the barrier energy for both the light and heavy holes. Since the lifetimes of the upper subbands were in all cases less than 100 fs, they were considered to be continuum states, as described in §4.7.12. However, this results in very sharp scattering functions even under large fields (eg.: 53 kV/cm at -0.5 V), as shown in Fig. 5.16. In fact, large peaks are generated at the edges of the HH-to-HH scattering functions, while the low energy tails due to the penetration of the final state wavefunction are comparatively small. Note that there is no tail in the HH2 scattering curves not because of an artificial cutoff but rather due to its proximity to the HH3 subband; scattering into the HH3 subband can occur directly from the HH2 subband minimum. Since the bias dependence observed previously in Chapter 4 was due to the combined effects of the smeared scattering function and the low energy tail below the barrier edge, the relative absence of these features in this case produces a much smaller bias dependence. If we consider instead a well where the loosely confined subbands are absent, the separation between the two experimental curves is well-reproduced. Given the band non-parabolicities expected in the valence band, it is conceivable that in the actual test structure, the upper subbands are absent resulting in the observed bias dependence.

It should be pointed out that although image charge lowering of the barriers was not included, because the hole escape corresponds to the majority unipolar case in an *intrinsic* well, the barrier lowering is *field-independent*. As a result, this effect would not produce

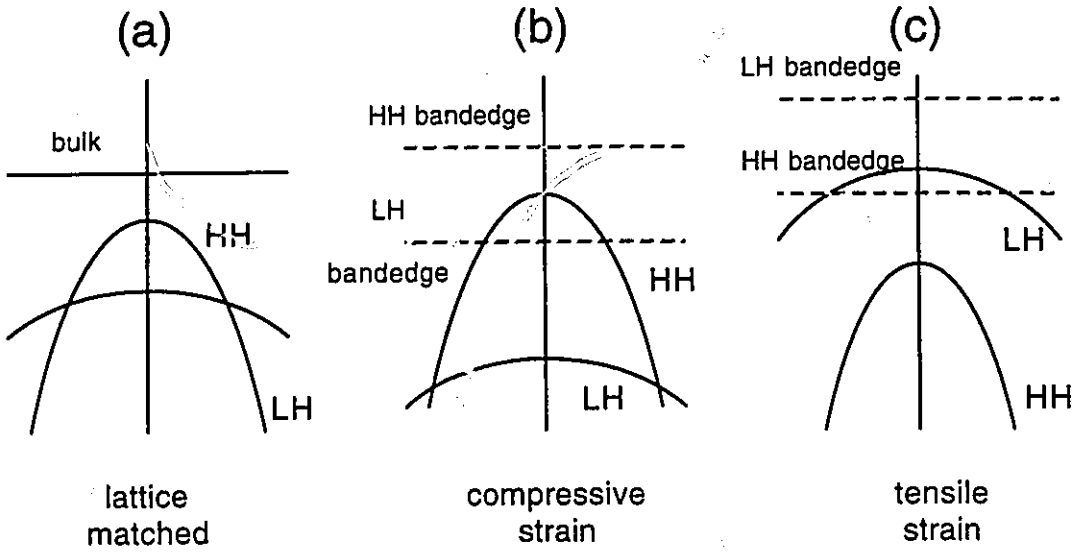

Fig. 5.14: Schematic illustration of light and heavy hole subbands in (a) unstrained, (b) compressively strained, and (c) tensile strained wells. Only the tensile strained well avoids the subband crossings that lead to large non-parabolicities.

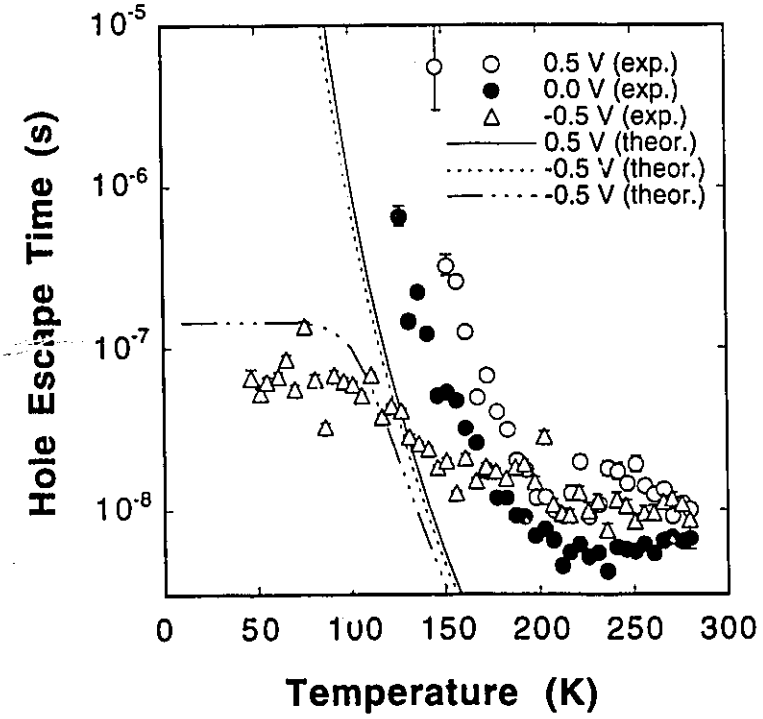

Fig. 5.15: Comparison of measured and calculated holes escape times for a tensile strained InGaAsP/InP MQW laser structure under applied biases of -0.5 V, 0.0 V and 0.5 V. A valence band offset of 65% was assumed in the calculations. While the general behaviour of the data is well reproduced, the calculations underestimate the measured values by as much as two orders of magnitude.

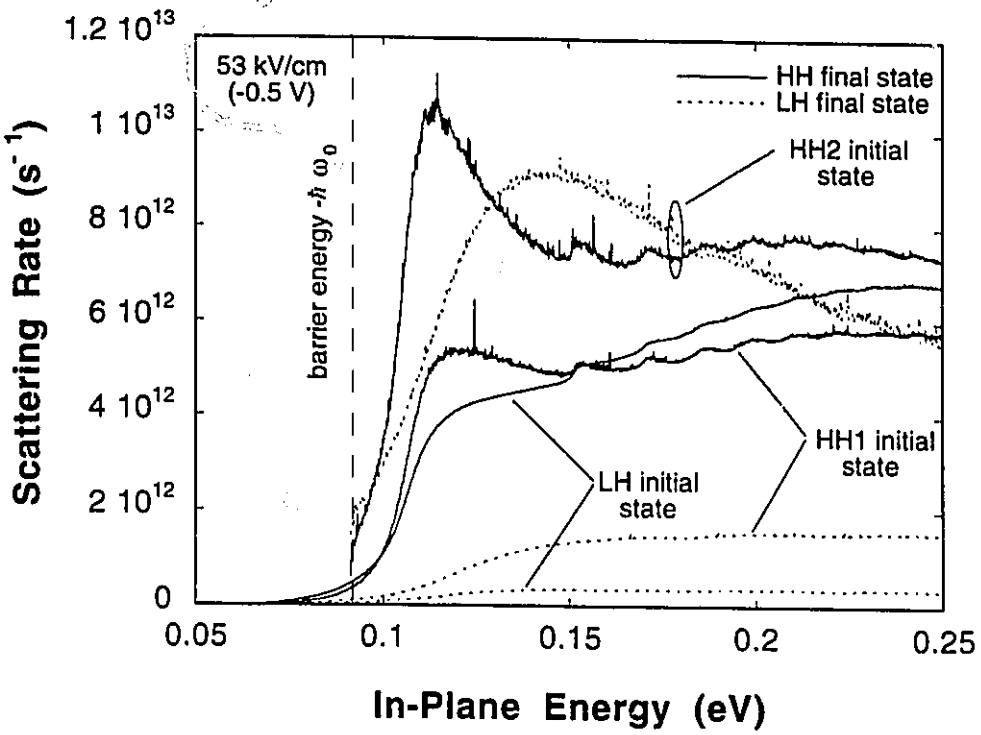

Fig. 5.16: Calculated LO-phonon scattering curves for the strained InGaAsP/InP MQW laser structure under -0.5 V reverse bias. The solid curves indicate scattering into heavy hole (HH) final states while the dotted curves indicate light hole (LH) final states. These are shown for scattering from the LH ground state and the first two HH subbands, denoted by HH1 and HH2. The vertical dashed line indicates the potential barrier height less the phonon energy, where the linear barrier lowering term has been included. The scattering functions all feature abrupt rising edges with comparatively small tails extending below the barrier energy. The loosely bound HH3 state produces peaks in both the HH1-to-HH and HH2-to-HH scattering rates. Note that the in-plane energy is relative to the LH ground state.

any additional separation between the curves. Furthermore, we can estimate the initial carrier density from the average photocurrent, based on an assumption of 100% internal quantum efficiency. This gives an average carrier density of ~10^{11} cm^{-2}, which corresponds to a barrier lowering of only 3 meV. This will produce only a minor increase in the thermionic emission rate.

The peaks in the scattering function due to the loosely confined upper subbands also significantly increase the overall scattering rate. To remove their effects from the scattering calculations we would have to set the lower E_z integration limit, E_{start}, to somewhere between the subband energy and the top of the well. However, in this case, the upper subbands are slightly *above* the potential barrier at the fields under consideration. Nonetheless, we can gain some insight into the impact of the upper subband on the escape rate by considering instead a slightly deeper well. For a 70% valence band offset, the uppermost heavy hole subband is ~4 meV below the potential barrier at 0.5 V, so that the

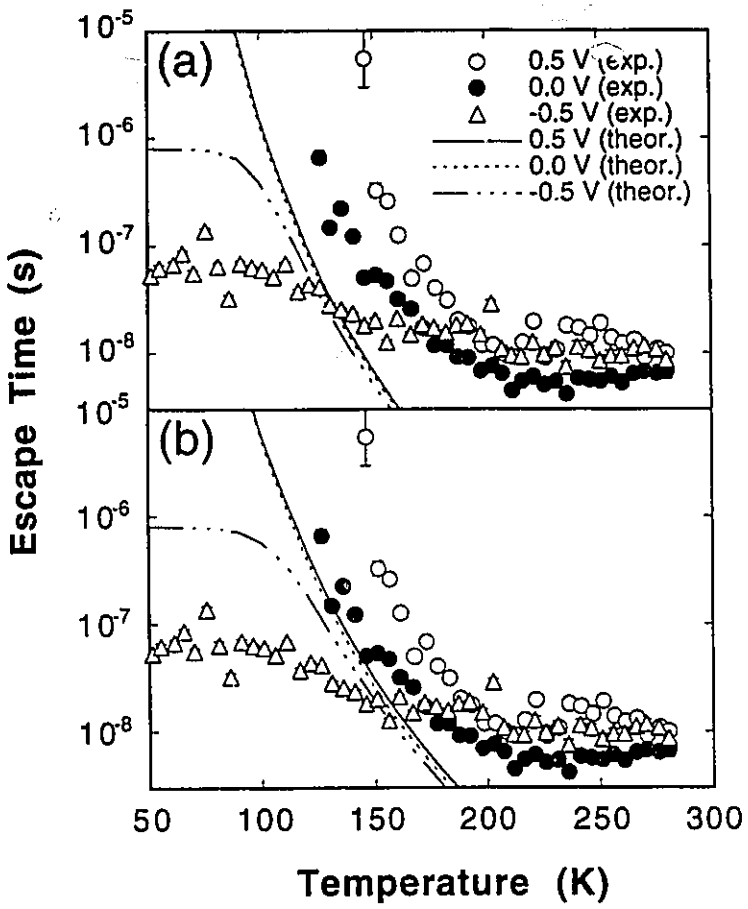

Fig. 5.17: Comparison of the measured and calculated hole escape times for a strained InGaAsP/InP MQW laser structure where the valence band offset has been increased to 70%. In (a) the loosely confined light and heavy hole subbands near the top of the well have been included in the continuum final states; in (b) the upper heavy hole subband has been excluded. Omitting the subband produces a 3-4 times increase in the thermionic emission time.

low energy cutoff was set equal to the potential barrier height. Note that this will exclude the low energy tail due to penetrating 3D states so that the field dependence will again be small. Fig. 5.17 (a) shows the measured and calculated escape times where scattering into the uppermost subbands has been included in the total 2D-to-3D scattering rate. Note that there is little difference from Fig. 5.15 where a 65% valence band offset was assumed. Fig. 5.17 (b) shows the measured and calculated escape times where the contributions due to scattering into the uppermost heavy hole subband have been omitted. The emission time is slower by a factor of 3-4 times relative to Fig. 5.17 (a). Since scattering into 3D continuum states at energies below the barrier edge has also been omitted, this procedure will slightly overestimate the effect of the uppermost subband. However, it does indicate that if in fact a loosely confined subband was not present near the top of the well, a

significantly longer escape time would be observed.

Since the band offset in this material system is not yet clearly established, this is another potential source of error. The choice of this parameter will affect the thermionic emission times by altering the subband energies, and moving the uppermost resonances away from the top of the well. However, as can be seen by comparing the plots in Figs. 5.15 and 5.17 (a), increasing the band offset only marginally improves the agreement with the thermionic emission time while increasing the error in the tunnelling time by a factor of ~9.

The large discrepancy between the calculated and measured data is perhaps expected, considering the potential complexity of the band structure involved. Previous calculations of hole escape times have met with a similar lack of success (Moss, 1994). Even though the occurrence of "band-crossings" should be minimized in this structure, significant non-parabolicities are likely. Valence band structure calculations for tensile strained InGaAsP/InP or InGaAs/InGaAsP quantum wells have been presented in the literature and a common feature is a dip or flattening of the light hole band near $k_{||} = 0$ (Chuang, 1991), (Chao and Chuang, 1992). This results in a very large density of states near the band minimum, which would increase the thermionic emission time. Furthermore, the assumption that the bulk effective mass can be used to calculate all of the subband energies will worsen at the higher energies (Ekenberg, 1989), (Chen and Andersson, 1991). Together, these effects will have a substantial impact on the calculated thermionic emission and thermally-assisted tunnelling times due to the changes in the hole distribution. A more accurate calculation of the escape times would require a detailed calculation of the valence band structure.

Also of significance is the fact that the measured times are for a multiple quantum well structure where there is the possibility of re-capture by adjacent wells. This has been shown to result in a slower overall escape time when compared to a single quantum well structure (Bambha, 1993). Finally, as suggested for the GaAs/AlGaAs calculation, the omission of impurity and interface scattering and the inaccuracies in the final state density of states may also contribute to the discrepancy between the measured and calculated escape times. However, where the escape time of electrons from the GaAs/AlGaAs wells was underestimated, the escape time from the strained hole wells is overestimated. Since both of these error sources would only reduce the escape rate, they cannot be responsible for the discrepancy here. We conclude, then, that the dominant sources of error in the strained InGaAsP/InP MQW laser calculations are the valence band structure and the omission of re-trapping effects in neighbouring wells.

5.7. Summary.

In this chapter, measured values of the hole escape time from quantum wells in a strained InGaAsP/InP laser structure have been presented. These were obtained from time-resolved photoconductivity experiments performed as a function of temperature and bias. The experimental apparatus consisted of a gain-switched diode laser to excite the electron-hole pairs in the wells and a 20 GHz digital sampling oscilloscope to measure the photocurrent generated by the escaping carriers. The high frequency signals required that special attention be paid to such considerations as parasitic inductances and capacitances, cables and connectors, and impedance mismatches.

The results of previous studies performed on these structures were briefly reviewed. The hole escape times were extracted from the slow time constant in the decaying PC signal. The slower holes were considered, rather than the electrons, due to the limitations imposed by the large parasitic capacitance. Arrhenius plots of the hole escape times were made in regimes where the escape was obviously thermally-activated. From the activation energies it was determined that a valence band offset of 65% provided the best agreement with the data. The hole escape times were then compared with calculated values at applied biases of -0.5 V, 0.0 V, and 0.5 V. While the general behaviour of the escape rates was well reproduced, particularly the transition between tunnelling and thermionic emission at -0.5 V, the quantitative agreement within the thermally-activated regions was poor. The minimal bias dependence exhibited by the calculated curves was attributed to the presence of loosely bound light and heavy hole states near the top of the well. In the absence of such states, the bias dependence would increase while the escape rate was shown to decrease by 3-4 times. The majority of the discrepancy between the measured and calculated escape times is expected to come from the valence band structure; a full calculation of the valence band structure is needed to further evaluate its effect on the emission rates. Re-capture by neighbouring wells is also expected to contribute to the observed discrepancy.

Chapter 6: Conclusions.

In this thesis, the escape processes from semiconductor quantum wells have been examined theoretically and experimentally, with an emphasis on the thermal escape processes. The problem of image charge lowering in a quantum well has been treated where the effects of the diffusion current have been included for the first time. It has been shown that the usual perfect conductor approximation applies only when the carrier densities are greater than $\sim 10^{12}$ cm^{-2}. For smaller densities, the diffusion current limits the accumulation or depletion of the carriers in the well resulting in a reduced image charge. To quantify the reduction in the barrier lowering, the concept of the *effective image charge* was introduced. In both the unipolar and bipolar wells, it was found that the effective image charge tends to zero for small (total) carrier densities and approaches the full electronic charge at high densities. In the case of a majority carrier escaping from a unipolar well, the image charge is further limited by the finite well carrier density. This leads to a field-independent barrier lowering at high fields, where the transition between the field-dependent and field-independent regimes occurs at an electric field that is proportional to the carrier density. In intrinsic unipolar wells, the electric field generated by the free carriers in the well is sufficient to make the majority unipolar barrier lowering independent of the applied field. In a doped unipolar well, some or all of the free charge will be compensated by the ionized dopants so that for sufficiently small excess carrier densities, the barrier lowering will be field-dependent.

The thermionic emission calculation was separated into low and high field regimes. At low fields, the emission rate is limited by the diffusion of continuum carriers away from the well, while at high fields, it is determined by the scattering rate from the 2D well states into the 3D continuum states. In order to predict the thermionic emission rate in the high

field regime, the 2D-to-3D scattering time was calculated for polar optical mode scattering by longitudinal optical phonons, and deformation potential and piezoelectric scattering by acoustic phonons. The effects of a perpendicular electric field were explicitly included. While similar scattering calculations have been reported previously (Shorthose, 1989), (Liang and Lent, 1990), (Tsai, 1994a, 1994b), (Rosencher, 1994), none included the acoustic phonon processes and either ignored the effects of an electric field (Liang and Lent, 1990), (Tsai, 1994a, 1994b) or, if included, presented calculations only for a particular structure (Shorthose, 1989), (Rosencher, 1994). It was found that, unlike in 2D-to-2D or bulk scattering, the 2D-to-3D scattering is dominated by LO phonons at all temperatures. This was shown to be due to an effective reduction in the electron barrier height by an amount equal to the LO phonon energy. Increasing the perpendicular electric field did *not* shift the onset of scattering to lower energies as predicted by the linear barrier lowering term, but instead produced a smearing effect in the rising edge of the scattering function. Furthermore, the rapid increase in scattering expected at energies just above the tip of the barrier was not observed under large fields. Instead the scattering rate rose gradually, starting well below the barrier energy. This effect suggests that image charge lowering will have only a minor effect on the emission rate, particularly at high temperatures and low carrier densities. Nonetheless, further investigations are necessary for a more complete assessment of its impact on thermionic emission calculations.

Two approaches for simplifying the thermionic emission calculations were presented, where the scattering function was approximated as a step-function or a Fermi-Dirac function. These are intended to form the basis for a simplified calculation of the thermionic emission time that does not require the complete scattering calculation described in §4.1-4.6 The step-function approximation was shown to be acceptable for quick calculations near room-temperature, otherwise the more complex Fermi-Dirac approximation would be required. The dependence of the scattering rate on the well width and depth was investigated only briefly. It was found that the escape rate increased with increasing well width until a new subband was confined to the well; this is analogous to the oscillations reported in calculated quantum well carrier capture rates. The sharpness of the rising edge of the scattering function was attributed to the proximity of the first continuum resonance relative to the top of the well. Both the step-function and Fermi-Dirac approximations suffered as the scattering function became more rounded; a more detailed study is needed to map out the dependence of the fitting parameters on the details of the well potential.

Calculated escape rates were compared with measured values for an asymmetric

GaAs/AlGaAs single quantum well studied by Cavaillès *et al* (1993). While the thermally-assisted tunnelling regime was well reproduced, the thermionic emission times were too slow by a factor of 3-5. This was attributed primarily to band non-parabolicities and the simplified continuum density of states. The discrepancy may also be due in part to uncertainties in the analysis of the raw data. The omission of other scattering mechanisms such as impurity or alloy scattering is not expected to contribute significantly to the error in the calculated escape times.

Measurements of the hole escape time from a strained InGaAsP/InP multiple quantum well laser structure were compared with the calculated escpe times. The agreement was poorer than in the asymmetric GaAs/AlGaAs well, however this was attributed to the increased complexity of the valence band structure and the resultant non-parobolicities.

It is not yet clear whether the scattering calculations presented here are innacurate or incomplete, or if the uncertainties in the material parameters are too great to overcome. Better experiments are needed to provide accurate comparisons of experiment and theory. High speed photoconductivity experiments provide the most direct access to the escape rates, and an asymmetric GaAs/AlGaAs single quantum well designed to contain only a single electron subband would be best suited to isolating the electron and hole contributions to the escape from the well. However, it is apparent from the comparisons between the experimental data and calculated escape times that accurate calculations of the thermal escape rates will require accurate band structures, including non-parabolicities.

Appendix A: Reduced Notation for the Strain and Piezoelectric Tensors.

The strain tensor is fully described by a (3×3) second rank tensor, where each component is given by

$$S_{ij} = S_{ji} = \frac{1}{2}\left(\frac{\partial u_i}{\partial x_j} + \frac{\partial u_j}{\partial x_i}\right). \tag{A.1}$$

The ij⇔ji symmetry displayed in Eq. (A.1) reduces the number of independent elements to six. In *reduced notation*, the strain tensor is written as a six-component vector where

$$xx \to 1,\ yy \to 2,\ zz \to 3,\ \ yz \to 4,\ \ zx \to 5,\ \ xy \to 6. \tag{A.2}$$

The piezoelectric polarization is given by

$$P_i = \frac{1}{\varepsilon_r}\sum_{jk} e_{ijk} S_{jk} \tag{A.3}$$

which in reduced notation becomes

$$P_i = \frac{1}{\varepsilon_r}\sum_{\alpha} h_{i\alpha} S_{\alpha}. \tag{A.4}$$

Thus, in reduced notation, the piezoelectric tensor is a 3×6 second rank tensor

$$\mathbf{h} = \begin{bmatrix} h_{x,xx} & h_{x,yy} & h_{x,zz} & h_{x,yz} & h_{x,zx} & h_{x,xy} \\ h_{y,xx} & h_{y,yy} & h_{y,zz} & h_{y,yz} & h_{y,zx} & h_{y,xy} \\ h_{z,xx} & h_{z,yy} & h_{z,zz} & h_{z,yz} & h_{z,zx} & h_{z,xy} \end{bmatrix}. \tag{A.5}$$

Appendix B: Angular Dependence of Transverse Mode Piezoelectric Scattering.

The angular dependence of the piezoelectric scattering matrix element is given by

$$a_x\beta\gamma + a_y\alpha\gamma + a_z\alpha\beta \tag{B.1}$$

which we wish to average over the plane of the well. We follow the method of Price (1980) and Zook (1964). We are required to express the wavevector, **k**, and the transverse mode polarizations, $\mathbf{a}^{(t1)}$ and $\mathbf{a}^{(t2)}$, in terms of the in-plane angle, φ, as shown in Fig. B.1. The two transverse modes are characterized by polarization vectors that are both mutually prependicular and perpendicular to the wavevector. Hence, $\mathbf{a}^{(t1)}$, $\mathbf{a}^{(t2)}$, and **k** form a set of orthogonal axes. We can arbitrarily choose one of the polarizations to lie within the xy-plane (ie: the plane of the well), as shown in the Fig. B.1. The three vectors can then be expressed in terms of the crystal axes as

$$\begin{aligned}
\mathbf{q} &= q\,(\sin\theta\sin\varphi,\ sin\theta\cos\varphi,\ cos\theta) \\
\mathbf{a}^{(t1)} &= (\cos\varphi,\ -\sin\varphi,\ 0) \\
\mathbf{a}^{(t2)} &= (-\cos\theta\sin\varphi,\ -\cos\theta\cos\varphi,\ sin\theta).
\end{aligned} \tag{B.2}$$

These can be re-written in terms of α, β, and γ as

$$\begin{aligned} \mathbf{q} &= q(\alpha, \beta, \gamma) \\ \mathbf{a}^{(t1)} &= \left(-\frac{\gamma\alpha}{\sigma}, -\frac{\gamma\beta}{\sigma}, \sigma\right) \\ \mathbf{a}^{(t2)} &= \left(\frac{\beta}{\sigma}, -\frac{\alpha}{\sigma}, 0\right) \end{aligned} \tag{B.3}$$

where

$$\sigma = \sqrt{\alpha^2 + \beta^2} \tag{B.4}$$

Substituting the expressions (B.3) in (B.1) yields

$$a_x^{(t1)}\beta\gamma + a_y^{(t1)}\alpha\gamma + a_z^{(t1)}\alpha\beta = \frac{\alpha\beta}{\sigma}\left(\sigma^2 - 2\gamma^2\right) \tag{B.5}$$

for $\mathbf{a}^{(t1)}$ and

$$a_x^{(t2)}\beta\gamma + a_y^{(t2)}\alpha\gamma + a_z^{(t2)}\alpha\beta = \frac{\gamma}{\sigma}\left(\beta^2 - \alpha^2\right) \tag{B.6}$$

for $\mathbf{a}^{(t2)}$.

To combine the contributions for the two transverse polarizations we square Eqs. (B.5) and (B.6) and add. Collecting terms and simplifying we obtain

$$\alpha^2\beta^2 + \alpha^2\gamma^2 + \beta^2\gamma^2 - (3\alpha\beta\gamma)^2 \tag{B.7}$$

for the combined angular dependence of the transverse modes.

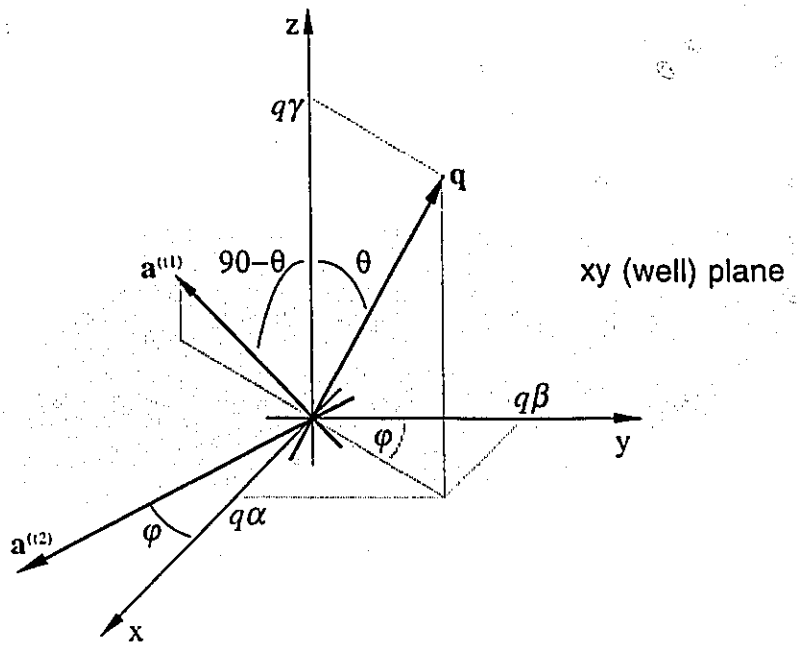

Fig. B.1: Coordinate axes defined by the wavevector and the two transverse polarization vectors in relation to the crystal axes, x, y, z. The alternate axes are rotated by an angle φ in the well plane (ie.: the xy-plane), and θ relative to the z-axis.

Appendix C: Symbol Definitions.

(listed in order of appearance)

E_c	energy of conduction band minimum
E_v	energy of valence band minimum
ΔE_c	conduction band offset
ΔE_v	valence band offset
$\mathbf{r}$	electron (hole) position vector
$\psi(\mathbf{r})$	electron (hole) spatial wavefunction
$\mathbf{u_k}(\mathbf{r})$	Bloch function of wavevector $\mathbf{k}$
$\mathbf{k}$	electron (hole) wavevector
$\phi_n(z)$	electron (hole) envelope function describing the n^{th} quantum state of the potential
V	crystal volume
E_n	energy of n^{th} quantum state
L_x, L_y, L_z	crystal dimensions in the x, y, and z directions
m^*	effective mass
w	well width
V_b	potential well depth
V_j	potential in j^{th} layer
E	electron (hole) total energy
$\mathscr{E}$	electric field
$Ai(z)$	Airy function
$Bi(z)$	Bairy function
$K_{1/3}$,$I_{1/3}$	modified Bessel functions of order 1/3
C_j, D_j	Airy and Bairy wavefunction coefficients for j^{th} layer

$\xi(E)$	confinement ratio function
τ	tunnelling lifetime
$\Gamma(E)$	Lorentzian width of energy resonance
$f(E)$	occupation factor
E_F	Fermi energy
T	temperature
$Tr(E)$	barrier transmission function
$n(E)$	electron (hole) density
$\tilde{e}$	charge on the free carrier, including its sign
j_z	z-component of the current density
v_z	z-component of the electron (hole) velocity
$g_{3D}(E)$	bulk (3D) density of states
ΔE	potential barrier height
ΔE_{eff}	effective barrier height
ΔE_0	zero field barrier height
$g_{2D}(E)$	2D density of states
$H(E)$	Heaviside step function
τ_{TE}	thermionic emission time
$\tau_s(E)$	2D-to-3D scattering function
$E_{b,eff}$	effective barrier energy
$\Delta E_{eff,i}$	effective barrier height relative to i^{th} confined level
σ	surface charge density
ε	dielectric constant
ρ	in-plane radial coordinate (cylindrical polar coordinates)
$\Delta\varphi_b$	barrier lowering
$\mathbf{j}_{drift}$	drift current density
$\mathbf{j}_{diff}$	diffusion current density
$\tau_{TT,i}$	thermally-assisted tunnelling time via i^{th} confined state
μ	elecron (hole) mobility
D_n, D_p	electron and hole diffusion coefficients
R_i	central radius of i^{th} ring-shaped bin in image charge simulation
Q_i	total charge in the i^{th} ring-shaped bin in image charge simulation
e_{eff}	effective image charge
$\mathbf{q}$	phonon wavevector
$\omega_{\mathbf{q}}$	phonon frequency for wavevector $\mathbf{q}$

$n_{b,\mathbf{q}}(\omega_{\mathbf{q}})$	occupation of phonon mode of wavevector q, from b^{th} branch
$\mathbf{R}$	lattice vector
$\mathbf{u}(\mathbf{R})$	ionic displacement
$\Omega_{\mathbf{q}}$	phonon normal coordinate
$\mathbf{a}_{\mathbf{q}}$	phonon polarization vector
N	number of unit cells in crystal
W_i	transition rate from state i
Ψ_i	total initial state wavefunction of the electron-phonon system
Ψ_f	total final state wavefunction of the electron-phonon system
$H_{e\text{-}ph}$	electron-phonon interaction Hamiltonian
dS_f	final state density of states
$\delta(E)$	Dirac delta function
$\delta_{\mathbf{q},\mathbf{q}'}$	Krönecker Delta
$\overline{M}$	unit cell reduced mass
$N^{\pm}(\omega_{\mathbf{q},b})$	phonon occupation factor - upper sign is for emission, lower sign for absorption
$C_{\mathbf{q},b}$	electron-phonon coupling constant
$G_{n',n}(q_z)$	electron-phonon overlap function
$\mathbf{P}(\mathbf{R})$	crystal polarization at $\mathbf{R}$
e^*	effective ionic charge
ω_0	LO-phonon frequency
V_0	unit cell volume
ε_p	reduced dielectric constant
ε_s	static dielectric constant
ε_∞	high frequency dielectric constant
$\rho(\mathbf{R})$	free charge density
$\varphi(\mathbf{R})$	electrostatic potential
Ξ	deformation potential tensor
Ξ_d	deformation potential for hydrostatic compression or dilation
$\mathbf{S}$	strain tensor
ρ_m	crystal mass density
$v_{s,l}$, $v_{s,t}$	speed of sound in crystal for longitudinal and transverse acoustic phonons, respectively
$\mathbf{h}$	piezoelectric tensor
ε_r	relative dielectric permittivity
α, β, γ	direction cosines

τ_s^{3D}	2D-to-3D scattering time not including phonon occupation factor
E_{start}	low energy (E_z) cutoff to integration over final states
W_0	average scattering rate (Fermi-Dirac fit to scattering function)
E_b	average effective barrier height (Fermi-Dirac fit to scattering function)
δE	scattering function transition width (Fermi-Dirac fit to scattering function)
δE_0	intercept of linear fit to δE vs. $\mathscr{E}$ (Fermi-Dirac fit to scattering function)
$d(\delta E)/d\mathscr{E}$	slope of linear fit to δE vs. $\mathscr{E}$ (Fermi-Dirac fit to scattering function)

Appendix D: Physical Constants

k_B	Boltzmann's constant	8.617086×10^{-5} eV/K
e	electronic charge	$1.602191770\times10^{-19}$ C
m_0	electron rest mass	9.109558×10^{-31} kg
$\hbar$	reduced Planck's constant ($h/2\pi$)	6.58218322×10^{-16} eV•s 1.05459198×10^{-34} J•s
ε_0	permittivity of free space	$8.854187818\times10^{-12}$ F/m

References.

Abromowitz, M., and I. A. Stegun (1964), Handbook of Mathematical Functions. Nat. Bureau of Standards, Washington, D.C.

Adachi, S. (1985), "GaAs, AlAs, and $Al_{1-x}Ga_xAs$: Material Parameters for use in research and device applications," J. Appl. Phys. **58** (3), pp. R1-R29.

Ashcroft, N. W. and N. D. Mermin (1976), Solid State Physics. Saunders College, Philadelphia.

Austin, E. J., and M. Jaros (1985), "Electronic structure of an isolated GaAs-AlGaAs quantum well in a strong electric field," Phys. Rev. B **31** (8), pp. 5569-5572.

Bambha, R., D. C. Hutchings, M. J. Snelling, P. LiKamWa, A. Miller, A. L. Moretti, R. W. Wickman, K. A. Stair, T. E. Bird, J. A. Cavaillès, and D. A. B. Miller (1993), "Carrier escape dynamics in a single quantum well waveguide modulator," Opt. and Quantum Electron. **25**, pp. S965-S970.

Bastard, G. (1981), "Superlattice band structure in the envelope function approximation," Phys. Rev. B **24** (10), pp. 5693-5697.

Bastard, G. (1982), "Theoretical investigations of superlattice band structure in the envelope-function approximation", Phys. Rev. B **25** (12), pp. 7584-7597.

Blom, P. W. M., J. E. M. Haverkort, P. J. van Hall, and J. H. Wolter (1993a), "Carrier-carrier scattering induced capture in quantum well lasers," Appl. Phys. Lett. **62** (13), pp. 1490-1492.

Blom, P. W. M., C. Smit, J. E. M. Haverkort, and J. H. Wolter (1993b), "Carrier capture into a semiconductor quantum well," Phys. Rev. B **47** (4), pp. 2072-2081.

Bransden, B. H., and C. J. Joachain (1989), Introduction to Quantum Mechanics. Longman Scientific and Technical, New York.

Brum, J. A., and G. Bastard (1986a), "Resonant carrier capture by semiconductor quantum wells," Phys. Rev. B **33** (2), pp. 1420-1423.

Brum, J. A., T. Weil, J. Nagle, and B. Vinter (1986b), "Calculation of carrier capture time of a quantum well in graded-index separate-confinement heterostructures," Phys. Rev. B. **34** (4), pp. 2381-2384.

Cavaillès, J. E., D. A. B. Miller, J. E. Cunningham, P. Li Kam Wa, and A. Miller (1992), "Simultaneous Measurements of Electron and Hole Sweep-out from Quantum Wells and Modeling of Photoinduced Field Screening Dynamics", IEEE J. Quantum Electron. **28** (10), pp. 2486-2497.

Chao, C. Y.-P., and S. L. Chuang (1992), "Spin-orbit-coupling effects on the valence-band structure of semiconductor quantum wells," Phys. Rev. B **46** (7), pp. 4110-4122.

Chen, W., and T. G. Andersson (1991), "Effect of the nonparabolic mass on the electron confinement in arbitrarily shaped quantum wells," Phys. Rev. B **44** (16), pp. 9068-9071.

Chuang, S. L. (1991), "Efficient band structure calculations of strained quantum wells," Phys. Rev. B **43** (12), pp. 9649-9661.

Crowell, C. R., and S. M. Sze (1966), "Current transport in metal-semiconductor barriers," Solid State Electron. **9**, pp. 1035-1048.

Coon, D. D. and H. C. Liu (1987), "Image Force Effects in Heterostructures and Quantum Wells," Superlattice and Microstructures **3** (1), pp. 95-98.

Drummond, T. J., and I. J. Fritz (1985), "Modulation-doped (Al, Ga)As/AlAs superlattice: electron transfer into AlAs," Appl. Phys. Lett. **47** (3), pp. 284-286.

Ekenberg, U. (1989), "Nonparabolicity effects in a quantum well: Sublevel shift, parallel mass, and Landau levels," Phys. Rev. B **40** (11), pp. 7714-7726.

Eppenga, R., M. F. H. Schuurmans, and S. Colak (1987), "New **k·p** theory for $GaAs/Ga_{1-x}As_xAs$-type quantum wells," Phys. Rev. B **36** (3), pp. 1554-1564.

Evans, J. D. (1994), The Effects of Intentionally-Induced Mismatch Strain on the Operating Characteristics and Temperature Performance of InGaAsP/InP Long Wavelength Semiconductor Lasers. Ph. D. Thesis, McMaster University, Hamilton.

Fawaz, H., J. Gest, and J. Zimmerman (1993), "A Novel Model of the Gate Current in Heterojunction FET's," IEEE Trans. Electron. Devices **40** (5), pp. 846-851.

Foreman, B. A. (1994), "Analytic model for the valence band structure of a strained quantum well," Phys. Rev. B **49** (3), pp. 1757-1773, and references contained within.

Forrest, S. R., P. H. Schmidt, R. B. Wilson, and M. L. Kaplan, (1984) "Relationship between the conduction band discontinuities and band-gap differences of InGaAsP/InP heterojunctions," Appl. Phys. Lett. **45** (11), pp. 1199-1201.

Fox, A. M., D. A. B. Miller, G. Livescu, J. E. Cunningham, and W. Y. Jan (1991), "Quantum Well Carrier Sweep Out: Relation to Electroabsorption and Exciton Saturation," IEEE J. Quantum Electron. **27** (10), pp. 2281-2295.

Fujiwara, A., Y. Takahashi, S. Fukatsu, and Y. Shiraki (1995), "Resonant electron capture in $Al_xGa_{1-x}As$/AlAs/GaAs quantum wells," Phys. Rev. B **51** (4), pp. 2291-2301.

Gabovich, A. M., and V. M. Rozenbaum (1984), "Image forces and quantum states in semiconductor heterostructures," Sov. Phys. Semicond. **18** (3), pp. 308-310.

Ghatak, A. K., K. Thyagarahan, and M. R. Shenoy (1988), "A Novel Technique for Solving the One-Dimensional Schroedinger Equation Using Matrix Approach - Application to Quantum Well Structures," IEEE J. Quantum Electron. **24** (8), pp. 1524-1531.

Ghatak, A. K., I. C. Goyal, and R. L. Gallawa (1990), "Mean Lifetime Calculations of Quantum Well Structures: A Rigorous Analysis," IEEE J. Quantum Electron. **26** (2), pp. 305-310.

Gurioli, M., J. Martinez-Pastor, M. Colocci, C. Deparis, B. Chastaingt, and J. Massies (1992), "Thermal escape of carriers out of GaAs/$Al_xGa_{1-x}As$ quantum-well structures," Phys. Rev. B **46** (11), pp. 6922-6927.

Halliday, D. P., D. Moss, S. Charbonneau, G. C. Aers, D. Landheer, F. Chatenoud, and D. Conn, (1992), "Ultrafast electron tunneling in a reverse-biased, high-efficiency quantum well laser structure," Can. J. Phys **70**, pp. 985-992.

Hensel, J. C., and G. Feher (1963), "Cyclotron Resonance Experiments in Uniaxially Stressed Silicon: Valence Band Inverse Mass Parameters and Deformation Potentials." Phys. Rev. **129** (3) pp. 1041-1062.

Hunt, N. E. J. (1991), Electro-Absorption in InGaAs-GaAs Strained-Layer Multiple Quantum Well Waveguide Modulators. Ph.D. Thesis, McMaster University, Hamilton.

Huang, K. and B. Zhu (1988), "Dielectric continuum model and Frölich interaction in superlattices," Phys. Rev. B **38** (18), pp. 13 377-13 386.

Jonsson, B. and S. T. Eng (1990), "Solving the Schrödinger Equation in Arbitrary Quantum-Well Potential Profiles Using the Transfer Matrix Method," IEEE J. Quantum Electron. **26** (11), pp. 2025-2035.

Korotkov, A. N. (1994), "Effect of the image charge on single-electron tunneling," Phys. Rev. B **49** (16), pp. 11508-11510.

Koteles, E. S. (1993), "Determining energy-band offsets in quantum wells using only spectroscopic data," J. Appl. Phys. **73** (12), pp. 8480-8484.

Landolt-Börnstein (1987), Numerical data and Functional Relationships in Science and Technology. Vol. 22 - Semiconductors, supplements and extensions to Vol. III/17, subvolume a. editor O. Madelung, Springer-Verlag, Berlin.

Larsson, A., P. A. Andrekson, S. T. Eng, and A. Yariv (1988), "Tunable Superlattice *p-i-n* Photodetectors: Characteristics, Theory and Applications," IEEE J. Quantum Electron. **24** (5) pp. 787-801.

Lau, K. Y., and A. Yariv (1985), Semiconductors and Semimetals, Vol. 22, Part B, edited by W. T. Tsang, Academic Press, Orlando.

Liang, L. and C. S. Lent (1990), "Escape from quantum wells via polar optical phonon scattering," J. Appl. Phys. **68** (4), pp. 1741-1749.

Lin, T. P., and G. Eng (1989), "Thermionic emission including both space-charge and image forces," J. Appl. Phys. **65** (8), pp. 3205-3211.

Liu, H. C., A. G. Steele, M. Buchanan, and Z. R. Wasilewski (1993), "Dark current in quantum well infrared photodetectors," Appl. Phys. Lett. **73** (4), pp. 2029-2031.

Lorrain, P., D. R. Corson, F. Lorrain (1988), Electromagnetic Fields and Waves. W. H. Freeman and Co., New York.

Manning, R. J., P. J. Bradley, A. Miller, J. S. Roberts, P. Mistry, and M. Pate (1989), "Electric-field-dependent photoresponse of multiple quantum well modulator," Electron. Lett. **25** (4), pp. 269-270.

Mead, C. A., E. H. Snow, and B. E. Deal (1966), "Barrier lowering and field penetration at metal-dielectric interfaces," Appl. Phys. Lett. **9** (1), pp. 53-55.

Mendez, E. E. (1986), "Electronic Mobility in Semiconductor Heterostructures," IEEE J. Quantum Electron. **QE-22** (9), pp. 1720-1727.

Meshkov, S. V. (1986), "Tunneling of electrons from a two-dimensional channel into the bulk," Sov. Phys. JETP **64** (6), pp. 1337-1343.

Miller, A., C. B. Park, and P. LiKamWa (1992), "Time resolved measurements of cross-well transport in a multiple quantum well p-i-n modulator at high photogenerated carrier densities," Appl. Phys. Lett. **60** (1), pp. 97-99.

Miller, D. A. B., D. S. Chemla, T. C. Damen, A. C. Gossard, W. Wiegmann, T. H. Wood and C.A. Burrus (1984a), "Bandedge electro-absorption in quantum well structures: the quantum confined Stark effect," Phys. Rev. Lett. **53** (22), pp. 2173-2177.

Miller, D. A. B., D. S. Chemla, T. C. Damen, A. C. Gossard, W. Wiegmann, T. H. Wood and C.A. Burrus (1984b), "Novel hybrid optically bistable switch: The quantum well self-electro-optic effect device," Appl. Phys. Lett. **4** (1), pp. 13-15.

Moss, D., D. Landheer, D. Conn, D. Halliday, S. Charbonneau, G. Aers, R. Barber, and F. Chatenoud (1992a), "High Speed Photodetection in a Reverse Biased GaAs/AlGaAs GRINSCH SQW Laser Structure," Photonics Technol. Lett. **4** (6), pp. 609-611.

Moss, D., D. Halliday, S. Charbonneau, G. Aers, D. Landheer, R. Barber, and F. Chatenoud and D. Conn (1992b), "Ultrafast electron tunnelling times in reverse biased quantum well laser structures," *in* SPIE - International Society for Optical Communications. Proceedings of "Quantum Wells and Superlattice Physics IV." Vol. 1675, *edited by* G. H. Döhler and E.S. Koteles, pp. 418-427.

Moss, D. J., T. Ido, and H. Sano (1994), "Calculation of Photogenerated Carrier Escape Rates from GaAs/$Al_{1-x}Ga_xAs$ Quantum Wells," IEEE J. Quantum Electron. **30** (4), pp. 1015-1026.

Nag, B. R., and S. Mukhopadhyay, (1991), "Band offset in InP/$Ga_{0.47}In_{0.53}As$ heterostructures," Appl. Phys. Lett. **58** (10), pp. 1056-1058.

Nagarajan, R., T. Kamiya, A. Kasukawa, and H. Okamoto (1989), "Observation of ultrashort (<4 ps) gain-switched optical pulses from long wavelength multiple quantum well lasers," Appl. Phys. Lett. **55** (13), pp. 1273-1275.

Nye, J. F. (1957), Physical Properties of Crystals; Their Representation by Tensors and Matrices, Clarendon Press, Oxford.

Press, W. H., S. A. Teukolsky, W. T. Vetterling, B. P. Flannery (1992), Numerical Recipes in C, 2nd Ed. Cambridge University Press, Cambridge.

Price, P. J. (1981), "Two-Dimensional Electron Transport in Semiconductor Layers. I. Phonon Scattering," Ann. Phys. **133**, pp. 217-239.

Queisser, I., V. Härle, A Dörnen, and F. Scholz (1994), "Band discontinuity of strained-layer GaInAs/GaInAsP heterostructures," Appl. Phys. Lett. **64** (22), pp. 2991-2993.

Ridley, B. K. (1982), "The electron-phonon interaction in quasi-two-dimensional semiconductor quantum-well structures," J. Phys. C: Solid State Phys. **15**, pp. 5899-5917.

Ridley, B. K. (1993), Quantum Processes in Semiconductors, 3rd ed. Clarendon Press, Oxford.

Rössler, U (1984), "Nonparabolicity and warping in the conduction band of GaAs," Solid State Commun. **49** (10), pp. 943-947.

Rücker, H., E. Molinari, and P. Lugli (1992), "Microscopic calculation of the electron-phonon interaction in quantum wells," Phys. Rev. B **45** (12), pp. 6747-6756.

Ruden, P. P., C. J. Han, and M. Shur (1988), "Gate current of modulation-doped field-effect transistors," J. Appl. Phys. **64** (3), pp. 1541-1546.

Schneider, H., and K. Von Klitzing (1988), "Thermionic emission and Gaussian transport of holes in a GaAs/$Al_xGa_{1-x}As$ multiple-quantum-well structure," Phys. Rev. B **38** (9), pp. 6165.

Shorthose, M. G., J. F. Ryan, and A. Moseley (1989), "Phonon-assisted tunnelling of photoexcited carriers from InGaAs quantum wells in applied electric fields," Solid State Electron. **32** (12), pp. 1449-1453.

Singh, J. (1993), Physics of Semiconductors and their Heterostructures. McGraw-Hill, New York.

Smythe, W. R. (1939), Static and Dynamic Electricity. McGraw-Hill, New York.

Soucail, B., P. Voisin, M. Voos, D. Rondi, J. Nagle, and B. de Crémoux (1990), "Optical investigation of the band offsets in an InGaAs-InGaAsP-InP double-step quantum well," Superlattices and Microstruct. **8** (3), pp. 279-282.

Sotirelis, P. and K. Hess (1994), "Electron capture in GaAs quantum wells," Phys. Rev. B **49** (11), pp. 7543-7547.

Stillman, G. E., and C. M. Wolfe (1976), "Electrical characterization of epitaxial layers," Thin Solid Films **31**, pp. 69-88.

Susa, N. and T. Nakahara (1993), "Design of AlGaAs/GaAs quantum wells for electroabsorption modulators," Solid-St. Electron. **36** (9) pp. 1277-1287.

Sze, S. M., C. R. Crowell, and D. Kahng, (1964), "Photoelectric Determination of the Image Force Dielectric Constant for Hot Electrons in Schottky Barriers," J. Appl. Phys. **35** (8), pp. 2534-2536.

Sze, S. M. (1981), Physics of Semiconductor Devices. John Wiley & Sons, New York.

Takasaki, B. W., J. S. Preston, J. D. Evans, J.G. Simmons, and N. Puetz (1993), "Observation of separate escape of electrons and holes from strained InGaAsP multiple quantum well laser structures," Appl. Phys. Lett. **62** (20), pp. 2525-2527.

Takasaki, B. W. (1992), Relaxation of Optically Generated Carriers in Strained InGaAsP Multiple Quantum Well Laser Structures. M. Sc. Thesis, McMaster University, Hamilton.

Thibaudeau, L. and B. Vinter (1994), "Phonon-assisted carrier capture into a quantum well in an electric field," Appl. Phys. Lett. **65** (16), pp. 2039-2041.

Trzeciakowski, W., and M. Gurioli (1991), "Electric-field effects in semiconductor quantum wells," Phys. Rev. B **44** (8), pp. 3880-3890.

Tsai, C.-Y., L. F. Eastman, Y.-H. Lo, and C.-Y. Tsai (1994a), "Breakdown of thermionic emission theory for quantum wells," Appl. Phys. Lett. **65** (4), pp. 460-462.

Tsai, C.-Y., L. F. Eastman, Y.-H. Lo, and C.-Y. Tsai (1994b), "Carrier Capture and Escape in Multisubband Quantum Well Lasers," IEEE Photon. Technol. Lett. **6** (4), pp. 1088-1090.

Uomi, K., S. Sakaki, T. Tsuchiya, and N. Chinone (1990), "Novel method of determining conduction-band discontinutities by using monolayer energy splitting in quantum-well structures," J. Appl. Phys. **67** (2), pp. 904-907.

Walukiewicz, W., H. E. Ruda, J. Lagowski, and H. C. Gatos (1984), "Electron mobility in modulation-doped heterostructures," Phys. Rev. B **30** (8), pp. 4571-4582.

Weisbuch, C., and B. Vinter (1991), Quantum Semiconductor Structures. Academic Press Inc., Boston.

Wood, T. H., C. A. Burrus, A. H. Gnauck, and J. M. Wiesenfeld, D. A. B. Miller, D. S. Chemla, and T. C. Damen (1985), "Wavelength-selective voltage-tunable photodetector made from multiple quantum wells," Appl. Phys. Lett. **47** (3), pp.190-192.

Wu, C. M., and E. S. Yang (1979), "Carrier transport across heterojunction interfaces," Solid State Electron. **22**, pp. 241-248.

Zhu, Q. S., S. M. Mou, X. C. Zhou, and Z. T. Zhong (1993), "Determination of the conduction-band offset of a single AlGaAs barrier layer using deep level transient spectroscopy," Appl. Phys. Lett.**62** (22), pp. 2813-2814.

Zook, J. D. (1964), "Piezoelectric Scattering in Semiconductors," Phys. Rev. **136** (3A), pp. A869-A878.